HELLENIC REPUBLIC
National and Kapodistrian University of Athens
EST. 1837

SCHOOL OF SCIENCE - DEPARTMENT OF PHYSICS
SECTION OF ASTROPHYSICS, ASTRONOMY AND MECHANICS

BLACK HOLES, RADIATION, AND ACCRETION DISKS

KOUTSANTONIOU ELPIDA – LEELA

DOCTOR OF PHILOSOPHY
DISSERTATION

ATHENS 2023

ΕΛΛΗΝΙΚΗ ΔΗΜΟΚΡΑΤΙΑ
Εθνικόν και Καποδιστριακόν Πανεπιστήμιον Αθηνών
ΙΔΡΥΘΕΝ ΤΟ 1837

ΣΧΟΛΗ ΘΕΤΙΚΩΝ ΕΠΙΣΤΗΜΩΝ – ΤΜΗΜΑ ΦΥΣΙΚΗΣ
ΤΟΜΕΑΣ ΑΣΤΡΟΦΥΣΙΚΗΣ, ΑΣΤΡΟΝΟΜΙΑΣ ΚΑΙ ΜΗΧΑΝΙΚΗΣ

ΜΕΛΑΝΕΣ ΟΠΕΣ, ΑΚΤΙΝΟΒΟΛΙΑ
ΚΑΙ ΔΙΣΚΟΙ ΠΡΟΣΑΥΞΗΣΗΣ

ΚΟΥΤΣΑΝΤΩΝΙΟΥ ΕΛΠΙΔΑ – ΛΗΛΑ

ΔΙΔΑΚΤΟΡΙΚΗ ΔΙΑΤΡΙΒΗ

e-mail: `leelamk@phys.uoa.gr`

ΑΘΗΝΑ 2023

To D., F., K., P. & S. Thicker

Also in remembrance of our guide to the stars
Dionysis P. Simopoulos

Let the horizon lead
Onto the ether of the night
Draped across the burning heavens
Flying homeward like a bird of the soul

Now is the time to leave
We lie awake, we stand afire
At the edge of the world
Above a myriad of light
Below the mantle of the stars
And strangely they fall

Shattered into a million brighter stars
Each fragile, naked, rare
Scattered across forever
Out from creation's core
An end beyond compare

CONTENTS

FIGURES

TABLES

FOOTNOTES & LINKS

VARIABLES

Latin

a	Black hole spin parameter
a^{α}, a_{α}	Four-acceleration contravariant and covariant components
a_{ν}	Absorption coefficient at frequency ν
B, B_j	Magnetic field and magnetic field three-components
B_{ν}	Planck function for frequency ν
c	Speed of light
$\mathrm{d}\Omega$, $\mathrm{d}\tilde{\Omega}$	Unit solid angle
$-e$	Electron charge
$e^{\alpha}_{\hat{\mu}}$, $e^{\hat{\mu}}_{\alpha}$	BL – LNRF transformation tensor
E	Particle total energy
$\mathcal{E}^{\mu}$	Impressed electromotive field
f^{α}	Four-force components
f_e, f_i, f_p	Radiation force on an electron, an ion, and a proton
f^{μ}_{PR}	Poynting – Robertson four-force components
f^{μ}_{rad}	Radiation four-force components
F^{a}	Four-flux components
F_{grav}	Classical force of gravity
F_{PR}	Classical Poynting – Robertson drag force
F_{rad}	Classical radiation force
$g^{\alpha\beta}$, $g_{\alpha\beta}$	Metric components
G	Gravitational constant
h	Accretion disk half-height
h, $\hbar$	Planck and reduced Planck constant
h^{α}_{β}, $h^{\alpha\beta}$	Projection tensor
$\mathbb{H}$	Hamiltonian

I	Frequency integrated specific intensity of the radiation
I_ν	Specific intensity at frequency ν
$\mathcal{I}_\nu$	Lorentz invariant specific intensity
j	Black hole dimensionless angular momentum
j_ν	Emission coefficient at frequency ν
$k, l, m, \ldots$ (Latin)	Space components: ϕ, r, θ
k	Boltzmann constant
k^a, k_α	Photon four-momentum contravariant and covariant components
$L, \bar{L}$	Particle angular momentum components and vector
$\mathbb{L}$	Lagrangian
$\mathcal{L}$	Luminosity of radiation source
$\mathcal{L}_{Edd}$	Eddington luminosity of radiation source
m	Particle rest mass, unless stated otherwise
$\bar{m}$	Mean molecular weight
m_e, m_i, m_p	Electron, ion, and proton mass
M	Central object mass
$\mathcal{M}$	Accretion disk mass
$\dot{\mathcal{M}}$	Accretion rate
$\dot{\mathcal{M}}_{Edd}$	Eddington accretion rate
n	Number density
$n^a, n^{\hat{a}}$	Unitary spacelike vector for the photon trajectory
n_p	Material pressure parameter determining the disk's vertical structure
N	Number of particles examined
$\mathfrak{N}$	Phase space number density
$p, \bar{p}$	Momentum components and vector
p^a, p_α	Massive particle four-momentum contravariant and covariant components
P	Radiation power
P	Material pressure
$\mathcal{P}r_m$	Magnetic Prandtl number
$\mathcal{P}r_m^{crit}$	Critical magnetic Prandtl number value
Q	Carter constant
r	Radius
$\bar{r}$	Radial distance or position vector
$r_{inner}, r_{outer}, r_{center}$	Accretion disk's inner, outer, and center radius
r_{ISCO}	Radius of the ISCO
r_g	Gravitational radius
r_K	Radius of Keplerian rotation speed
r_S	Schwarzschild radius

r_{torus}	Cross section radius of the circular cross section torus
s	Proper length, unless stated otherwise
t	Time
T	Temperature
$\mathbb{T}$	Particle motion effective potentials function
$T^{\alpha\beta}$	Radiation stress – energy tensor
u^{α}, u_{α}	Particle four-velocity contravariant and covariant components
$u_e^{\alpha}, u_p^{\alpha}$	Four-velocity components for an electron and a proton
v	Viscosity, viscous diffusion rate
$\mathcal{V}$	Phase space volume
$\bar{V}$	Three-velocity vector
V_j	Three-velocity components
$\mathbb{V}_r, \mathbb{V}_{\theta}$	Particle motion effective potentials
x^{α}	Four-position components
x_e^{μ}, x_p^{μ}	Four-position components for an electron and a proton

Greek

$\alpha, \mu, \nu, \ldots$ (Greek)	Spacetime components: t, ϕ, r, θ
β	Ratio of gas pressure to total pressure
γ	Lorentz factor
Γ	Radiation pressure supported polish doughnut polytropic index
$\Gamma^{\mu}_{\alpha\beta}$	Christoffel symbols
$\Delta, \Sigma, \mathrm{A}$	Kerr metric functions
η	Magnetic diffusivity
θ	Poloidal angle from the vertical axis
ι	Accretion disk inclination relative to the line of sight
λ	Affine parameter for photon trajectory
μ	Target particle rest mass, unless stated otherwise
ν	Frequency
ρ	Volumetric mass density
σ	Particulate cross section
σ_{pl}	Plasma conductivity
σ_{SB}	Stefan – Boltzmann constant
σ_T	Thomson cross section
τ	Proper time
τ_ν	Optical depth at frequency ν
$\upsilon, \vec{\upsilon}$	Generic particulate three-velocity and three-velocity vector, unless stated otherwise
υ^α	Photon in fluid four-velocity, unless stated otherwise
ϕ	Azimuthal angle
$\hat{\phi}$	Unitary azimuthal angle vector
ψ	Angle between source motion direction and photon emission
Ψ	Magnetic flux
ω	Spacetime angular velocity
$\vec{\omega}$	Angular velocity vector
Ω	Orbit coordinate angular velocity

Acknowledgements

I would like to thank from the bottom of my heart my friends and colleagues Theofanis Gkountras, Dr. Nikolaos Davis, and Dr. Stavros Dimitrakoudis for lending me and allowing me to use their personal home computers to run calculations and simulations for my research.

I would also like to deeply thank my friends and colleagues Dr. Stavros Dimitrakoudis, Dr. Konstantinos Karampelas, Dr. Dimitrios Millas, and Georgios Xystouris (soon Dr.), for trying to get me other available computers for me and my work.

Furthermore, I would like to profoundly thank Dr. Stavros Dimitrakoudis for our conversations and his valuable comments.

Additionally, I would like to extend my greatest gratitude to Dr. George Pappas for his valuable comments and precious time.

Moreover, I would like to thank Dr. Dimitrios Millas for his very useful comments and additions.

Additionally, I would like to thank Dr. Alexander Hillaris for allowing me for years to use the computers of his office for my work.

Furthermore, sincere gratitude is extended to Dr. Konstantinos N. Raftopoulos for our conversations.

In addition, I would like to thank colleague Dr. Achilles Strantzalis and Sophia Zarbuti for checking and booting the University computers after power outages, when they were closer to the University than I was.

Last but certainly not least, deepest thanks are due to P.K. for the contribution, ethics, and the leap of faith.

Finally, I would like to thank all the people that helped me in the course of my work, even though they might not be mentioned here by name.

Abstract

In this work, we study the thermal radiation emitted by the material of an accretion disk that swirls around an astrophysical black hole. This radiation has important repercussions on systems in strong gravity environments due to the consequent emergence of Poynting – Robertson braking. This force alters the plasma electron kinematics and restates the matter equilibrium conditions and hence the disk stability. We formulate and execute computational calculations in curved spacetimes in order to determine if the observed radiation is as negligible as it is often considered to be, or if it is strong enough to bring about modifications. We additionally investigate which disk models of different properties display stronger exerted radiation forces, particular accelerations, or notable phenomena.

The results of our study reveal that these radiation forces are indeed noteworthy and cannot be deemed inconsequential or redundant in studies involving accretion disks orbiting massive objects. The various disk models examined demonstrate particular properties each, along with characteristics that do not appear in the same manner for the rest of the models. Our results also suggest that the primary attribute determining the magnitude of the recorded radiation forces is not the disk volume, but instead the density gradient. Furthermore, by using the generated radiation data, we can recalculate the stability of the particle trajectories. These data demonstrate that the thermal radiation can effortlessly lead to prompt material escape, a fact that is counteracted, however, by the electric and magnetic forces acting at particle level. Moreover, we present numerically generated images of the anticipated stellar black hole observations and a related method used to estimate the black hole spin with promising results.

Finally, we examine the consequences of the electron orbit modification and the ensuing electromagnetic phenomena. We study the Cosmic Battery mechanism and ascertain the capability of magnetic field generation by the radiation without the presence of a seed field. Our results show that there are several cases where this mechanism can generate equipartition-level magnetic fields in adequately short timescales.

Πρόλογος

Τα μαγνητικά πεδία στο Σύμπαν είναι ένα από τα πιο πολύπλοκα και δαιδαλώδη θέματα της Αστροφυσικής και έχει απασχολήσει πολλούς επιστήμονες του κλάδου για πολλά χρόνια. Τα μαγνητικά αυτά πεδία φαίνεται να εμφανίζονται παντού στο Σύμπαν και να είναι παρόντα σχεδόν σε όλες τις αστροφυσικές διαδικασίες και μάλιστα να παίζουν σημαντικούς ρόλους σε αυτές. Τα παρατηρούμε από τη γένεση και τη ζωή των άστρων ως τις μελανές οπές και από τα τυπικά και συνήθη ηλιακά φαινόμενα ως τη δημιουργία του ίδιου του Σύμπαντος. Παρόλα αυτά όμως, ακόμα και ως σήμερα δε γνωρίζουμε εάν αυτά τα πεδία προϋπάρχουν των διαδικασιών που τα απαιτούν ή και αν δημιουργούνται κατά τη διάρκεια αυτών. Παραμένει επομένως άγνωστο το που λαμβάνει χώρα η γένεση των μαγνητικών αυτών πεδίων και μέσω ποιών διαδικασιών. Δε διαθέτουμε ακόμη γνώση του κατά πόσον αυτά τα πεδία υπάρχουν διεσπαρμένα στο χώρο και συμπυκνώνονται σε συγκεκριμένα σημεία, ή αν αντιθέτως δημιουργούνται σε συγκεκριμένα σημεία και στη συνέχεια διαχέονται προς τα έξω. Οι ερωτήσεις είναι πολλές για όλα αυτά τα ζητήματα και οι απαντήσεις αναζητούνται με επιμονή για δεκαετίες, χωρίς όμως να έχουν βρεθεί με βεβαιότητα και χωρίς αμφιβολίες ως και σήμερα.

Τα μοντέλα που έχουν προταθεί ανά τα χρόνια σαν απαντήσεις στα παραπάνω είναι δεκάδες, το καθένα με τα δικά του προτερήματα και μειονεκτήματα. Σε γενικές γραμμές όμως, δε φαίνεται να υπάρχουν αρκετές κοινές γραμμές ή συμπεράσματα για την προέλευση των μαγνητικών πεδίων καθώς και τις διαδικασίες δημιουργίας τους. Στη συντριπτική πλειοψηφία των φαινομένων όπου η ύπαρξή τους είναι απαραίτητη, θεωρούμε εν τέλει ότι αυτά τα πεδία έρχονται στο σημείο που εξετάζουμε από κάπου «απέξω» από το σύστημα. Ωστόσο, εξακολουθούμε να μη γνωρίζουμε ποια είναι η προέλευσή τους, ποιες οι διαδικασίες δημιουργίας και μεταφοράς τους, ακόμα και κατά πόσο είναι δυνατόν να διαχωρίσουμε τα διάφορα φαινόμενα που μελετάμε από την ύπαρξη και τη δημιουργία των ίδιων των μαγνητικών πεδίων.

Η παρούσα έρευνα ξεκίνησε με σκοπό τη μελέτη μιας διαδικασίας που έχει την ικανότητα να δημιουργήσει μαγνητικά πεδία εκ του μηδενός, παρουσία διαφόρων ειδών δίσκων προσαύξησης και της θερμικής τους ακτινοβολίας. Ειδικότερα, θελήσαμε να μελετήσουμε έναν μηχανισμό παραγωγής μαγνητικών πεδίων εφαρμόζοντας ένα φαινόμενο που πρώτα προτάθηκε και παρατηρήθηκε σε κόκκους σκόνης που περιφέρονται σε τροχιές γύρω από τον Ήλιο. Αυτό είναι το φαινόμενο Poynting – Robertson, το οποίο είναι γνωστό και ως πέδηση

Poynting – Robertson. Αυτό προέρχεται από τις πρώτες παρατηρήσεις του φαινομένου εντός του Ηλιακού Συστήματος. Σε αυτό το περιβάλλον, παρότι τα ηλιακά φωτόνια εκπέμπονται κινούμενα ακτινικά προς τα έξω, εξαναγκάζουν τους περιφερόμενους κόκκους σκόνης που τα απορροφούν να επιβραδύνονται και τελικά να προσπίπτουν στον Ήλιο, τη Γη ή οποιοδήποτε άλλο γειτονικό μαζικό σώμα. Η δύναμη αυτή είναι σχετικιστικής προέλευσης ακόμη και σε πρώτη προσέγγιση και είναι ανάλογη της αζιμουθιακής ταχύτητας του σωματιδίου στόχου. Ένας απλός, μη σχετικιστικός υπολογισμός δίνει ότι μια εκτίμηση της δύναμης της ακτινοβολίας f_{rad} $(1 dyne = 1 g \cdot cm/s^2)$ στην r και τη ϕ κατεύθυνση αντίστοιχα, για ηλεκτρόνια που περιφέρονται γύρω από ένα άστρο λαμπρότητας $\mathcal{L}$ (erg/s) είναι:

$$f_{rad}^{r} = \frac{\mathcal{L}\sigma_T}{4\pi r^2 c},$$

$$f_{rad}^{\phi} \equiv f_{PR}^{\phi} = -f_{rad}^{r}\frac{V_\phi}{c} = -\frac{\mathcal{L}\sigma_T V_\phi}{4\pi r^2 c^2},$$

όπου V_ϕ (cm/s) είναι η αζιμουθιακή τρία-ταχύτητα του στόχου, c (cm/s) η ταχύτητα του φωτός, σ_T η διατομή Thomson (cm^2) και r (cm) η ακτινική απόσταση του στόχου από το κεντρικό αντικείμενο.

Στην παρούσα εργασία επιθυμούμε να μελετήσουμε μελανές οπές με θερμούς δίσκους προσαύξησης που περιφέρονται γύρω τους και παράγουν σημαντικές ποσότητες θερμικής ακτινοβολίας. Η ακτινοβολία αυτή, σε αντίθεση με τη συνήθη αντιμετώπισή της, είναι πολύ συχνά αξιόλογα ισχυρή και απέχει μακράν από το να μπορεί να θεωρηθεί αμελητέα. Ο πρωτεύων στόχος της παρούσας μελέτης είναι να κατασκευαστούν υπολογιστικοί κώδικες που να προσομοιάζουν περιβάλλοντα με δίσκους προσαύξησης υψηλής θερμοκρασίας που περιφέρονται γύρω από συμπαγή αντικείμενα. Οι δίσκοι αυτοί αναμένεται να ακτινοβολούν θερμικά και να παράγουν πολύπλοκα πεδία ακτινοβολίας, τα οποία περιπλέκονται περεταίρω λόγω των παρόντων σχετικιστικών φαινομένων που εμφανίζονται σε συστήματα ισχυρής βαρύτητας. Επιθυμούμε επομένως να συζητήσουμε τα παραχθέντα αποτελέσματα και να εξάγουμε συμπεράσματα σχετικά με τα παρατηρούμενα φαινόμενα σχετικιστικής οπτικής, τη μετρούμενη ένταση και κατανομή της ακτινοβολίας, καθώς και τη σταθερότητα αλλά και την εξέλιξη του εκάστοτε μοντέλου δίσκου. Για παράδειγμα, αναλογιζόμαστε τη δυνατότητα των ασκούμενων δυνάμεων ακτινοβολίας να επηρεάζουν ή και να πυροδοτούν τις διαδικασίες προσαύξησης υλικού. Επιπλέον, μελετάμε την πιθανότητα εμφάνισης διαφορετικών φαινομένων και αντιδράσεων στα ποικίλα πρότυπα δίσκων, αλλά και τη σχέση τους με τα διάφορα γεωμετρικά χαρακτηριστικά αυτών, τις βαθμίδες πυκνότητας και θερμοκρασίας και άλλα.

Αναλογιζόμαστε και επιχειρούμε έπειτα να επεκτείνουμε τα συμπεράσματά μας για τα επακόλουθα δυναμικά φαινόμενα που προέρχονται από αυτές τις εκτεταμένες και ιδιαίτερες πηγές ακτινοβολίας. Τα φαινόμενα που προκύπτουν λόγω αυτών των σύνθετων διαδικασιών έχουν, όπως αναμένεται, επιπτώσεις πολύ πιο σύνθετες από αυτές που μπορούν να διακριθούν από τις παραπάνω εξισώσεις. Μια άμεση συνέπεια αυτών των διαδικασιών είναι η επιβράδυνση των ηλεκτρονίων και επομένως η γένεση αζιμουθιακού ηλεκτρικού ρεύματος εντός του δίσκου. Η διεργασία αυτή στη συνέχεια οδηγεί στη δημιουργία και στη διεύρυνση πολοειδών βρόγχων μαγνητικού πεδίου που σταδιακά γεμίζουν το χώρο του αντικειμένου και έπειτα επεκτείνονται και έξω από αυτόν.

Ξεκινάμε την παρουσίαση της δουλειάς μας με μια ιστορική αναδρομή σχετικά με την έρευνα πάνω στο φαινόμενο και τις απόπειρες εξήγησής του, καθώς και των προβλημάτων που προκλήθηκαν. Κοιτάμε έτσι τις πρώτες προσπάθειες επεξήγησης και τα πρώτα αποτελέσματα που δόθηκαν από ονομαστούς φυσικούς του $20^{ου}$ αιώνα όπως ο J. H. Poynting, ο H. P. Robertson, ο J. Larmor, ο H. N. Russell και ο L. Page.

Στην επόμενη ενότητα συνεχίζουμε δίνοντας όλα τα μαθηματικά εργαλεία που θα χρησιμοποιήσουμε για τη μελέτη του αντικειμένου. Παρουσιάζουμε τις μετρικές Minkowski, Schwarzschild και Kerr και επιπροσθέτως εισάγουμε την απαραίτητη έννοια των τοπικά μη περιστρεφόμενων συστημάτων ή των παρατηρητών μηδενικής στροφορμής. Στη συνέχεια χρησιμοποιούμε τα προαναφερθέντα εργαλεία για να εξετάσουμε τροχιές μαζικών και άμαζων σωματιδίων σε τέτοια περιβάλλοντα. Έπειτα, συζητάμε την ακτινοβολία και τις εξισώσεις κίνησης των διαφόρων σωματιδίων, κατασκευάζοντας και επιλύοντας την Εξίσωση Διάδοσης Ακτινοβολίας σε κλασσική μορφή καθώς και τη Γενική Σχετικιστική Εξίσωση Διάδοσης Ακτινοβολίας. Συνεχίζουμε μετά εξηγώντας πιθανά προβλήματα που συναντάμε σε ιδιάζοντα περιβάλλοντα, όπως πολύ πυκνοί δίσκοι προσαύξησης ή δίσκοι με ιδιαίτερα μεγάλη βαθμίδα πυκνότητας.

Αμέσως μετά, παρουσιάζουμε και εξηγούμε μοντέλα δίσκων προσαύξησης που αναφέρονται συχνά και χρησιμοποιούνται σε αστροφυσικές εφαρμογές. Έπειτα, κατασκευάζουμε και επεξηγούμε τα διάφορα χρησιμοποιούμενα πρότυπα οπτικά πυκνών, διαφανών, ημιδιαφανών δίσκων, καθώς και συνδυασμός αυτών. Επίσης αναφέρουμε και προτείνουμε κάποια επιπλέον γεωμετρικά και φυσικά πρότυπα δίσκων που μπορούν να χρησιμοποιηθούν για επέκταση των προγραμμάτων μας.

Στην επόμενη ενότητα, συζητάμε τη μέθοδο προσέγγισης των διαφόρων μερών της έρευνάς μας και παρουσιάζουμε τις πέντε κύριες οικογένειες κωδίκων που έχουμε κατασκευάσει και χρησιμοποιούμε στη μελέτη μας για τα διάφορα αντικείμενά της. Επίσης, παραθέτουμε αποτελέσματα αυτών των κωδίκων και δείχνουμε έτσι εικόνες αντικειμένων, τροχιές φωτονίων, διαγράμματα πυκνότητας δυνάμεων, μορφές δίσκων προσαύξησης, τροχιές σωματιδίων που περιλαμβάνουν επιδράσεις ακτινοβολίας και παρουσιάζουμε επίσης και τη μέθοδό μας για την αύξηση της ανάλυσης των αποτελεσμάτων των προσομοιώσεων.

Στο τελευταίο κεφάλαιο συζητάμε το πρότυπο της Κοσμικής Μπαταρίας. Παρουσιάζουμε το μηχανισμό και εξηγούμε τη διαδικασία της μετατροπής ενέργειας. Το υπό μελέτη σύστημα αρχικά κατέχει, μεταξύ άλλων, μεγάλες ποσότητες θερμότητας αποθηκευμένη στο υλικό του δίσκου. Αυτή η ενέργεια εκπέμπεται με τη μορφή θερμότητας και επαναρροφάται από το υλικό μεταβάλλοντας την κινηματική του κατάσταση. Αυτό επιφέρει αλλαγές στο σύστημα και οδηγεί στην εμφάνιση ηλεκτρικών φαινομένων και κατά συνέπεια στη γένεση επακόλουθων μαγνητικών πεδίων από το μηδέν. Ως εκ τούτου, μελετάμε πως η Κοσμική Μπαταρία μπορεί να εκμεταλλευτεί διάφορα χαρακτηριστικά των διάφορων ιδιοτήτων των δίσκων και να δημιουργήσει ισχυρότερα μαγνητικά πεδία που διαχέονται πιθανόν και στο χώρο. Τέλος, εκτιμούμε την επιρροή του μηχανισμού στην εξέλιξη πολυπλοκότερων συστημάτων, όπως τα ζεύγη αστέρων ακτινών Χ και ειδικότερα της μικρής κλίμακας μεταβλητότητάς τους και του επαναλαμβανόμενου διαγράμματος σκληρότητας – έντασης.

CHAPTER 1

INTRODUCTION

1.1. Preface

Magnetic fields in the Universe are one of the most puzzling questions and greatest mysteries Astrophysics has faced over the years. Magnetic fields seem to appear everywhere in the Universe and play very important parts in almost every astrophysical process, from the birth and life of stars to black holes, and from typical Solar phenomena to the creation of the Universe itself. Still to the present day, however, no one can certainly say if these fields preexist the aforementioned processes or are created by the processes themselves. It remains thus unknown where and how they are created, if they exist spread out in space and at times they concentrate in a certain point or if, on the contrary, they are created in specific places and then diffuse outward. There are many such questions and the answers have been passionately sought out with perseverance for decades without, nonetheless, been definitively discovered.

The various models proposed as answers to the above questions over the years are hundreds, each with its own advantages and disadvantages. In general, nevertheless, there does not appear to be a common ground about magnetic fields and their origin. In the vast majority of the cases where their existence is necessary, we eventually assume that these fields are preexistent and come from somewhere "outside" the system we examine. We, however, do not possess any knowledge of their origin, the procedures of their creation, how they are brought in, or if it is at all even possible to separate the phenomena we study from the existence and the creation of the magnetic field itself.

This work started in order to study the possibility of magnetic field generation in the assorted kinds of accretion disks utilizing their thermal radiation. Specifically, we attempted to investigate a process of producing magnetic fields in the Universe by applying a phenomenon first observed and described for dust grains orbiting the Sun, the "Poynting – Robertson effect". This phenomenon is additionally often called a "drag". This stems from its first description and ramifications within the Solar System. In this setup, even though the Solar photons are emitted radially outward, they force the dust particulates in orbit absorbing them to gradually brake and infall onto the Sun, the Earth, or any other nearby massive object. The origin of this force is purely relativistic, even to the first order, as it is proportional to the absorbing matter's azimuthal velocity. A plain nonrelativistic approximation of the radiation f_{rad} or the Poynting – Robertson force f_{PR} $(1 dyne = 1 g \cdot cm/s^2)$ exerted in the r and the ϕ direction respectively, on electrons orbiting a central source of luminosity $\mathcal{L}$ (erg/s) is:

$$\begin{aligned} f_{rad}^{r} &= \frac{\mathcal{L}\sigma_T}{4\pi r^2 c}, \\ f_{rad}^{\phi} &\equiv f_{PR}^{\phi} = -f_{rad}^{r}\frac{V_\phi}{c} = -\frac{\mathcal{L}\sigma_T V_\phi}{4\pi r^2 c^2}, \end{aligned} \tag{1.1.1}$$

where V_ϕ (cm/s) is the target's azimuthal three-velocity, c (cm/s) the speed of light, σ_T the Thomson cross section (cm^2), and r (cm) the target's radial distance from the central mass.

Here, we wish to study black holes and the hot accretion disks around them that turn out to produce notable amounts of thermal radiation. This radiation, on the contrary to common practice, is usually markedly potent and all but negligible. Our primary objective is to create computational codes that emulate environments of high-temperature accretion disks orbiting compact objects. These disks are expected to radiate and generate intricate radiation fields that get further complicated due to the relativistic effects present in such strong gravity arrangements. We then wish to discuss the extracted results and draw conclusions about the present relativistic optics, the intensity and distribution of the exerted radiation forces, and the particular disk models' stability and evolution. For instance, we contemplate the possibility of the exerted radiation forces triggering or regulating parts of the accretion process. Moreover, we survey the possibility of dissimilar phenomena occurring in the diverse types of disks and their relation to distinct geometrical characteristics, the density and temperature gradients, and more.

We thus consider and attempt extending our deductions for all the ensuing dynamical effects emanating from such expanded and particular sources of radiation that are much further than Equations (1.1.1). A direct aftermath of such procedures is the electrons' deceleration and hence the generation of an azimuthal electric current in the disks. This process then subsequently leads to the generation and expansion of poloidal magnetic field loops that slowly fill the configuration area and then continue spreading further out the systems.

In the beginning of this work, we mention some interesting historical notes in the research of this topic and the attempts at solving the problems it created. We look thus into the early attempts and the work results given by renowned physicists of the 20th century such as J. H. Poynting, H. P. Robertson, J. Larmor, H. N. Russell, and L. Page.

In the next Section, we continue on to provide all the mathematical tools we use for our study. We present the Minkowski, Schwarzschild, and Kerr metrics, and we introduce the locally nonrotating frames. We then use the aforementioned tools to investigate massive and massless particle trajectories in strong gravity environments. We go on to discuss the radiation and the particle equations of motion, and move further on to build and solve the Classical, as well as the General Relativistic Radiative Transfer Equation. We then see how we can bypass different issues appearing in problematic environments and situations, such as very thick disks or disks with extremely high density gradients.

We go on to discuss and present a variety of accretion disk models often mentioned and used in astrophysical research. We build and explain many models of optically thick and thin disks, semi-opaque accretion disks, or combinations of those that we have used in our study. We also discuss other disk models proposed and consider possible extensions to our applications.

In the following Section, we discuss our method of approaching our assorted research subjects and we present the five main families of codes written in our work for our different research subjects. We also show many of the results of said codes, which are trajectories, radiation force plots, accretion disk setup and appearance pictures, particle trajectories including radiation contributions, and simulation results enhancement procedures.

In the final Chapter, we discuss the Cosmic Battery model. We describe the mechanism and explain the process of energy conversion. The system initially possesses, amongst other forms, thermal energy stored in the accretion disk matter. This energy is then emitted as thermal radiation and reabsorbed by the disk material, altering its kinematics. This change of the system kinematics then leads to electrical phenomena and subsequently the generation of magnetic fields from zero. We hence consider how the Cosmic Battery can take advantage and utilize the various accretion disk setup properties in order to build stronger magnetic fields and possibly diffuse them outward. We additionally contemplate the influence this mechanism can have on the development of different and more complex systems, such as X-ray binaries (XRBs) and in particular their short scale evolution and the recurrent hardness – intensity diagram.

1.2. Description of the Poynting – Robertson effect

Poynting – Robertson effect or Poynting Robertson drag is a process first studied and discussed in the beginning of the previous century. It describes the effects of photons hitting dust grains or other similar particulates in orbit around the Sun. The absorption of this radiation causes the recipient to gradually lose energy and angular momentum. Consequently, the target falls to lower orbits and finally infalls onto the Sun, the Earth or any nearby massive object. This is the physical phenomenon responsible for the zodiacal light (Fig. 1.1).

The first description of the phenomenon was made by J. H. Poynting in the beginning of the 20th century (Poynting 1903), before the Special Theory of Relativity was formulated (Einstein 1905). That study, even though it gave results in the same order of magnitude as the real force, was not perfectly accurate. It would, instead, require many years of investigation and numerous failed attempts in order to be fully understood and explained. Many physicists of the time tried for years to resolve the issue, the most well-known of those being J. Larmor (Larmor 1917), whose contribution was of great value.

The final answers for this problem would be finally given by H. P. Robertson (Robertson 1937) 34 years after the first published study of the phenomenon. Robertson started by collecting and reviewing all the studies

Figure 1.1: Zodiacal light seen behind the Submillimeter Array from the summit of Mauna Kea, Hawaii, USA. Photo by Steven H. Keys and http://www.keysphotography.com

done on the subject before him. He then extended the existing theory, giving thus eventually the correct interpretation of the phenomenon and formulating the complete equations describing it.

Even today, the examination of the Poynting – Robertson effect often brings confusion and misunderstandings. This happens mainly because it is hard to comprehend how a force exerted perpendicularly to the direction of motion can brake and decelerate the body. The answer to this riddle is given by the Special Theory of Relativity, since the effect cannot be explained classically. The physical phenomenon responsible for the emergence of the drag force is the aberration of light[1] (Fig. 1.2). The particle under examination, due to its strongly or mildly relativistic movement, perceives the radiation field to be different than that recorded by an observer at rest. Namely, the moving particle in its rest frame registers and absorbs the approaching radiation coming mainly from in front of it, while it reemits it isotropically.

We note also that the process gets additionally complicated if the target mass is taken into consideration. Namely, the phenomenon develops slightly differently if it pertains to particles with specific standard mass or larger and more complex bodies with alterable mass. For example, we can consider an isolated hot moving body. This body, even though it emits

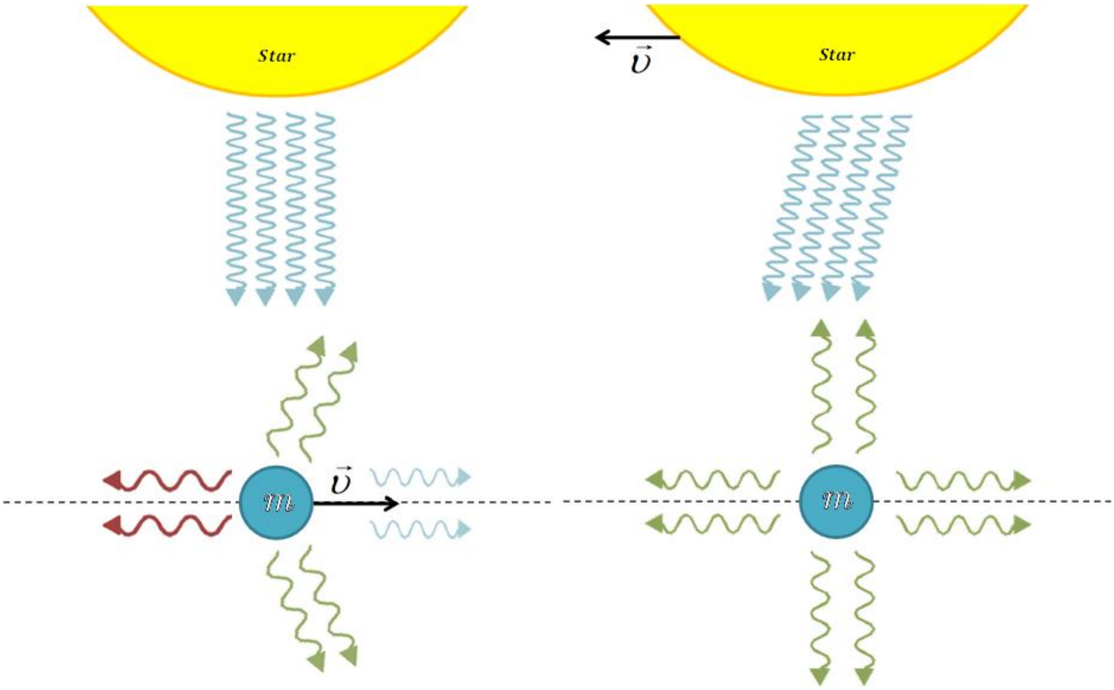

Figure 1.2: Aberration of light and its results: (*left*) In the lab frame the moving particle appears to emit light slightly concentrated toward its direction of motion. (*right*) In the particle's rest frame the radiation is emitted isotropically but appears to be coming concentrated toward its direction of motion.

---

[1] *An informative and very interesting video depicting the optical effects appearing in Special Relativity can be found here: https://apod.nasa.gov/apod/ap111018.html.*

thermal radiation in the forward direction, does not decelerate. This happens because as the body emits energy by radiation, its mass decreases. Consequently, even though the energy is diminished, its additionally reduced mass results in the body keeping a constant speed.

We can now examine the process in more detail by starting from the lab frame. The emitting star is situated in the center of the system and the particulate is orbiting it. In these circumstances, we observe the photons being emitted by the star and absorbed by the target solely in the radial direction. The particulate's angular velocity remains hence unchanged. The subsequent photon emission by the target particle is, nonetheless, done anisotropically and more concentrated toward the direction of motion. This anisotropic photon emission thus removes angular momentum from the particulate, causing it to brake and infall into lower orbits.

Another way to understand the process is to examine it using the particulate's properties as it moves around the star. For instance, the target's angular momentum vector $\vec{L}$ $(g\cdot cm^2/s)$ is given by:

$$\vec{L}=\vec{r}\times\vec{p}=\vec{r}\times m\vec{\upsilon}=mr^2\vec{\omega}=m\omega r^2\hat{\phi}=m\sqrt{GMr}\hat{\phi}\,, \qquad (1.2.1)$$

where m (g) is the particulate's rest mass, $\vec{r}$ its position vector, $\vec{\upsilon}$ (cm/s) its velocity and $\vec{p}$ $(g\cdot cm/s)$ its momentum vector, $\vec{\omega}$ (s^{-1}) its angular velocity vector, M (g) the central star's mass, G $(dyn\cdot cm^2/g^2)$ the gravitational constant, and $\hat{\phi}$ the unitary ϕ-direction vector. As the target now absorbs the incoming radiation, we register its mass increasing due to the mass – energy equivalence. Since, nonetheless, the particulate's angular momentum $\vec{L}$ is conserved for the circular orbit we infer that its orbital radius r must decrease. This consequently leads the particulate to constantly fall to lower orbits.

Equivalently to the above, we can choose to move to the particulate's rest frame. There, due to the aberration of light, the photons emitted by the central star appear to be coming from directions more concentrated toward the front and not isotropically. The photon reemission by the target is, however, done isotropically. This, nonetheless, results in the target perceiving a force against its direction of motion. The particulate thus is decelerated and finally infalls onto the central star. The same also occurs in the case where the target radiates the energy at the same rate at which it absorbs it. There, even though the total mass – energy of the particulate remains constant, the phenomenon persists. This is again due to the fact that, even though the reemission of radiation is done isotropically, its absorption is anisotropic. The result is a net force exerted against the direction of motion and the abduction of angular momentum. This hence brakes the target and drives it to fall into lower orbits.

It is also worth mentioning that while the target particle moves helically toward the star, its orbital speed υ keeps increasing steadily as expected, since it is given by the formula:

$$\upsilon=\sqrt{\frac{GM}{r}}\,. \qquad (1.2.2)$$

In conclusion, for completeness we mention the formula that gives the magnitude for the Poynting – Robertson force F_{PR} in brief, as we see more in detail in a following Section:

$$F_{PR} = \frac{\upsilon}{c}\mathrm{P} = \frac{\sigma\mathcal{L}}{4\pi r^2 c}\cdot\frac{\upsilon}{c} = \frac{a^2\mathcal{L}}{4c^2}\sqrt{\frac{GM}{r^5}}\,, \qquad (1.2.3)$$

where P (erg/s) is the incident radiation power, $\mathcal{L}$ the Solar luminosity, r the orbital radius, σ the particulate cross section, and a its radius. The ratio of the radiation force F_{rad} over the force of gravity F_{grav} is then given by:

$$\frac{F_{rad}}{F_{grav}} = \frac{3\sigma\mathcal{L}}{16\pi GMca\rho}\,, \qquad (1.2.4)$$

where ρ (g/cm^3) is the particulate density.

1.3. History of discovery

The basis for describing the Poynting – Robertson effect was set rather early in the history of Modern Physics. The outset was so early in fact, that in the first written attempts to explain and describe it, the study was done without taking into consideration Special Relativity, as the theory was not yet formulated. As it is revealed by the name of the phenomenon, two pioneers that applied themselves with it were John Henry Poynting, the British physicist also known for his involvement with the Electromagnetic Theory and Howard Percy Robertson, the American physicist and mathematician (Fig. 1.3). Some other well-known scientists of the time that also worked on this puzzling subject were the Irish and British physicist and mathematician Joseph Larmor, and Henry Norris Russell (Russell 1929), the American astronomer (Fig. 1.4).

The first steps in discovering the baffling physical processes responsible for the Poynting – Robertson effect were made by Poynting in 1903, when he published the paper titled "Radiation in the Solar System: Its effects on temperature and its pressure on small bodies". By making calculations in Classical Physics and using the notion of Aether, the physicist starts with observational data about the Solar constant, namely the rate of incident energy on a certain surface located one astronomical unit away from the Sun, the same as the distance of the Earth to the Sun. He then goes on to calculate an effective temperature for the Sun and an

Figure 1.3: John Henry Poynting (*left*) and Howard Percy Robertson (*right*). The pioneer scientists who studied and explained the Poynting – Robertson effect. The effect was named in their honor.

effective temperature for space. He subsequently uses the results to hypothesize on a value for the mean temperature of planets in various distances away from the Sun, as well as small objects moving at the distance of Earth's orbit.

In the second part of the paper, the author attempts to calculate the effect of Solar radiation on small objects due to the pressure it exerts on them. He begins by formulating the suitable set of equations describing the phenomenon and then calculates the forces developing due to the radiation exchange between two bodies. Subsequently, he compares the radiation forces to the mutual gravitational attraction between these bodies. He afterward applies the same process for the pair of a particle and the Sun, and concludes that the ratio of the radiation force F_{rad} to the gravitational force F_{grav} is:

$$\frac{F_{rad}}{F_{grav}}=\frac{\dfrac{\pi a^2 b^2 \mathcal{L}}{cd^2}}{\dfrac{16G\pi^2 a^3 b^3 \rho\rho'}{9d^2}}=\frac{12\pi a^2 b^2 \mathcal{L}}{16Gc\pi b^3 \rho' \dfrac{4}{3}\pi a^3 \rho}=\frac{12\sigma\mathcal{L}}{16\pi GMcb\rho'}\approx 4\times\left[\frac{F_{rad}}{F_{grav}}\right]_{real}, \quad (1.3.1)$$

where a, b the radii of the two bodies, ρ, ρ' their densities, and d the distance between them. This calculation, however, is inopportunely performed using solely Classical Physics and thus the ratio result is four times larger than its real value.

The author then continues on to calculate the dragging lag force

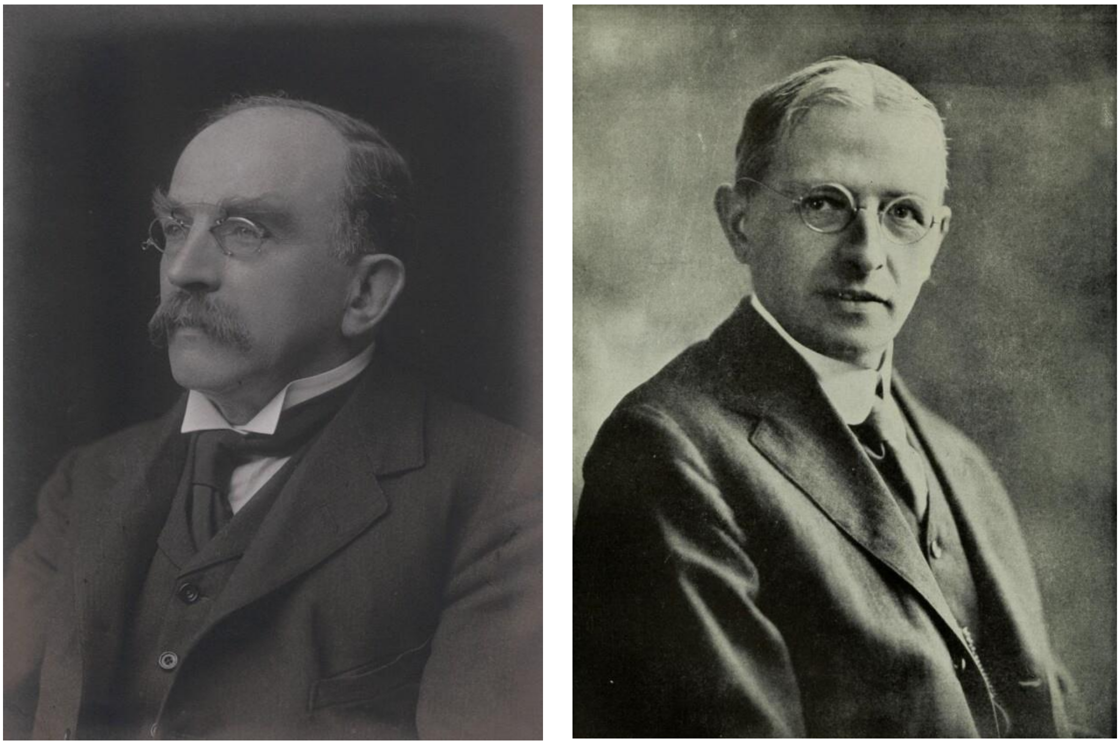

Figure 1.4: Joseph Larmor (*left*) and Henry Norris Russell (*right*). Two of the scientists that spent much time contemplating and attempting to explain the phenomenon.

exerted on the moving particle due to the Solar radiation and the form taken by the equation of motion in that case. He thus determines the required time for the phenomenon effects on the speed and orbital radius to become apparent. Using the above, the author eventually derives the total time and the maximum rotations required until the target particle finally infalls onto the Sun.

Even though Poynting's analysis is detailed and well documented, it gives incorrect results for the effects it attempts to describe by approximately a factor of four. The errors occur because the calculations are done within the Classical Theory of Physics. This fact specifically, causes an extra factor to appear in some equations, depending on the method of solution. This is because the Poynting – Robertson effect is a phenomenon relativistic in nature, even at first-order calculations.

Larmor will later on consider the subject and make an intensive effort to resolve the matter. He firstly reveals his correct observation that an isolated particle that moves in the void of space will not have any change on its speed. Such a change would primarily violate the principle of relativity. Furthermore, we notice that a possible drag would be compensated by the increase of speed due to the conservation of momentum and the decrease of the particle's mass. This is the point where, for the first time, the true reason for the drag is stated by Larmor. He explains that for the particle under study, as the Solar radiation hits it, the energy lost by cooling gets restored and thus the braking force reappears. Despite the correct justification given for the drag, Larmor then goes on to mistakenly, assume the existence of an additional force equal in magnitude to the drag, caused by the aberration of light. This way, he finally ends up with a total force twice the magnitude of the true decelerating force.

Shortly after Larmor, the American theoretical physicist Leigh Page (Fig. 1.5) will confront the problem and spend considerable time to investigate the subject and resolve its perplexities. Through his work, shown in Page 1918a, 1918b, and 1918c, he examined the topic from various perspectives seeking the effects of radiation emission on moving sources. Leigh Page's reasoning and conclusions will prove valuable and provide insight that would later on be

Figure 1.5: Leigh Page, Chairman of Mathematical Physics at the Sloane Physics Laboratory of Yale University and the namesake of Yale's Leigh Page Prize Lectures. Photograph courtesy of AIP Emilio Segrè Visual Archives, Physics Today Collection.

utilized in the final interpretation of the phenomenon.

Many years later, in 1929, H. N. Russell will also apply himself with the ramifications of Solar radiation hitting massive particles. He will examine the effects on the assorted types of targets such as smaller interstellar or larger Solar System meteoroids, as well as the volatilized material they leave behind. He will perform calculations and examine in which cases the incoming light will be simply scattered away and in which cases the particles will be driven away by the light.

The mystery of the process will be solved once and for all years later by Robertson that will dismiss the notion of Aether and use the General Theory of Relativity. In his paper "Dynamical effects of radiation in the Solar System", Robertson clears up the field from the logical and physical errors done in the previous attempts to resolve the problem. He gives credit to Joseph Larmor for all his work, corrects some errors in his theory, and thus decidedly gives the solution to a riddle that puzzled some of the most notable researchers of physics of the era for quite some time.

In particular, Robertson explains that Poynting attributed the drag force to the exerted radiation pressure that pushes against the direction of motion of the particle. He perceived this to be the result of the concentration of radiation on the forward part of the particle along with the corresponding radiation rarefaction at the backward part. Following this, he explains that the case where the radiation force could brake the particle is in direct contrast with the Theory of Relativity. The Theory of Relativity, however, was already in agreement with the Theory of Electromagnetism through which the force itself was calculated. According to Robertson, this was precisely the reason why Page was compelled to work on the subject and to demonstrate that in the order of magnitude the study was made, the target speed would not display any lag. This fact would later on prove to be correct.

For his calculations, Robertson begins by assuming that the target absorbs all the incident radiation and reemits it at the same rate in its rest frame. This means that the particle rest mass remains constant. He also notes that the calculation can be done using Special Relativity and later on add the necessary general relativistic corrections. In the first step, he assumes a reference frame in which the Sun is at rest, a four-velocity for the target particle, and a lightlike vector for the direction of the incident radiation. Using these, he subsequently defines the relevant stress – energy tensor for the radiation. Later on, by defining a new reference frame in which the particle is momentarily at rest, he continues on to transfer all of the above to the new reference frame. There, he notes that the spatial momentum transformation rate is equal to the force exerted onto the particle and therefore can be calculated as a function of the particle dimensions and the incident radiation energy density.

Subsequently, the author states the equation of motion at the particle's rest frame and gives the formula:

$$\frac{\mathrm{d}m\upsilon^{\mu}}{\mathrm{d}\tau}=\frac{\phi}{c\lambda^{0}}\left(\lambda^{\mu}-\lambda^{0}\upsilon^{\mu}\right), \qquad (1.3.2)$$

where υ^{α} is the particle's four-velocity, τ its proper time (s), ϕ the drag force, and λ^{μ} the lightlike vector components of the incident radiation's direction in the particle’s rest frame. The first term $\frac{\phi\lambda^\mu}{c\lambda^0}$ at the right hand side is the total force four-vector caused by the incident radiation. The second term $\frac{\phi\upsilon^\mu}{c}$ is caused by the radiation reemission at a rate of ϕc. In the lab frame, the equation takes the form:

$$\frac{\mathrm{d}mu^\mu}{\mathrm{d}\tau} = \frac{fw}{c}\left(l^\mu - wu^\mu\right), \tag{1.3.3}$$

where u^α is the particle four-velocity, $f = \phi / w^2$ the drag force, w a scalar given by the formula $w = l_\mu u^\mu = \lambda^0$ that results from coordinate system change, and l^μ the lightlike vector components that give the incident radiation direction in the lab frame. If we include the general relativistic correction to the above, the equation of motion then takes the final form:

$$\frac{\mathrm{d}mu^\mu}{\mathrm{d}\tau} + m\Gamma^\mu_{\nu\sigma}u^\nu u^\sigma = \frac{fw}{c}\left(l^\mu - wu^\mu\right), \tag{1.3.4}$$

where $\Gamma^\mu_{\nu\sigma}$ the Christoffel symbols given by the metric $g_{\mu\nu}$ from the formula $\Gamma^i_{kl} = \frac{1}{2}g^{im}\left(g_{mk,l} + g_{ml,k} - g_{kl,m}\right)$. In the above equation, one can see again that the second term on the right hand side represents the drag force. This force is, nonetheless, equal to zero in the case where the first term is ignored. That is so, since in that case we would have:

$$m\frac{\mathrm{d}u^\mu}{\mathrm{d}\tau} + \frac{\mathrm{d}m}{\mathrm{d}\tau}u^\mu = -\frac{\phi}{c}u^\mu. \tag{1.3.5}$$

Then, the particle would lose mass at a rate of $\frac{\phi c}{c^2}$ and the second term at the left would counterbalance the term on the right, causing the speed to remain constant.

Concluding the calculations section, Robertson analyzes and sheds light into Larmor’s error. He explains that any effect caused by the aberration of light appearing in the problem, must be already included in the aforementioned equations. Hence, the separate introduction of such terms must only be considered as an alternative way to describe the same problem.

In the following Sections, we make an approximation of the particle’s equation of motion to a first-order of $\frac{\upsilon}{c}$:

$$m\frac{\mathrm{d}\upsilon^a}{\mathrm{d}t} = f\left(1 - \frac{\upsilon_n}{c}\right)n^a - f\frac{\upsilon^a}{c}, \tag{1.3.6}$$

with n^α being the incident radiation’s direction and υ_n the particle velocity component parallel to the photons’ direction. The first term on the right is a result of the radiation pressure, corrected by a factor brought in by the Doppler shift and the second term is the tangential drag force. He also explains that the total drag force results from both those terms. For directions vertical to the incident photons, like in the case of target particles orbiting a central star, this force has a magnitude of $f\,\dfrac{\upsilon'}{c}$, with υ' the υ^a component in said direction. Finally, he states the complete formula for the Poynting – Robertson drag:

$$F_{PR} = \frac{\upsilon'}{c} f = \frac{\sigma \mathcal{L}}{4\pi r^2 c} \cdot \frac{\upsilon'}{c}, \tag{1.3.7}$$

where r is the particle's orbital radius.

CHAPTER 2

SPACETIMES AND PARTICLE TRAJECTORIES

In this work, we study the intensity of radiation pressure and its possible effects onto the rapidly moving accretion disk material around a black hole. In environments such as those close to a stellar black hole, it is imperative to work within the limits of General Relativity in order to acquire results close to their real values. It is also necessary in certain cases to restate some of the known equations of motion and radiative transfer in order to be able to use them in Lorentz invariant forms. In this work we use typical relativity notation and formalism. We thus utilized widely known relativity bibliography, including Chandrasekhar 1983, Dewitt & Dewitt 1973, Frolov & Novikov 1998, Gualtieri & Ferrari 2011, Landau & Lifshitz 1975, MacDonald & Thorne 1982, Schutz 2009, Shapiro & Teukolsky 1983, Synge 1956 and 1960, Thorne & MacDonald 1982, Visser 2007, Wald 1984, Weinberg 1972, and Koliopanos, Menis, Pantiskos 2010 (Greek).

2.1. Spacetimes and metrics

In this Section, we present the assorted spacetimes used in our analysis, along with the respective metrics utilized to describe the problem at hand. For this work we use the geometrized units system, where $c=G=1$, to express the equations below. Distances are hence measured in units of gravitational radii $r_g = GM/c^2 = M$, with M the central body mass. We also assume the Einstein notation for summation over double indices. Spacetime components are denoted by Greek indices and space components by Latin indices.

The simplest spacetime encountered is the Minkowski spacetime (Minkowski 1908, Minkowski 1909 - English, Italian), which resembles Euclidean space but also includes the direction of time (Fig. 2.1a). The Minkowski metric giving the length element $\mathrm{d}s$ in Cartesian and spherical coordinates respectively is:

$$\mathrm{d}s^2 = -\mathrm{d}t^2 + \mathrm{d}x^2 + \mathrm{d}y^2 + \mathrm{d}z^2 , \qquad (2.1.1)$$

$$\mathrm{d}s^2 = -\mathrm{d}t^2 + \mathrm{d}r^2 + r^2\mathrm{d}\theta^2 + r^2 \sin^2\theta\,\mathrm{d}\phi^2 , \qquad (2.1.2)$$

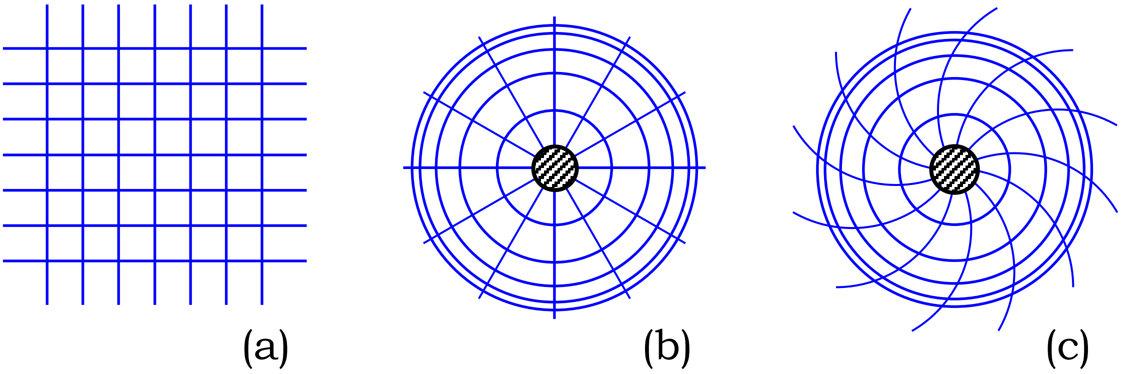

Figure 2.1: Schematic representation of the various spacetimes used in this work. Minkowski (*a*), Schwarzschild (*b*) and Kerr spacetime (*c*).

where s (cm) is the proper length, t (s) the time, r the radius, θ the polar angle or inclination, and ϕ the azimuthal angle. In contravariant form it is:

$$\left(\frac{\partial}{\partial s}\right)^2 = -\left(\frac{\partial}{\partial t}\right)^2 + \left(\frac{\partial}{\partial x}\right)^2 + \left(\frac{\partial}{\partial y}\right)^2 + \left(\frac{\partial}{\partial z}\right)^2, \quad (2.1.3)$$

$$\left(\frac{\partial}{\partial s}\right)^2 = -\left(\frac{\partial}{\partial t}\right)^2 + \left(\frac{\partial}{\partial r}\right)^2 + \frac{1}{r^2}\left(\frac{\partial}{\partial \theta}\right)^2 + \frac{1}{r^2 \sin^2\theta}\left(\frac{\partial}{\partial \phi}\right)^2. \quad (2.1.4)$$

The Minkowski metric is used in flat spacetime and in the zero angular momentum observer (ZAMO) frame (see Sect. 2.3).

Next, we consider the spacetime around a static, uncharged, and nonrotating mass. This could be a black hole, a nonrotating star the size of the Sun, or even a nonrotating planet. In environments like this, the spacetime is a Schwarzschild spacetime (Fig. 2.1b, Schwarzschild 1916). Since in such systems there is a spherical symmetry, we choose to employ spherical coordinates and the metric there is:

$$ds^2 = -\left(1-\frac{r_S}{r}\right)dt^2 + \left(1-\frac{r_S}{r}\right)^{-1} dr^2 + r^2 d\theta^2 + r^2 sin^2\theta d\phi^2. \quad (2.1.5)$$

In contravariant form the metric then is:

$$\left(\frac{\partial}{\partial s}\right)^2 = -\left(1-\frac{r_S}{r}\right)^{-1}\left(\frac{\partial}{\partial t}\right)^2 + \left(1-\frac{r_S}{r}\right)\left(\frac{\partial}{\partial r}\right)^2 + \frac{1}{r^2}\left(\frac{\partial}{\partial \theta}\right)^2 + \frac{1}{r^2 \sin^2\theta}\left(\frac{\partial}{\partial \phi}\right)^2, \quad (2.1.6)$$

where $r_S = 2M$ is the Schwarzschild radius of the central mass.

From the above form of the metric, we see that in this spacetime the lines of time and radial distances get distorted from straight lines into circles. One can also see that the time distances become greater the closer we get to the central mass. This phenomenon is known as gravitational time dilation. In addition, the opposite happens for the radial distances as they become smaller the closer we get to the central object.

We continue on to examine the case where the central uncharged mass is rotating, the Kerr spacetime (Fig. 2.1c, Kerr 1963). Here, as the mass rotates around its axis, it drags the spacetime along with it. This results in the coordinate lines to become curved and get entrained along with the rotation, lagging behind their original position from the previous spacetime setup. This makes the spacetime appear to be dragged along the rotation axis following the central mass, with its innermost sections rotating faster than the outermost. This is what gives this phenomenon the name frame dragging.

Another effect introduced by the central mass rotation is the fact that photons moving with the direction of rotation have their frequency boosted and those moving against the direction of rotation have their frequency de-boosted. The physical quantity best describing and quantifying these effects is the rotation speed of the central mass. This rotation is measured with the angular momentum J, the dimensionless angular momentum j (scalar) or more often the spin parameter a (mass or units of mass M) of the central object. The above are connected to each other through these equations:

$$a=\frac{cJ}{GM},\ j=\frac{cJ}{GM^2},\ a=jM\ , \tag{2.1.7}$$

or in geometrized units:

$$a=\frac{J}{M},\ j=\frac{J}{M^2},\ a=jM\ , \tag{2.1.8}$$

where now the spin parameter a has the same dimension as mass (see e.g., Schutz 1985 and Miller & Lamb 1996). The spin parameter a takes values from $a=0$ for a nonrotating Schwarzschild black hole to $a=M$ for a maximally rotating one. Alternatively, we may use $j=0$ and $j=1$ respectively, for the dimensionless angular momentum $j=a/M$.

One can see from the above discussion that the spacetime is no longer spherically but axially symmetric, since there is now dependence on the polar angle θ. The associated metric in Boyer – Lindquist (BL) coordinates (Boyer & Lindquist 1967) is:

$$\begin{aligned} \mathrm{d}s^2 = &-\left(1-\frac{r_S r}{\Sigma}\right)\mathrm{d}t^2 - \frac{2r_s rasin^2\theta}{\Sigma}\mathrm{d}\phi\mathrm{d}t \\ &+\left(r^2+a^2+\frac{r_s ra^2sin^2\theta}{\Sigma}\right)sin^2\theta\mathrm{d}\phi^2+\frac{\Sigma}{\Delta}\mathrm{d}r^2+\Sigma\mathrm{d}\theta^2, \end{aligned} \tag{2.1.9}$$

where:

$$\begin{aligned} &\Delta = r^2 - r_S r + a^2, \\ &\Sigma = r^2 + a^2cos^2\theta, \\ &\mathrm{A} = \left(r^2+a^2\right)^2 - a^2\Delta sin^2\theta. \end{aligned} \tag{2.1.10}$$

In contravariant form the metric is:

$$\begin{aligned} \left(\frac{\partial}{\partial s}\right)^2 = &-\frac{\mathrm{A}}{\Sigma\Delta}\left(\frac{\partial}{\partial t}\right)^2 - \frac{2r_S ar}{\Sigma\Delta}\left(\frac{\partial}{\partial t}\right)\left(\frac{\partial}{\partial \phi}\right) + \frac{\Delta - a^2\sin^2\theta}{\Sigma\Delta\sin^2\theta}\left(\frac{\partial}{\partial \phi}\right)^2 \\ &+\frac{\Delta}{\Sigma}\left(\frac{\partial}{\partial r}\right)^2 + \frac{1}{\Sigma}\left(\frac{\partial}{\partial \theta}\right)^2. \end{aligned} \tag{2.1.11}$$

The Kerr spacetime metric is also often expressed by using the exponential form, which is:

$$\mathrm{d}s^2 = g_{\alpha\beta}\mathrm{d}x^\alpha \mathrm{d}x^\beta = -e^{2\nu}\mathrm{d}t^2 + e^{2\psi}\left(\mathrm{d}\phi - \omega \mathrm{d}t\right)^2 + e^{2\mu_1}\mathrm{d}r^2 + e^{2\mu_2}\mathrm{d}\theta^2 \qquad (2.1.12)$$

$$\mathrm{d}s^2 = -\left(e^{2\nu} - \omega^2 e^{2\psi}\right)\mathrm{d}t^2 - 2\omega e^{2\psi}\mathrm{d}t\mathrm{d}\phi + e^{2\psi}\mathrm{d}\phi^2 + e^{2\mu_1}\mathrm{d}r^2 + e^{2\mu_2}\mathrm{d}\theta^2, \qquad (2.1.13)$$

where the exponentials are given by:

$$\begin{aligned} e^{2\nu} &= \frac{\Sigma\Delta}{\mathrm{A}}, \\ e^{2\psi} &= \frac{\mathrm{A}sin^2\theta}{\Sigma}, \\ e^{2\mu_1} &= \frac{\Sigma}{\Delta}, \\ e^{2\mu_2} &= \Sigma. \end{aligned} \qquad (2.1.14)$$

Additionally, $\omega = \omega(r,\theta)$ measures the spacetime angular speed and is given by:

$$\omega = -\frac{g_{\phi t}}{g_{\phi\phi}} = \frac{r_S ra}{\mathrm{A}}, \qquad (2.1.15)$$

(Bardeen 1970a, Bardeen 1970c, Bardeen et al. 1972).
Equivalently, the exponential contravariant form is:

$$\begin{aligned} \left(\frac{\partial}{\partial s}\right)^2 &= -e^{-2\nu}\left(\frac{\partial}{\partial t}\right)^2 - 2\omega e^{-2\nu}\left(\frac{\partial}{\partial t}\right)\left(\frac{\partial}{\partial \phi}\right) \\ &+ \left(e^{-2\psi} - \omega^2 e^{-2\nu}\right)\left(\frac{\partial}{\partial \phi}\right)^2 + e^{-2\mu_1}\left(\frac{\partial}{\partial r}\right)^2 + e^{-2\mu_2}\left(\frac{\partial}{\partial \theta}\right)^2. \end{aligned} \qquad (2.1.16)$$

It is now easy to see from the above equations for the Kerr metric, that if one were to set $a = 0$, it would mean that the central object would no longer be rotating. Consequently, as expected the Kerr metric would be reduced to the Schwarzschild case. Additionally, it is worth taking note of the cross-term $\mathrm{d}t\mathrm{d}\phi$ that reveals the coupling of time and rotation. It is an off-diagonal term of the metric matrix that gives rise to many significant effects for this type of spacetime and disappears when $a = 0$. Finally, it is also straightforward to recognize that the Kerr spacetime has two symmetries as it retains time translations and rotations around the mass rotation axis.

2.2. Notable surfaces and particle orbits around a central mass

2.2.1. Surfaces

In this Section, we look into some mentionable surfaces that appear around nonrotating or rotating central masses. Some of these surfaces are the result of singularities of the metric, while others appear due to the roots or extrema of certain quantities. We thus conclude that the dimensions of these surfaces depend upon the spin parameter a of the central object. We should note here that these surfaces exist for objects of any mass, but are situated inside the outer surface for objects other than the compact black holes. The mass M for a stellar mass black hole is estimated to range approximately between 5 and 100 Solar masses (e.g., Hughes 2005 [2]). In most cases, we observe stellar mass black holes surrounded by accretion disks for longer or shorter periods of time. These times depend on the configuration setup and the greatly varying accreting mass quantity, usually ranging from a few days to a few hundreds of days, (see e.g., Lasota 2016).

At first, when examining metric (2.1.9) one can see the problematic points arising from the g_{rr} term as Δ goes to zero. The first pair of surfaces therefore appears as the solutions to $\Delta = 0$, namely for $r^2 - 2Mr + a^2 = 0$. These

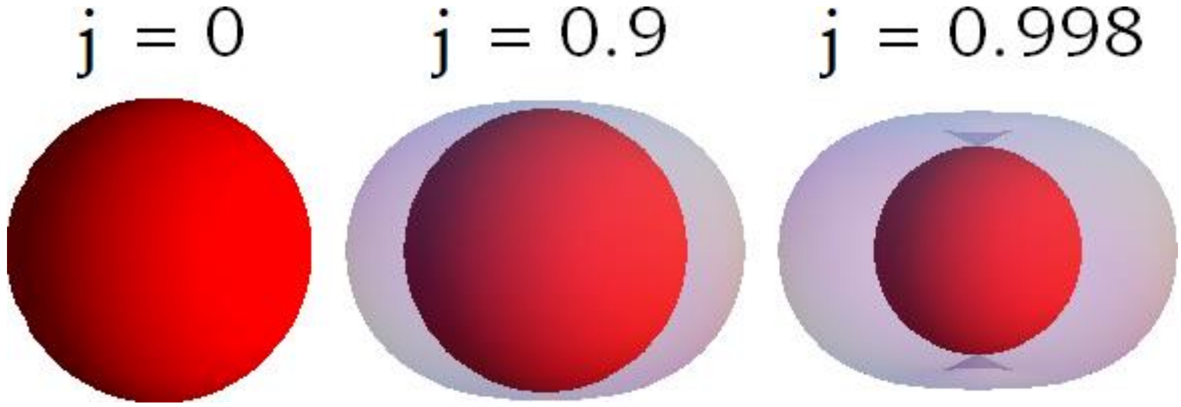

Figure 2.2: Event horizon (*red*) and ergosphere (*gray*) for a black hole with assorted angular momentum values. The ergosphere in low spin j is an ellipsoid and turns into a spindle torus[3] for high j. We also observe that the black hole event horizon shrinks for increasing values of j.

---

[2] *The lower limit for black hole mass, the Tolman–Oppenheimer–Volkoff limit is still under active research, see Bombaci (1996), Kalogera & Baym (1996), Thompson et al. (2019), Abbott et al. (2020), but also Jayasinghe et al. (2021) and El-Badry et al. (2022).*

[3] *A spindle torus is a three-dimensional geometrical shape that is produced by the rotation of a circle around an axis in the same plane as the circle. The distance of this axis from the center of the circle is smaller than the circle radius. Objects approximating a spindle torus are an apple and a pumpkin.*

solutions are:

$$r_{evh} = M \pm \sqrt{M^2 - a^2}\,. \qquad (2.2.1)$$

These two surfaces, that appear to be singular but generally are not, are the outer and the inner event horizon with the + and – sign respectively. The outer event horizon, or plainly the event horizon (Fig. 2.2) of the black hole is also known as "the point of no return" and the "one-way membrane". Objects passing through it and into the interior of the black hole are cut off from the rest of the Universe, as they can no longer communicate with the environment outside the event horizon. This is so, because for points within that radius, the escape velocity is equal or larger than the speed of light and hence, any object, particle or wave there is forced to fall inward.

The shape of the inner and outer event horizon is spherical in Boyer – Lindquist coordinates. In Kerr – Schild coordinates it is an oblate spheroid, whose aspect ratio depends on the black hole spin. If $a = 0$, the spacetime is Schwarzschild and the event horizon in both coordinate systems is a sphere of Schwarzschild radius. Furthermore, the inner event horizon is a true physical singularity, a gravitational singularity at the axes origin. As a increases from zero, the inner event horizon stops being a gravitational singularity. Instead, the inner horizon moves away from a single point into a three-dimensional shape. Meanwhile, the outer event horizon shrinks into a smaller size but always remains larger than the inner horizon.

Another set of coordinate singularities arises from the root of the g_{tt} component of the metric that changes from positive to negative. This happens when $\Sigma - 2Mr = 0$, namely for:

$$r_{ergo} = M \pm \sqrt{M^2 - a^2 \cos^2\theta}\,. \qquad (2.2.2)$$

The outer solution is known as the static limit. The area of space enclosed within the static limit is the ergosphere (Fig. 2.2). For nonmaximal black holes, the ergosphere has the shape of an oblate spheroid, as there is dependence on the polar angle θ. As the black hole spin increases and approaches unity, the black hole gets maximal and the ergosphere takes the shape of a spindle torus[3]. Even though the ergosphere's size and shape changes for every spin parameter, there are some maintained properties. Namely, we notice that the ergosphere always remains in contact with the event horizon at the rotation axis of the system and its section with the equatorial plane is a circle of radius $2M$.

The ergosphere is a particular volume of space within which $g_{tt} < 0$. This implies that any physical observer is forced to move in the positive azimuthal direction, meaning that close enough to the rotating black hole all objects, including photons must corotate with it. This happens because for any particle to maintain a positive proper time, it is necessary for it to rotate in the same direction as the black hole with an angular speed of at least ω. This fact therefore excludes any counterrotating trajectories.

In addition, it is worth mentioning explicitly that that the event horizon and the static limit are neither real surfaces, nor actual physical singularities but merely coordinate singularities. This means that they can be eliminated by the using another coordinate system and physical objects do not face any restrictions in crossing them, at least in one direction.

2.2.2. Trajectories

Particle trajectories in Kerr spacetime are governed by four constants of motion. These are the particle rest mass μ, the total energy E, the angular momentum component parallel to the rotation axis L, and the Carter constant Q (Carter 1968). The latter three conserved quantities are given by the particle four-momentum components p_α by the formulae:

$$E=-p_t, \tag{2.2.3}$$

$$L=p_\phi, \tag{2.2.4}$$

$$Q=p_\theta{}^2+cos^2\theta\left[a^2\left(\mu^2-p_t{}^2\right)+p_\phi{}^2/sin^2\theta\right]. \tag{2.2.5}$$

We note that for photons, the rest mass is $\mu=0$ and for massive particles, we may normalize into $\mu=1$. The nonnegative Carter constant is also a valuable quantity that reveals useful information about the particle motion. Firstly, $Q=0$ is a necessary and sufficient condition for a particle motion initially in the equatorial plain to remain there forever. Consequently, all the trajectories that have $Q>0$ must at some point intersect the equatorial plane and vice versa. Solving the above equations reveals the orbital trajectory laws:

$$\Sigma\frac{\mathrm{d}t}{\mathrm{d}\lambda}=-a\left(aE\,sin^2\theta-L\right)+\left(r^2+a^2\right)\frac{\mathbb{T}}{\Delta}, \tag{2.2.6}$$

$$\Sigma\frac{\mathrm{d}\phi}{\mathrm{d}\lambda}=-\left(aE-\frac{L}{sin^2\theta}\right)+a\frac{\mathbb{T}}{\Delta}, \tag{2.2.7}$$

$$\Sigma\frac{\mathrm{d}r}{\mathrm{d}\lambda}=\pm\sqrt{\mathbb{V}_r}, \tag{2.2.8}$$

$$\Sigma\frac{\mathrm{d}\theta}{\mathrm{d}\lambda}=\pm\sqrt{\mathbb{V}_\theta}, \tag{2.2.9}$$

where:

$$\begin{gathered}\mathbb{T}=E\left(r^2+a^2\right)-aL,\\ \mathbb{V}_r=\mathbb{V}_r(r)=\mathbb{T}^2-\Delta\left[\mu^2r^2+(L-aE)^2+Q\right],\\ \mathbb{V}_\theta=\mathbb{V}_\theta(\theta)=Q-cos^2\theta\left[a^2\left(\mu^2-E^2\right)+\frac{L^2}{sin^2\theta}\right],\end{gathered} \tag{2.2.10}$$

and λ is an affine parameter for massless particles, while it is connected to the particle's proper time τ via $\lambda=\tau/\mu$ for massive particles (Bardeen et al. 1972, Wilkins 1972, Gralla & Lupsasca 2020a, 2020b, Gralla 2020, Gralla et al. 2020).

We continue on to study the most common and perhaps the most useful family of orbits around objects of this kind, orbits in the equatorial plane. Firstly, we look into an important subcategory of these circular equatorial orbits (see also Bardeen 1970b). In order for an orbit to be circular, $\mathrm{d}r/\mathrm{d}\lambda$ must equal zero for all times and infinitesimal moments. From Equation (2.2.8) this means that $\mathbb{V}_r(r)=0$ and $\mathbb{V}_r'(r)=0$. Solving for E and L we get:

$$\frac{E}{\mu}=\frac{r^{3/2}-2Mr^{1/2}\pm aM^{1/2}}{r^{3/4}\left(r^{3/2}-3Mr^{1/2}\pm 2aM^{1/2}\right)^{1/2}}, \tag{2.2.11}$$

$$\frac{L}{\mu}=\frac{\pm M^{1/2}\left(r^2\mp 2aM^{1/2}r^{1/2}+a^2\right)}{r^{3/4}\left(r^{3/2}-3Mr^{1/2}\pm 2aM^{1/2}\right)^{1/2}}, \tag{2.2.12}$$

where the upper signs refer to direct (corotating) orbits with $L>0$ and the lower signs to retrograde (counterrotating) orbits with $L<0$. From the above, the coordinate angular velocity $\Omega=\Omega(r)$ for circular equatorial orbits is given by:

$$\Omega=\Omega(r)=\frac{\mathrm{d}\phi}{\mathrm{d}t}=\frac{u^\phi}{u^t}=\frac{\pm M^{1/2}}{r^{3/2}\pm aM^{1/2}}. \tag{2.2.13}$$

From Equations (2.2.11) and (2.2.12), we see that for the energy and angular momentum of an orbit to be real numbers, we must have:

$$r^{3/2}-3Mr^{1/2}\pm 2aM^{1/2}\geq 0, \tag{2.2.14}$$

where the equality occurs for an orbit of infinite energy per unit rest mass, namely, the orbit of a photon. This gives the possibility of circular photon orbits around the black hole, a photon “sphere”, whose equatorial radius can be calculated from the above to be:

$$r_{ph}=2M\left\{1+cos\left[\frac{2}{3}cos^{-1}\left(\mp\frac{a}{M}\right)\right]\right\}. \tag{2.2.15}$$

For Schwarzschild space time ($a=0$), this gives a single photon orbit radius of $r_{ph}=3M$ and for a Kerr spacetime, infinite radii in between a pair of limiting photon orbits, one for a prograde and one for a retrograde orbit. As $a\to 0$, these two limiting orbits approach each other and finally degenerate into the one single radius. Conversely, as a increases, the direct and the retrograde photon orbits move away from each other. The inner photon orbit is followed by photons moving in the same direction as the black hole spin and the outer one, by photons moving in the direction opposite to the spin. The space in between the two is filled by orbiting photons with angular momentums perpendicular to the symmetry axis.

Continuing on, we examine circular orbits for massive particles. These orbits can be stable or bound if their energy is below a certain threshold $(E/\mu<1)$ and unbound otherwise. The limiting case is the marginally bound energetically parabolic circular orbit $(E/\mu=1)$ with radius:

$$r_{mb}=2M\mp a+2M^{1/2}(M\mp a)^{1/2}. \tag{2.2.16}$$

Orbits with $r>r_{mb}$ are bound circular orbits. Any parabolic orbit $(E/\mu=1)$ that crosses into the $r<r_{mb}$ regime, cannot escape outward and infalls into the black hole.

From the above equations, we can search for the existence of not only bound but also stable circular orbits. In order to find those, we solve the inequality $\mathbb{V}_r''(r) \leq 0$, which gives the solution for marginally stable orbits and the innermost circular case:

$$r_{ISCO} = M\left\{3 + Z_2 \mp \left[(3 - Z_1)(3 + Z_1 + 2Z_2)\right]^{1/2}\right\}, \qquad (2.2.17)$$

where

$$\begin{aligned} Z_1 &= 1 + \left(1 - \frac{a^2}{M^2}\right)^{1/3}\left[\left(1 + \frac{a}{M}\right)^{1/3} + \left(1 - \frac{a}{M}\right)^{1/3}\right], \\ Z_2 &= \left(\frac{3a^2}{M^2} + Z_1^{\,2}\right)^{1/2}. \end{aligned} \qquad (2.2.18)$$

This special marginally stable orbit is known as the innermost stable circular orbit or ISCO.

Before concluding this Section, we briefly discuss the various cases for the aforementioned notable orbits and surfaces presented above (see Fig. 2.4). The event horizon r_{evh} starts from the value of $2M$ in the Schwarzschild case and decreases to M as the spin parameter increases to from 0 to M. The equatorial radius of the ergosphere r_{ergo} remains equal to $2M$, independently of the spin parameter. The static limit, however, changes shape as the spin increases. For a Schwarzschild black hole, the ergosphere starts as a sphere and for increasing values of a it changes into to an oblate spheroid. For the maximal case, the ergosphere adopts the shape of a spindle torus. The single photon sphere radius r_{ph} begins for $a = 0$ with a value of $3M$ and splits into two as the spin increases. The inner, direct

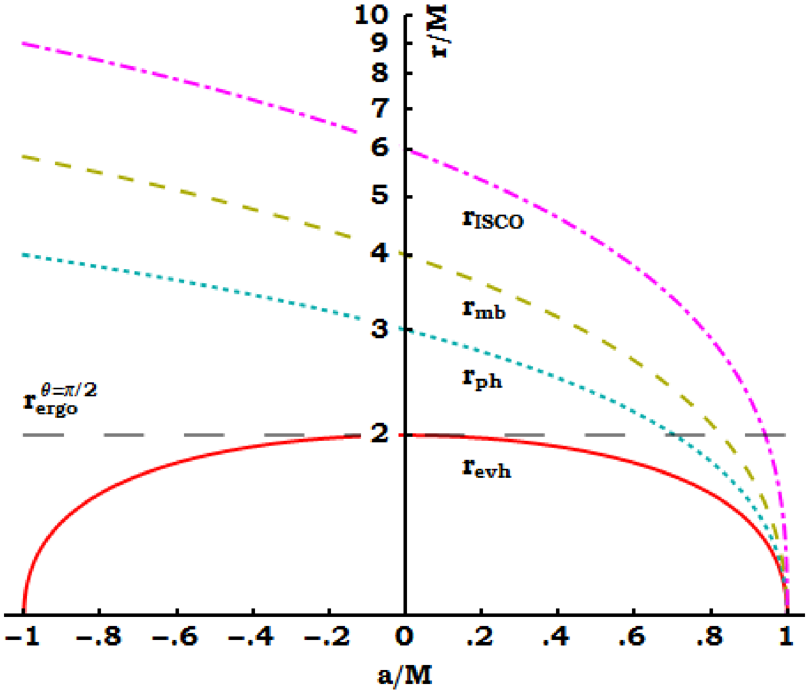

Figure 2.3: Plot of black hole spin to notable equatorial orbits radii: event horizon, equatorial ergosphere cross section, photon sphere, marginally bound orbit and ISCO. For $a \geq 0$ we can see the direct orbits radii and for $a < 0$ the retrograde orbits radii. We additionally notice that for a maximally rotating black hole, the notable orbits seem to coincide but in reality are distinct and separate.

photon sphere radius decreases to M as a reaches M and the outer, retrograde orbit radius increases to $4M$. As for the marginally bound orbit's radius r_{mb}, it starts at $4M$ for Schwarzschild spacetime and again splits into a direct orbit radius of M and a retrograde radius of $5.83M$ as $a \to M$. Finally, the ISCO starts at $a = 0$ with a direct radius of $6M$ and decreases to M, while the retrograde orbit goes to $9M$ for a maximally rotating black hole. Figure 2.3 shows a plot of the above changes in the radii as functions of the dimensionless spin parameter j of the black hole. We also note here that even though all the above direct orbits appear to degenerate to a single orbit of radius M for $a = M$, in reality they do not. Instead, the metric solutions describing the surfaces reveal that they do not coincide but remain separate and distinct, differing in proper radial distance (e.g., Bardeen et al. 1972, Chandrasekhar 1983).

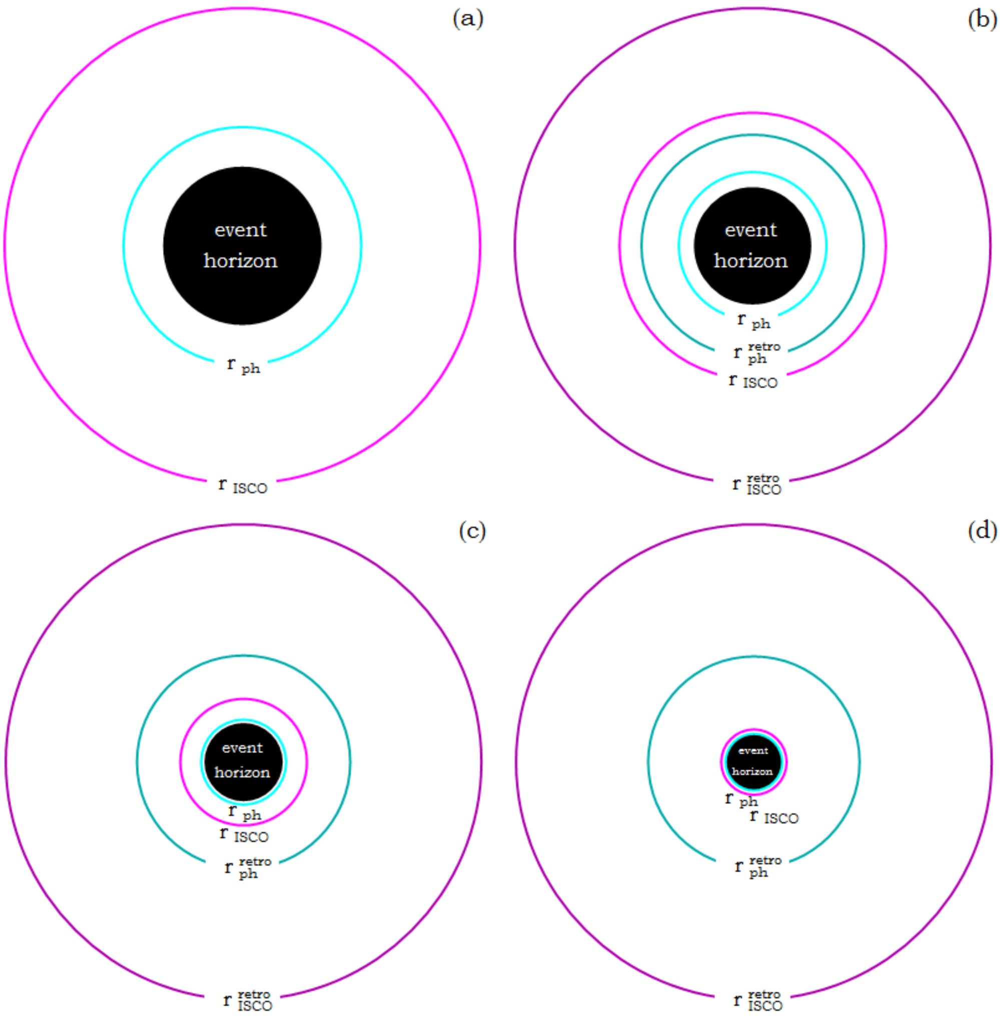

Figure 2.4: Change in radii for the equatorial black hole event horizon, the direct and retrograde photon sphere (r_{ph} and r_{ph}^{retro} respectively) and direct and retrograde ISCO (r_{ISCO} and r_{ISCO}^{retro} respectively) for spins *(a)* $a = 0$, *(b)* $a = 0.5M$, *(c)* $a = 0.9M$, and *(d)* $a = 0.998M$.

2.3. Locally nonrotating frames and zero angular momentum observers

Spacetime around an uncharged astrophysical black hole is, as discussed previously, adequately described by the Kerr metric. The axisymmetric Kerr metric is a generalization of the earlier defined spherically symmetric Schwarzschild metric. The Kerr metric, however, takes additionally into account the rotation of the spacetime itself and its consequences. The rotation of the central mass introduces differential rotation to the area of space around it that drags the spacetime frame around it. The closer a region is to the central mass, the more it is dragged, and the faster it rotates.

For the above, it is evident that there is great advantage in using an observer that moves along and rotates with the geometry. This is known as the zero angular momentum observer (ZAMO) or the locally nonrotating frame (LNRF), that rotate with angular speed ω around the central mass. Such a nonstatic observer is valuable, since the motion greatly eliminates the effects of frame dragging. This results in considerable simplification of the calculations and easy detection of errors, alternatives, and peculiar situations. In this locally Minkowskian coordinate system, each point in the spacetime has an orthonormal four-vector basis that is carried along with it. The fact that the ZAMO frame is locally Minkowskian also facilitates the calculations by significantly reducing the complexity of raising and lowering indices. This is due to the fact that there are no more nondiagonal components in the corresponding metric. The local frame of any arbitrary observer can be easily found by applying the appropriate Lorentz boost, when knowing the velocity of said observer relative to the ZAMO.

For a ZAMO at position $(t,\phi,r,\theta)_{BL} \equiv \left(\hat{t},\hat{\phi},\hat{r},\hat{\theta}\right)_{LNRF}$, the gravitational time dilation between that point of proper time $\hat{t}$ and an observer at infinity measuring with time t is:

$$\frac{t}{\hat{t}} = \sqrt{\frac{\mathrm{A}}{\Sigma\Delta}} = \sqrt{\frac{\left(r^2+a^2\right)^2 - \left(r^2-2Mr+a^2\right)a^2\sin^2\theta}{\left(r^2+a^2\cos^2\theta\right)\left(r^2-2Mr+a^2\right)}}\,. \qquad (2.3.1)$$

The azimuthal angle ϕ in the Boyer – Lindquist frame is measured in the ZAMO frame as $\hat{\phi}$. The two quantities are connected to each other using cross-terms, via the formula:

$$\phi = \omega\sqrt{\frac{\mathrm{A}}{\Sigma\Delta}}\cdot\hat{t} + \sqrt{\frac{\Sigma}{\mathrm{A}\sin^2\theta}}\cdot\hat{\phi}\,. \qquad (2.3.2)$$

The Boyer – Lindquist radius r is related to the ZAMO radius $\hat{r}$ via the canon:

$$\frac{r}{\hat{r}} = \sqrt{\frac{\Delta}{\Sigma}} = \sqrt{\frac{r^2-2Mr+a^2}{r^2+a^2\cos^2\theta}} \qquad (2.3.3)$$

and the Boyer – Lindquist polar angle θ to the ZAMO polar angle ϑ using the formula:

$$\frac{\theta}{\hat{\theta}} = \sqrt{\frac{1}{\Sigma}} = \sqrt{\frac{1}{r^2 + a^2\cos^2\theta}} \,. \tag{2.3.4}$$

Tensors and four-vectors in the ZAMO are denoted using hatted superscripts and subscripts as $T^{\hat{\alpha}\hat{\beta}}$ and $v^{\hat{\alpha}}$ respectively. The four-vector v^{α} and its tetrad components $v^{\hat{\mu}}$ are related by the formulae:

$$v^{\alpha} = e^{\alpha}_{\hat{\mu}} v^{\hat{\mu}} \text{ and } v^{\hat{\mu}} = e^{\hat{\mu}}_{\alpha} v^{\alpha} \,, \tag{2.3.5}$$

while for the tensor $T^{\alpha\beta}$ and its tetrad components $T^{\hat{\mu}\hat{\nu}}$ it is:

$$T^{\alpha\beta} = e^{\alpha}_{\hat{\mu}} e^{\beta}_{\hat{\nu}} T^{\hat{\mu}\hat{\nu}} \text{ and } T^{\hat{\mu}\hat{\nu}} = e^{\hat{\mu}}_{\alpha} e^{\hat{\nu}}_{\beta} T^{\alpha\beta} \,. \tag{2.3.6}$$

The transformation tensor components for the Kerr metric are:

$$e^{t}_{\hat{t}} = e^{-\nu} \,,\ e^{\phi}_{\hat{t}} = \omega e^{-\nu} \,,\ e^{\phi}_{\hat{\phi}} = e^{-\psi} \,,\ e^{r}_{\hat{r}} = e^{-\mu_1} \,,\ e^{\theta}_{\hat{\theta}} = e^{-\mu_2} \,, \tag{2.3.7}$$

$$e^{\hat{t}}_{t} = e^{\nu} \,,\ e^{\hat{\phi}}_{t} = -\omega e^{\psi} \,,\ e^{\hat{\phi}}_{\phi} = e^{\psi} \,,\ e^{\hat{r}}_{r} = e^{\mu_1} \,,\ e^{\hat{\theta}}_{\theta} = e^{\mu_2} \,, \tag{2.3.8}$$

with all other components equal to zero and the exponentials given by Equation (2.1.14). In a Kerr spacetime these quantities are:

$$e^{t}_{\hat{t}} = \sqrt{\frac{\mathrm{A}}{\Sigma\Delta}} \,,\ e^{\phi}_{\hat{t}} = \omega\sqrt{\frac{\mathrm{A}}{\Sigma\Delta}} \,,\ e^{\phi}_{\hat{\phi}} = \sqrt{\frac{\Sigma}{\mathrm{A}\sin^2\theta}} \,,\ e^{r}_{\hat{r}} = \sqrt{\frac{\Delta}{\Sigma}} \,,\ e^{\theta}_{\hat{\theta}} = \sqrt{\frac{1}{\Sigma}} \,, \tag{2.3.9}$$

$$e^{\hat{t}}_{t} = \sqrt{\frac{\Sigma\Delta}{\mathrm{A}}} \,,\ e^{\hat{\phi}}_{t} = -\omega\sin\theta\sqrt{\frac{\mathrm{A}}{\Sigma}} \,,\ e^{\hat{\phi}}_{\phi} = \sin\theta\sqrt{\frac{\mathrm{A}}{\Sigma}} \,,\ e^{\hat{r}}_{r} = \sqrt{\frac{\Sigma}{\Delta}} \,,\ e^{\hat{\theta}}_{\theta} = \sqrt{\Sigma} \,. \tag{2.3.10}$$

For a Schwarzschild spacetime, the above simplify to:

$$e^{t}_{\hat{t}} = \left(1 - \frac{2M}{r}\right)^{-1/2} ,\ e^{\phi}_{\hat{\phi}} = \frac{1}{r\sin\theta} ,\ e^{r}_{\hat{r}} = \left(1 - \frac{2M}{r}\right)^{1/2} ,\ e^{\theta}_{\hat{\theta}} = \frac{1}{r} , \tag{2.3.11}$$

$$e^{\hat{t}}_{t} = \left(1 - \frac{2M}{r}\right)^{1/2} ,\ e^{\hat{\phi}}_{\phi} = r\sin\theta \,,\ e^{\hat{r}}_{r} = \left(1 - \frac{2M}{r}\right)^{-1/2} ,\ e^{\hat{\theta}}_{\theta} = r \,. \tag{2.3.12}$$

Further information about all the assorted methods and selections of suitable spacetime segmentation can be found in Bini et al. 2015c.

2.4. Particle trajectories and Hamiltonian formulation

In Subsection 2.2.2, we wrote the equations of orbital trajectories for particles moving around a black hole. Equations (2.2.6) – (2.2.9), however, appear to have various problematic points. Even though the equations are rather elegant and compact in form, numerical integration quickly accumulates errors, mostly due to the presence and bimodality of the square roots. In order to avoid these difficult and time-consuming points, we choose to restate the equations of motion in Hamiltonian formulation, avoiding as much problems as possible.

The Lagrangian $\mathbb{L}$ for a free particle with mass μ in our environment is:

$$\mathbb{L}(q,\dot{q}) = \frac{1}{2}\mu g_{\alpha\beta}\dot{q}^{\alpha}\dot{q}^{\beta} = \frac{1}{2}\mu g^{\alpha\beta}\dot{q}_{\alpha}\dot{q}_{\beta} \tag{2.4.1}$$

and for its four-momentum, we have:

$$p^{\alpha} = \mu u^{\alpha} = \mu\dot{q}^{\alpha} . \tag{2.4.2}$$

The above give:

$$\mathbb{L}(q,\dot{q}) = \frac{1}{2\mu} g^{\alpha\beta} p_{\alpha} p_{\beta} \tag{2.4.3}$$

and by taking into account the four-velocity norm:

$$p^{\alpha} p_{\alpha} = g^{\alpha\beta} p_{\alpha} p_{\beta} = -\mu^{2} , \tag{2.4.4}$$

we get:

$$\mathbb{L} = -\frac{1}{2}\mu , \tag{2.4.5}$$

which shows that the Lagrangian is constant.

Continuing on to calculate the Hamiltonian, we use the restatement for the covariant four-momentum components:

$$p_{\alpha} = \frac{\partial\mathbb{L}}{\partial\dot{q}^{\alpha}} = \frac{1}{2}\mu g_{\alpha\sigma}\dot{q}^{\sigma} + \frac{1}{2}\mu g_{\rho\alpha}\dot{q}^{\rho} = \mu g_{\alpha\beta}\dot{q}^{\beta} = g_{\alpha\beta} p^{\beta} . \tag{2.4.6}$$

The components of the four-momentum thus are:

$$p_t = \mu\left(g_{tt}\dot{t} + g_{t\phi}\dot{\phi}\right) , \tag{2.4.7}$$

$$p_{\phi} = \mu\left(g_{t\phi}\dot{t} + g_{\phi\phi}\dot{\phi}\right) , \tag{2.4.8}$$

$$p_r = \mu g_{rr}\dot{r} = \mu\frac{\Sigma}{\Delta}\dot{r} , \tag{2.4.9}$$

$$p_{\theta} = \mu g_{\theta\theta}\dot{\theta} = \mu\Sigma\dot{\theta} \tag{2.4.10}$$

and the Hamiltonian $\mathbb{H}$ is given by:

$$\mathbb{H}(q,p) = p_{\alpha}\dot{q}^{\alpha} - \mathbb{L} . \tag{2.4.11}$$

In order to avoid some cumbersome algebra we notice that:

$$\begin{aligned} &\mathbb{H} = p_{\alpha}\dot{q}^{\alpha} - \mathbb{L} = \\ &= \frac{1}{\mu} p_{\alpha} p^{\alpha} - \mathbb{L} = \frac{1}{\mu} g^{\alpha\beta} p_{\alpha} p_{\beta} - \frac{1}{2\mu} g^{\alpha\beta} p_{\alpha} p_{\beta} = \frac{1}{2\mu} g^{\alpha\beta} p_{\alpha} p_{\beta} \end{aligned} \tag{2.4.12}$$

and for the Lagrangian:

$$\begin{aligned}\mathbb{L}&=\frac{1}{2\mu}\left(g^{rr}p_r{}^2+g^{\theta\theta}p_\theta{}^2+g^{\alpha\beta}p_\alpha p_\beta\right)=\\&=\frac{\Delta}{2\mu\Sigma}p_r{}^2+\frac{1}{2\mu\Sigma}p_\theta{}^2+f\left(r,\theta,p_t,p_\phi\right),\end{aligned}\tag{2.4.13}$$

where $\alpha,\beta=t,\phi$. Furthermore, from the equations of motion (2.2.6), we get that:

$$p_r{}^2=\frac{\mathbb{V}_r}{\Delta^2},\tag{2.4.14}$$

$$p_\theta{}^2=\mathbb{V}_\theta.\tag{2.4.15}$$

From this, we see that the Lagrangian takes the form:

$$\mathbb{L}=\frac{\mathbb{V}_r}{2\mu\Sigma\Delta}+\frac{\mathbb{V}_\theta}{2\mu\Sigma}+f=\frac{\mathbb{V}_r+\Delta\mathbb{V}_\theta}{2\mu\Sigma\Delta}+f\tag{2.4.16}$$

and therefore the Hamiltonian is:

$$\mathbb{H}=\frac{\mathbb{V}_r+\Delta\mathbb{V}_\theta}{2\mu\Sigma\Delta}+f.\tag{2.4.17}$$

Since we consider the case of a free particle, that consequently has only kinetic terms in its Lagrangian, it is:

$$\mathbb{H}=-\frac{1}{2}\mu\tag{2.4.18}$$

and by combining Equations (2.4.17) and (2.4.18), we have that:

$$f\left(r,\theta,p_t,p_\phi\right)=-\frac{\mathbb{V}_r+\Delta\mathbb{V}_\theta}{2\mu\Sigma\Delta}-\frac{\mu}{2}.\tag{2.4.19}$$

Finally, combining (2.4.13), (2.4.17), and (2.4.19), we get the complete form of the Hamiltonian:

$$\mathbb{H}=\frac{\Delta}{2\mu\Sigma}p_r{}^2+\frac{1}{2\mu\Sigma}p_\theta{}^2-\frac{\mathbb{V}_r+\Delta\mathbb{V}_\theta}{2\mu\Sigma\Delta}-\frac{\mu}{2}.\tag{2.4.20}$$

The Hamilton equations describing thus the particle motion are:

$$\dot{q}_\alpha=\frac{\partial\mathbb{H}}{\partial p_\alpha},\tag{2.4.21}$$

$$\dot{p}_\alpha=-\frac{\partial\mathbb{H}}{\partial q_\alpha}.\tag{2.4.22}$$

For the four components of the first Equation (2.4.21), we get:

$$\dot{t}=\frac{\partial\mathbb{H}}{\partial p_t}=-\frac{\partial\mathbb{H}}{\partial E}=\frac{1}{2\mu\Sigma\Delta}\frac{\partial}{\partial E}\left(\mathbb{V}_r+\Delta\mathbb{V}_\theta\right),\tag{2.4.23}$$

$$\dot{\phi}=\frac{\partial\mathbb{H}}{\partial p_\phi}=\frac{\partial\mathbb{H}}{\partial L}=-\frac{1}{2\mu\Sigma\Delta}\frac{\partial}{\partial L}\left(\mathbb{V}_r+\Delta\mathbb{V}_\theta\right),\tag{2.4.24}$$

$$\dot{r}=\frac{\partial\mathbb{H}}{\partial p_r}=\frac{\Delta}{\mu\Sigma}p_r,\tag{2.4.25}$$

$$\dot{\theta}=\frac{\partial\mathbb{H}}{\partial p_\theta}=\frac{1}{\mu\Sigma}p_\theta.\tag{2.4.26}$$

Respectively, for the four components of Equation (2.4.22) we have:

$$\dot{p}_t = -\frac{\partial \mathbb{H}}{\partial t} = 0, \tag{2.4.27}$$

$$\dot{p}_\phi = -\frac{\partial \mathbb{H}}{\partial \phi} = 0, \tag{2.4.28}$$

$$\dot{p}_r = -\frac{\partial \mathbb{H}}{\partial r} = -{p_r}^2 \frac{\partial}{\partial r}\left(\frac{\Delta}{2\mu\Sigma}\right) - {p_\theta}^2 \frac{\partial}{\partial r}\left(\frac{1}{2\mu\Sigma}\right) + \frac{\partial}{\partial r}\left(\frac{\mathbb{V}_r + \Delta\mathbb{V}_\theta}{2\mu\Sigma\Delta}\right), \tag{2.4.29}$$

$$\dot{p}_\theta = -\frac{\partial \mathbb{H}}{\partial \theta} = -{p_r}^2 \frac{\partial}{\partial \theta}\left(\frac{\Delta}{2\mu\Sigma}\right) - {p_\theta}^2 \frac{\partial}{\partial \theta}\left(\frac{1}{2\mu\Sigma}\right) + \frac{\partial}{\partial \theta}\left(\frac{\mathbb{V}_r + \Delta\mathbb{V}_\theta}{2\mu\Sigma\Delta}\right), \tag{2.4.30}$$

where Q is a constant and $\mathbb{V}_r = \mathbb{V}_r(r,E,L)$, $\mathbb{V}_\theta = \mathbb{V}_\theta(\theta,E,L)$ the effective potentials (see Eq. (2.2.10)).

In the case where we want to study the motion of photons or we want a more general expression for the particle's equation of motion, we use the λ parameter and the relation $\tau = \mu\lambda$. We can then replace derivation by proper time τ with derivations by λ using:

$$\frac{\mathrm{d}}{\mathrm{d}\tau} = \frac{1}{\mu}\frac{\mathrm{d}}{\mathrm{d}\lambda}. \tag{2.4.31}$$

If we wish to study the motion of photons or other massless particles, we notice that this λ parameter is nothing more that the regular affine parameter. Hence, for such particles the equations of motion as functions of the parameter λ are:

$$\frac{\mathrm{d}t}{\mathrm{d}\lambda} = \frac{1}{2\Sigma\Delta}\frac{\partial}{\partial E}\left(\mathbb{V}_r + \Delta\mathbb{V}_\theta\right), \tag{2.4.32}$$

$$\frac{\mathrm{d}\phi}{\mathrm{d}\lambda} = -\frac{1}{2\Sigma\Delta}\frac{\partial}{\partial L}\left(\mathbb{V}_r + \Delta\mathbb{V}_\theta\right), \tag{2.4.33}$$

$$\frac{\mathrm{d}r}{\mathrm{d}\lambda} = \frac{\Delta}{\Sigma} p_r, \tag{2.4.34}$$

$$\frac{\mathrm{d}\theta}{\mathrm{d}\lambda} = \frac{1}{\Sigma} p_\theta, \tag{2.4.35}$$

$$\frac{\mathrm{d}p_t}{\mathrm{d}\lambda} = 0, \tag{2.4.36}$$

$$\frac{\mathrm{d}p_\phi}{\mathrm{d}\lambda} = 0, \tag{2.4.37}$$

$$\frac{\mathrm{d}p_r}{\mathrm{d}\lambda} = -{p_r}^2 \frac{\partial}{\partial r}\left(\frac{\Delta}{2\Sigma}\right) - {p_\theta}^2 \frac{\partial}{\partial r}\left(\frac{1}{2\Sigma}\right) + \frac{\partial}{\partial r}\left(\frac{\mathbb{V}_r + \Delta\mathbb{V}_\theta}{2\Sigma\Delta}\right), \tag{2.4.38}$$

$$\frac{\mathrm{d}p_\theta}{\mathrm{d}\lambda} = -{p_r}^2 \frac{\partial}{\partial \theta}\left(\frac{\Delta}{2\Sigma}\right) - {p_\theta}^2 \frac{\partial}{\partial \theta}\left(\frac{1}{2\Sigma}\right) + \frac{\partial}{\partial \theta}\left(\frac{\mathbb{V}_r + \Delta\mathbb{V}_\theta}{2\Sigma\Delta}\right), \tag{2.4.39}$$

(but see also Gralla & Lupsasca 2020a, 2020b, Gralla 2020, Gralla et al. 2020).

Our final set of equations is now composed of smoothly differentiable equations and can be directly integrated. In addition, we note that

Equations (2.4.36) and (2.4.37) are null, and represent the two conserved quantities of motion, the total energy and the angular momentum component parallel to the symmetry axis.

CHAPTER 3

RADIATION

In this Chapter, we examine how we can calculate and study the radiation absorbed by the accretion disk material in various directions. We examine radiation reaching the target particle from a skin layer of optically thick accretion disks, as well as radiation propagating through the disk's quasi-opaque material by solving the general relativistic radiative transfer equation. Using these two methods, we show how we can calculate the resulting radiation force, the ensuing radiation field generated, and its effects onto the disk material and motion.

The first steps in such a procedure were taken by Guess 1962, Abramowicz, Ellis & Lanza 1990, Miller & Lamb 1993 and 1996, Lamb & Miller 1995, and Oh et al. 2010. These studies, however, differ from our own in one key element. The radiation source considered there is taken to be central and spherical. In our research, nonetheless, the photons source is noncentral and extends in large volumes of space in azimuthal and poloidal angles. Closer to our research perspective is the work of Fuerst 2006, Fuerst & Wu 2004, 2007, and 2008, Wu et al. 2008a and 2008b, and Younsi et al. 2012 that study and consider the radiation and appearance of hot accretion disks around central objects.

Extensive work concerning the radiation present in such systems and the Poynting – Robertson effect acting there are done by D. Bini in numerous works. These include Bini et al. 2009, 2011a, 2011b, 2015a, and 2015b, and Bini & Geralico 2010, 2012, and 2016.

Finally yet importantly, it is certainly worth mentioning the works of V. De Falco concerning the relativistic Poynting – Robertson effect and its repercussions on disk material shown in De Falco 2019 and 2020, and De Falco et al. 2020.

3.1. Radiation force and acceleration

In this Section, we discuss the components we need to calculate along with the series of equations required in order to determine the radiation forces recorded in the systems we study.

We start by identifying that what we wish to calculate are the effects of radiation on a moving particulate. The formula that defines the equations of motion is:

$$\frac{\mathrm{d}^2 x^\alpha}{\mathrm{d}\tau^2} + \Gamma^\alpha_{\mu\nu} \frac{\mathrm{d}x^\mu}{\mathrm{d}\tau} \frac{\mathrm{d}x^\nu}{\mathrm{d}\tau} = a^\alpha , \tag{3.1.1}$$

where x^α the particulate position components, τ the proper time, and $\Gamma^\alpha_{\mu\nu}$ the Christoffel symbols or connection coefficients (Mueller & Grave 2009).

The acceleration a^α here includes all the nongravitational forces, hence for us all the radiation forces. This acceleration is given by the following relativistic equation of motion:

$$a^\alpha = \frac{f^\alpha}{m} , \tag{3.1.2}$$

where m the target particulate's rest mass and f^α the radiation four-force.

To calculate this four-force, we require the radiation flux F^α and application of the formula:

$$f^\alpha = \sigma F^\alpha , \tag{3.1.3}$$

with σ the particulate cross section for the momentum transfer.

The flux of radiation can be found by applying the law:

$$F^\alpha = h^\alpha_\beta T^{\mu\beta} u_\mu , \tag{3.1.4}$$

where u_μ the target particulate's covariant four-velocity and $T^{\alpha\beta}$ the radiation stress–energy tensor. The quantity h^α_β is the projection tensor and is given by:

$$h^a_\beta = \delta^\alpha_\beta + u^\alpha u_\beta , \tag{3.1.5}$$

where δ^α_β is the typical Kronecker delta function.

For the calculation of the Boyer – Lindquist stress-energy tensor, we need to know the stress – energy tensor in the ZAMO frame and apply the formula:

$$T^{\alpha\beta} = e^\alpha_{\hat{\mu}} e^\beta_{\hat{\nu}} T^{\hat{\mu}\hat{\nu}} , \tag{3.1.6}$$

where the matrix components $e^\alpha_{\hat{\mu}}$ are given in (2.3.7), (2.3.9), and (2.3.11).

The ZAMO stress – energy tensor $T^{\hat{\mu}\hat{\nu}}$ must be calculated using the distribution of radiation in the local sky and applying the formula:

$$T^{\hat{\mu}\hat{\nu}} = \int I\left(r, \theta, \tilde{a}, \tilde{b}\right) n^{\hat{\mu}} n^{\hat{\nu}} \mathrm{d}\tilde{\Omega} , \tag{3.1.7}$$

where $\mathrm{d}\tilde{\Omega} = \sin\tilde{a}\, d\tilde{a}\, d\tilde{b}$ is the solid angle element with $\tilde{a}$ and $\tilde{b}$ the related appropriate local angles (Fig. 3.1), $n^{\hat{\mu}} = p^{\hat{\mu}} / p^{\hat{t}}$, and $I\left(r, \theta, \tilde{a}, \tilde{b}\right)$ the frequency-integrated specific intensity of the radiation. The unitary spacelike vector $n^{\hat{a}}$ components of the incoming photon's direction are given by:

$$n^{\hat{\phi}} = \sin\tilde{a} \sin\tilde{b} ,\ n^{\hat{r}} = \cos\tilde{a} ,\ n^{\hat{\theta}} = \sin\tilde{a} \cos\tilde{b} . \tag{3.1.8}$$

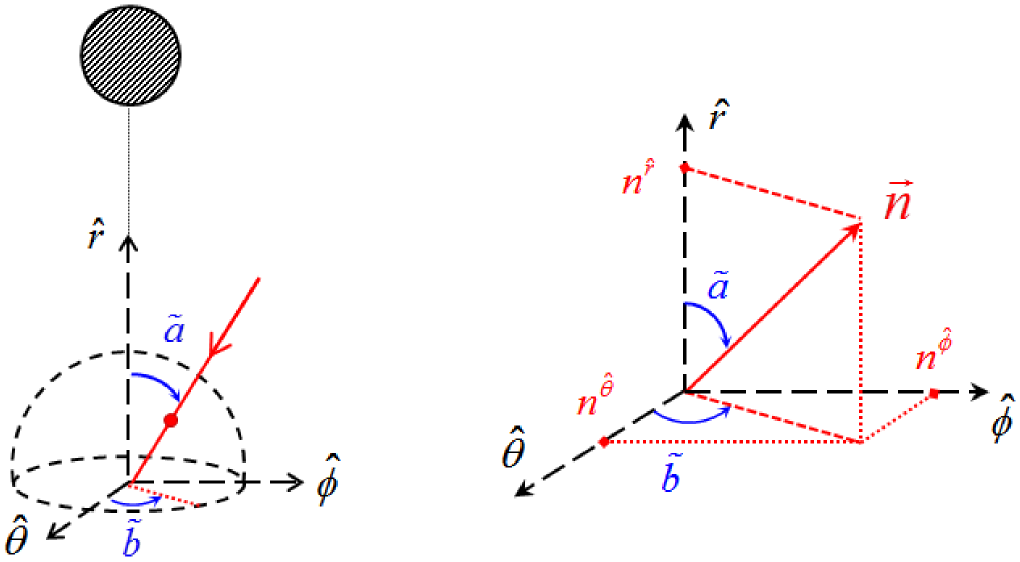

Figure 3.1: Local sky around the target particle: (*left*) forward in time (received photon moves toward the target) and (*right*) moving backward in time (the photon moves away from the target). For the examined photon, we define angles $\tilde{a}$ and $\tilde{b}$ similar to the typical polar angle θ and azimuthal angle ϕ of spherical coordinate systems respectively. The disk in stripes at the top left is the black hole event horizon.

The frequency-integrated specific intensity $I\left(erg\, s^{-1}\, cm^{-2}\, ster^{-1}\right)$ is, as mentioned above, dependent on the local sky emission source distribution. Therefore, it is a function of the target particulate's location and its position in spacetime with respect to the accretion disk. We can calculate the frequency-integrated specific intensity I:

$$I = \int_{\nu} I_{\nu}\, \mathrm{d}\nu\,, \tag{3.1.9}$$

where $I_{\nu}\left(erg\, s^{-1}\, cm^{-2}\, ster^{-1}\, Hz^{-1}\right)$ the specific intensity at frequency $\nu\left(Hz\right)$. The above procedure can be used to calculate the radiation intensity of different objects such as blackbody distribution, thermal radiation, single-energy beam of light, frequency-independent radiation, and other.

We would like to observe now, that in cases where the radiation is emitted by a thin surface layer of the source, the radiation intensity calculation is much simplified and done in the manner described in Section 3.3. On the contrary, in cases where the above is not true, the equations presented there cannot be used. The appropriate method to use in such cases is to solve the radiative transfer equation. The problem solution for these circumstances is discussed in Section 3.2.

3.2. Radiative transfer

In this Section, we discuss the radiative transfer equation and its solution in the general case (see Rybicki & Lightman 1986), which is accretion disks with finite optical depth. In such cases, the radiation is emitted and absorbed throughout the entire volume of the disk, and then possibly escapes the system. In general, emission and absorption simplifications can be made in cases where General Relativity is not required. Additionally, further simplifications can be made in cases where the emission and the absorption take place in a thin surface layer of the radiative disk material (see Sect. 3.3).

Let us assume a source material that is thermalized and has a number density $n\left(cm^{-3}\right)$. The material is made up of particles or particulates that act as radiation emitters and absorbers simultaneously. Let us first consider the absorption processes in the material and consider the disk matter as solely absorbers. Later on, we examine anew the material considering only emission processes. We define the absorption coefficient $a_\nu\left(cm^{-1}\right)$ at frequency ν as:

$$a_\nu = n\,\sigma_\nu\,, \tag{3.2.1}$$

where $\sigma_\nu\left(cm^2\right)$ is the absorbing area cross section at frequency ν and n the material number density. We assume at frequency ν an initial specific intensity I_ν, at which the material's absorption causes decrease dI_ν in a propagation length ds equal to:

$$\mathrm{d}I_\nu = -a_\nu I_\nu \mathrm{d}s\,. \tag{3.2.2}$$

We then go on to define the emission coefficient as $j_\nu\left(erg\,cm^{-3}\,s^{-1}\,ster^{-1}\,Hz^{-1}\right)$. If we assume a ray propagating for distance ds inside the emitting material, it traverses a material of volume $d\mathcal{V}$ and its specific intensity increases as:

$$\mathrm{d}I_\nu = j_\nu \mathrm{d}s\,. \tag{3.2.3}$$

If we combine the previous two equations, we can get the differential form of the radiation transfer equation as:

$$\frac{\mathrm{d}I_\nu}{\mathrm{d}s} = -a_\nu\, I_\nu + j_\nu\,. \tag{3.2.4}$$

In order to move along with simpler equations, we go on by defining the optical depth $\tau_\nu\left(scalar\right)$ at frequency ν as:

$$\mathrm{d}\tau_\nu = a_\nu \mathrm{d}s\,. \tag{3.2.5}$$

Integration along the ray path gives the function of optical depth as:

$$\tau_\nu\left(s\right) = \int_{s_0}^{s} a_\nu\left(s'\right)\mathrm{d}s'\,, \tag{3.2.6}$$

where s_0 is an arbitrarily selected initial point of the scale. Equation (3.2.4) can then be restated as:

$$\frac{\mathrm{d}I_\nu}{\mathrm{d}\tau_\nu} = -I_\nu + \frac{j_\nu}{a_\nu}\,. \tag{3.2.7}$$

Integration of the above gives the Classical Physics form of the radiative transfer equation as:

$$I_\nu(s) = I_\nu(s_0)e^{-\tau_\nu} + \int_{s_0}^{s} j_\nu(s')\, e^{-\left[\tau_\nu(s)-\tau_\nu(s')\right]}\, \mathrm{d}s' . \qquad (3.2.8)$$

In the case where we want to study the phenomenon within the frame of General Relativity (Misner, Thorne, & Wheeler 1973), we need to restate the above equation in a manner that the magnitudes involved are Lorentz invariant. In order to achieve that, we start by giving the phase space number density $\mathfrak{N}$:

$$\mathfrak{N} = \frac{N}{\mathcal{V}}, \qquad (3.2.9)$$

where N is the number of particles under examination and $\mathcal{V}$ the phase space volume they occupy. We go on to apply Liouville's theorem in curved spacetime and have that:

$$\frac{\mathrm{d}\mathcal{V}}{\mathrm{d}\lambda} = 0, \qquad (3.2.10)$$

where λ is the affine parameter. If we combine this with the conservation of the number of particles in a world line of the bundle, we get that:

$$\frac{\mathrm{d}\mathfrak{N}}{\mathrm{d}\lambda} = 0, \qquad (3.2.11)$$

which can be recognized as the collisionless Boltzmann kinetic equation. It is clear then that the number density $\mathfrak{N}$ is Lorentz invariant.

If we go back to the phase space, we can consider an element of volume, which is:

$$\mathrm{d}\mathcal{V} = \mathrm{d}^3x\, \mathrm{d}^3p = \mathrm{d}A\, \mathrm{d}t\, h^3\nu^2\, \mathrm{d}\nu\, \mathrm{d}\Omega, \qquad (3.2.12)$$

where h $(erg \cdot s)$ is the Planck constant, $\mathrm{d}A$ the area element for the photon bundle, and $\mathrm{d}\Omega$ the unit solid angle. Then by implicating the number density, we have that:

$$\mathfrak{N} = \frac{\mathrm{d}N}{h^3\nu^2 \mathrm{d}A\, \mathrm{d}t\, \mathrm{d}\nu\, \mathrm{d}\Omega}. \qquad (3.2.13)$$

Since for the specific intensity it is:

$$I_\nu = \frac{h\nu\, \mathrm{d}N}{\mathrm{d}A\, \mathrm{d}t\, \mathrm{d}\nu\, \mathrm{d}\Omega}, \qquad (3.2.14)$$

then for the number density, it is that:

$$\mathfrak{N} = \frac{1}{h^4}\frac{I_\nu}{\nu^3}. \qquad (3.2.15)$$

From the above, we get the Lorentz invariant specific intensity $\mathcal{I}_\nu$ as:

$$\mathcal{I}_\nu = \frac{I_\nu}{\nu^3} = \text{Lorentz invariant}. \qquad (3.2.16)$$

In addition, we can consider that the optical depth τ is used to count photon quantity fractions and is thus a scalar quantity. The optical depth is hence invariant:

$$\tau = \text{Lorentz invariant}. \qquad (3.2.17)$$

We move along to establish as well the Lorentz invariant absorption and emission coefficients. Firstly, we work onto the absorption and we look

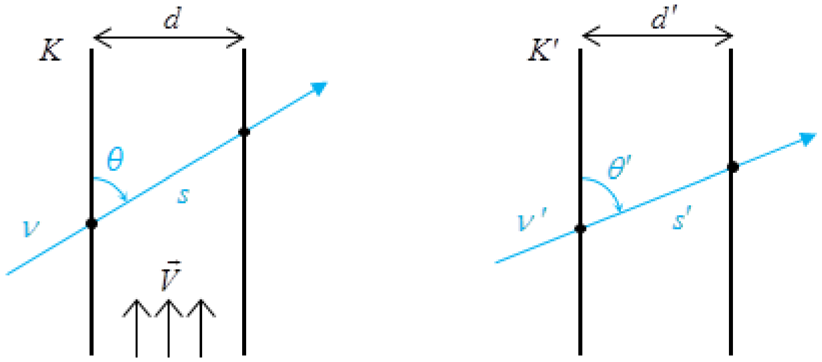

Figure 3.2: Emitting material in the lab frame K (*left*) moving with three-velocity $\vec{V}$ in a tube of width d along the vertical axis. A photon with frequency ν crosses the tube traveling at an angle θ from the vertical axis. Emitting material in its rest frame K' in the tube (*right*). The photon with frequency ν' here appears to cross the tube at angle θ'.

at Figure 3.2 of material flowing through a tube with three-velocity $\vec{V}$. Observing the material's vertical motion, we notice that the tube's width $d = d'$ is perpendicular to the motion and thus the same in both the lab and the matter rest frame. For the same reason, the horizontal material momentum is the same in both frames and $k_x = k_x'$. For the total momentum k we have then that $k \sin\theta = k' \sin\theta'$ and thus $\nu \sin\theta = \nu' \sin\theta'$. Keeping in mind the optical depth's $\tau_\nu = a_\nu\, s$ Lorentz invariance, we have then that the Lorentz invariant absorption coefficient $\mathscr{a}_\nu$ is:

$$\mathscr{a}_\nu = \nu\, a_\nu = \nu'\, a_\nu' = \text{Lorentz invariant}\,. \tag{3.2.18}$$

For the emission coefficient finally, we use Equations (3.2.7), (3.2.16), and (3.2.18) and conclude that the Lorentz invariant emission coefficient $\mathscr{j}_\nu$ then is:

$$\mathscr{j}_\nu = \frac{j_\nu}{\nu^2} = \frac{j_\nu'}{\nu'^2} = \text{Lorentz invariant}\,. \tag{3.2.19}$$

Collecting the above, we have that the Lorentz invariant form of the radiative transfer Equation (3.2.7) is:

$$\frac{\mathrm{d}\mathcal{I}_\nu}{\mathrm{d}\tau_\nu} = -\mathcal{I}_\nu + \frac{\mathscr{j}_\nu}{\mathscr{a}_\nu}\,. \tag{3.2.20}$$

Since for the optical depth, it is that $\mathrm{d}\tau_\nu = a_\nu\, \mathrm{d}s$, Equations (3.2.18), (3.2.19), and (3.2.20) give that:

$$\frac{\mathrm{d}\mathcal{I}_\nu}{\mathrm{d}s} = -a_\nu \mathcal{I}_\nu + \frac{j_\nu}{\nu^3}\,. \tag{3.2.21}$$

In order to take into account the path length variation $\frac{\mathrm{d}s}{\mathrm{d}\lambda}$, we calculate the photon velocity $(\upsilon')^\alpha$ in the fluid frame K' using the projection tensor $h^{\alpha\beta}$:

$$\left(\upsilon'\right)^{\alpha} = h^{\alpha\beta}k_{\beta} = k^{\alpha} + \left(k_{\beta}u^{\beta}\right)u^{\alpha}, \qquad (3.2.22)$$

where u^{α} is the fluid four-velocity, k_{β} the photon momentum components, and $h^{\alpha\beta} = g^{\alpha\beta} + u^{\alpha}u^{\beta}$ the projection tensor. The path length variation then is:

$$\frac{\mathrm{d}s}{\mathrm{d}\lambda} = -\left\|\left(\upsilon'\right)^{\alpha}\right\|\Big|_{obs} = -\sqrt{g_{\alpha\beta}\left(\upsilon'\right)^{\alpha}\left(\upsilon'\right)^{\beta}}\Big|_{obs} = -k_{\beta}u^{\beta}\Big|_{obs}. \qquad (3.2.23)$$

The frequency ratio consequently is:

$$\frac{\nu}{\nu\,'} = \frac{k_{\beta}u^{\beta}\Big|_{obs}}{k_{\alpha}u^{\alpha}\Big|_{\lambda}}. \qquad (3.2.24)$$

Magnitudes denoted with accents, such as $\upsilon\,'$ and $\nu\,'$ above, are assumed measured in the local rest frame. Putting together the above gives that:

$$\frac{\mathrm{d}s}{\mathrm{d}\lambda} = -k_{\alpha}u^{\alpha}\Big|_{\lambda}\frac{\nu}{\nu_0} \qquad (3.2.25)$$

Equations (3.2.18), (3.2.19), (3.2.21), and (3.2.25) give then the differential form of the Lorentz invariant radiative transfer equation as:

$$\frac{\mathrm{d}\mathcal{I}_{\nu}}{\mathrm{d}\lambda} = -k_{\alpha}u^{\alpha}\Big|_{\lambda}\left(-a_{\nu}{'}\mathcal{I}_{\nu} + \frac{j_{\nu}{'}}{\nu\,'^{3}}\right). \qquad (3.2.26)$$

Integrating the above gives then:

$$\begin{aligned}\mathcal{I}_{\nu}\left(\lambda\right) = \mathcal{I}_{\nu}\left(\lambda_0\right)e^{\int_{\lambda_0}^{\lambda}a_{\nu}{'}\left(\zeta\right)k_{\alpha}u^{\alpha}\big|_{\zeta}\mathrm{d}\zeta} - \\ -\int_{\lambda_0}^{\lambda}\frac{j_{\nu}{'}\left(\xi\right)}{\nu\,'^{\,3}}e^{\int_{\xi}^{\lambda}a_{\nu}{'}\left(\zeta\right)k_{\alpha}u^{\alpha}\big|_{\zeta}\mathrm{d}\zeta}\,k_{\alpha}u^{\alpha}\Big|_{\xi}\mathrm{d}\xi,\end{aligned} \qquad (3.2.27)$$

the formula for the Lorentz invariant specific intensity. In order to make the above equation shorter and more elegant, we use the optical depth as:

$$\tau_{\nu}\left(\lambda\right) = -\int_{\lambda_0}^{\lambda}a_{\nu}{'}\left(\zeta\right)k_{\alpha}u^{\alpha}\Big|_{\zeta}\mathrm{d}\zeta \qquad (3.2.28)$$

and the above is rewritten as:

$$\mathcal{I}_{\nu}\left(\lambda\right) = \mathcal{I}_{\nu}\left(\lambda_0\right)e^{-\tau_{\nu}\left(\lambda\right)} - \int_{\lambda_0}^{\lambda}\frac{j_{\nu}{'}\left(\xi\right)}{\nu\,'^{\,3}}e^{-\left[\tau_{\nu}\left(\lambda\right)-\tau_{\nu}\left(\xi\right)\right]}k_{\alpha}u^{\alpha}\Big|_{\xi}\mathrm{d}\xi\;. \qquad (3.2.29)$$

3.3. Single emission source radiation

In the previous Section, we discussed the radiative transfer equation in Classical Physics (3.2.8) and in General Relativity (3.2.29). After that, we built its solution for the general case by accounting for the intensity increase due to the emitting intervening material and the decrease due to the absorbing targets. Nonetheless, we also mentioned that in cases of large enough density gradients, the emission and absorption of radiation only takes place within a rather thin surface layer of the disk. In such cases, notable modifications enter the problem, bringing along significant simplifications to the calculations required (see e.g., Abramowicz et al. 1990, Miller & Lamb 1996, Koutsantoniou & Contopoulos 2014, Koutsantoniou 2022, 2023 and online material [4]).

This is because the material density, and hence the optical depth, has so steep a gradient that numerical integration is notably challenging. Namely, the steeper the density increment is, the finer the affine parameter partition should be. When this increase is so abrupt, however, the estimated intensity (the lower limit) is far from its actual value. This results in the need of an ever-denser partition mesh that is computationally unattainable. Consequently, another solution should be found, one that includes and accounts for all the relativistic effects brought on by the spacetime grid distortion due to the central mass. In this Section, we thus study said environments of optically thick disks and examine the different forms the radiative transfer equation takes.

Earlier, we saw in Eq. (3.2.16) that the Lorentz invariant specific intensity is $\mathcal{I}_\nu = I_\nu / \nu^3$. For the frequency-integrated specific intensity, it is

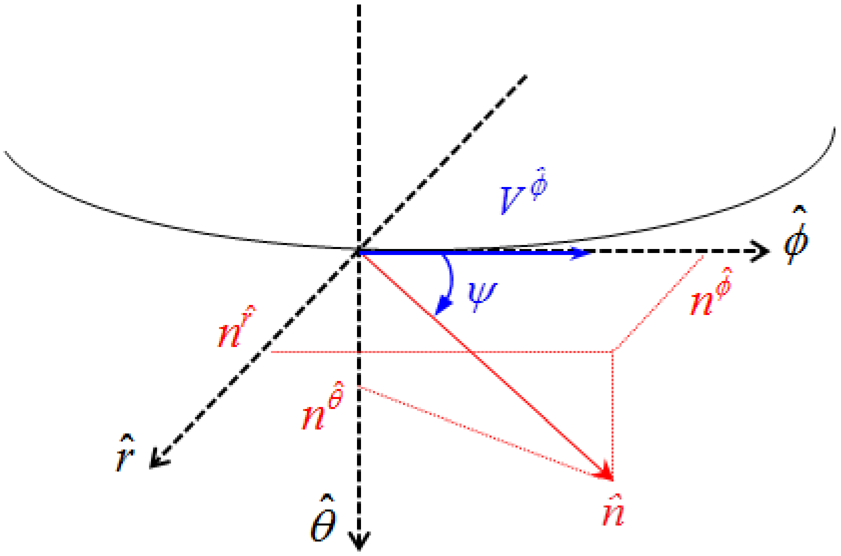

Figure 3.3: Emission of a photon from the hot accretion disk material. The photon is emitted in the direction of $\hat{n}$ from an element of matter that moves with three-velocity $V^{\hat{\phi}}$. The photon is emitted at angle ψ relative to the accreting material motion.

---

[4] *Link URL:* https://gitlab.com/leelamichaels/aandrt-ii-online-material

thus:

$$\frac{I_1}{\nu_1^4} = \frac{I_2}{\nu_2^4} = \text{Lorentz invariant} \qquad (3.3.1)$$

for any two random points P_1 and P_2. From the above we get that the emitted and the received frequency-integrated specific intensity of a photon I_{em} and I_{rec} respectively, are related to each other as:

$$I_{rec} = \left(\frac{\nu_{rec}}{\nu_{em}}\right)^4 I_{em}, \qquad (3.3.2)$$

where the frequency ratio ν_{rec}/ν_{em} does not depend on the frequencies themselves, but only on the spacetime properties and the emission angle of the photon. We note that the frequency ratio appearing above as the factor connecting the emitted and received frequencies, accounts for the correction due to gravitational time dilation, the Doppler correction due to the relative motion of the radiating material and the correction due to frame dragging.

Firstly, we introduce thus the gravitational time dilation that causes a frequency shift to the emitted frequency. This shift is equal to:

$$\begin{aligned} \nu_{rec} &= \left[\frac{g_{tt}(r_{em},\theta_{em})}{g_{tt}(r_{rec},\theta_{rec})}\right]^{1/2} \nu_{em} \\ &= \left(\frac{g_{tt,em}}{g_{tt,rec}}\right)^{1/2} \nu_{em}, \end{aligned} \qquad (3.3.3)$$

where ν_{em} the emitted frequency and ν_{rec} the received frequency.

Then, in order to take into account the Doppler shift due to the motion of the emitting surface, we momentarily ignore the negligible possible radial or poloidal move-

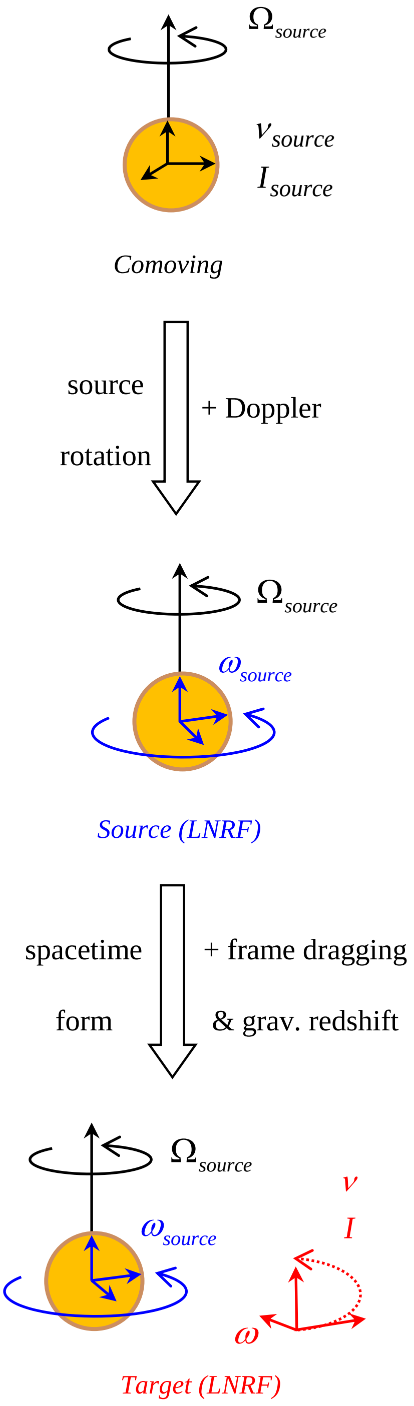

Figure 3.4: Schematic of the frequency changes. A Doppler shift is used to move from the frame comoving with the emitting surface to the LNRF at the radius of the surface, taking into account the emission source rotation. We then move to the receiving particle LNRF, accounting for two more frequency modifications. We have the introduction of gravitational time dilation and frame dragging effects, both due to the target radial distance transformation.

ment. We have then a frequency-changing factor:

$$\nu_{rec} = \frac{1}{\gamma\left(1 - V^{\hat{\phi}}\cos\psi\right)}\nu_{em}, \tag{3.3.4}$$

where $V = V^{\hat{\phi}}$ the source three-velocity, $\gamma = \left(1 - V^2\right)^{-1/2}$ the emitting material Lorentz factor (scalar), and ψ the angle between the emitting matter velocity and the photon emission direction (Fig. 3.3).

Finally, we have the frequency correction due to frame dragging, which brings in a factor:

$$\nu_{rec} = \frac{1 + \omega_{rec}\, k_\phi / k_t}{1 + \omega_{em}\, k_\phi / k_t}\nu_{em}, \tag{3.3.5}$$

where ω_{rec} and ω_{em} are the spacetime angular speed at the point of reception and emission respectively, and k_a the photon covariant four-momentum components, which are also conserved quantities. The ratio k_ϕ / k_t here only depends on the direction of the photon emission and is thus also a conserved quantity.

Combining all of the above, we have then for the received frequency ν_{rec} that:

$$\nu_{rec} = \left(\frac{g_{tt,\,em}}{g_{tt,\,rec}}\right)^{1/2} \frac{1 + \omega_{rec}\, k_\phi / k_t}{1 + \omega_{em}\, k_\phi / k_t} \frac{1}{\gamma\left(1 - V^{\hat{\phi}}\cos\psi\right)}\nu_{em} \tag{3.3.6}$$

and for the frequency-integrated specific intensity I_{rec} that:

$$I_{rec} = \left(\frac{g_{tt,\,em}}{g_{tt,\,rec}}\right)^{2} \left(\frac{1 + \omega_{rec}\, k_\phi / k_t}{1 + \omega_{em}\, k_\phi / k_t}\right)^4 \frac{1}{\gamma^4\left(1 - V^{\hat{\phi}}\cos\psi\right)^4} I_{em}. \tag{3.3.7}$$

In Figure 3.4, one can see a breakdown of the process presented here. For visual simplicity, we depict the photon emission done by a central spherical object. From the above equations, we can see that the shifts in frequency for the incoming photons do not practically depend on the original frequency of the emitted photons, but on the spacetime curvature and the emission angle.

CHAPTER 4

ACCRETION DISKS

The very first steps in the theory of accretion were taken in the middle of the 20th century, when Hermann Bondi introduced the theory of spherical accretion onto compact objects, what is now known as Bondi accretion (Bondi 1952). Some of the most well-known and fundamental subsequent resources regarding accretion disks, their shape, structure, and physics up to this date are Shakura & Sunyaev 1973, Novikov & Thorne 1973, Cunningham 1975, 1976, Shapiro et al. 1976, Ichimaru 1977, Abramowicz et al. 1978, 1988, 1995, and 1996, Kozlowski et al. 1978, Bisnovatyi-Kogan & Blinnikov 1977, Rees et al. 1982, Narayan & Yi 1994, 1995a, 1995b, Narayan et al. 1997, 2003, and 2012, Gammie & Popham 1998, Popham & Gammie 1998, Paczynski 1998, Frank et al. 2002, Blandford et al. 2002, Narayan & McClintock 2008, and Penna et al. 2013b. In addition to these, we should also add the work of Cabanac et al. 2009 and the work of Sądowski 2009, and Sądowski et al. 2013a.

Extensions of the aforementioned works were later on created, including more complex interactions and physics. These works took into account the disk's hydrodynamics and magnetohydrodynamics (MHD), and reexamined concepts such as the disk stability and evolution. Articles that include studies considering and examining these more complex disk physics are Lovelace et al. 1994, Igumenshchev et al. 2003, Takahashi 2007, Penna et al. 2010, 2013a, 2013b, Sadowski 2011, Moeen et al. 2012, Penna 2013, Sądowski et al. 2013b, 2014, 2015, 2016, Yuan & Narayan 2014, and Sądowski 2016a, 2016b.

4.1. Accretion tori

In this Section, we present the accretion tori we used for our codes. Some of the tori are optically thick while others are stratified and semi-opaque. In general, we examine tori of various geometrical and density gradient profiles. This is advantageous since it allows the accumulation of valuable information about a plethora of various system environments. For example, the material can be used in order to cover the various stages of matter infall into the black hole and the different stages of accretion disk evolution in X-ray binary systems (see e.g., Esin et al. 1997, Verbunt 1999, Bildsten & Rutledge 2001, Fender 2002, Haggard et al. 2004, Müller 2004, Done et al. 2007, Meyer-Hofmeister et al. 2009, van Haaften et al. 2012, Heinke et al. 2013).

We consider and examine accretion disks that follow various disk models and temperature profiles such as Shakura – Sunyaev (Shakura & Sunyaev 1973), Advection-Dominated Accretion Flows (ADAF; Abramowicz, Chen, Kato, Lasota, Regev 1995, Chen, Abramowicz, Lasota, Narayan, Yi 1995, Abramowicz, Chen, Granath, Lasota 1996, Narayan, Kato, Honma 1997, Gammie & Popham 1998, Popham & Gammie 1998, Lasota 1999), SANE (Standard And Normal Evolution), and MAD (Magnetically Arrested Disk) (see Narayan, Igumenshchev, Abramowicz 2003, Narayan, Sądowski, Penna, Kulkarni 2012, Penna, Sądowski, Kulkarni, Narayan 2013). We also consider combinations of these to better approximate the assorted observationally recorded disks or certain temperature and velocity curves. Additionally, we look into the luminosity limits (e.g., Abramowicz 2005), as well as the interactions between MAD accretion processes and general relativistic radiation magnetohydrodynamics (GRRMHD; see Curd & Narayan 2023).

The disks we present further on, can thus be split into two categories: optically thick and optically thin or quasi-opaque disks. The main repercussions of the disk's thermal radiation, along with its impact onto the disk's geometry, vertical height, and optical thickness were described and studied in Thorne & Price 1975, Inoue & Hoshi 1987, Takahashi et al. 1995, Beloborodov 1998, 1999, 2001, Bisnovatyi-Kogan 2001, Abramowicz & Fragile 2013. For the finer points that differentiate the optically and geometrically thin and thick disks, and segregate the categories, one could look for example into Artemova et al. 1996, Quataert 2001 and Dubus 2003.

We note here, that the accretion disks we considered for this work are just a sample for the study of the most commonly considered models. Many other frequently used accretion disk models, such as Novikov–Thorne disks (Novikov & Thorne 1973) for example, could also be implemented and studied using our codes, should the need arise. The reason why we chose to consider more simplistic perhaps disk models than the latest general relativistic magnetohydrodynamics (GRMHD) researches (e.g., Chatterjee et al. 2019, Mahlmann et al. 2020), is because of the number of code executions this work required. This results in any model improvement, such as a more realistic, a nonaxisymmetric, or a time-variant accretion disk, greatly increasing the total execution time.

The first group is used to represent disks that increase their density abruptly and very close to their outer surface. They are mostly rotationally supported and totally optically thick. This practically means that there is no reason to solve the radiative transfer equation for these tori and instead another method of calculation must be used. These disks can be used to describe physical tori that are either cold or compact or both. An interesting case they can also be used to describe is transient stages of the X-ray binary systems (Tauris & van den Heuvel 2006). During the quiescent stages of these systems their accretion disks tend to be cooler and at a larger distance from the compact object (e.g., Esin et al. 1997, Narayan & McClintock

2008). They remain in a similar state for an indefinite amount of time and at some point later on, they start increasing their temperature and swelling up while reducing their density and density gradient. From that point on, they can no longer be described by these opaque models but require usage of the semi-opaque disk models. More information about X-ray binaries and their cycles of evolution can be found in Tauris et al. 2000, Podsiadlowski et al. 2002, and Chen & Podsiadlowski 2016.

The latter group of tori, the quasi-opaque ones, describes more common and familiar perhaps cases of accretion disks. There is a measurable density and temperature gradient. For these cases, one must use a ray tracing process and solve the radiative transfer equation along the photon trajectory. This allows the calculation of how much radiation is produced by the hot material in every step and how much of this is absorbed away by it. Depending on the direction and angle of motion of the traveling photon, it can at times be absorbed by the disk material and, at other times, it can traverse part of the disk without it being absorbed. This means that at some points the disk is optically thick and at other ones optically thin, hence the name quasi-opaque or semi-opaque. In these cases, effects such as limb darkening (Fig. 4.1) and transparency (Fig. 4.2) can be observed.

The tori mentioned above can rotate in various ways. In our program executions we assume that the disk material can move rotating circularly $(u^r = 0)$ with the typical coordinate angular velocity Ω (Eq. (2.2.13)) or with more detailed profiles such as the one in Equation (4.2.19) further on. Additionally, we examine cases where the disk material follows inspiral motion profiles $(u^r \neq 0)$ attempting to mimic the SANE and MAD models (Narayan et al. 2003 and 2012, Penna et al. 2013a). In each execution run, our codes give results not for one, but for all of the aforementioned different velocity profiles for the accretion disk material.

We should also mention here that although in many of the accretion disk simulations and studies it is assumed that the material is in a stationary condition, geometrically at least, in reality it is far from that. There are increased amounts of turbulence, instabilities (e.g., Tchekhovskoy et al. 2011, McKinney et al. 2012, Narayan et al. 2012), and other phenomena taking place, often in smaller scales, that are at times ignored. One such phenomenon is the flow and diffusion of angular momentum throughout the different disk sectors. The main cause of this diffusion is considered to be the material viscosity and is treated in various ways. One of the best-known and more frequently used methods is the α-viscosity approach (Shakura & Sunyaev 1973, Abramowicz et al. 1988). This method, nevertheless, cannot be applied to all disk models, such as non-α-disks, where other solutions must be found.

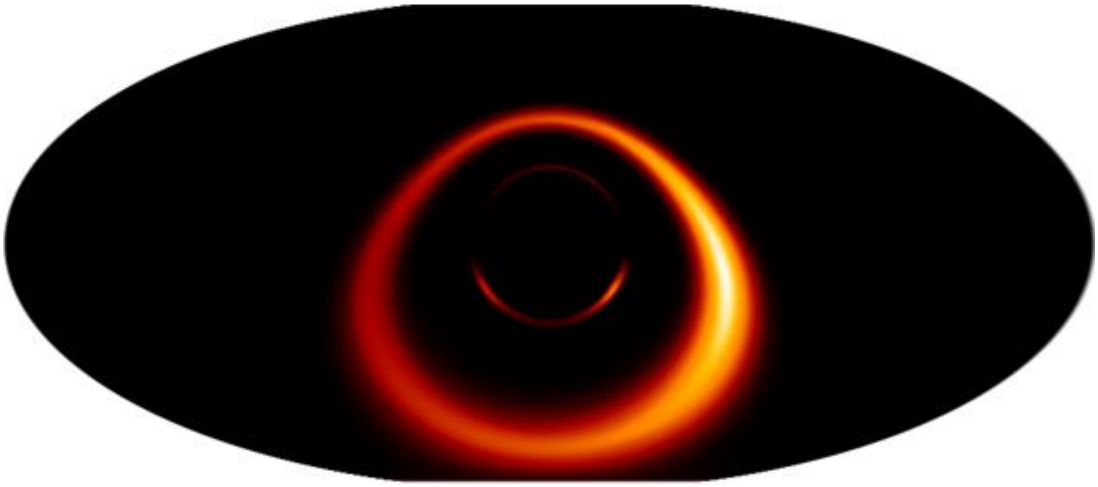

Figure 4.1: Semi-opaque torus seen from further away showing visible limb darkening.

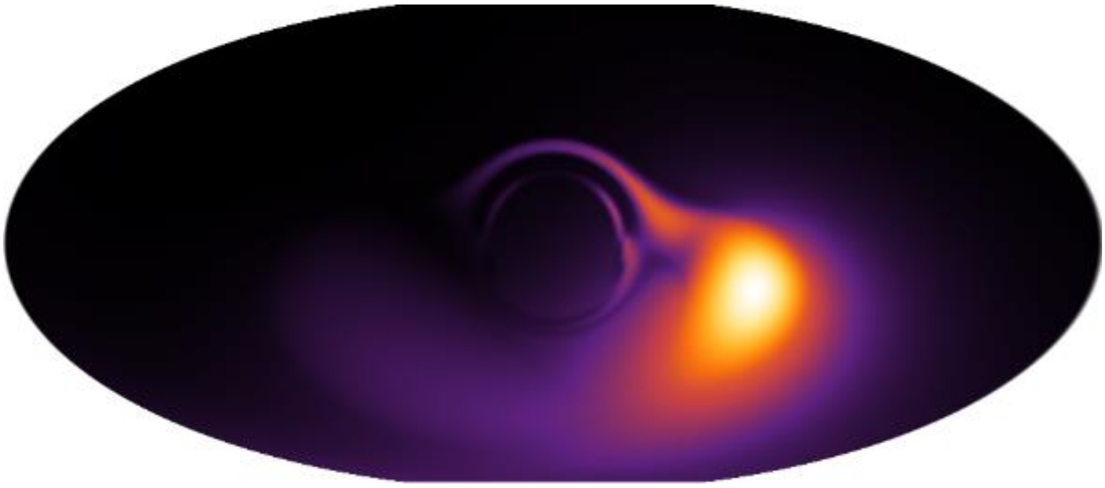

Figure 4.2: Semi-opaque torus seen from further away. Transparency is visible, as the Einstein rings and disk material can be seen in the background through the disk.

4.2. Optically thick accretion tori

In this Section, we discuss optically thick accretion disks and describe the various models we used in our study. Most of the disks considered have simple setups and poloidal cross sections corresponding to simple polygons. They were chosen, however, as some of the most often chosen simple disk models considered in works that study phenomena further away from the disks and closer to black holes, X-ray binaries, etc. These disks can be viewed either as toy models or as initial condition "snapshot" states of setups whose evolution one would wish to study taking into account the presence of radiation. In addition to these, we also consider more complex and more realistic disk models. These models are built self-consistently by assuming that the disk material is supported and kept in place by the rotation of the disk itself.

Optically thick accretion disks are in general geometrically thin. This is caused by the "inefficiency" of the radiation: since the material of the disk is opaque, the radiation emitted by its hotter elements does not reach other, more distant parts of the disk. The result is each matter segment having a notably smaller "inflating" radiation pressure component than a "deflating" gravitational force component. The outcome is an accretion disk with smaller geometrical thickness and a notably larger pressure gradient, specifically near its outer surface.

In our tori we consider a temperature $\mathrm{T}\ (K)$ distribution that follows $\mathrm{T} \propto r^{-3/4}$ (see Shakura & Sunyaev 1973), but an isothermal disk case was also considered and checked into. We thus considered both disk temperature profiles for a better understanding of the phenomena. The isothermal disks are rather unnatural setups, but are simple enough to allow us to anticipate certain results and check our work.

For the more natural case of rotationally supported disks, the temperature is regulated by mass accretion itself. Assuming for the object an Eddington luminosity $\mathcal{L}_{Edd} = 4\pi G\mathcal{M}m_p c/\sigma_T$, the resulting accretion rate $\dot{\mathcal{M}}$ is the Eddington accretion rate $\dot{\mathcal{M}}_{Edd}$:

$$\dot{\mathcal{M}}_{Edd} = \frac{4\pi G\mathcal{M}m_p}{c\,\sigma_T}, \tag{4.2.1}$$

where $\mathcal{M}$ the disk mass and m_p the mass of the proton. If we consider the naturally expected case of a large enough amount of scatterings, then the disk material can be well approximated by a blackbody radiation system and its temperature can be then described by:

$$\mathrm{T} = \left(\frac{3G\dot{\mathcal{M}}\mathcal{M}}{8\pi\sigma_{SB}}\right)^{1/4} r^{-3/4}, \tag{4.2.2}$$

where σ_{SB} the Stefan – Boltzmann constant ($erg \cdot cm^{-2} \cdot s^{-1} \cdot K^{-4}$; Longair 2011).

We notice here, however, the problem arising when we simplistically assume the aforementioned situation. If we hypothesize the disk's accretion luminosity to be equal to the Eddington luminosity, then the disk cannot remain geometrically thin. This is because, with the accretion luminosity increasing, the radiation pressure exerted onto the disk matter increases steadily and finally becomes comparable to the local gravitational forces. As this change occurs, the disk inflates, and the material maximum height and width increases. At this point hence, the accretion disk gradually turns from geometrically thin and optically thick into a geometrically thick and optically thin disk (Thorne & Price 1975). A simple way to circumvent this intricate situation is to plainly consider the radiating matter emitting only a fraction ϵ of the Eddington luminosity:

$$\dot{\mathcal{M}} = \dot{\mathcal{M}}_{acc} = \epsilon\, \dot{\mathcal{M}}_{Edd} \tag{4.2.3}$$

and thus, it is:

$$\mathrm{T} = \left(\frac{3\epsilon G \dot{\mathcal{M}} \mathcal{M}}{8\pi\sigma_{SB}} \right)^{1/4} r^{-3/4} . \tag{4.2.4}$$

After picking the disk temperature profile, we can determine the emitting radiation profile as:

$$I_{em} = \frac{\sigma_{SB}}{\pi} \mathrm{T}\left(r_{em}\right)^{4} . \tag{4.2.5}$$

We should also mention here that although in the vast majority of accretion disk simulations and studies it is assumed that the material is in a stationary condition, in reality it is far from that. There are increased amounts of turbulence, instabilities, and other phenomena taking place, often in smaller scales, that are frequently ignored. One such phenomenon is the flow and diffusion of angular momentum throughout the various disk sectors. The main cause of this diffusion is considered to be the material viscosity and is treated in various ways, one of the best known and more frequently used ones being the α-viscosity (Shakura & Sunyaev 1973, Abramowicz et al. 1988). This method, however, cannot be used for all disk models, such as in non-α-disks, where other solutions should be found in order to deal with the problem.

In addition to the above, another phenomenon closely associated with the presence of magnetic fields in hydrodynamic systems is the generation of magnetorotational instabilities (MRI). This potent instability appears in environments of conductive magnetized fluids rotating differentially. Namely, in accretion disks orbiting massive objects, the disk fluid does not rotate as a solid with constant angular velocity. Instead, it rotates differentially around the center with its inner regions rotating faster than its outer regions. The presence of magnetic field in the system causes the Lorentz force to be exerted on the material freely moving charges. This means that any fluid element that deviates from the circular motion even to a very small extent, has its orbit increasingly destabilized. This destabilizing force is also increasing proportionally to the orbit displacement from the circular orbit. This then results in the accretion disk becoming unstable and consequently turbulent. The magnetorotational instability thus creates noteworthy ramifications in these systems directly connected to the distribution and flux of angular momentum through the disk, as well as its diffusion toward the material outer strata (Balbus & Hawley 1991, 1992, and 1998, Hawley & Balbus 1991, and 1992, Hawley et al. 1995, Krolik 1999a, and 1999b,

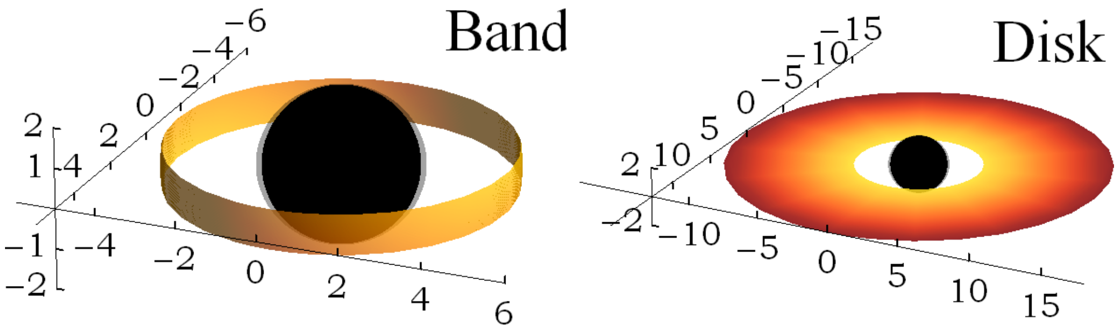

Figure 4.3: Two-dimensional disks “Band” (*left*) and “Disk” (*right*). In the center of each image, we see in black color the black hole event horizon and in grey around it, the corresponding ergosphere. The accretion disk is shown in yellow (hotter) to red colors (colder).

Turner et al. 2003, Bisnovatyi-Kogan & Lovelace 2007, Pessah et al. 2007, Rothstein & Lovelace 2008, Balbus 2012). The magnetorotational instability is additionally expected to exercise influence on the formation and evolution of active galactic nuclei (Krolik 1999a), the X-ray emissions in systems of compact objects (Blaes 2004), and gamma-ray burst phenomena (Popham et al. 1999, Wheeler 2004).

For our work, we considered six different models for opaque, optically thick accretion disks. Specified by their given names, we have the following models: band, disk, slab, wedge, torus, and opaque rotationally supported torus. In more details, we have:

a) Band (toy, snapshot model): a cylindrical surface of half-height h from its highest point to the equatorial plane at the distance of the ISCO (Fig. 4.3). The half-height h and the cylinder radius can be freely chosen without restrictions. This model is used to study for instance the radiation received only at the innermost surface of the disk.

b) Disk (toy, snapshot model): an infinitesimally thin disk at the equatorial plane (Fig. 4.3; see Bardeen & Wagoner 1971). The inner radius r_{inner} is situated at the ISCO radius and the outer radius r_{outer} at twice or thrice this distance. The innermost and outermost radius of the disk can be freely adjusted.

c) Slab (toy, snapshot model): a flat disk of half-height h with its inner edge r_{inner} at the radius of the ISCO and its outer radius r_{outer} at three times the ISCO radius. The disk’s poloidal cross section is a rectangle (Fig. 4.4). The half-height h is freely chosen without restrictions. The innermost and outermost radius of the accretion disk can easily be adjusted.

d) Wedge (toy, snapshot model): a disk with a cross section of an isosceles trapezoid, centered above and below the equatorial plane. The inner radius r_{inner} is the radius of the ISCO and the outer radius r_{outer} three times that. The disk is constructed in such a way that an angle with its vertex at the location of the black hole (the origin) extending outward reaches the ISCO cylinder intersecting a ring of half-height h. The angle sides extend outward in the same direction

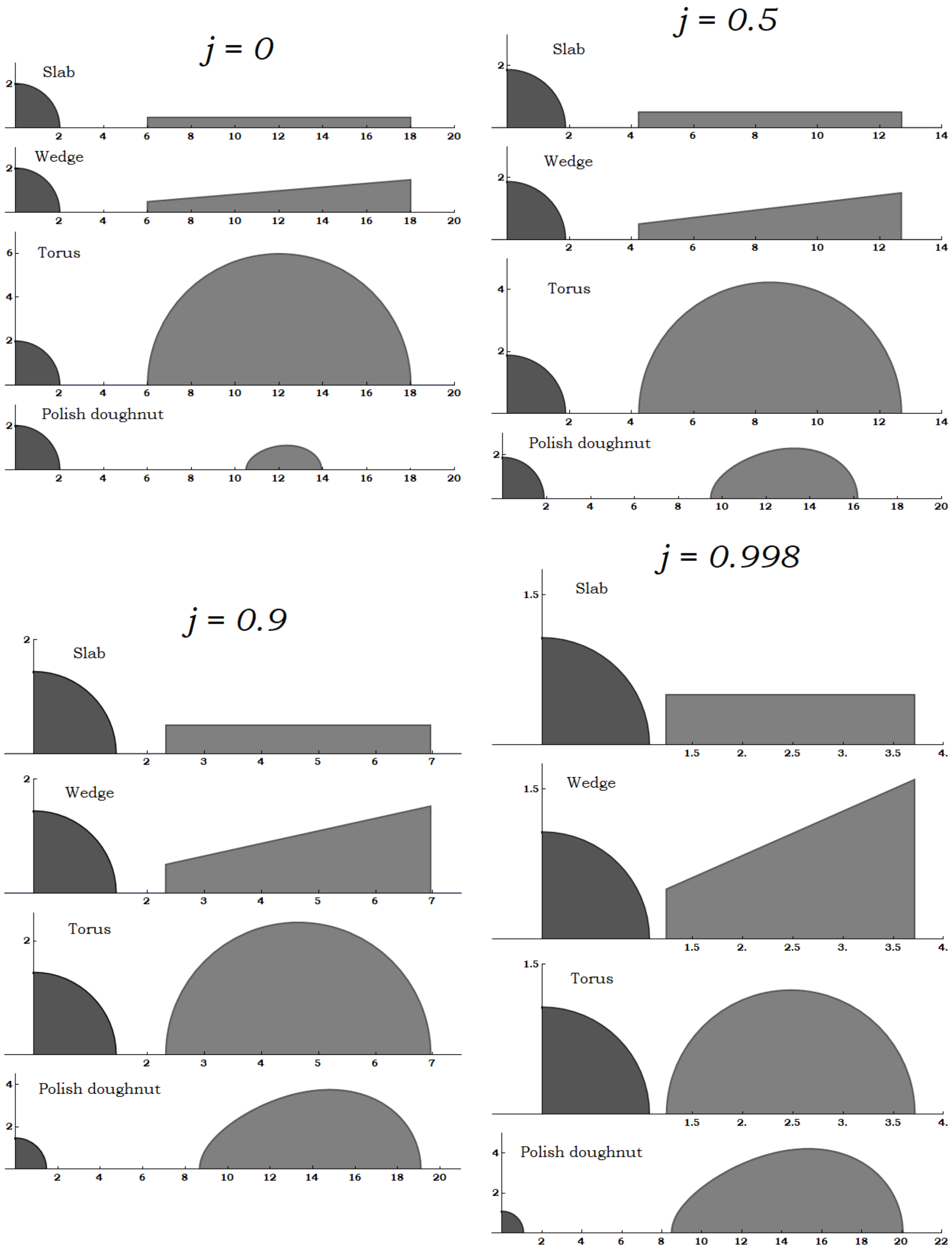

Figure 4.4: Opaque accretion disks cross sections for the spins studied.

until crossing the disk's outer edge (Fig. 4.4). The disk half-height h, its inner, and outer radius can be freely modified.

e) Torus (toy, snapshot model): a disk with a circular poloidal cross section. The cross section center is at distance $r_{center} = 2r_{ISCO}$ on the equatorial plane and its radius is equal to the ISCO radius. The disk's inner edge is thus at $r_{inner} = r_{ISCO}$ and the outer edge at $r_{outer} = 3r_{ISCO}$. In this form, the disk is considered borderline opaque. The center and radius of the cross section are freely adjustable (Fig. 4.4).

f) Opaque rotationally supported torus (ORST – self-consistent model): a rotationally supported torus. The disk model is one of the more composite cases considered for optically thick disk examples. This disk here is stationary and axisymmetric, while its rotation axis is aligned with the rotation axis of the black hole. For this study, we assume the two angular velocity vectors collinear, but it is straightforward to consider the opposite case to study retrograde disks. Afterward, we assume that this setup is created by the material accretion process, which thus specifies its shape. The acceleration along the particle trajectory is given by:

$$a^{\alpha} = \frac{Du^{\alpha}}{d\tau} = u^{\alpha}{}_{;\beta}u^{\beta} = u^{\alpha}{}_{,\beta}u^{\beta} + \Gamma^{\alpha}_{\beta\rho}u^{\beta}u^{\rho}, \qquad (4.2.6)$$

where $\Gamma^{\alpha}_{\beta\rho}$ are the Christoffel symbols that can be calculated from the metric (2.1.9), using the formula:

$$\Gamma^{\alpha}_{\kappa\lambda} = \frac{1}{2}g^{\alpha\mu}\left(g_{\mu\kappa,\lambda} + g_{\mu\lambda,\kappa} - g_{\kappa\lambda,\mu}\right) \qquad (4.2.7)$$

(see Choquet-Bruhat et al. 1977). The disk assumed here, like in the majority of disks in works of this type, has negligible radial and poloidal velocity components, so (4.2.6) can be simplified. We then get for the acceleration components that:

$$a^{t} \equiv 0, \qquad (4.2.8)$$

$$a^{\phi} \equiv 0, \qquad (4.2.9)$$

$$a^{r} = -\frac{\Delta}{\Sigma}\left[M\frac{\Sigma - 2r^{2}}{\Sigma^{2}}\left(u^{t} - a\sin^{2}\theta\, u^{\phi}\right)^{2} + r\sin^{2}\theta\left(u^{\phi}\right)^{2}\right], \qquad (4.2.10)$$

$$a^{\theta} = -\frac{\sin\theta\cos\theta}{\Sigma}\left\{\frac{2Mr}{\Sigma^{2}}\left[a\,u^{t} - \left(r^{2} + a^{2}\right)u^{\phi}\right]^{2} + \Delta\left(u^{\phi}\right)^{2}\right\}. \qquad (4.2.11)$$

The first two Equations (4.2.8) and (4.2.9) obey our initial assumption that the disk is stationary and axisymmetric respectively. The latter two Equations respectively, (4.2.10) and (4.2.11), are used to give the isobaric surfaces, namely the surface of constant acceleration using:

$$a_{\alpha}u^{\alpha} = 0. \qquad (4.2.12)$$

The components of the above equation then give:

$$a_{r}u^{r} + a_{\theta}u^{\theta} = \frac{\Sigma}{\Delta}a^{r}u^{r} + \Sigma a^{\theta}u^{\theta} = 0. \qquad (4.2.13)$$

This reveals the pair of differential equations:

$$\frac{\mathrm{d}r}{\mathrm{d}\xi} = \frac{Y}{\sqrt{Y^2 + \Delta\, X^2}}, \tag{4.2.14}$$

$$\frac{\mathrm{d}\theta}{\mathrm{d}\xi} = -\frac{X}{\sqrt{Y^2 + \Delta\, X^2}}, \tag{4.2.15}$$

where

$$X = M\,\frac{\Sigma - 2r^2}{\Sigma^2}\left(\Omega^{-1} - a\sin^2\theta\right)^2 + r\sin^2\theta \tag{4.2.16}$$

$$Y = \sin\theta\cos\theta\left[\frac{2Mr}{\Sigma^2}\left(a\,\Omega^{-1} - r^2 - a^2\right)^2 + \Delta\right] \tag{4.2.17}$$

and $\Omega = u^{\phi}/u^{t}$ is as earlier the material angular velocity. The final necessary information in order to solve the above and acquire the resulting disk is its inner edge at the equator. This can be found by solving the equation for marginal stability orbits:

$$\begin{aligned} &2aM\sin^4\theta\left[\frac{r^2}{\Sigma} - \frac{\Sigma - 2r^2}{\Sigma^2}\left(r^2 + a^2 + \frac{a^2 Mr\sin^2\theta}{\Sigma}\right)\right]\Omega^3 + \\ &+\sin^2\theta\left\{M\,\frac{\Sigma - 2r^2}{\Sigma^2}\left[\frac{6Mr\left(r^2 + a^2\right)}{\Sigma} + 3\Delta - \Sigma\right] + \left(1 - \frac{2Mr}{\Sigma}\right)r\right\}\Omega^2 - \\ &-\frac{\Sigma - 2r^2}{\Sigma^2}\,\frac{6aM^2 r\sin^2\theta}{\Sigma}\,\Omega + \Delta\sin^2\theta\,\Omega\,\frac{\partial\Omega}{\partial r} - M\,\frac{\Sigma - 2r^2}{\Sigma^2}\left(1 - \frac{2Mr}{\Sigma}\right) = 0. \end{aligned} \tag{4.2.18}$$

In order to solve Eq. (4.2.18), we define the angular velocity function $\Omega(\varpi)$. We use here the angular velocity profile proposed in Fuerst & Wu 2004 and 2007, and Younsi et al. 2012:

$$\Omega(\varpi) = \Omega(r\sin\theta) = \frac{\sqrt{M}}{(r\sin\theta)^{3/2} + a\sqrt{M}}\left(\frac{r_K}{r\sin\theta}\right)^{n_p}, \tag{4.2.19}$$

where $\varpi = r\sin\theta$ is the cylindrical radius, r_K is the equatorial plane radius at which the material moves with Keplerian velocity, and the parameter n_p corresponds to pressure forces and is responsible for the geometry of the torus determining its thickness. Rotationally supported disks for various r_K and n_p values can be seen in Figure 4.5. The disks selected and used in our simulations are shown in Figure 4.4.

The above models and setups can be found in a compact and concise form in Table 1.

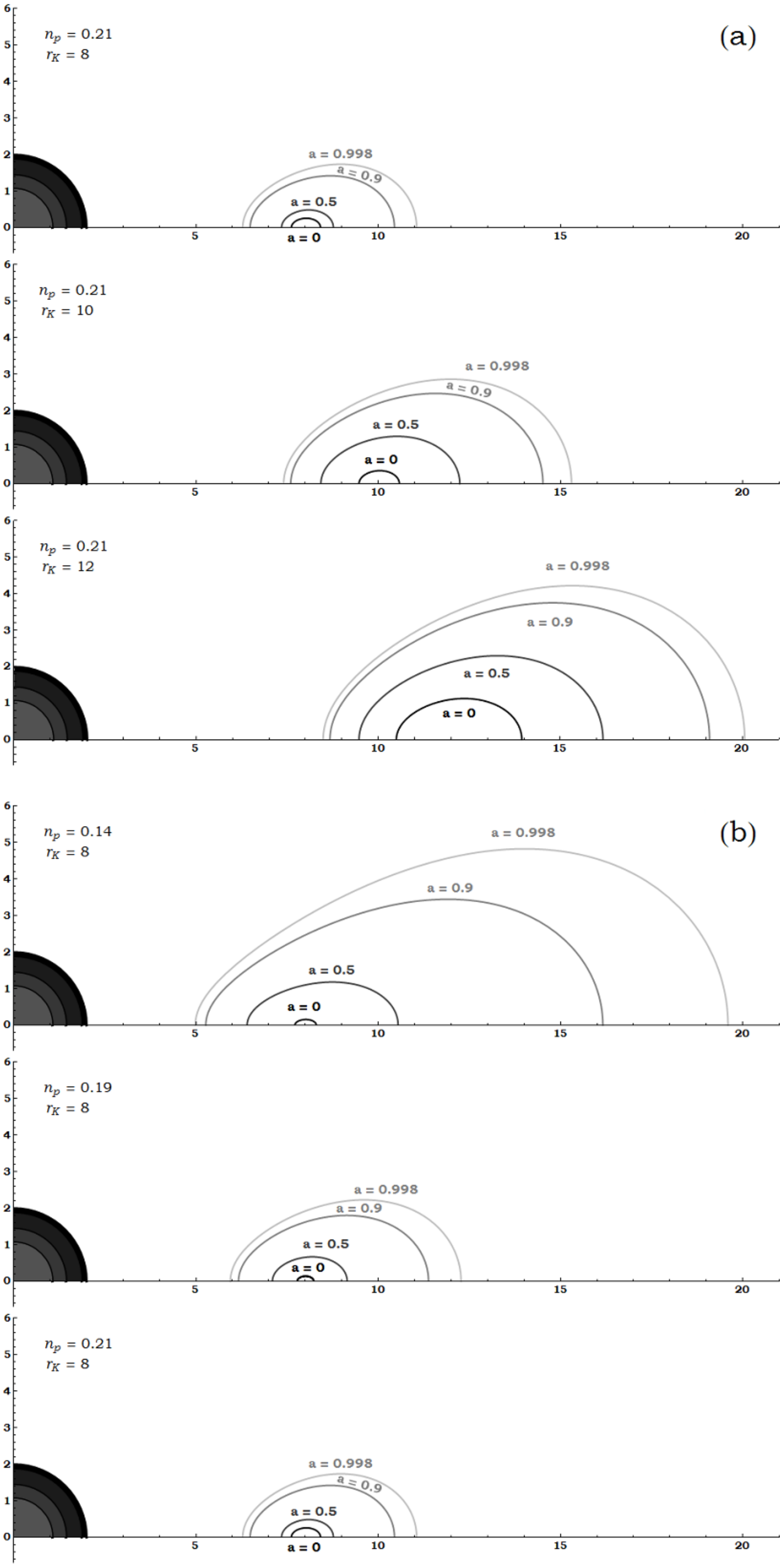

Figure 4.5: ORST cross sections. In (*a*) we see the effects caused by the change of the radius of Keplerian rotation speed r_K. In (*b*) we see the disk shapes and sizes for assorted values of the parameter n_p. Spin in M units.

The final step in the dynamics calculation of accretion disks of this kind is to determine the generated frequency-integrated specific intensity I. This can be done by utilizing the method found in Section 3.3. Subsequently, we can apply the material of Section 3.1 in order to ascertain the radiation flux and force thus the ensuing acceleration caused by the disk's thermal content.

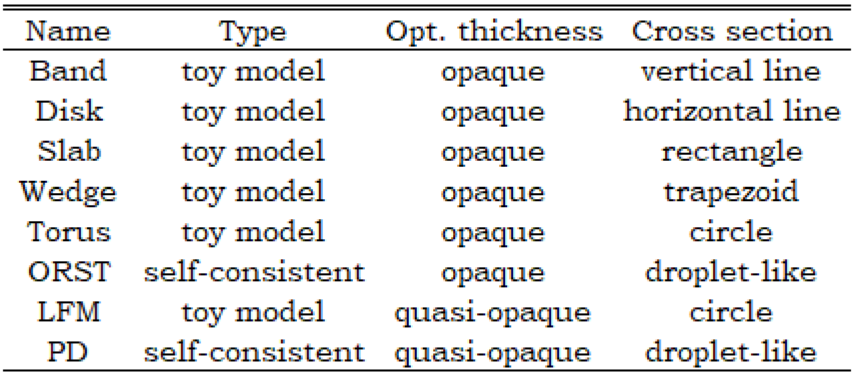

Name	Type	Opt. thickness	Cross section
Band	toy model	opaque	vertical line
Disk	toy model	opaque	horizontal line
Slab	toy model	opaque	rectangle
Wedge	toy model	opaque	trapezoid
Torus	toy model	opaque	circle
ORST	self-consistent	opaque	droplet-like
LFM	toy model	quasi-opaque	circle
PD	self-consistent	quasi-opaque	droplet-like

Table 1: Disk models considered.

4.3. Semi-opaque accretion tori

In this Section, we discuss the semi-opaque and translucent disk models we used in our studies. As before, some of the models set up here are simplistic but provide a good test for our work. Meanwhile, some other models are built upon relativistic physical conditions self-consistently and are hence more complex.

We have considered and studied so far five different disk models. These model setups are:

a) No torus: there is no accretion disk around the black hole. Photon trajectories unfurl uninterrupted until they either cross the event horizon or escape the system entirely by crossing an adjustable outer boundary.

b) Semi-opaque radiation pressure supported polish doughnuts (PS PD – self-consistent model): stationary and axisymmetric radiation pressure supported polish doughnut. An accretion torus constructed following Abramowicz et al. 1978 and Kozlowski et al. 1978 (see also Qian et al. 2009, Younsi et al. 2012). The maximum number density observed for this disk is $n_{center} = 10^{18}\,cm^{-3}$ and is situated here in $\left(r_{center}, \theta_{center}\right) = \left(12M, \pi/2\right)$. For this disk we record $a_{abs} \cdot r_{outer} \sim 1-5$, where a_{abs} is the absorption coefficient and r_{outer} the disk's outer radius. Extending now the aforementioned assumption, we adopt the hypothesis that the disk material has no significant radial or poloidal velocity components. Thus, the disk components exhibit a four-velocity $u^{\alpha} = \left(u^{t}, u^{\phi}, 0, 0\right)$. We continue on and follow Younsi et al. 2012 assuming that the torus has a polytropic equation of state $P = \kappa n^{\Gamma}$, where n is the material number density, Γ the polytropic index, and $\kappa = \hbar c \left\{ 45(1-\beta) \Big/ \left[\pi^{2} \left(\bar{m}\, m_{p}\, \beta \right)^{4} \right] \right\}^{1/3}$, with $\hbar$ the reduced Planck constant, $\bar{m}$ the mean molecular weight, and β the ratio of gas pressure to total pressure. The disk is then described by:

$$\partial_{r} \xi\left(r, \theta\right) = -a_{r}\left(r, \theta\right) \qquad (4.3.1)$$

$$\partial_{\theta} \xi\left(r, \theta\right) = -a_{\theta}\left(r, \theta\right) \qquad (4.3.2)$$

where $\xi\left(r, \theta\right) = \ln\left[\Gamma - 1 + \Gamma \kappa\, n\left(r, \theta\right)^{\Gamma - 1}\right]$ is a function of the material number density $n\left(r, \theta\right)$ and the acceleration components are $a_{\alpha}\left(r, \theta\right) = u_{\alpha;\beta}\left(r, \theta\right) u\left(r, \theta\right)^{\beta}$. We can see some poloidal cross sections of the disks used in Figure 4.6.

c) Translucent PS PD: translucent radiation pressure supported polish doughnut. It is the same as the previous disk, but records no radiation absorption by the material of the disk.

d) Semi-opaque "LFM" torus (toy, snapshot model): stationary and axisymmetric semi-opaque torus with a circular poloidal cross section.

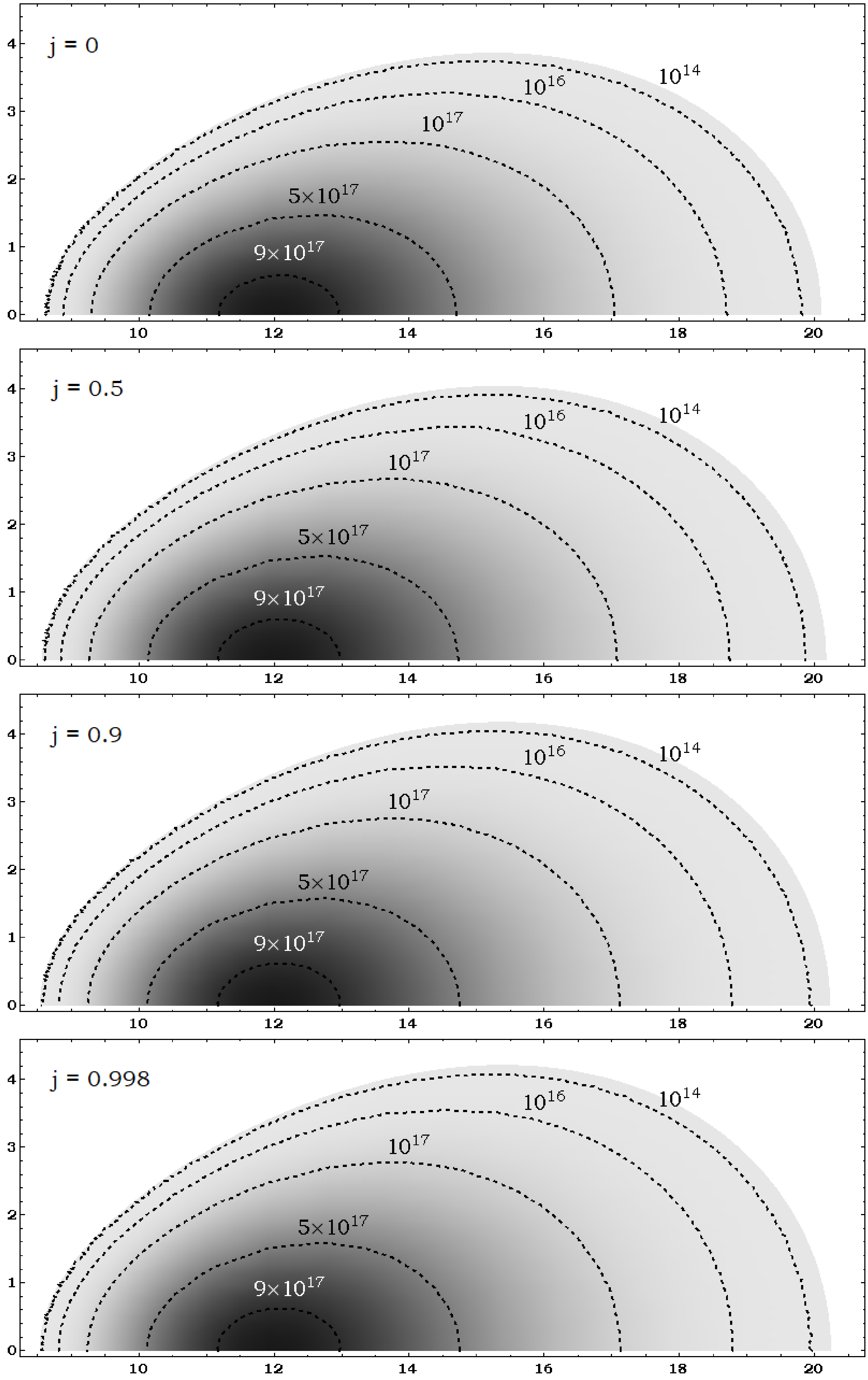

Figure 4.6: Polish doughnut number density cross sections. The center of all tori lies at $(12,0)$ and has a number density of $10^{18} cm^{-3}$. The black hole spins from top to bottom are $a = 0$, $a = 0.5M$, $a = 0.9M$ and $a = 0.998M$.

The cross section center is located in the equatorial plane and at a radial distance $r_{center} = 2\,r_{ISCO}$. The torus cross section has a radius of $r_{torus} = r_{ISCO}$. Consequently, the torus stretches from an inner radius $r_{inner} = r_{ISCO}$ to an outer radius $r_{outer} = 3\,r_{ISCO}$, and its maximum height is $\mathrm{h}_{torus} = r_{torus} = r_{ISCO}$. The maximum number density of the material is $n_{center} = 10^{18}\,cm^{-3}$. It is situated in the torus cross section center location $(r_{center}, \theta_{center}) = (2r_{ISCO}, \pi/2)$ and decreases to zero moving toward the torus surface. For the torus, material we have that the product $a_{abs} \cdot r_{outer}$ is $\sim 1-5$ throughout the cross section. We also note that the density gradient increase is much less abrupt for this model than for the radiation pressure supported torus mentioned earlier. Images of the cross section and the number density are shown in Figure 4.7.

e) Translucent LFM torus (toy, snapshot model): translucent LFM torus of circular poloidal cross section. It is the same as the previous model, but without recording radiation absorption by the disk material.

The disk models described here provide the material's number density $n(r,\theta)$. From this, we acquire other important quantities, such as the material's temperature $\mathrm{T}(r,\theta)$ or pressure $P(r,\theta)$ (dyn/cm^2):

$$\mathrm{T}(r,\theta) = \frac{\hbar c}{\mathrm{k}} \left[\frac{45(1-\beta)}{\pi^2 \bar{m}\, m_p\, \beta} \right]^{1/3} \rho(r,\theta)^{1/3}, \qquad (4.3.3)$$

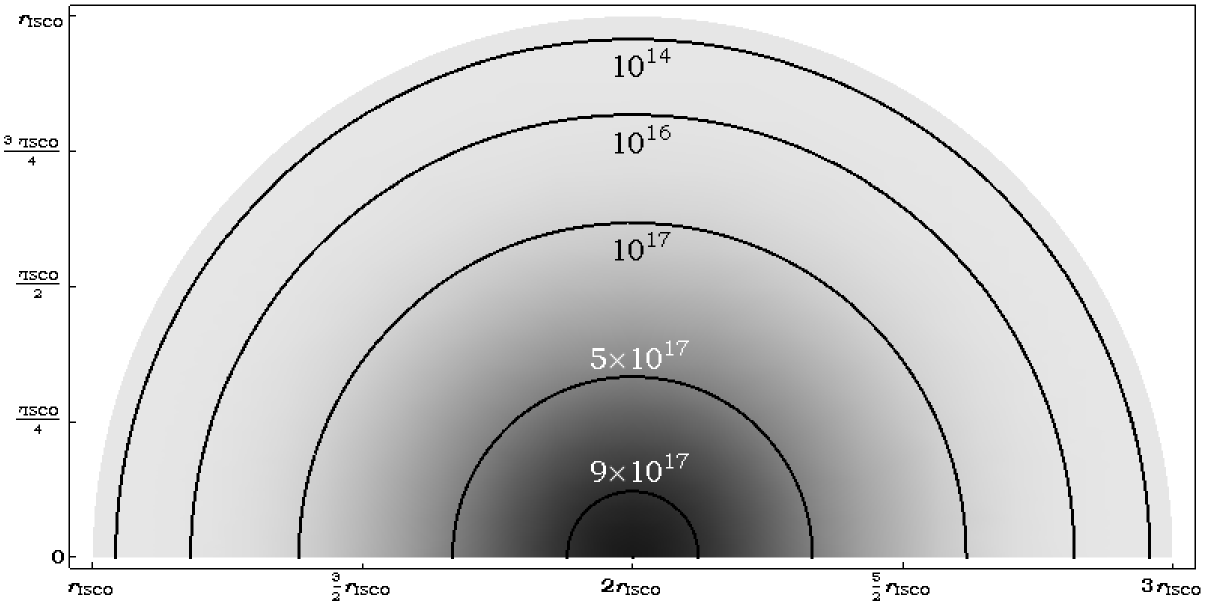

Figure 4.7: LFM model number density cross section for any spin parameter. The center of the tori lies at $(2\,r_{ISCO}, 0)$ and has a number density of $10^{18}\,cm^{-3}$.

$$P(r,\theta)=\hbar c\left[\frac{45(1-\beta)}{\pi^2\bar{m}\,m_p\,\beta}\right]^{1/3}\rho(r,\theta)^{4/3}, \qquad (4.3.4)$$

where $\rho\left(g/cm^3\right)$ is the volumetric mass density and k (erg/K) is the Boltzmann constant. We move on by calculating the material's absorption coefficient as:

$$a_\nu(r,\theta)=\sigma_\nu\, n(r,\theta), \qquad (4.3.5)$$

where $\sigma_\nu\left(cm^2\right)$ the absorption cross section for the processes. Then, the material's corresponding emission coefficient is given by:

$$j_\nu(r,\theta)=a_\nu(r,\theta)\,B_\nu(\mathrm{T}), \qquad (4.3.6)$$

using the thermal emission and blackbody radiation properties for our disk. Here, $\mathrm{B}_\nu(\mathrm{T})$ is the Planck function and T the corresponding temperature (see Rybicki & Lightman 1986). The Planck function (Planck 1910) is calculated using blackbody properties and in specific:

$$\mathrm{B}_\nu(\mathrm{T})=\frac{2h\nu^3/c^2}{\exp(h\nu/\mathrm{kT})-1}. \qquad (4.3.7)$$

From the above, we calculate the emission coefficient j_ν as:

$$j_\nu(r,\theta)=\sigma_\nu\, n(r,\theta)\frac{2h\nu^3/c^2}{\exp\left[h\nu/\mathrm{kT}(r,\theta)\right]-1}. \qquad (4.3.8)$$

We notice here, however, that in these equations one can add shaping functions f to modify the emission and absorption of the material, and study other disk models or different physical properties. A more general form of the above functions could thus be:

$$a_\nu(r,\theta)=C_{abs}\,\sigma_\nu\,\mathrm{f}\left(n(r,\theta),\mathrm{T}\left[n(r,\theta)\right],E\left[n(r,\theta)\right]\right), \qquad (4.3.9)$$

$$j_\nu(r,\theta)=C_{em}\,\mathrm{f}\left(n(r,\theta),\mathrm{T}\left[n(r,\theta)\right],E\left[n(r,\theta)\right]\right), \qquad (4.3.10)$$

where C_{abs} and C_{em} are absorption and emission coefficients. We can see that f is the number density $n(r,\theta)$ shaping function with $\mathrm{T}\left[n(r,\theta)\right]$ the material temperature and $E\left[n(r,\theta)\right]$ the photon energy function. From the calculations we described here, we can get the resulting radiation intensity $I\left(r,\theta,\tilde{a},\tilde{b}\right)$. We then only need to apply the method explained in Section 3.1 in order to go on and obtain the stress – energy tensor, the radiation flux, and the force of the radiation.

4.4. Differentiation between disk models

In this Section, we discuss the disk models we examined for our research. We clearly explain their differences and the reasons why we selected them for the cross-examination of setups. In Chapter 3, we discussed the disks we studied and we split them in two categories, the opaque and the quasi-opaque models. We note here that the assorted configurations we investigated possess substantial differences between them. These differences are not primarily related, for example, to the material density or opacity and thus even setups of the same category diverge markedly from each other.

There are three noteworthy properties of the arrangements we wish to investigate for their implications. First of all, we review the role of the material opacity and analyze if indeed as expected the opaque disks generate stronger radiation field than the semi-opaque models. We then go on to further investigate the material density ramifications in the radiation field created. Specifically, we survey the density gradient of the disks and draw conclusions on the importance and repercussions of higher or lower density increase rate. Finally yet importantly, we examine the aftermath of the geometrical setup of the disks. For instance, we assess which arrangements record larger force magnitudes in the outflow region, in the vicinity of the disk's inner edge or slightly above the disk, possibly altering the material accretion or expulsion.

We start the disk juxtapositions by comparing the opaque disk models "Slab" (Sect. 4.2c) and "Wedge" (Sect. 4.2d). These two arrangements are similar and very commonly used to examine disk dynamics and evolution in a variety of environments, such as binary stars and X-ray binaries. In addition, combinations of these two setups are often utilized for example in systems with disks of multiple components, such as hotter and thicker interior segments encompassed by colder and thinner outer segments. Such arrangements are expected to appear and later disappear regularly within the periodic development of the aforementioned X-ray binaries (see e.g., Fig. 5.1a).

The opaque disk models we discussed above generally produce an adequately strong radiation field. However, if their vertical height is not large enough, the field generated can be at certain points too spread out or too diffuse and thus the radiation forces exerted are of smaller effect. For this reason, we decided to test the upper limits of this category of disks. We thus considered a large borderline opaque accretion disk, the setup "Torus" (Sect. 4.2e), which is expected to record more concentrated and stronger radiation fields. Furthermore, we appose and compare this latter model with the aforementioned pair of opaque arrangements in an effort to assess the repercussions of the various geometrical characteristics. We thus examine which features of each model cause mentionable outcomes, such as larger radial or poloidal force components.

We continue further on by investigating the opaque rotationally supported torus ORST model (Sect. 4.2f). This is a self-consistent configuration and is expected to be in good proximity to the accretion disk naturally created around a black hole in circumstances of high opacity. A noteworthy feature of this arrangement is the strong dependence of the disk's size and volume on the central compact object spin (e.g., see Fig. 4.4 and 4.5). We also observe that, in contrast to the majority of the setups considered, the ORST disk model increases its size and volume along with the black hole spin.

Moving on, we examine the semi-opaque accretion disk setups. We first encounter the "LFM" model (Sect. 4.3d), which is the semi-opaque variant of the "Torus" model (Sect. 4.2e). Careful comparisons between these two configurations can reveal hidden but valuable information about the ramifications of the material opacity. Finally, we consider the radiation pressure supported polish doughnut "PD" (Sect. 4.3b). This configuration is also self-consistent, but unlike the rotationally supported ORST disk, this arrangement is supported by the hot disk material's radiation pressure. The most important difference between the "PD" and the "LFM" setups is the material's density gradient. The radiation supported "PD" configuration builds up the material density quite faster than the "LFM", even though both models are designed to reach the same number density maximum. This fact then allows us to survey the possible effects of the density gradient and its increase rate on the radiation field created and the forces exerted.

In the following Chapter, we examine how we can combine and integrate all the previous chapters and information as the foundation of our research. We additionally determine the most suitable ways to incorporate all the theory in algorithms that consider the presence of radiation and calculate its effects on the arrangement equilibrium and the latter's possible evolution.

CHAPTER 5

ALGORITHMS AND CODES

As an introduction to this Chapter, we refer the reader to the thorough article of L. Rezzolla (2014) "Three little pieces for computer and relativity". In this article, the reader is introduced to the new millennium computational capabilities and is presented with three of the most significant milestones of numerical relativity. Furthermore, we would like to mention the work presented in Davelaar et al. 2018, since it is a detailed and complete research in very close proximity of parts of our own studies. In this examination, the environment around a supermassive black hole (SMBH) is studied. In addition, advanced computational methods are developed and applied in order to investigate the radiative transfer and the material motion magnetohydrodynamics in strong gravity settings.

The primary goal of our study is to survey the Cosmic Battery mechanism and estimate its capabilities (see Chapter 6). This phenomenon was first described in Contopoulos & Kazanas 1998. Later on, it was criticized by Bisnovatyi-Kogan et al. 2002 for certain points of the theory and the setup. Finally, it was revisited in Contopoulos et al. 2006, clearing up some delicate points and misconceptions on the arrangement. Its effects on X-ray binaries were also examined in Kylafis et al. 2012. Our principal objective for this work is to investigate the generation and the intensity of the radiation field produced by the hot accretion disk orbiting an astrophysical black hole. Subsequently, the immediate and secondary dynamical effects of this radiation field are looked into in order to specify their further repercussions on the system dynamics and equilibrium.

For this purpose, we additionally surveyed various studies concerning strong gravity environments and photon fields. Some of the most important researches for our work on relevant subjects, that also include general relativistic magnetohydrodynamics are Broderick & Loeb 2005, 2006a, 2006b, and 2009, Noble et al. 2007 and 2011, Nakamura et al. 2018, Chatterjee et al. 2019, and Event Horizon Telescope Collaboration 2019a, 2019b, 2019c, 2021a, 2021b, 2022a, 2022b, 2022c, and 2022d.

It is worth mentioning, nonetheless, that the above researches principally pertain to studies of supermassive black holes and not typical stellar black holes of a few Solar masses. They include, however, valuable concepts, suggestions, and methods that are very helpful and can be utilized for both cases.

5.1. Algorithms and numerical codes

In this Chapter, we present the codes we created and used in our work, explain their capabilities and show various results of the code execution, most in the form of color-enhanced images. After that, we show images and numerical data that show their results and outputs.

Before moving along, the reader should be made aware of the fact that all of the codes used in our work and presented here, were designed in order to be executed with extremely limited computational resources. This has important consequences on the design, speed and effectiveness required from the codes.

We note that the research presented here is an extension of the earlier works Koutsantoniou 2014 and Koutsantoniou & Contopoulos 2014. In these studies, we investigated environments with noncentral opaque radiation sources orbiting a central black hole. Our methods and algorithms have since been markedly improved for speed, capabilities, and data security. Numerous post-processing procedures were additionally created and incorporated into the programs providing additional information and perspectives on various aspects of the subject. These processes include, for instance, a procedure that increases the algorithm resolution more than a hundredfold by only doubling the execution time. We also mark that machine learning algorithms can be employed to further enhance and improve the process.

The expansions mentioned earlier had an intense impact on the programs and their capabilities. For example, the new methods of execution and processing allowed us to simultaneously execute a multitude of simulations. This also enabled the stream-like execution of lengthy lists of computations and calculations lasting for several weeks or even months. These sessions could be executed on single or network connected machines equally well, with the code automatically skipping completed or currently executed runs by other machines or kernels. Furthermore, they allowed interrupting the executions at any moment without loss of data and also transferring calculations mid-execution between different machines of distinct operating systems.

Before moving on to the code specifics, we should mention that the fully ray tracing nature of our algorithms allows us to set observers and collect data from numerous locations in the systems. This permits us to make observations from critical system locations, such as the static limit area, the event horizon vicinity, the proximity to the system rotation axis, and the inner and outer edges of the accretion disk.

In this Chapter, we start by presenting the `Omega` code that studies and draws photon trajectories in the environment in a black hole system. The black hole can be rotating or nonrotating and the target point can be on the equatorial plane or further away from it. Depending on the required form of the output data, we can select between various editions of the code. We identify paradigm trajectories for massless and massive particles, and examine the results of the sky scanning process for various spacetimes and disks.

We continue on to the `Infinity` code, that is our most complete, potent, and detailed algorithm. It uses the `Omega` code routine to scan the entire sky around the target point and calculate the photon trajectories reaching it. Then, `Infinity` tracks the detailed particle path and calculates the additional energy transferred onto the target particle absorbing the light. At the end of each run for a target point, the code outputs numerical data and images depicting the incoming radiation and its intensity. There are several velocity profiles the target particle can be following, depending on its location and the accretion disk considered in the run. Hence, in every execution there are a number of different radiation force outputs. We validate the program's accuracy and inspect its numerical and graphic results revealing the radiation field generated by the accretion disk. We additionally investigate and compare the properties of the assorted disk models.

The next code we look into is the `Elysium` code. This code was written in order to allow us to take pictures of the black hole and accretion disk systems from infinity. It is a complement of the `Infinity` code that follows the opposite direction of photon movement. It starts from "infinity" and looks toward the black hole, taking a high-resolution picture of these systems. We thus replicate the observation of disks around compact objects at infinity in various ways and record the information we can then extract for these systems.

The following code is named `Tranquillity` and uses techniques from other aforementioned codes in order to estimate a black hole spin from pictures taken from observational data. Its purpose is to create divergence plots for different accretion disk models of various spins and inclinations. Afterward, we can use these divergence plots in order to estimate the spin of the central black hole. We see results about our method and we mark the good quality of spin estimation compared to its real value in randomized tests.

Finally, we explain the code `Burning Arrow`. This code studies massive particle motion and examines the effects of radiation onto their trajectories. Its most important application is, perhaps, on the radiating hot accretion disk of the black hole itself. This allows us to see if the disk's thermal radiation has effects on the disk material's motion and evolution. We finally present our results about the modified electron orbits due to radiation and their interactions with the spacetime and the field's special regions.

The algorithms created and used for this study can be found online at the following addresses:

`Omega`: https://gitlab.com/leelamichaels/Omega

`Infinity`: https://gitlab.com/leelamichaels/Infinity

`Elysium`: https://gitlab.com/leelamichaels/Elysium

`Tranquillity`: https://gitlab.com/leelamichaels/Tranquillity

`Burning Arrow`: https://gitlab.com/leelamichaels/Burning_Arrow

5.2. Code `Omega`

(URL: https://gitlab.com/leelamichaels/Omega)

5.2.1. The algorithm and capabilities

Code `Omega` was the first main code written for our work and its first version was written in 2013. It has since been further developed, kept improved, and in constant update with more than 109 versions. So far, it is still one of the most important parts of almost all the following codes.

`Omega` records the incoming radiation by determining all the possible photon trajectories reaching a specific point in a Schwarzschild spacetime (Schwarzschild 1916) or a Kerr spacetime (Kerr 1963) of any spin. It is also easily modifiable in order to provide orbits and solutions for other spacetimes, such as Reissner – Nordström (Reissner 1916, Weyl 1917, Nordström 1918, Jeffery 1921), Kerr – Newman (Newman et al. 1965, Adamo & Newman 2016), Hartle – Thorne (Hartle & Thorne 1968), etc.

When executing the `Omega` code, the user can choose between various tori models that describe many sources of radiation and systems. Some of these systems are as described in Sections 4.2 and 4.3, and in Figures 4.4, 4.6, and 4.7. We mark here, however, that in the case where the already set up disk models do not cover the environment we wish to study, it is possible to add new disk models. An addition of this kind is rather easy, especially when the desired disk is a combination of already existing disk models, such as those shown in Figure 5.1.

The `Omega` code works by solving the particle trajectory equations we mentioned in Section 2.4 for a photon ($\mu = 0$), finding its trajectory and then pinpointing its point of origin. The “start” of each such trajectory can be on the accretion disk, the event horizon of the black hole, or somewhere outside, far away from the accretion disk – black hole system. If said trajectory only intersects with the event horizon or the system exterior, then it carries no additional radiation or energy to the absorbing target.

Depending on the environment in which it is used, `Omega` code can have different outputs. In its original form, which is visual, the program has

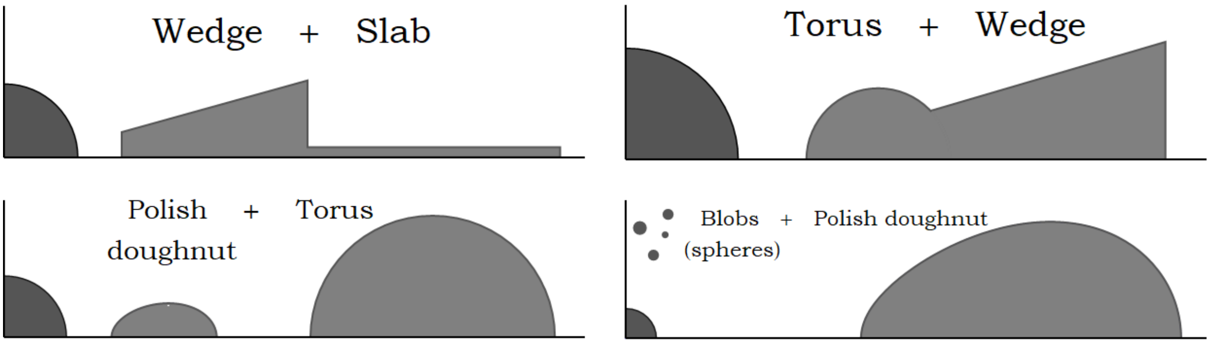

Figure 5.1: Accretion disks created from combinations of previously referred models: (*top*) wedge & slab, torus & wedge, (*bottom*) polish doughnut & torus and polish doughnut & spheres.

an interface (Fig. 5.2) that allows the user to select primary properties for the environment, such as the disk model, the black hole spin parameter, and the disk height. Also, one can select important options for a trajectory, including its maximum length, its point of origin and angle of emission, and the two emission angles $\tilde{a}$ and $\tilde{b}$. Finally, some additional visualization options include the choice of frame size of the visual box and the depiction of obscured parts of the outer disk. The code's dynamic output picture shows the black hole event horizon and its ergosphere, the accretion disk and the requested photon trajectory. The photon trajectory is drawn in different styles and colors for escaping particles, particles infalling in the black hole, and particle trajectories intersecting the accretion disk. In addition, some trajectory information are displayed on the picture, including the photon energy and angular momentum, the trajectory's Carter constant and the initial "TARGET" momentum magnitude. Finally, at the bottom appear the requested experiment "SOURCE" information, the received photon source coordinates, and the momentum magnitude at emission. We also mark that there is a version of `Omega` to specifically study the equatorial particle orbits and the effects of spacetime rotation (see e.g., Fig. 5.3, Fig. 5.8). In these circumstances, we observe paradigm particle orbits and we additionally mark trajectory interactions with the spacetime rotation. This interaction results in the orbit-dragging along the black hole rotation and the consequent source image modifications.

The latest version of the `Omega` code has no visual outputs but is the most complex and compact version. It was redesigned and from an

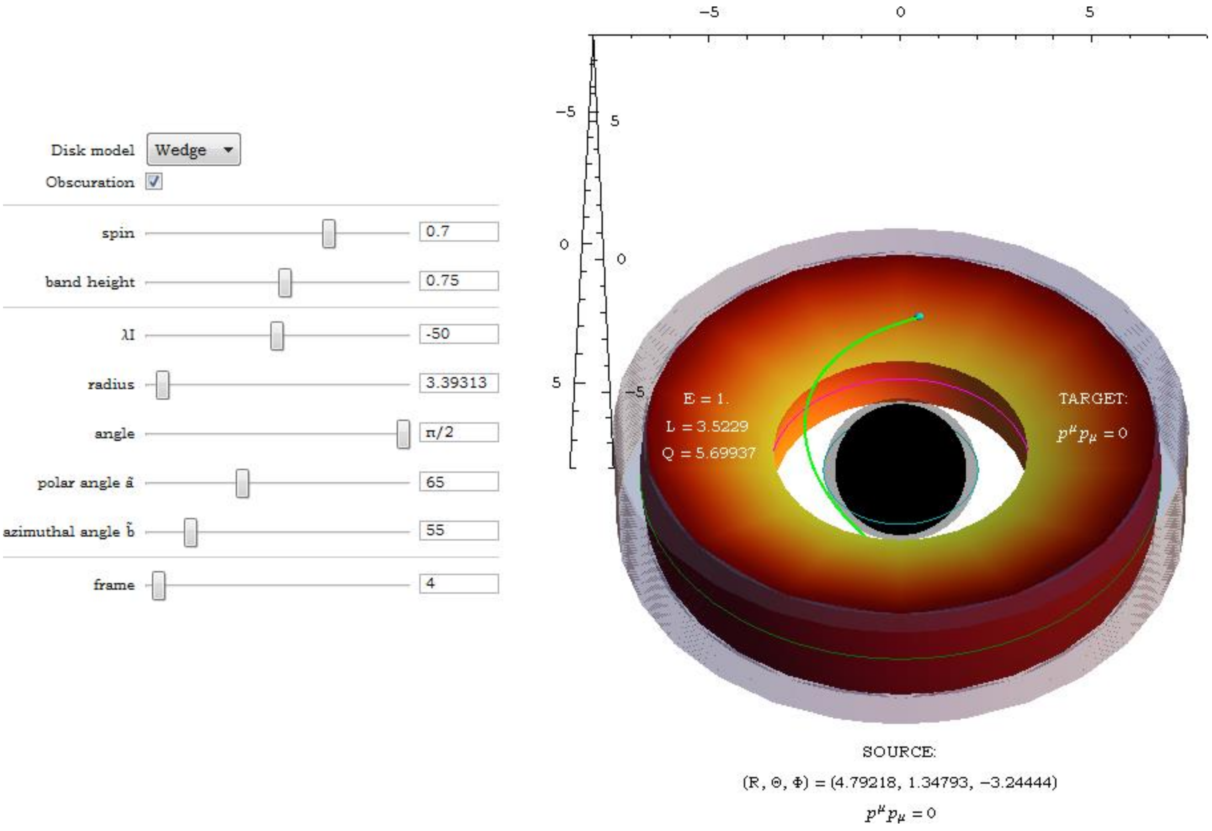
Disk model: Wedge
Obscuration ☑
spin 0.7
band height 0.75
λI -50
radius 3.39313
angle π/2
polar angle ã 65
azimuthal angle b̃ 55
frame 4

E = 1.
L = 3.5229
Q = 5.69937

TARGET:
$p^\mu p_\mu = 0$

SOURCE:
$(R, \Theta, \Phi) = (4.79218, 1.34793, -3.24444)$
$p^\mu p_\mu = 0$

Figure 5.2: Control interface of the `Omega` code, as described here.

independent code, it was rewritten into a function form. It now creates only numerical outputs for the equations of motion and the photon emission points. It runs a single photon trajectory per execution and returns information for its path. This information concerns the particular local sky direction and the existence of radiation influx or not. It also provides the exact trajectory followed by the photon and the coordinates of the trajectory source, whether that is on the disk or not. The `Omega` code, even though it was the first step, we consider it one of the most important parts of all our work so far. This is because it is an irreplaceable part of almost all the subsequent codes and works.

We continue on by explaining some of the tests `Omega` was subjected to in order to test and verify its validity. Firstly, we built an alternative approach to the accretion disk setup named “Star”. In this model, the radiation is emitted by a central spherical star of isotropic and uniform radiation instead of a noncentral accretion disk. This mode was mainly used in order to cross-check the accuracy of our results compared to analytical formulae provided by relevant significant researches. The results of these executions verified the apparent source contraction due to relativistic effects and its apparent displacement or variation due to frame dragging. Additionally, the sum of the data comparisons proved rather encouraging and revealed information on the increased intensity of incoming radiation on the orbiting material. This information is looked upon further and discussed

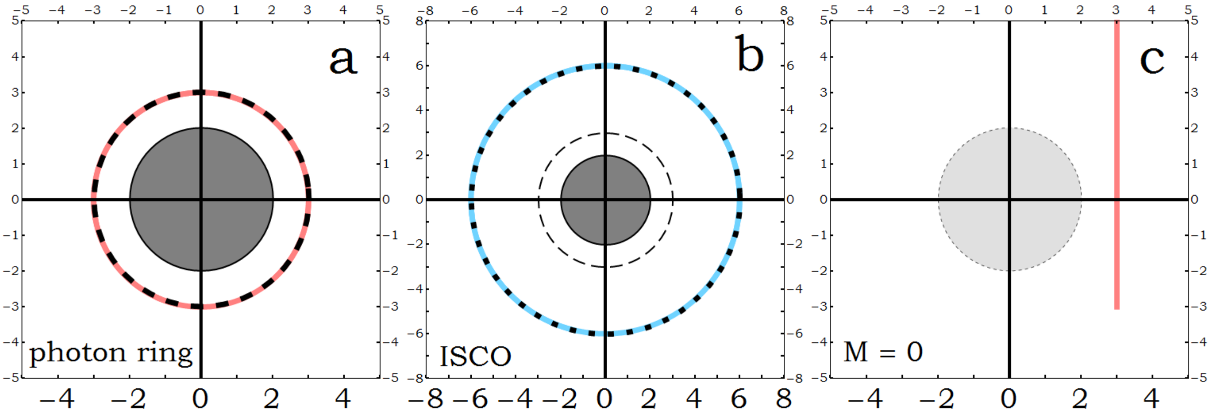

Figure 5.3: Verifying the validity of the `Omega` code. We corroborate that paradigm orbits of massless and massive particles (see Sect. 2.2) are successfully produced by the code. In each figure the black hole is situated on the axes origin and displayed with a gray disk. In (*a*) we see in a red circle the photon ring as it is numerically created by the code. On top of it we have in a black dashed circle the theoretically expected position of the orbit. In (*b*) we see in a blue circle the ISCO numerically created by `Omega` and on top of it the theoretically expected orbit in the black dotted circle. In (*c*) we cancel out the black hole presence by setting its mass $M = 0$ and in the light gray disk we see where the event horizon should have been. For any black hole with mass $M > 0$, the spacetime would be curved, forcing the photon to infall and cross the event horizon. For a zero mass black hole the spacetime is, however, flat and the photon continues traveling in a straight line.

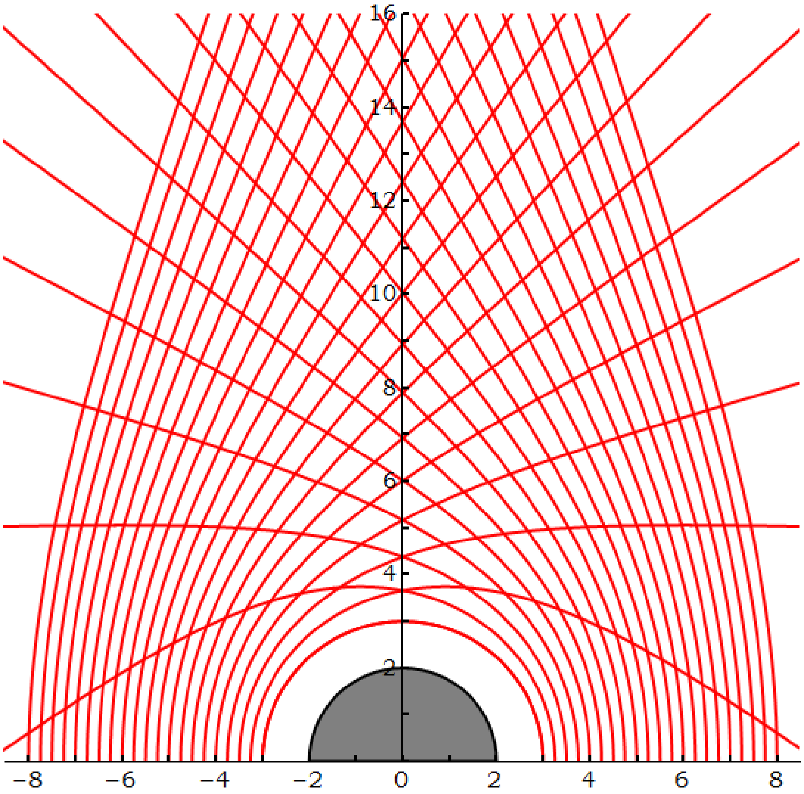

Figure 5.4: Free photon trajectories in the poloidal $x-z$ plane. Photons are emitted from the equatorial plane perpendicularly upward at assorted points. The closest emission points to the black hole are $(3,0)$ and $(-3,0)$ and correspond to the photon ring.

in Section 5.3. We also note here that, if need be, the code can be further modified in order to study more complex objects, such as nonspherical or nonuniformly emitting stars.

Another test we subjected `Omega` to was to confirm that it indeed produces specific paradigm orbits. Such examples are the fundamental notable orbits discussed, for example, in Bardeen et al. 1972. As we can see in Figure 5.3, `Omega` successfully produces the photon orbit (massless particles) and the ISCO (massive particles). Furthermore, we attempt setting the black hole mass equal to zero and assess how the spacetime curvature changes. This modification does indeed change the nature of the spacetime and transforms it from a curved Schwarzschild or Kerr form spacetime into a flat Minkowski one. This results in particle orbits turning from curved into straight lines.

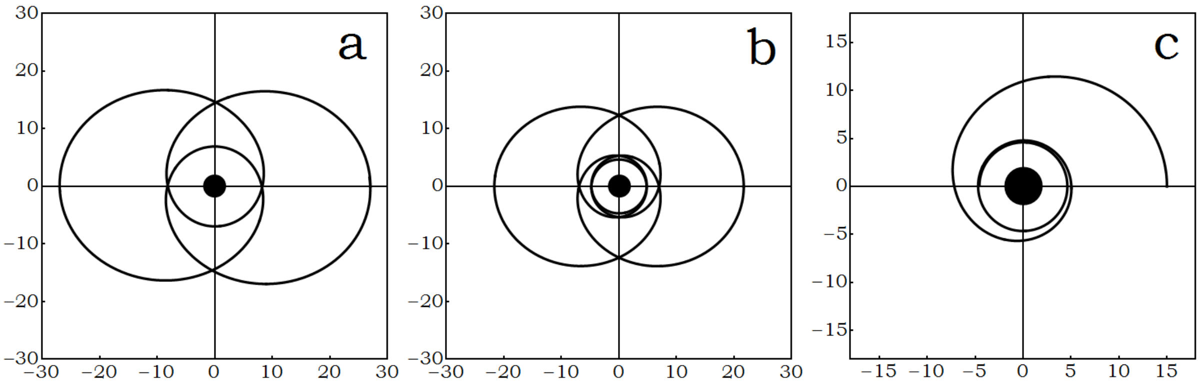

Figure 5.5: `Omega` successfully plots massive particle trajectories in agreement with Levin & Perez-Giz 2008.

Subsequently, we compare our program with the work of Bini et al. 2015b for the photon orbit creation accuracy and we note agreement. We observe in Figure 5.4 the free photon trajectories plotted by `Omega`. These photons are launched in Schwarzschild spacetime from the equatorial plane of the accretion disk perpendicularly upward. Comparing with Bini et al. 2015b, Figure 1, we observe the coincidence of results.

Before closing we also mention that, even though `Omega` is used to calculate photon trajectories, it can be modified and used to study massive particle trajectories, such as electrons or protons (see e.g., Levin & Perez-Giz 2008, Levin & Grossman 2009, Grossman & Levin 2009). We have performed this modification in a version of the code and compared our results, for instance, with Levin & Perez-Giz 2008 and also notice agreement. For example, we can examine Figure 5.5 and compare our results with the aforementioned study. Additional information about geodesic – spin deviations can be found in Bini & Geralico 2011c.

5.2.2. Results: Bundles of photons & spacetime rotation

As explained earlier, the `Omega` code is of paramount significance in our study, since it is the program producing massless and massive particle trajectories. In the vast majority of cases, `Omega` is utilized by the subsequent algorithms, where it is incorporated as an additional function. Since under these circumstances, no visual information is requested from this routine, no graphical trajectory or environment outputs are created or stored.

In the version where it is an independent program, it produces and provides a multitude of visual information about the trajectories, such as differentiated trajectory formats depending on their origins. Thorough research on the subject of particle trajectories in strong gravity can be found, for instance, in Levin & Perez-Giz 2008 and Levin & Grossman 2009 or relevant and future studies.

One notable application for this edition is the one plotting and displaying complete photon bundles. The program user here, has the liberty to freely choose the bundle size and thickness, depending on the specific research characteristics. In Figure 5.6, we can see various photon trajectories reaching an observer on the edge of the accretion disk. This means that we stand on the position of the observer and backtrack the photon paths, seeking the location of their source. If a trajectory intersects with the accretion disk at any point, then there can be incoming photons carrying energy. If not, then the only possible incoming photon trajectories can have their origin at the event horizon or the system exterior. Namely, even though such trajectories are allowed, they do not bring in additional light or energy. Again, we observe here the spacetime curvature evolving and the arrangement critical areas (event horizon, ISCO, and static limit) being altered and displaced with increasing values of the black hole spin. We can furthermore study the sky scanning procedure (Fig. 5.7), the notable surfaces development and their apparent approach in a video depicting the

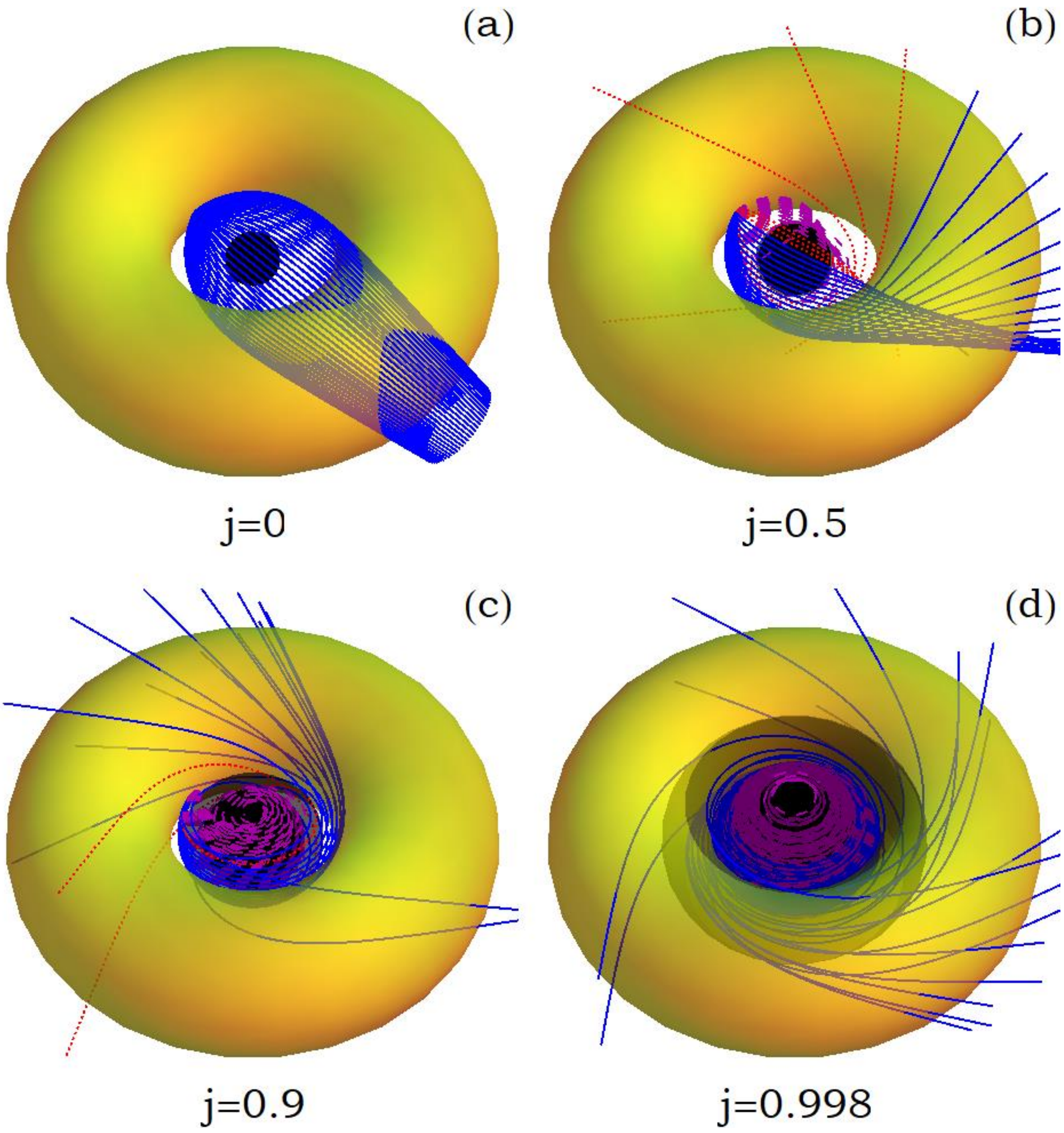

Figure 5.6: Results of `Omega` plotting photon bundles in assorted black hole angular momentum environments j: 0, 0.5, 0.9 and 0.998. In each figure, we have the event horizon as the central *black* sphere, the ergosphere as the *gray* ellipsoid or spindle torus and the accretion disk as the *yellow* torus. *Solid blue* lines are photons emitted by the hot accretion disk material and carry along energy. *Dashed purple* lines are trajectories of photons that should have been emitted the event horizon and *dotted red* lines are photons paths that originate from the system exterior. The latter two trajectories do not bring radiation to the disk.

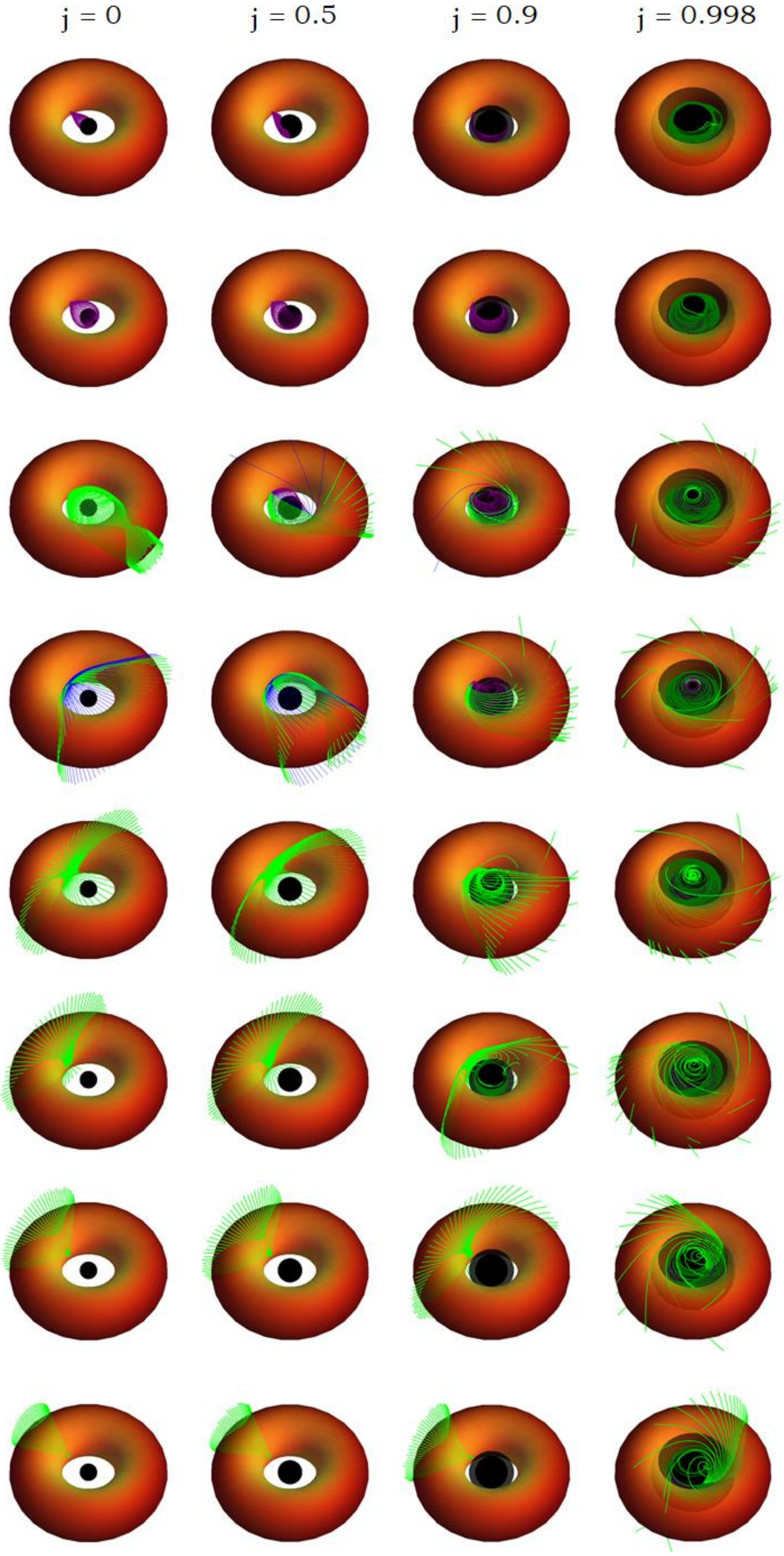

Figure 5.7: Sky scanning process. *Purple* lines only intersect the event horizon and carry no radiation. *Blue* trajectories originate from outside the system and also carry no radiation. *Green* trajectories cross the accretion disk and bring in radiation and energy.

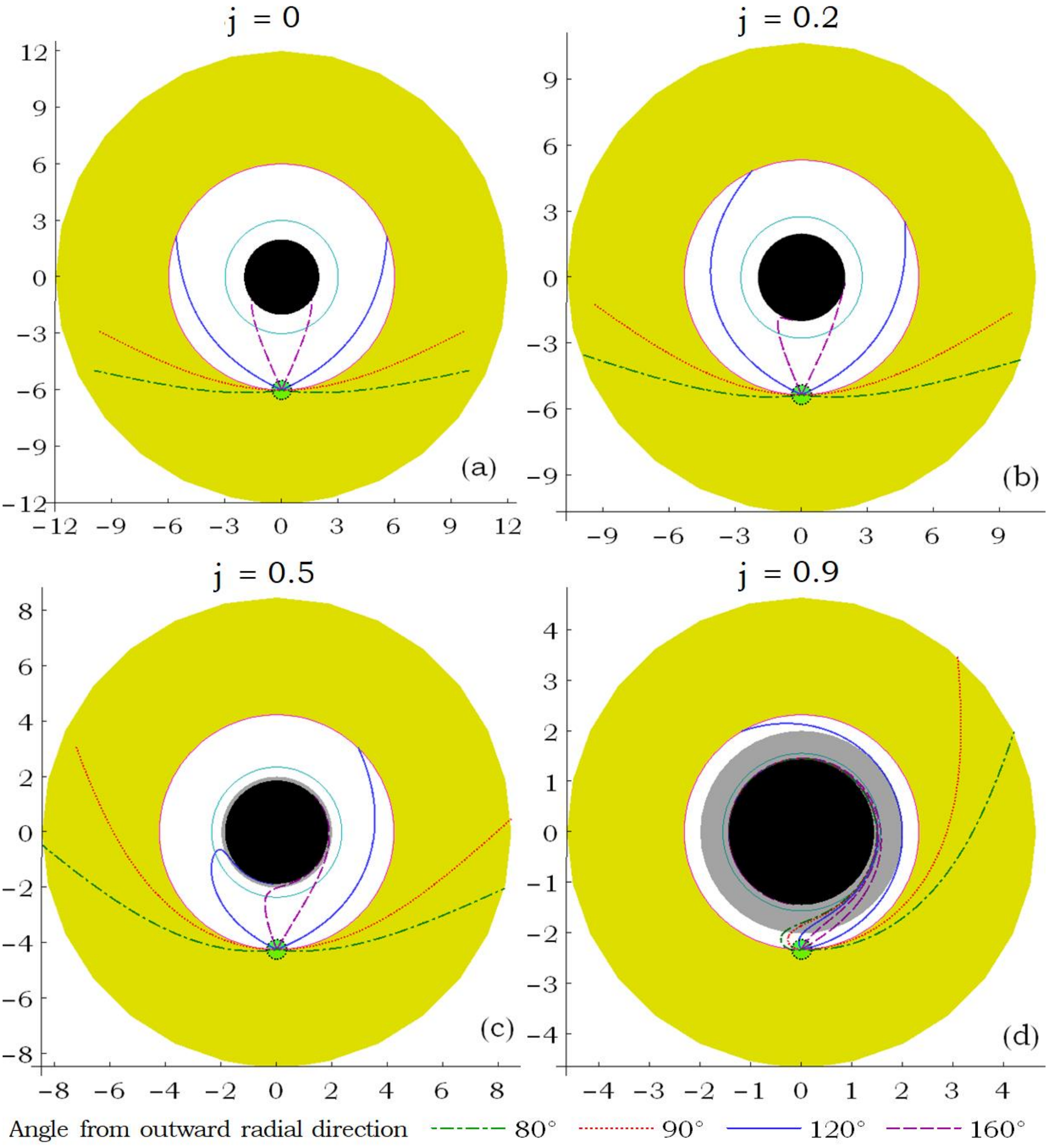

Figure 5.8: Equatorial plane and photon orbits launched by the accretion disk rotating clockwise, in the same direction as the central black hole, with various angular momentums j. The *black disk* is the event horizon, the *gray annulus* is the ergosphere, the inner, *cyan circle* is the photon sphere, the outer, *magenta circle* is the ISCO, and the *yellow area* outside it, is the rest of the accretion disk. The trajectory angles are measured from the outward radial direction and as the angular momentum increases, we zoom into the picture to better see the details. The effects of the spacetime rotation on the photon trajectories are clearly visible as the angular momentum increases. The allowed photon trajectories tend to concentrate in the spacetime grid direction of motion.

algorithm process for various spin parameters here[5].

Another aspect of our studies that could benefit from this algorithm is the observation and examination of how photon trajectories are influenced by the rotation of the spacetime grid. Namely, we wish to closely examine how the increasing frame dragging affects photon or massive particle orbits around compact objects. As an example, we can survey Figure 5.8 and investigate the consequences of the central mass rotation onto photon orbits in the equatorial plane. We notice that as the black hole spin increases (clockwise), the rotating mass forces the spacetime grid to rotate along and the particles to get dragged as well with it.

Before we proceed to the next subject, we explain our concepts of possible extensions of this program, as abundant further applications can be implemented. For instance, `Omega` can expand and investigate particle trajectories in X-ray binaries, light rays in multiple-star systems, and more. In addition, the potential of tracking photons in strong gravity environments can be used to study gravitational lensing phenomena (e.g., Refsdal 1964, Blandford & Narayan 1992, Narayan & Bartelmann 1996, Bozza 2010, Gralla & Lupsasca 2020a, 2020b, Gralla 2020). Moreover, `Omega` can be used to examine other spacetime environments, such as Hartle – Thorne metric (e.g., Abramowicz et al. 2003, Bini et al. 2013, Younsi et al. 2023) or modified gravity theories.

Furthermore, our work should also be examined while taking into consideration studies such as Gralla et al. 2015 that set particle orbits and system radiation sources into quite a different perspective. Expanding on photon orbits, we can also investigate light projections and material interactions in the "near-field" areas of the arrangements (see e.g., Gralla et al. 2019, but also Gralla & Lupsasca 2020a, 2020b, Gralla 2020, Gralla et al. 2020). We can thus investigate the interactions between the black hole shadows and the secondary images created by the superposition of the thin photon ring (generated by near-field photons) and the dominant radiation background (created by the gravitational redshift and the material emission characteristics).

---

[5] *Link URL:* https://www.youtube.com/watch?v=x195P-ShqCo

5.3. Code `Infinity`

(URL: https://gitlab.com/leelamichaels/Infinity)

5.3.1. The algorithm and capabilities

Code `Infinity` was first written in 2013 and it currently has more than 139 versions. It is the next step after `Omega` and completes the first part of our research goals, having executed more than 10,500 runs. The code is of central importance in our research and pertains to the majority of code extensions and capability enhancements. Its main goal is to calculate the radiation forces exerted on a target and hence the radiation field generated by the hot accretion disk.

In the beginning, it was designed as a code that would execute and give the orbit and radiation information about a target absorbing material at a single and specific point in space. Now `Infinity` is an extended and fully automatic autonomous program that can run entire streams of simulations in large packets. It can run simulations separately or simultaneously, without stopping, and without the need for human intervention. The requested stream of executions can be of any size and the simulations are not required to be for the same object, in the same spacetime, or with the same characteristics. The code is additionally written in the appropriate way to automatically save its various outputs, creating numerical data files, images, output information files for users, and information used in collective runs and aggregated compilations.

`Infinity` has also had a series of version updates in order to face power and network problems that would cause damage to the simulations and result in the loss of hours or days of work. The resulting versions of `Infinity` now allow any code to be stopped at any time during execution without losing any results and then be restarted later on, when the system becomes again available. This was very useful in order to face common problems, such as power outages or memory leaks and to accommodate simultaneous usage of the machines by more than one user.

In the current and latest version of the `Infinity` code, the user chooses the desired system setup and a point of interest in it. This target point can be situated further in the disk's inner edge of further out, above the accretion disk and if possible inside the disk material. The program then sets there an observing point and scans the entire local sky around it. It subsequently solves the General Relativistic Radiative Transfer Equation (GRRTE) there and returns the radiation reaching the observer from each of the angles of the local sky. It goes on to calculate the radiation stress – energy tensor at the particular point, also creating images of the various steps and setups of the system, depending on the physics and properties of each torus model. A very significant step of the execution follows up, as we run a procedure that increases the code resolution up to 625 times or even more, while only doubling the execution time (see Fig. 5.9).

`Infinity` then goes on to calculate the radiation flux and the radiation force four-vectors applied on the assorted observers, moving and stationary. This includes observers at rest in the local frame rotating with $\omega=\omega(r,\theta)$ as seen from infinity (Eq. (2.1.15)), observers in circular orbits moving with Ω (Eq. (2.2.13)) or (Eq. (4.2.19)) depending on the selected disk model, observers on accreting material attempting to mimic the SANE and MAD models, and finally observers in two possible outflow regions close to the system rotation axis and above a certain height (see Fig. 5.10). Let us note here, that even though we have made our choice on certain velocity profiles for the assorted disk models, this can easily be adjusted to suit the needs of other disk models with different material velocities. We mark here, that such a change would simply affect the final step of the program that only takes a few minutes to run and does not require a re-execution.

The program then finishes its execution by creating save files and outputting its results. Firstly, it incorporates its minimum and maximum radiation values to the relevant files for each model for the aggregated compilations. It goes on to write in the selected model's four and three-force values files for the various observer velocities. Then, it

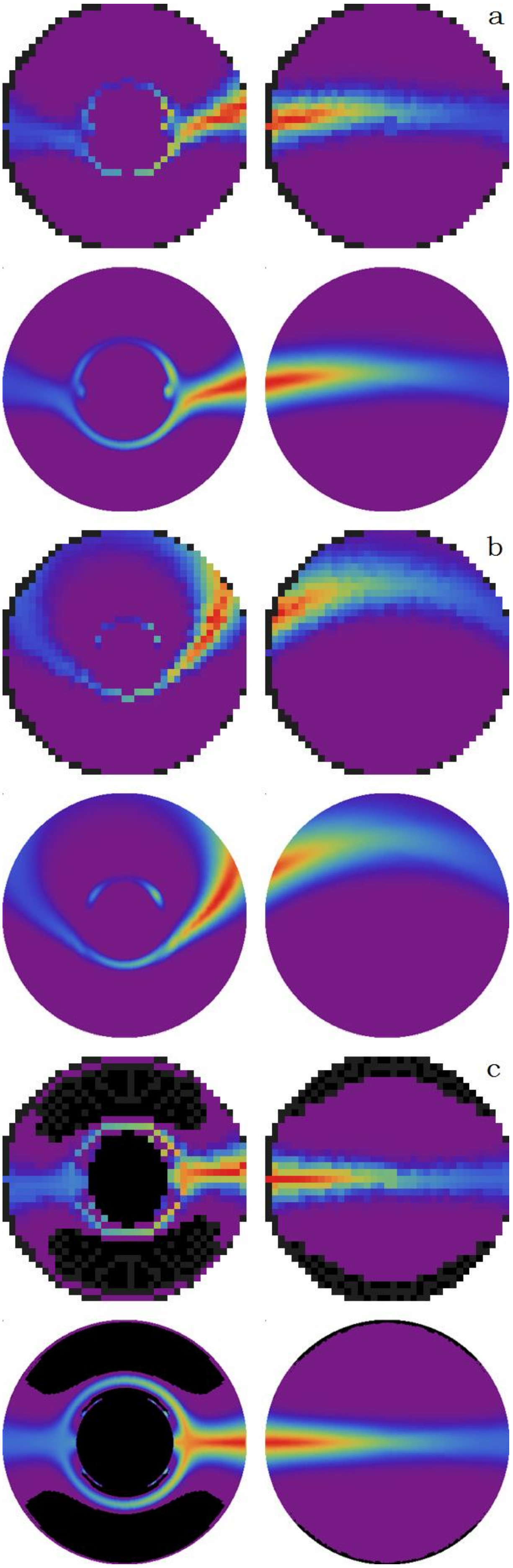

Figure 5.9: Three instances of the first version of the resolution enhancement process (625 times here). In the *top row* of each figure we see the original algorithm results for accretion disk observation. On the *bottom* we see the results after the execution of the resolution enhancement process. The appropriate processes are now rewritten and assimilated into `Infinity`, automatically improving the results by a number of times in every execution.

creates numerical computer-friendly data files of the simulation and a Mollweide map picture (Fig. 5.11) of the specific observer's location. Finally, it creates a graphical user-friendly output file that includes short but important information on the simulation it is describing, along with several pictures of the important matrices for the simulation. It also includes numerical and visual tables for the assorted profiles' force components and the radiation stress – energy tensor matrix. In addition to the program-created-figures, we created videos of flights around and if possible through the disk material for all the models examined. These can be found on youtube.com under the name of the creator "Leela Elpida Koutsantoniou"[6].

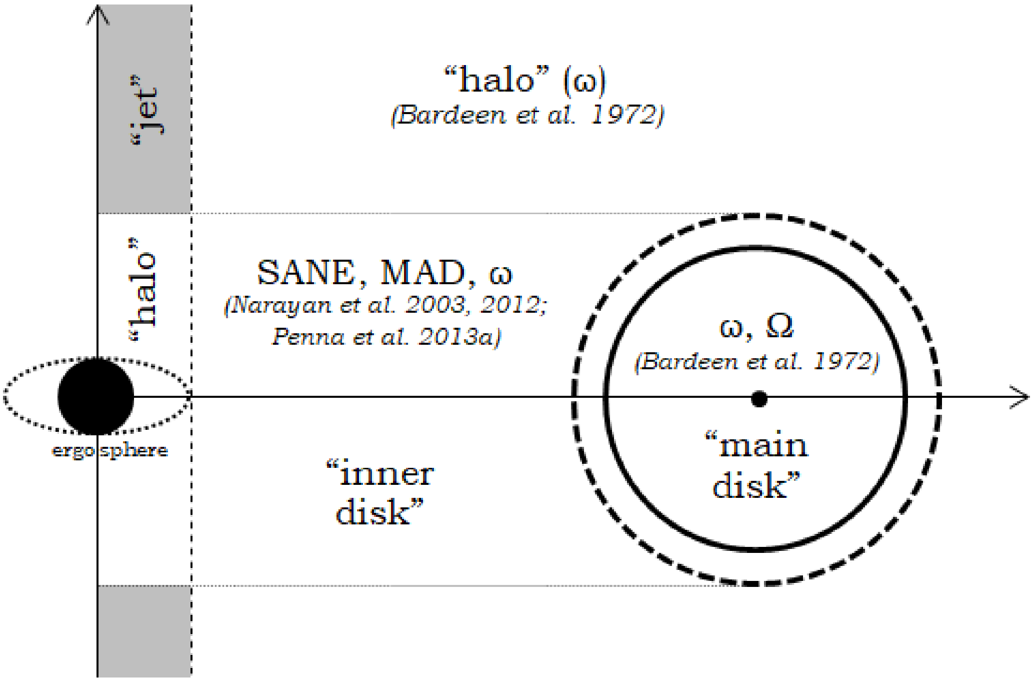

Figure 5.10: Assorted regions of a system. The solid line is the disk cross section and the dashed, a thin region near the material edge, where matter is slowly escaping or accreting onto the disk. For this transition area, we also mark the field noted by a target moving with velocity a negligible divergence away from the disk's. "*Halo*" includes observers at rest in the local rest frame rotating with ω. "*Main disk*" is the main disk, where material moves in four different ways: at rest in the local rest frame rotating with ω, purely azimuthally with angular velocity Ω, or by slowly infalling in a manner like SANE and MAD. "*Inner disk*" is the region of infalling material and includes matter at rest in the local rest frame or infalling mimicking SANE and MAD. The "*Outflow*" region is part of a cylinder centered at the system's rotation axis that includes the ergosphere, having a radius $r = 2M$. The region is considered to exist above a certain height, further away from the black hole. In this region, we have matter at rest in the local rest frame and matter flowing outward with a certain velocity. We may also consider a subregion there, a narrower cylinder with radius $r = M$ with stronger outflows and faster velocity, such as those suggested in Lovelace 1976, Contopoulos 1995, Mastichiadis 2002, Asada et al. 2016, Park et al. 2019.

---

[6] *Link URL:* https://www.youtube.com/channel/UCJ4v8rSg390gt9kQfVtfx5A

Before closing, we discuss the tests we subjected our code to in order to verify the validity of the results. For this purpose, we used the mode "Star" for `Omega` and cross-checked our outputs with researches concerning radiation fields created by stars in strong gravity. We thus began with a central nonrotating star emitting photons isotropically from each point of its surface. The star radius can have various values and so does the observer radial distance. Subsequently, we execute `Infinity` and observe the system from various points, making note of the star's optical dimensions and the recorded stress – energy tensor. Afterward, we cross-examine our output with the anticipated results provided by analytical formulae.

In the first assessment, we look into a static Schwarzschild spacetime and examine the environment of a nonrotating star, comparing our results with the analytical formulae provided by Abramowicz et al. 1990. Looking at Table 2, we see that we are in good agreement with the theoretically anticipated source dimensions and force values. We additionally note that even better estimations can be provided by increasing the algorithm resolution.

We continue on to examine the phenomena in a stationary, rotating spacetime in the vicinity of a Kerr black hole, since we expect that this is the most common situation encountered. In Table 3 we confirm that the `Infinity` code provides good estimations for the forward and backward radiation source dimensions, compare to their theoretical values provided by formulae in Lamb & Miller 1995 and Miller & Lamb 1996. In Table 4, we

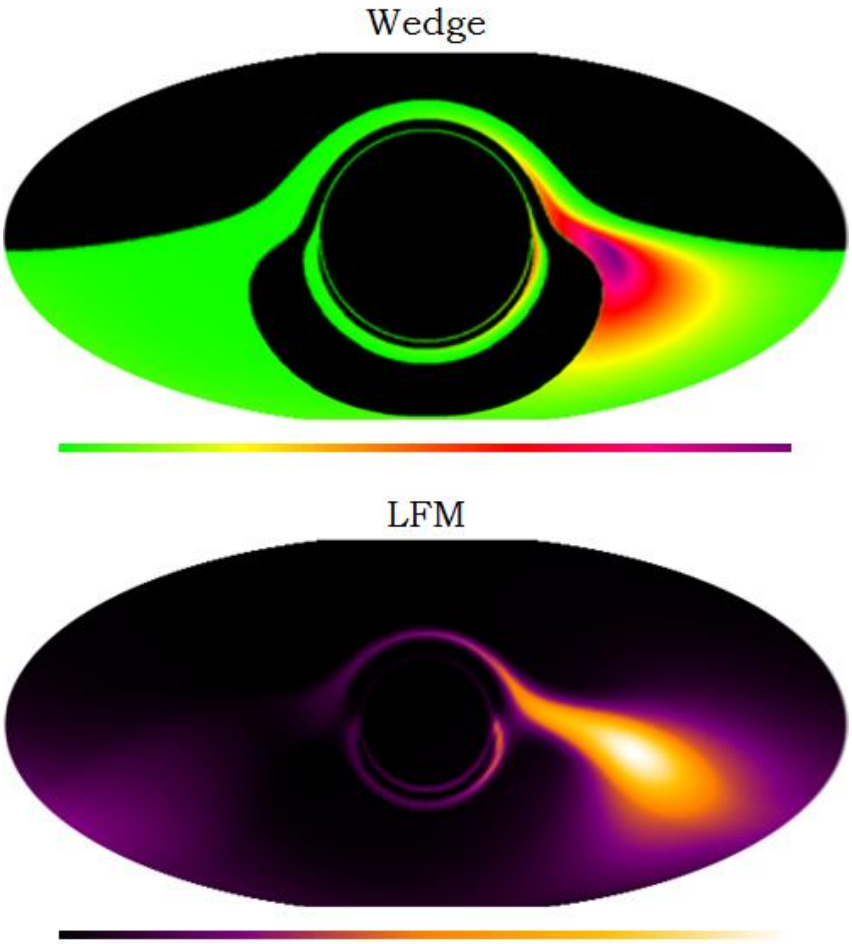

Figure 5.11: Code `Infinity`: algorithm generated Mollweide sky maps of the frequency – integrated specific intensity. The black hole is situated in the center of the image and its angular velocity points downward. Below each image is the color scale used from minimum to maximum. The accretion disk models displayed are "Wedge" (*top*, opaque, Sect. 4.2d) and "LFM" (*bottom*, semi-opaque, Sect. 4.3d).

Star radius R(M)	Orbit radius r(M)	Approx. radius (°)	Formula radius (°)	$T^{\hat{\alpha}\hat{\beta}}$ errors (%)
4	4.1	80.8	80.9	0.17
4	5	61.2	61.2	0.65
4	6	50.0	50.3	0.62
4	7	42.8	43.1	0.44
4	8	37.6	37.8	0.25
5	6	61.2	61.5	0.17
5	8	44.0	44.3	0.70
5	10	35.2	35.3	0.98
6	7	62.4	62.5	0.23
6	8	52.4	52.7	0.43
6	9	46.0	46.1	0.71
6	10	40.8	41.1	0.55

Table 2: Comparing `Infinity` results with formulae in Schwarzschild spacetime.

Notes: Radiation from a nonrotating star of radius R(M) in Schwarzschild spacetime. Observer is in orbit of radius r(M). The optical radius of the star in degrees (°) is given by `Infinity`. Results in satisfying agreement with analytical formulae from Abramowicz et al. 1990. In the last column we see the errors percent for our calculations of the stress-energy tensor in comparison to the bibliographic formulae.

Star radius R(M)	Orbit radius r(M)	fw rad. error (%)	bk rad. error (%)
$a = 0.2$			
4	4.1	0.	0.1
4	6	0.4	0.2
4	7	0.	0.4
4	8	0.	0.3
4	9	0.	0.3
5	5.1	0.1	0.1
5	6	0.2	0.
5	9	0.	0.
5	10	0.3	0.
6	6.1	0.1	0.
6	8	0.2	0.2
6	10	0.5	0.
$a = 0.5$			
4	4.1	0.4	0.1
4	6	0.4	0.5
5	6	0.	0.3
5	7	0.6	0.
5	8	0.5	0.4
5	9	0.3	0.2
5	10	0.3	0.3
6	6.1	0.	0.
6	7	0.	0.2
6	8	0.	0.4
6	9	0.2	0.2
6	10	0.5	0.
$a = 0.7$			
4	4.1	0.3	0.2
5	5.1	0.4	0.1
5	6	0.7	0.6
5	7	0.8	0.4
5	8	0.7	1.1
5	9	0.8	0.7
5	10	1.5	0.3
6	6.1	0.2	0.1
6	7	0.3	0.5
6	8	0.2	0.
6	9	0.7	0.6
6	10	0.8	0.5
$a = 0.9$			
4	4.1	0.6	0.7
5	5.1	0.3	0.
5	6	1.4	0.8
5	7	1.7	1.4
5	8	1.7	1.7
5	9	2.	1.6
5	10	2.5	1.6
6	6.1	0.5	0.4
6	7	0.5	0.8
6	8	0.6	0.2
6	9	0.9	1.
6	10	1.3	1.1

Table 3: Comparison of `Infinity` results with formulae in Kerr spacetime.

Notes: Investigating the agreement between `Infinity` code results and the formulae in Lamb & Miller 1995 and Miller & Lamb 1996 for the source forward (fw) and backward (bk) optical radius.

Table 4: Convergence of `Infinity` results with increasing resolution.

Notes: The increase of observation resolution (degrees) by `Infinity` seen decreasing the calculation errors of central body optical radius.

Star radius R(M)	Orbit radius r(M)	Resolution (°)	Approx. radius (°)	Formula radius (°)	calcul. error (%)
4	5	10	60	61.2	2.
4	5	5	60	61.2	2.
4	5	2	60	61.2	2.
4	5	1	61	61.2	0.3
4	5	0.4	61.2	61.2	0.
4	8	10	30	37.8	20.6
4	8	5	35	37.8	7.3
4	8	2	36	37.8	4.7
4	8	1	37	37.8	2.
4	8	0.4	37.6	37.8	0.4
4	9	10	30	33.7	10.9
4	9	5	30	33.7	10.9
4	9	2	32	33.7	4.9
4	9	1	33	33.7	2.
4	9	0.4	33.6	33.7	0.2
5	9	10	60	61.5	2.4
5	9	5	60	61.5	2.4
5	9	2	60	61.5	2.4
5	9	1	61	61.5	0.7
5	9	0.4	61.2	61.5	0.4
5	9	10	30	39.2	23.5
5	9	5	35	39.2	10.8
5	9	2	38	39.2	3.2
5	9	1	39	39.2	0.6
5	9	0.4	39.2	39.2	0.1
5	10	10	30	35.3	14.9
5	10	5	35	35.3	0.7
5	10	2	34	35.3	3.6
5	10	1	35	35.3	0.7
5	10	0.4	35.2	35.3	0.2
6	7	10	60	62.5	4.
6	7	5	60	62.5	4.
6	7	2	62	62.5	0.8
6	7	1	62	62.5	0.8
6	7	0.4	62.4	62.5	0.2
6	9	10	40	46.1	13.2
6	9	5	45	46.1	2.3
6	9	2	46	46.1	0.1
6	9	1	46	46.1	0.1
6	9	0.4	46.	46.1	0.1

examine the reduction of calculation errors with the increase of the algorithm resolution. We notice that resolutions of one degree (1°) and below appear adequate for a satisfactory approximation of the source dimensions. For our calculations, however, we decided to adopt a 0.4-degree resolution for more accurate results, even in complicated and perplexing cases. We mark, nonetheless, that the algorithm resolution can easily be changed if the need arises for increased accuracy of results.

5.3.2. Results: Disk images and radiation forces

We continue further on and discuss the results and conclusions generated by a multitude of `Infinity` code executions. Using this program, we have run many thousands of calculations over the years of our work. The latest and most complete version was used for the procurement of results about the radiation forces and accretion disk dynamics for more than 10,000 executions, the majority of which are discussed here (see Table 5). For these calculations, we considered the disk models "Slab" (Sect. 4.2c), "Wedge" (Sect. 4.2d), "Torus" (Sect. 4.2e), "ORST" (Sect. 4.2f), "LFM" (Sect. 4.3d), and "PD" (Sect. 4.3b), as can be seen in Figure 5.12.

These executions are for various target locations in each of the systems. These can be in the configuration's interior ($r < r_{inner}$) or exterior sectors ($r > r_{outer}$), on the surface of the accretion disk or away from it, inside the system outflow regions or scattered in the halo. Observers are thus

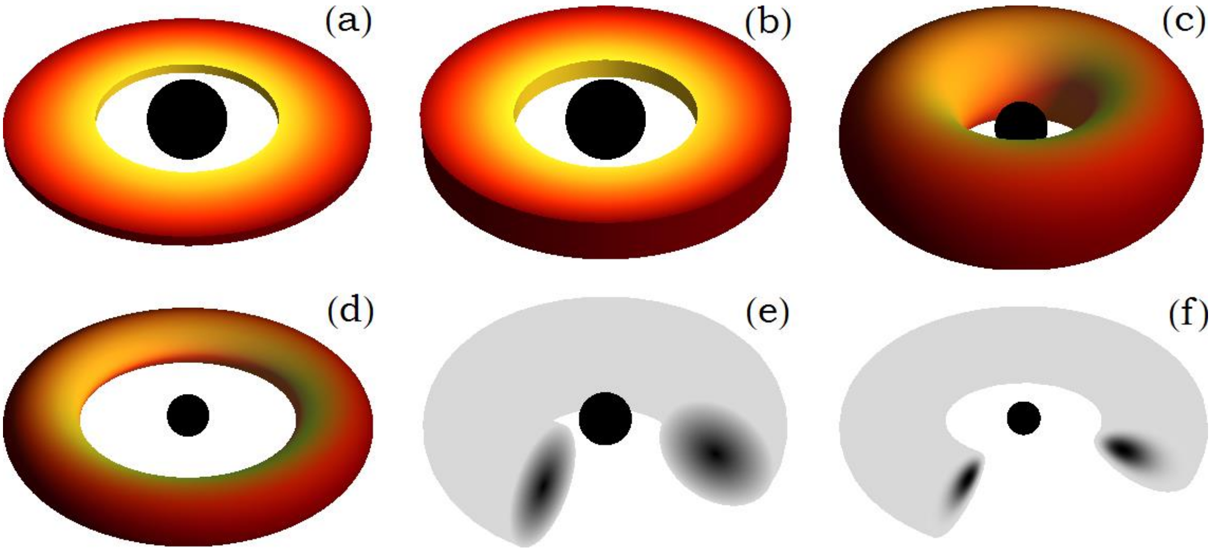

Figure 5.12: Accretion disks for which we studied the radiation field. Disks (*a*)-(*d*) are optically thick, with temperatures higher for sections closer to the central black hole (Sect. 4.2c-f). Disks (*e*) and (*f*) are semi-opaque, with higher density toward their material center (Sect. 4.3d, b). Namely, the darker the material color in the cross sections appears, the higher the density in that point is. We can notice that the density increase in (*e*) in smoother than in (*f*).

spread throughout the entire volume of the configurations and record the incoming radiation and the respective force. Each of these execution targets can be seen as colored dots or triangles in Figures 5.14 and 5.15, and Figures 2-7 of the online material [7]. More information on the selected accretion disk characteristics can also be found in the online material[7].

The depiction of the accretion disk and the emitted radiation as recorded by the assorted observers scattered throughout the system is an automated process that has been embedded into the algorithm. For example, we can survey Figure 5.13 and examine Mollweide projection sky maps for the frequency-integrated specific intensity documented for various locations and inclinations for all the disk models discussed earlier. The disk models displayed are the same models mentioned in Table 5.

We continue on to investigate Figures 5.14 and 5.15 that reveal plots for the Boyer – Lindquist radiation force magnitude by our algorithms. In these plots, we show results for two of the accretion disk models in Schwarzschild spacetime. A multitude of additional high-resolution results concerning the radiation four-forces for all the assorted disk models, spin parameters, and coordinate systems can be found in the online database[7].

Let us now explain what we see in the aforesaid figures and discuss the implications that are brought upon. In these force density plots, we encounter positive (magenta, orange) and negative (blue, green) radiation force magnitudes with the color legend seen to the right of each plot. Each color scale is set in such a way that the darker the plot hue is at a point, the higher the force absolute value is. Zero radiation force magnitudes hence always correspond to white color in all scales. Furthermore, in order to make the density plot reading easier and faster, we have included markers to clarify the magnitude sign in ambiguous situations. Consequently, we use red filled "up" arrows to signify a positive force and blue or green empty "down" arrows to signify a negative force value. The markers act in the same manner as the density plot diffuse colors and assist in the sign distinction in

BH	Disk model					
spin	slab	wedge	torus	ORST	LFM	PD
0	168	170	163	184	496	454
0.5	182	177	176	188	478	484
0.9	156	158	148	179	424	488
0.998	-	-	-	191	414	488
Sums	506	505	487	742	1812	1914
Total number of runs: 5966						

Table 5: Numbers of `Infinity` executions per spin and disk model.

Notes: The first four models are opaque and are discussed earlier. The "Slab" can be found in Sect. 4.2c, "Wedge" in Sect. 4.2d, "Torus" in Sect. 4.2e and "ORST" in Sect. 4.2f. The latter two models are quasi-opaque and were also described earlier. "LFM" can be found in Sect. 4.3d and "PD" in Sect. 4.3b. (Any results can be made available upon request.)

---

[7] *Link URL:* https://gitlab.com/leelamichaels/dissertation-online-material

areas where the force magnitude approaches zero and thus the diffuse colors approach white. Moreover, in some plots we encounter black empty circle markers that are used to represent force values exactly equal to zero. These markers are for the most part utilized in verification circumstances, such as stationary observers in the ZAMO frame. In addition to the above, we can also find large gray dot markers. These signify null force values in the system due to disk model or spacetime restrictions (e.g., static limit). We lastly clarify that each one of these markers stands for the output of one full

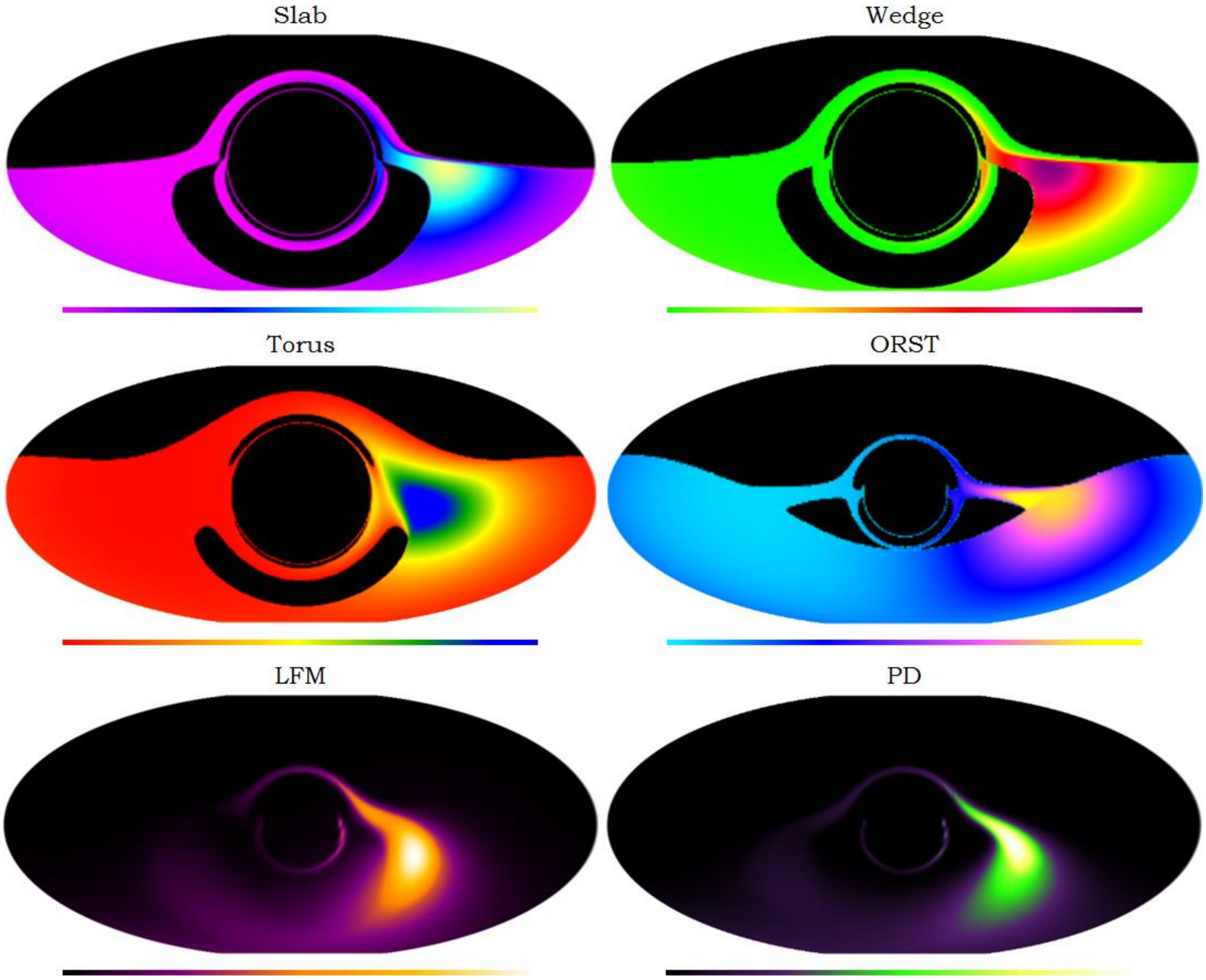

Figure 5.13: Frequency-integrated specific intensity I sky maps in Mollweide projection of the various accretion disk models considered. "Slab" is in Sect. 4.2c, "Wedge" in Sect. 4.2d, "Torus" in Sect. 4.2e, "ORST" in Sect. 4.2f, "LFM" in Sect. 4.3d and "PD" in Sect. 4.3b. *Below* each of the figures, we have the color legend used, displayed from minimum to maximum. The circle of light appearing in the *center* of the images is an Einstein, Khvolson[8] or "echo" ring[9]. It is generated by photons from the source crossing the system above and below the event horizon or the disk plane and then reaching the observer. The asymmetry noticed between the left and right halves of each figure is caused by the rotation of the accretion disk and the emitting material. This means that radiation emitted by matter moving toward the recording observer will be boosted and radiation emitted by receding material will be deboosted.

`Infinity` execution. We also note that in some of the results provided, we have implemented the enhancement process discussed earlier in Section 5.3.1 and Figure 5.9, in order to increase the code resolution by 25 times. We keep in mind though, that this resolution enhancement can also be increased to higher numbers, be applied recursively or even bypassed completely.

We now carry on to the detailed examination of Figures 5.14 and 5.15, and the revealing results they provide. In Figure 5.14, we encounter an analysis for the semi-opaque LFM disk model (Sect. 4.3d) and in Figure 5.15 for the opaque ORST model (Sect. 4.2f). Both figures display density plots for radiation four-force component magnitudes in a Schwarzschild spacetime and in Boyer – Lindquist coordinates. The forces displayed in the plots are measured in dynes $(1dyn = 1g \cdot cm/s^2 = 10^{-5} N)$. The magnitudes are looked upon for various areas of the systems, such as further in the disk's inner edge and further out the disk's outer edge, in the equatorial plane and farther away from it and, if possible, through the material of the disk. Each

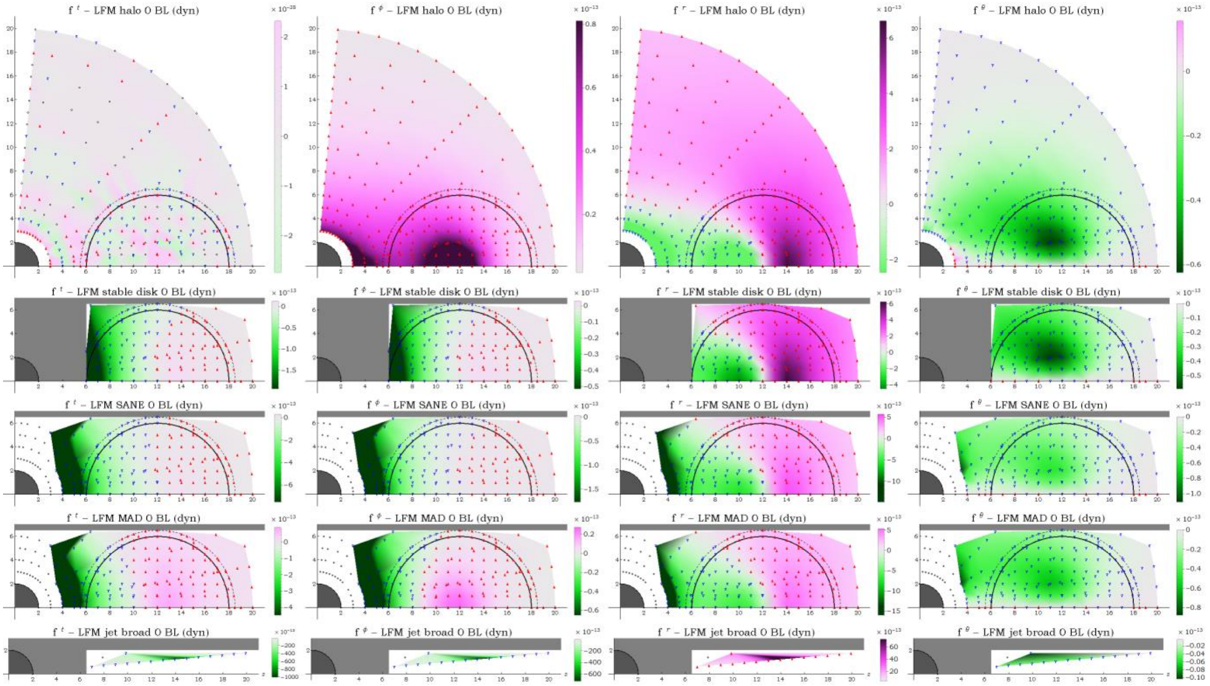

Figure 5.14: Radiation forces in dynes exerted on an electron for the LFM semi-opaque disk model (Sect. 4.3d) for a Schwarzschild black hole $(a = 0)$ in Boyer – Lindquist coordinates. Axes use geometrized units and the numbers shown are measured in M. The *first line* (axes $x - z$) gives the radiation force applied onto particles at rest in the local rest frame (Eq. (2.1.15)). The *second line* (axes $x - z$) shows forces exerted on particles in circular motion (Eq. (2.2.13)) in the applicable spacetime area. The *third* and *fourth line* (axes $x - z$) display the radiation force applied onto targets moving with SANE and MAD velocity profiles approximation. The *fifth line* (axes $z - x$) demonstrates the radiation force measured in the system outflow regions. More spin parameter values, disk models and coordinate systems can be found in the online material [5].

of the lines in these groups of plots refers to one of the various observers mentioned and discussed earlier (see Sect. 5.3.1 and Fig. 5.10). In the first line of each plot group, we have “halo” observers. This means that the target particle is simply moving along with the spacetime rotation ω (Eq. (2.1.15)). The second row, referred to as “stable disk”, pertains to targets in circular orbits moving with Ω (Eq. (2.2.13) or Eq. (4.2.19)). The third line follows the velocity profiles of SANE disks and the fourth line of MAD disks (see Narayan et al. 2003 and 2012, Penna et al. 2013a). The aforementioned four lines are typical poloidal plots with the horizontal axis measuring the cylindrical distance ϖ from the system rotation axis z. The vertical axis measures the height z from the equatorial plane, which is additionally a symmetry plane for the system and in the vast majority of cases, the accretion disk as well. The fifth line, “jet”, studies radiation forces in the system outflow regions. Namely, target particles there have an additional radial outflow velocity component pointing outward. The plots here have a horizontal axis z measuring the height in the equatorial plane and a vertical axis ϖ measuring the cylindrical distance from the rotation axis. The four columns of plots refer to the assorted components of the four-force vector in the $t-$, $\phi-$, $r-$, and $\theta-$direction.

When we review the force density plots presented, we notice that the plots have different and not matching color legends. This is because the various models are dissimilar, as are the radiation forces recorded in their environments. This means that they cannot be measured in the same scale,

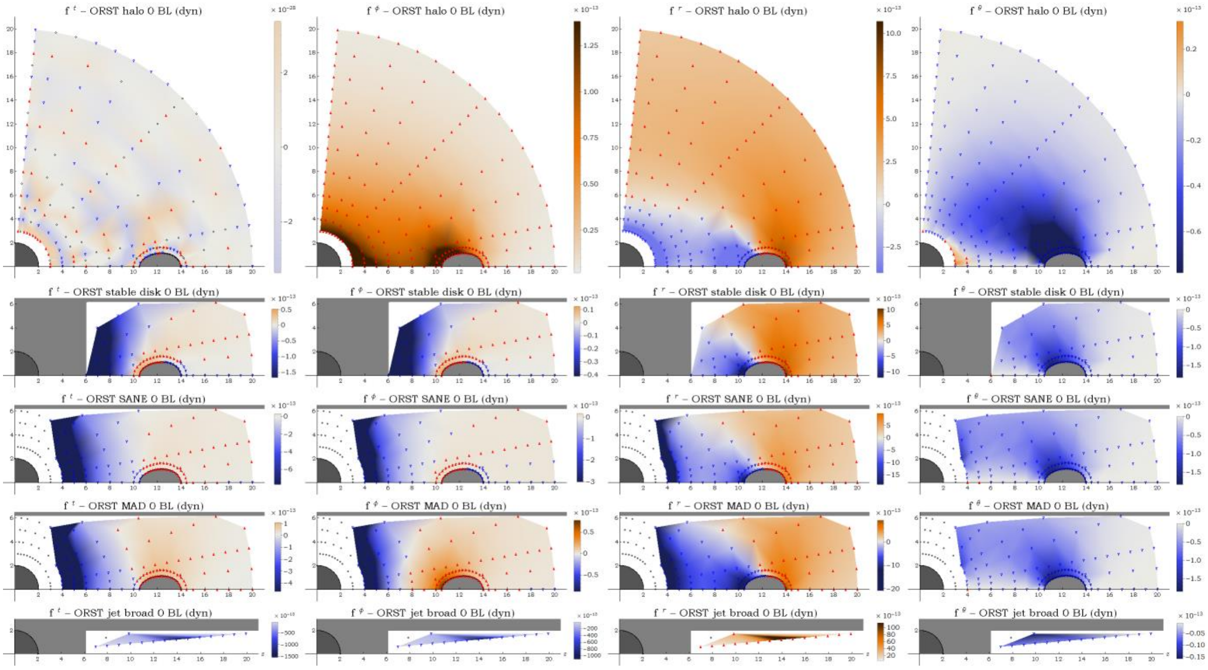

Figure 5.15: Radiation forces in dynes exerted on an electron for the ORST opaque disk model (Sect. 4.2f) for a Schwarzschild black hole ($a = 0$) in Boyer – Lindquist coordinates. Plots displayed in the same manner as explained for Figure 5.14. More spin parameter values, disk models and coordinate systems can be found in the online material [5].

as the divergences and disparities would be obscured, especially for milder models. In general, most of the results revealed by the assorted force density plots are, qualitatively at least, expected. However, there are also some outcomes that are unforeseen and require further and more thorough investigation.

The first observation of the density plots worth mentioning is the peculiar, perhaps, halo f^t plot (first line, first column). This figure seems irregular and could indicate, for example, execution errors but is on the contrary a source of invaluable information for the algorithm and the machine reliability. Considering the physics of the system and the experiment, the f^t component should be equal to zero. Therefore, the code result deviations from zero provide us with an estimation of the numerical and the computational errors developing during the code execution. This allows us to establish that the emerging errors $\leq 10^{-26}\,dyn$ are adequately below the radiation forces we are attempting to calculate and are thus within acceptable limits.

We move forward and examine the first column of density plots. These plots carry information about the energy absorption quantity and rate. The graphs agree with the expected results, as we mark stronger energy transfer when we move closer to the compact object and thus more energetic and perturbed environments. There, we have emitters and absorbers moving faster, with the relativistic effects, such as beaming, becoming more prominent and dominant. We additionally note that in these areas, we are outside the disk material and constantly departing further away from radiation isotropy and hence we expect increasing radiation forces. The above remarks lead a priori to the expectation of such radiation force behavior due to the stronger Poynting – Robertson braking. We thus do note the anticipated braking force magnitude increase as we move inward, approach the disk’s inner edge, surpass it, and then progress closer to the event horizon.

The opposite process from the above occurs, nonetheless, when we move farther out from the disk’s inner edge. The absorption of radiation becomes more isotropic and thus the Poynting – Robertson drag gets effortlessly obscured. This procedure is also further amplified by the relativistic beaming of the radiation emitted by the hot material moving inside the disk that provides acceleration to the target. If we continue moving outward and approach the disk’s outer edge, we note the gradual decrease of accelerating forces, and when crossing the disk’s outer edge and proceed in the interstellar region its eventual extinction. Overall, we detect robust braking forces $f^t < 0$ in regions with $\varpi \lesssim r_{inner}$ and closer toward the rotation axis. For larger cylindrical distances from the rotation axis $\varpi \gtrsim r_{inner}$, we accordingly notice the radiation force first disappearing and then turning positive $f^t > 0$. The positive force magnitude, nevertheless, in the majority of cases remains smaller than the negative force absolute value. This force behavior holds both for the opaque and for the semi-opaque disk models. For the semi-opaque disks, however, the force magnitudes are somewhat smaller and the zero force surfaces move slightly toward the system exterior.

This event is, nonetheless, expected due to the necessary accumulation of optical depth values required for the procedure to occur.

We go on to examine the second column of density plots that refer to the azimuthal radiation force f^{ϕ}. This component follows the pattern of the previous f^{t} component in the qualitative characteristics and the distribution. Therefore, in the inner regions of the systems, where $\varpi \lesssim r_{inner}$, the radiation force is braking, namely $f^{\phi} < 0$. As the cylindrical distance increases with $\varpi \gtrsim r_{inner}$, the azimuthal force first disappears and later on turns positive $f^{\phi} > 0$. Subsequently, proceeding further outward and departing the system, we again note the radiation force decrease and its consequent fading away.

We would also like to discuss at this point a particular volume of space detected in systems with optically thick accretion disks. In such configurations, we notice the presence of an additional "obscured" or "shadow" area around the disk (Fig. 5.16). These regions are similar to shadows behind planets and are located outside the disk's outer edge, up to a small or medium height from the equatorial plane. In these regions the intervening opaque material covers part of the absorbing targets' local sky, largely prohibiting the influx of rays originating from the brighter interior regions and the entire opposite segment of the disk. This results in a noticeable decrease of radiation absorption and the resurfacing of the Poynting – Robertson effect. This fact, in combination with the substantial incoming light anisotropy then leads to a braking azimuthal radiation force anew.

We proceed next, to the examination of the third column of density plots. This column displays the radial components of the radiation force f^{r}. The algorithm outputs are again in qualitative agreement with the expected outcome. What we observe is that for absorbing targets closer to the event horizon the radial radiation force reaches its maximum negative value. This $f^{r}_{inner} < 0$ is anticipated since in these circumstances the target records an increased quantity of light reaching it from the exterior half of its local sky and a greatly diminished amount reaching it from the interior half. The radiation reaching the target in the interior hemisphere of the local sky

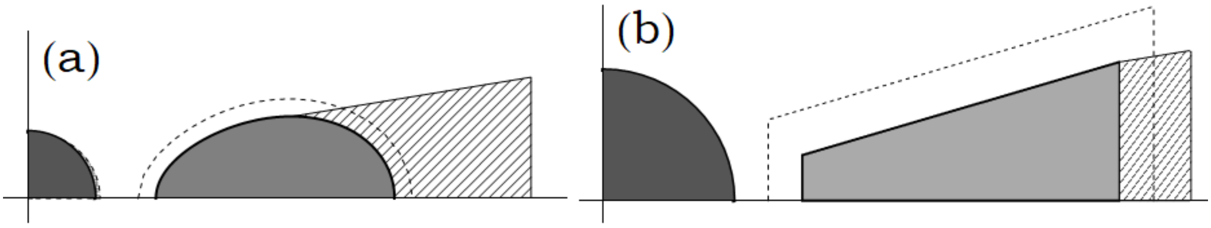

Figure 5.16: Accretion disk "shadows". We see in stripes the partially shielded areas next to the accretion disk material because of its total optical thickness. The material opacity blocks incoming radiation from reaching observers in these regions and hence makes the Poynting – Robertson drag effect more prominent.

comes from the opposite side of the disk, going around the event horizon obstacle. Hence, the more the target approaches the horizon, the greater the optical coverage of its interior local sky gets and the stronger it is pushed inward by the radiation. Conversely, when the target is situated farther outward than the disk's radiation center, the majority of the light reaching it comes from the interior hemisphere of the local sky. Thus, the radiation resultant is positive, $f^{r}_{outer} > 0$, and points radially outward, pushing the target particle toward interstellar space.

We continue on to inspect the poloidal radiation forces recorded for the $\theta-$direction in the forth column and interpret their significance. We should mention here for clarity that the poloidal angle θ is measured in the typical way. It starts from a value $\theta = 0$ on the positive $z-$axis, reaches $\theta = \pi/2$ for the equatorial $x-y$ plane and is maximized at $\theta = \pi$ for the negative $z-$axis. We start by considering the selected spacetime and configuration symmetries. Namely, we first know that the equatorial level is a symmetry plane for the system. This means that the poloidal radiation force must disappear in the equatorial plane and our numerical results reveal that indeed it does. Additionally, we recall that the rotation axis $z'z$ is a spacetime rotational symmetry. This means that we also expect the poloidal radiation force to vanish along the vertical rotation axis, a fact that is also observed in our results.

For the poloidal force sign, we observe it to be negative, $f^{\theta} \leq 0$, in the vast majority of observers situated above the equatorial plane. This is also an anticipated effect, since the poloidal radiation emitted by the disk material is expected to push the targets above it toward the system rotation axis Oz. Respectively, the same but reflective procedure occurs beneath the equatorial plane, where the radiation propels the material away from the disk and toward the negative $z-$axis. In the very few situations where we observe a positive force sign, a more attentive look is required. These events are observed to take place in close proximity to the event horizon and at a small height above the equatorial plane. Due to their special positions, the targets there have a very particular local sky view. Firstly, due to their small height they record a more or less symmetric view between the top and bottom hemispheres of the sky and therefore the total poloidal force, proportional to the radiation flux, is extremely small. The most critical element in this uncommon case is the fact that these targets observe in their sky a quite unfilled scenery governed by a strong and very eminent Einstein, Khvolson[8], or "echo" ring[9] (see also Sauer 2008). Additionally, this ring, due to the target's location, appears very far away from the equatorial plane, near the local zenith and nadir points, further enhancing the differences. In conjunction with this event, we note that since the particle is situated in the upper hemisphere, it receives measurably more radiation coming from the top than from the bottom, both coming from the opposite side of the disk. This further intensifies the poloidal force effects and the final combination of all the aforementioned situations results in the observed net force pointing toward the equatorial plane, namely $f^{\theta} > 0$. Again, the reflectively symmetric procedure is registered when analyzing the exact same phenomenon in the hemisphere below the equatorial plane. The radiation forces there are almost everywhere positive, $f^{\theta} \geq 0$, pushing matter toward the Oz' semi-axis, apart from a small group of points recording $f^{\theta} < 0$, governed by the echo ring.

We proceed to review the radiation effects encountered in the system outflow regions (fifth line in each plot group) and assess their significance. In such areas, we assume the existence of a directed outflow or a jet with material moving outward and away from the black hole. In these regions we can assume one, two, or more velocity profiles with smaller, larger, or even opposite magnitude (see e.g., Asada & Nakamura 2012, Nakamura & Asada 2013, Asada et al. 2016, Nakamura et al. 2018, Park et al. 2019). We thus look into the reverberations of light interactions with the outflowing material as it gradually moves into less curved and more classical flat spacetime. One of the first things we notice is that the radial force component is always positive $f_{jet}^{r} > 0$. This is in agreement with our expectations, since as the material flows outward the emitting matter is situated below it and emits light that hits the targets from behind as they move outward, providing them thus with acceleration and further pushing them away from the disk and the system. Examining now the poloidal $\theta-$direction force, we note again the same principles as before, $f_{jet}^{\theta} < 0$ for the upper hemisphere and $f_{jet}^{\theta} > 0$ for the lower hemisphere. That is to say, that as the emitting source is below the receiving targets, the emitted radiation tends to push the material toward the rotation axis zz'. For the remaining two directions t and ϕ, we again note them assenting with each other and appearing negative, $f_{jet}^{t} < 0$ and $f_{jet}^{\phi} < 0$. For the azimuthal $\phi-$direction, as well as for the $t-$direction, we note again the radiation source being highly anisotropic and incoming in angles close to $90°$. Therefore, we register again the enhancement of the Poynting – Robertson effect and the application of a drag force.

A relevant, but dissimilar enough, situation can also be observed in comparable configurations. The key difference for such situations is that the outflow region is not filled with particles or particulates, but instead contains blobs of matter that can also simultaneously emit radiation of their own. This setup is not in the least far-fetched or unnatural, since it is expected to be the standard situation of jets and outflows. In such

---

[8] *An Einstein, Khvolson, or echo ring is created by photons from the hot disk traveling near the compact object and reaching the observer. Because of the black hole – accretion disk setup studied here, the relative locations of the configuration members causes the gravitational lensing occurring in the system to create a complete ring of light, produced by the accretion disk's upper and lower parts.*

[9] *We choose to refer to this ring as an "echo" due to its affinity to the light echo phenomenon. This phenomenon is similar to the typical sound echo, but involves radiation instead of sound. We should also note here that the typical light echo phenomenon is more frequently observed along with nova and supernova events (e.g., V838 Monocerotis 2002 outburst) than with black holes (e.g., V404 Cygni 2015 outburst).*

situations, we anticipate somewhat differentiated results because of the additional radiation emitting, even though small enough, sources. We thus expect more entangled situations with the outflowing material due to the presence of emitting matter moving with similar velocities before, after, and adjacent to receiving targets.

The force density plots we show here (Figs. 5.14 and 5.15) and in the online material [7] provide a large quantity of information. This information includes, first of all, the sign and the magnitude of the radiation forces for all the spacetime components. Second, and perhaps most important, they reveal the spatial distribution of forces, their geometry, their minima and maxima locations, and the entire distributions of the radiation field generated by each model of accretion disk and velocity profile. Additionally, they unveil various differences between the models and the repercussions they could have on the system structure, equilibrium, and dynamics. Furthermore, the density plots exhibit the smoother and most turbulent field areas, which often provide crucial information about the system dynamics. Moreover, they divulge the existence and location of zero force areas, turning points if you will, where in a relatively narrow transition zone, the force reduces in magnitude, vanishes, and then reappears as force of the opposite sign, causing accelerations of the opposite sign. We can also use these plots in order to investigate how the increase of the black hole spin affects and changes the locations, widths, and smoothness of these sectors. In addition, we can examine explicitly the various force components and see if some of them display significant magnitudes or characteristics that would influence the disk stability and affect its evolution. For instance, we can investigate if the observed positive and negative azimuthal forces recorded can have an actual effect influencing the disk material rotation.

The force density plots discussed up to this point are very useful for the geometry and the allocation of the radiation forces. However, in order to better estimate the force magnitudes and compare the force dynamics in the various disk models, a more convenient method is to create and investigate the appropriate sets of histograms comparing the above. We can thus peer into Figure 5.17 and the online material [7], and compare the force magnitudes in the assorted disk models and velocity profiles. Some of the phenomenon aspects we can examine and draw valuable conclusions about are the disk's volume in comparison to its optical thickness, its maximum height from the equatorial plane, its inner and average distance from the compact object, its rotational speed profile, and other intriguing facets.

One of the first conclusions drawn by examining the histograms is that the Torus model is generally marked producing the largest radiation forces onto the material in many of the system regions and velocity profiles. This is not unanticipated since the Torus is the most voluminous, borderline opaque accretion disk studied here. Following Torus, the next models in radiation force magnitudes are Wedge and then Slab, both of which are also opaque. The Wedge model has notably smaller vertical height than Torus and hence, as expected, generates smaller radiation forces than that. Afterward, we note the radiation forces exerted by the Slab disk model material that closely follow Wedge. The Slab disk is similar to Wedge but possesses an even smaller vertical height and a null inclination, compared to the equatorial level. We thus expect the recorded forces to be comparable to Wedge and perhaps somewhat smaller and indeed we mark so. In particular, the disparity between these two models is the different inclination of their topmost and lowermost surfaces. Because of their structural closeness, these two setups demonstrate radiation component magnitudes in proximity to each other and repeatedly interweaving. In general, nevertheless, radiation forces in Wedge tend to be somewhat stronger than those in the Slab model. However, the constructional vicinity of the two arrangements allows us to examine the radiation ramifications and

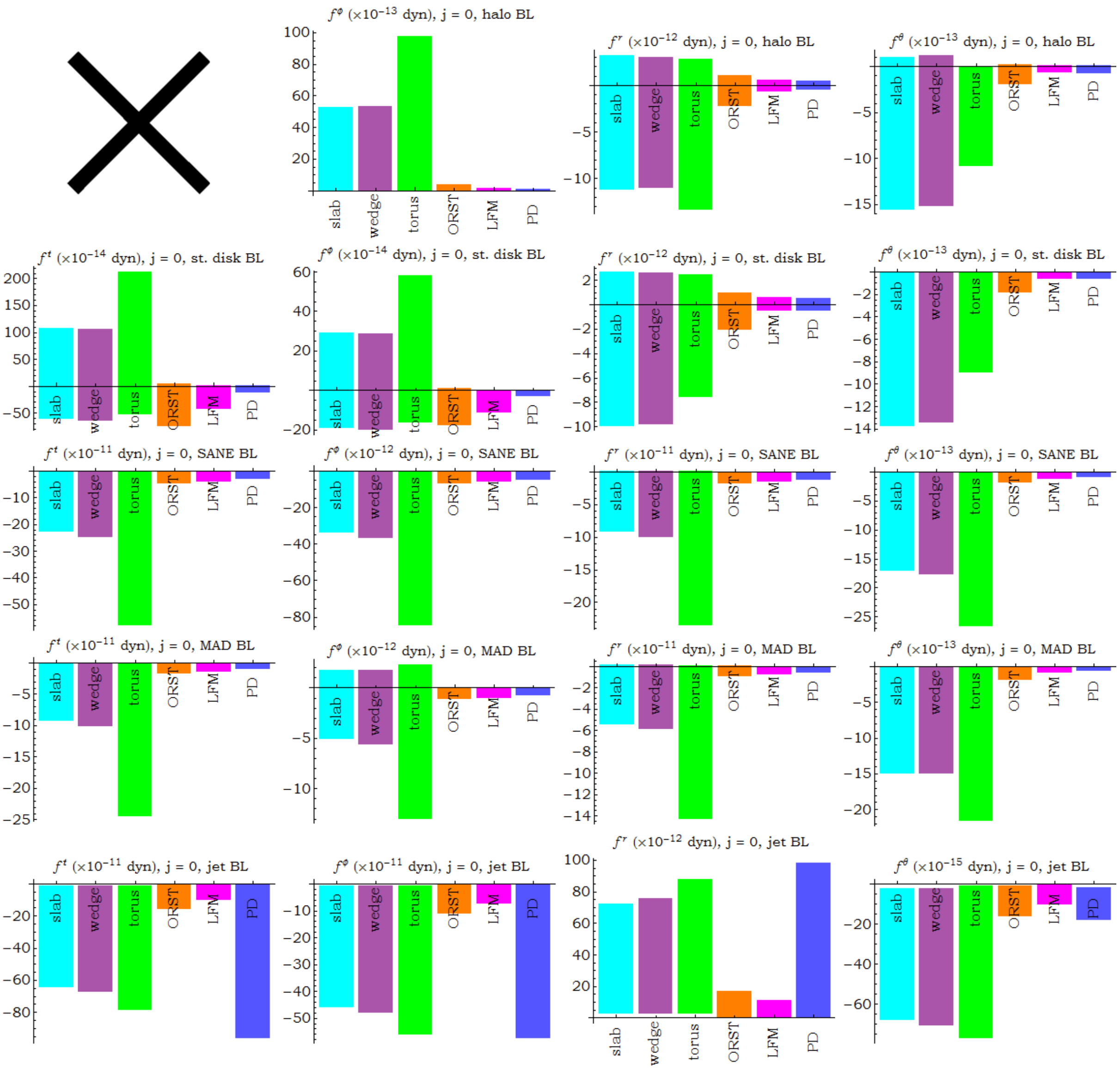

Figure 5.17: Comparative histograms of the radiation force components exerted on electrons for all disk models and velocity profiles for $a=0$. The disk models are described in Chapter 4: "*Slab*" in Sect. 4.2c, "*Wedge*" in Sect. 4.2d, "*Torus*" in Sect. 4.2e, "*ORST*" in Sect. 4.2f., "*LFM*" in Sect. 4.3d and "*PD*" in Sect. 4.3b. The halo $t-$force plot (*top left*) is not displayed since it only gives information about computational errors. Other spins and coordinate systems can be found in the online material[5].

repercussions in the distinct characteristics and components of each model. One such area of particular interest is the polar axis area and the outflow region, where for example we expect the Wedge to display stronger poloidal forces due to its better inclinational profile.

Further on, we encounter the next disk in radiation force magnitude generated, the ORST, the opaque rotationally supported torus. These disks display large differentiations among them as the black hole spin increases, something that is more or less expected. Namely, for a spin of $a=0$ the resulting accretion disk is noticeably small, particularly when compared to the other setups. For $a=0.5M$ it attains a somewhat larger volume, yet remains smaller than its counterparts. Then finally, for spins $a=0.9M$ and $a=0.998M$ its volume is of the same extent as the rest of the models and perhaps larger. Even though, however, the disk's size and shape changes drastically with the spin, its radiation density peak region remains in the same area and only moves by a very small amount outward. Moreover, we may notice the ORST disk featuring some noteworthy radiation force characteristics that were quite unexpected. For example, these include the large force magnitudes in halo and jet targets in spin $a=0.5M$, as well as the stable disk and outflow regions for spin $a=0.9M$ and the majority of spin $a=0.998M$ areas. After some study, the results point to the specific geometrical characteristics and outer surface inclination angles to be the most important factor responsible for these stronger forces. In addition to the above, it is worth discussing the notably strong forces recorded for $a=0.998M$ by the ORST generated field. This situation is only toppled for material moving with the stable disk velocity profile, where the LFM model prevails in force magnitude due to its geometrical arrangement that compels the material to move closer to the event horizon and thus faster.

Continuing on, we encounter the semi-opaque disk models that in general demonstrate softer radiation fields. First, we have the semi-opaque radiation pressure supported polish doughnut model PD. Accretion disks of this type prove to be very potent in exerting strong radiation forces in the outflow regions, as can be seen in the result histograms. The PDs along with the ORST disks are documented to exert by far higher outflow region forces on outgoing material than the rest of the models. Extending the discussion from above, we note that for smaller spins a the PD prevails over the rest of the models on radiation force magnitude. As the central black hole spins increase, however, ORST inflates and keeps becoming continuously larger. This finally results in ORST becoming more voluminous and eventually more radiantly effective than PD. This is a very significant topic for further research, since it sheds light onto the enigmatic polar and outflow regions. We can examine hence how this radiation interacts and affects the material and its movement, the energy distribution and diffusion, and perhaps most importantly its contribution onto the outflow collimating forces.

Finally, after the polish doughnut PD, we have the semi-opaque LFM disk. This model also generates a soft radiation field but additionally marks noteworthy differentiations from PD. We should also remember here that this disk is of the same volume and geometrical profile as the Torus, but instead of opaque it is quasi-opaque. We can therefore use these two models and the comparisons between them to draw valuable conclusions about the reverberations of disk opacity gradients and material stratification. That is to say, that although the two models include an accretion torus of exactly the same size, the LFM displays a far weaker radiation field produced, even though it possesses adequate optical depth buildup. Respectively, the radiation field created by markedly smaller opaque disk models, such as ORST, often appears stronger than the field generated by LFM. We could hence experiment with different values of the density gradient and investigate on the resulting radiation fields. In this fashion, we could also examine if the stronger generated fields are gradually constructed by increasing this gradient or if these stronger circumstances can only be achieved with a totally opaque disk of practically infinite optical depth. Subsequently, we may juxtapose the LFM disk (smaller density gradient) with PD (larger density gradient). We thus see that even though LFM occupies a larger relative area of space than PD, it registers far lower forces than PD, a fact that also points toward the dominant role of the density gradient instead of the disk volume. If we therefore combine the above observations, it appears that indeed the primary factor regulating the radiation field strength is not the emitting material volume but the density increase rate.

We conclude this Section by discussing some mentionable conclusions from our experiments that pertain to all the disk models and the physics of the study itself. Firstly, we should state and explain here positively that the exerted radiation forces may perhaps appear small or negligible, but in reality, they are far from it. This happens because these radiation forces are being primarily exerted on the material electrons, since $f_e/f_p \sim \left(m_p/m_e\right)^2$. This then is precisely the reason why the Poynting – Robertson effect in its original form is also called a “drag”; the radiation is gradually decelerating the moving electrons since they continuously lose energy. This consequently leads to the electrons spiraling inward toward the central mass. In our environment, nonetheless, depending on the exerted radiation, these forces may also be accelerating, providing the electrons with energy and causing them to be flung outward. In both cases, the radiation absorption by the disk electrons results in a charge separation tendency between the material components. This charge separation, nonetheless, does not occur as the disk material holds its place due to enhanced electric and magnetic processes. These processes force the disk protons or ions to infall into lower orbits or to be launched into higher orbits following the electrons. The final, episodic perhaps, outcome is smaller or larger portions of the disk material to infall onto the central mass or be flung outward.

A very interesting and noteworthy procedure also takes place due to the aforementioned process of electron motion destabilization. This is none other than the Poynting – Robertson Cosmic Battery mechanism (Contopoulos & Kazanas 1998, Kylafis et al. 2012) we mentioned earlier. Since the matter electrons change their orbit radius and angular velocity, we have the generation of a ring electric current inside the disk material itself. The most affected areas by this phenomenon are the disk’s inner and outer edges, since there the radiation field is further away from uniformity, making the Poynting – Robertson effect more prominent. The outcome hence is the steady generation of poloidal magnetic field loops in the system, particularly in its inner edge, where the deceleration and the related processes are stronger. Under these circumstances, some parts of the disk material bring one polarity of the magnetic loops inward as they infall and let the opposite polarity escape outward. This process is principally regulated by the material's magnetic Prandtl number $\mathcal{P}r_m$[10]. The growth and evolution of these loops continue on further assisted by the disk's differential rotation. This particular material motion results in the magnetic loops getting continuously more twisted and subsequently opening up. This process results thus in the gradual filling of the entire system with smaller field loops, as well as open field lines (e.g., see Contopoulos et al. 2006 and 2015b).

From the above analysis, we can see how the generation, growth, and evolution of the magnetic field created by radiation interactions in the vicinity of black holes and accretion disk systems is a very extensive and fruitful field of research. For instance, an important consequence of the described procedure is the collapse of standard expected notable orbits in such environments. Namely, the radii of common surfaces that refer to trajectories of charged particles in the system, such as the innermost stable circular orbit and the marginally bound orbits, are reconsidered and reevaluated due to the presence of magnetic fields (see e.g., Bini et al. 2011b, Contopoulos & Papadopoulos 2012). In addition to the aforementioned processes, we should also take into consideration the upcoming and unavoidable magnetic reconnection that occurs as the opposite magnetic loops continue expanding and approaching each other. These developments undoubtedly have significant implications on the energy allocation and flow in the systems, their stability, and their evolution.

Furthermore, a fact well worth an attentive examination are the forces recorded in the outflow regions and the ramifications they bring along. Our results provided some very useful information about the dynamics of these areas. Firstly, we noted the radiation field accelerating the material outward and slowly decelerating its rotation rate around the system axis. Additionally, we observed the disk thermal radiation exerting negative poloidal forces to outflowing targets. This event is noteworthy and merits more investigation because it reveals that the matter exerts noticeable magnitudes of collimating forces onto the outflowing material. This means that the disk's thermal radiation could contribute in some part to an early collimation of the outflowing matter.

Another notable fact can be discovered when looking meticulously into the radiation force density plots (Figs. 5.14, 5.15, and online database[7]). If we carefully inspect these plots, we notice that the zero force curves for the $t-$force are not situated at the same location as the zero force curves for the space $\phi-$, $r-$, and $\theta-$force components. This was certainly not a foreseen result and should perhaps be looked into elaborately, since such an event leads to the emergence of unexpected and at cases problematic three-force

---

[10] *The magnetic Prandtl number* $\mathcal{P}r_m$ *(dimensionless quantity) is set as the ratio of viscosity (viscous diffusion rate)* v *to magnetic diffusivity* η *:* $\mathcal{P}r_m = \mathrm{v}/\eta$ *.*

components exerted onto the disk material.

To conclude, we discuss our thoughts about the possible extensions that could be made to the `Infinity` algorithm, expanding its capabilities and its possible applications. First of all, we can broaden our setup and undertake radiation and energy experimentations on more complex systems or systems of multiple components. Namely, we could investigate the energy exchanges via radiation between the various components of multiple-star systems that may, or may not involve disks of material. These stars are not required to be main sequence or common stars, as atypical stellar objects can also be included (e.g., gas giants, protostars, brown or white dwarves, giants, supergiants, neutron stars, or black holes). For example, we can carefully explore the contributions and repercussions of the disk material radiation onto X-ray binary cycles and the consequent features of their hardness – intensity diagrams. In addition, following the relevant expansion of `Omega`, these studies can be performed outside the limits of General Relativity and instead be conducted in modified gravity situations.

Moreover, new and separate editions of the program can be written, in which electric and magnetic phenomena are studied in strong gravity environments instead of radiation related procedures. This is something that can prove to be very useful, particularly for the cases of ring currents and the charge separation we discussed earlier, since in such situations we have the consequent generation of expanding and dispersing poloidal magnetic field loops. The subsequent evolution of these loops then leads to the saturation of the space inside and further out the systems with infalling or escaping material, dragging along magnetic field loops with them. We thus have step-by-step the gradual construction of favorable grounds for magnetic reconnection episodes and hence the emergence of particle acceleration, newfound kinetic energy, thermal radiation emission, and more. Before closing the Section, we mark that we should also contemplate reconsidering and reevaluating the particle trajectories under the light of our observations about the new emerging fields that rearrange the radiation and magnetic fields and reestablish the environment dynamics and equilibria (see e.g., Bini et al. 2011b).

5.4. Code `Elysium`

(URL: https://gitlab.com/leelamichaels/Elysium)

5.4.1. The algorithm and capabilities

The `Elysium` code was first written in 2014. It has since had abundant updates and changes that allow for better and smoother applications. The current version is number 14 and in total it has had more than 85 editions. Its purpose is to create recording screens of pixels further away from the black hole and accretion disk systems, and record its findings as if it was taking pictures of these systems from "infinity".

The user first selects the desired accretion disk model from the list of provided setups (see Chapter 4), the black hole spin, the disk temperature profile, and the inclination ι. If the disk models do not cover the requested experiment specifications, it is readily possible to add supplementary arrangements to the code, such as Novikov – Thorne disks (Novikov & Thorne 1973), for example. Subsequently, the user chooses the desired resolution for the run and the code creates a screen with the corresponding amount of pixels. From each of those pixels, a light ray is emitted perpendicularly to the screen and travels toward the black hole and the accretion disk arrangement (Fig. 5.18). Depending on what the light ray

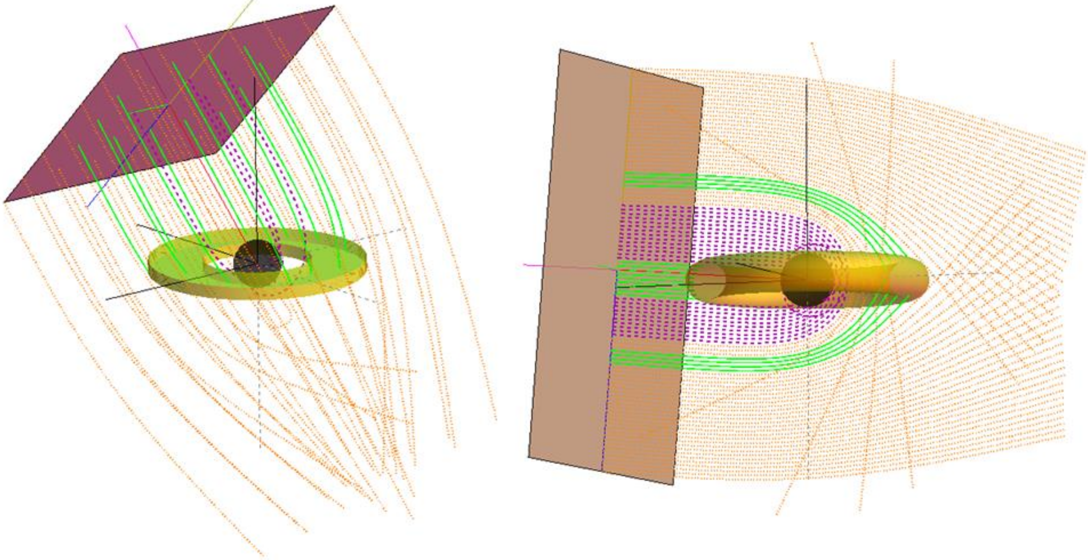

Figure 5.18: Workings of the `Elysium` code. On the *left* we have a run for a 7×7 pixels screen with $j=0.5$, at an inclination $45°$. On the *right* we see the central column pixels of a 100×100 screen with $j=0$ at inclination $85°$. Photon trajectories intersecting the accretion disk and hence contributing radiation energy are depicted with solid green lines. On the contrary, trajectories that end up in the event horizon are shown with purple dashed lines and trajectories originating from infinity with orange dotted lines. The latter two contribute no additional radiation or energy.

finds in its path, the code returns its possible origin, its path, and the radiation, if any, received. This way, generated photograph pictures of such arrangements can be produced allowing the further investigation of these composite configurations (Fig. 5.19).

This code appears similar to the aforementioned `Infinity` code, but is practically its complement. `Elysium` is, thus, positively different from `Infinity`, but possesses the same quantity and quality of options, capabilities, and output information standards. What differentiates the two programs is the point of view. The `Infinity` code begins from the single end point of multiple trajectories and integrates backward in time, tracing the rays' track through the system. In this manner, the algorithm investigates if the light path crosses any areas of radiation emission. On the other hand, `Elysium` has an assemblage of trajectory end points, the pixels of the screen. It then integrates and reconstructs the trajectories, seeking if light rays from any of the emitting components can reach the observer pixel. Each of the two algorithms has its advantages and disadvantages and depending on the nature of the research, the user can select which one of the two procedures is better suited for the management of the problem.

In this Section, we discuss `Elysium` and its results in order to reveal all the information that can be extracted from this imaging algorithm. The material assembled from the various execution subroutines convey valuable clues concerning the configuration under study. The list of information recovered includes, for example, the system's mass and its distribution, the angular momentum allotment and diffusion, an estimate of the central black hole spin (see also Sect. 5.5), and more.

We make the choice of working with `Elysium` in cases where the primary objective is the examination of the configuration as a whole, with no smaller scale physics taken into consideration. For instance, we can look into and compare this work with the studies presented in Fuerst & Wu 2004 and 2007, Wu et al. 2008a and 2008b, as well as Younsi et al. 2012 and Younsi 2014. Another example where we could apply `Elysium` is to investigate the equilibrium and evolution of black hole – accretion disk setups and compare with general relativistic magnetohydrodynamic simulations and results (see e.g., Event Horizon Telescope 2019b, 2019c, 2022a, 2022c). A further related utilization is a rapid construction of the expected results this category of simulations are expected to give earlier than the time consuming calculations are run and completed. A specific example of such an application of `Elysium` is the study of radiant hot material orbiting a black hole in close proximity. Such cases were looked into and investigated, for instance, in Broderick & Loeb 2005 and 2006a.

In addition to the above, we can construct the expected images of infinite or finite optical depth accretion disks around a compact object at various inclinations, equivalently to what is shown in Noble et al. 2007. Furthermore, we can study the radiation conditions and effects in various configurations, such as those considered in Mościbrodzka et al. 2009. Moreover, particular environments could be looked upon, such as radiatively inefficient accretion flows (RIAFs) and jet outflows, as examined for example in Mościbrodzka et al. 2014. Additionally, we can also assess notable and

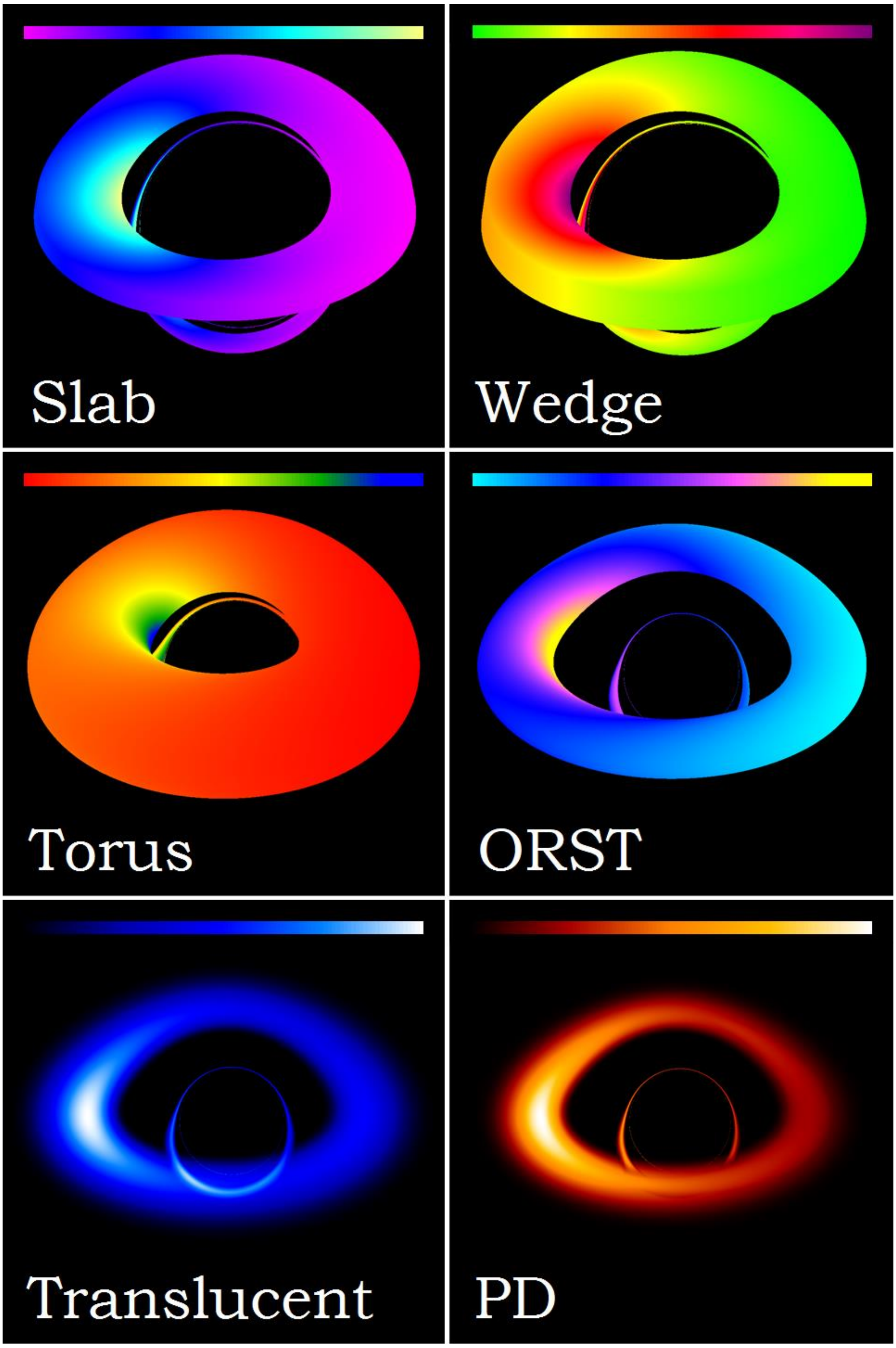

Figure 5.19: `Elysium` results: generated pictures of the frequency-integrated specific intensity of the radiation in different black hole – accretion disk systems. The disk models used are: *Slab* (opaque, Sect. 4.2c), *Wedge* (opaque, Sect. 4.2d), *Torus* (opaque, Sect. 4.2e), *ORST* (opaque, Sect. 4.2f), translucent Polish doughnut (semi-opaque, Sect. 4.3c) and Polish doughnut (semi-opaque, Sect. 4.3b). The radiation intensity color legends are shown above each image from minimum to maximum. The last row of figures is similar to those seen in Younsi et al. 2012.

uncommon situations, such as the anticipated imaging results of the Galactic center supermassive black hole and its outflows, discussed in Mościbrodzka et al. 2018. Another relevant study in combinations with observational data is hence presented in Event Horizon Telescope Collaboration 2019a, 2019b, 2019c, 2021a, 2021b, 2022a, 2022b, 2022c, 2022d.

Finally, we can use the `Elysium` code to establish finer testing procedures for the spacetime properties, structure, and metrics. Such an investigation is, for instance, the quality and the validity of the Kerr metric approximation, a method widely used in environments like the ones considered in this work. One such noteworthy research is Broderick & Loeb 2006b, which examines the legitimacy and structural stability of General Relativity in the vicinity of compact objects. Another relevant noteworthy study on the subject examining strong-field general relativity is Gralla et al. 2020. Additionally, one could also examine environments under modified gravity theories.

5.4.2. Results: Accretion disk & black hole generated pictures from infinity

We show here some of the results of high-resolution observation executions of various accretion disk models with different sizes, shapes, temperature profiles, and spins. In Figure 5.20, we show six images of an opaque Slab disk (Sect. 4.2c), in Figure 5.21 six images of an opaque ORST disk (Sect. 4.2f), in Figure 5.22 six images of a semi-opaque PD disk (Sect. 4.3b), and in Figure 5.23 six images of a translucent PD (Sect. 4.3c) of various spins j and inclinations ι. We can note that the program outputs are in agreement with relevant works, such as Fuerst & Wu 2007, Wu et al. 2008a, and Younsi et al. 2012. Additionally, if we look closely into Figure 5.22, we can easily notice clear limb darkening in the disk's outlining surfaces. Furthermore, in Figure 5.23, we can notice the transparency of the intervening disk material. From the aforementioned images, we can see that the `Elysium` code is, as designed, ideal in order to produce black hole and accretion disk images as seen from further away from the disk, or from "infinity".

When we examine the aforementioned figures, we must keep in mind that the black pixels observed in them do not necessarily signify the absence of material. This is because of the more natural form of the color legend used. That is to say, even in real photographs of such objects, low-density portions of material are not visible. A typical example of this situation can be noted for the outer layers of the disk material in Figures 5.22 - 5.23. In order to make this abundantly clear and reveal the actual volume covered by the accretion disk, we provide Figure 5.24. In that picture, we can see an `Elysium`-produced image of the same accretion disk – black hole system in natural colors and in pseudocolor, and observe the greatly revised disk volume.

This program, as said earlier, is optimal for generating observation-like images of systems in strong gravity environments. It, nonetheless, has

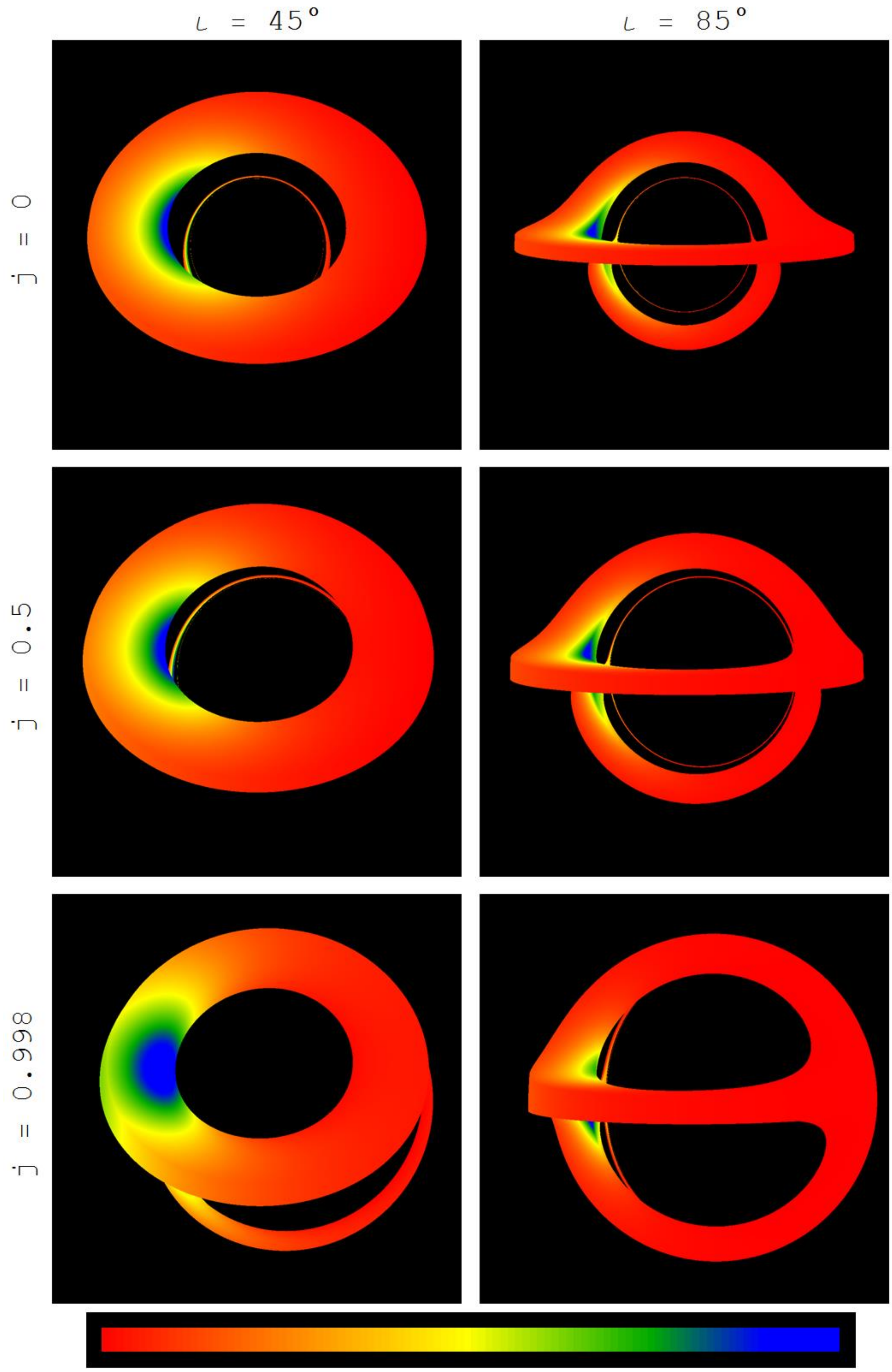

Figure 5.20: Frequency-integrated specific intensity for an opaque slab by `Elysium`. On the *left*, the disk is at a 45° and on *the right* at an 85° inclination. Each line has a different black hole spin parameter, from *top to bottom*: $j = 0$, $j = 0.5$, and $j = 0.998$. The color scheme legend is displayed at the bottom from minimum to maximum.

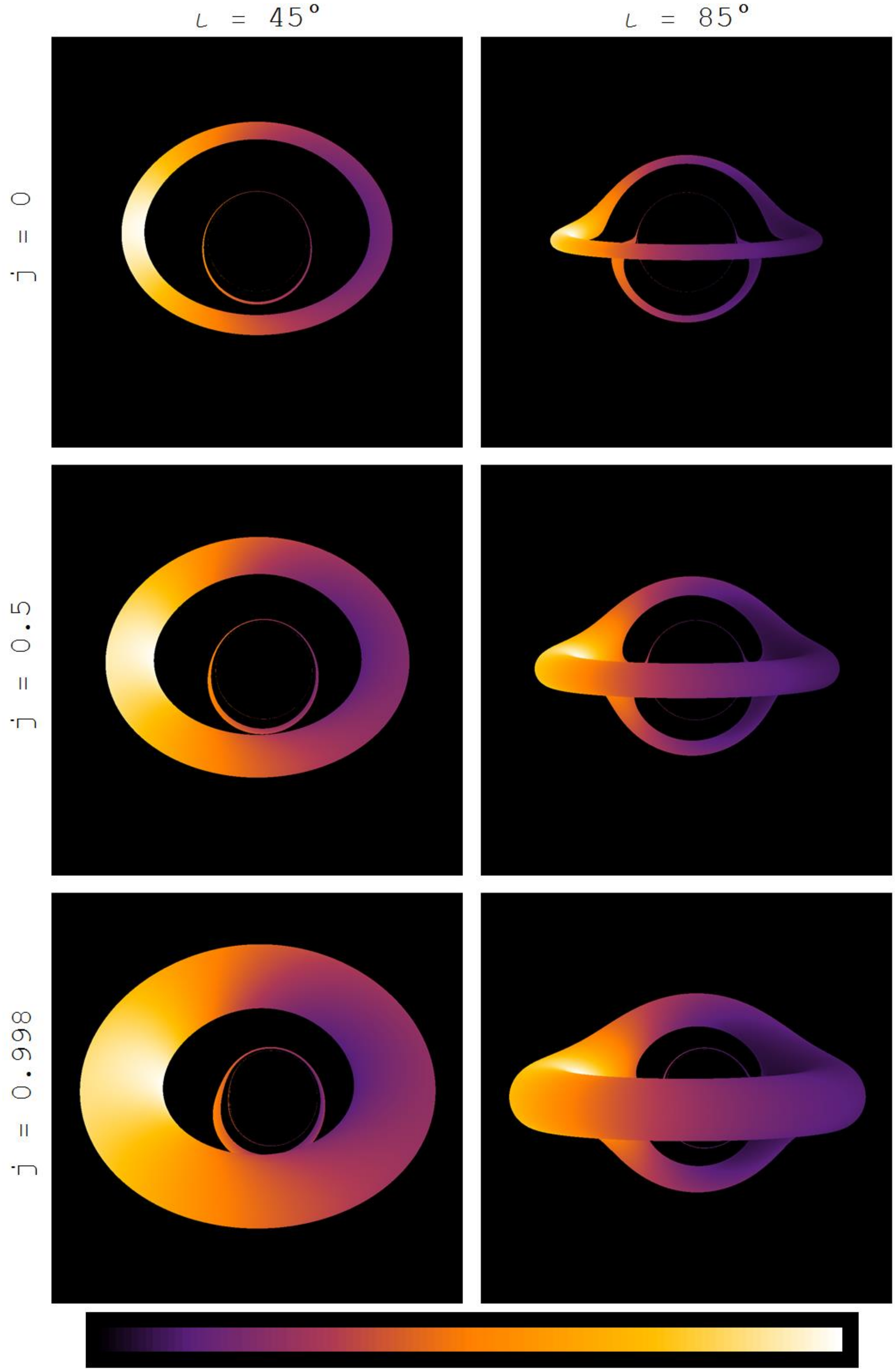

Figure 5.21: Frequency-integrated specific intensity for an ORST by `Elysium`. On the *left*, the disk is at a 45° and on *the right* at an 85° inclination. Each line has a different black hole spin parameter, from *top to bottom*: $j = 0$, $j = 0.5$, and $j = 0.998$. The color scheme legend is displayed at the bottom from minimum to maximum.

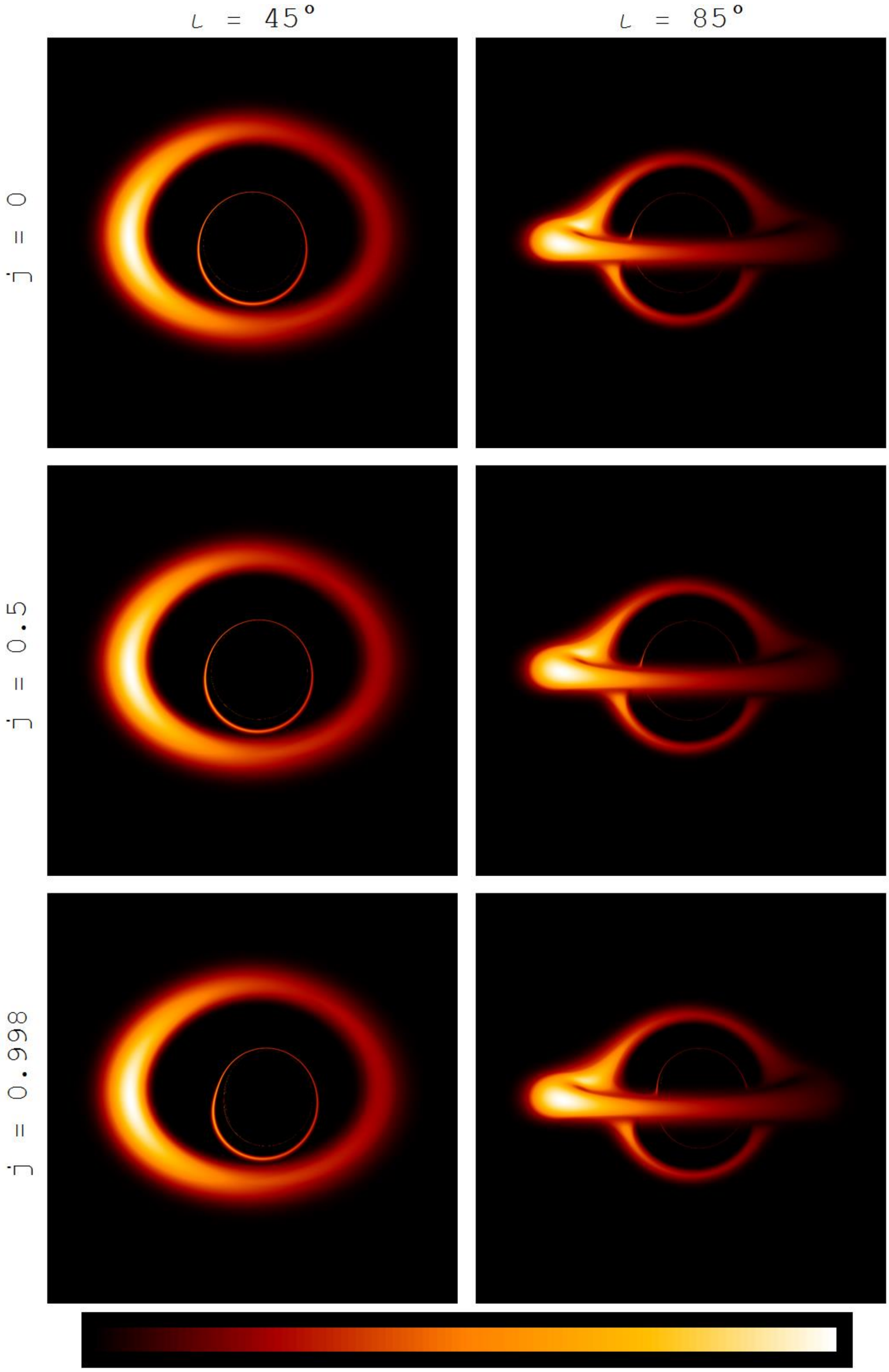

Figure 5.22: Frequency-integrated specific intensity for a semi-opaque PD by `Elysium`. On the *left*, the disk is at a 45° and on *the right* at an 85° inclination. Each line has a different black hole spin parameter, from *top to bottom*: $j = 0$, $j = 0.5$, and $j = 0.998$. The color scheme legend is displayed at the bottom from minimum to maximum.

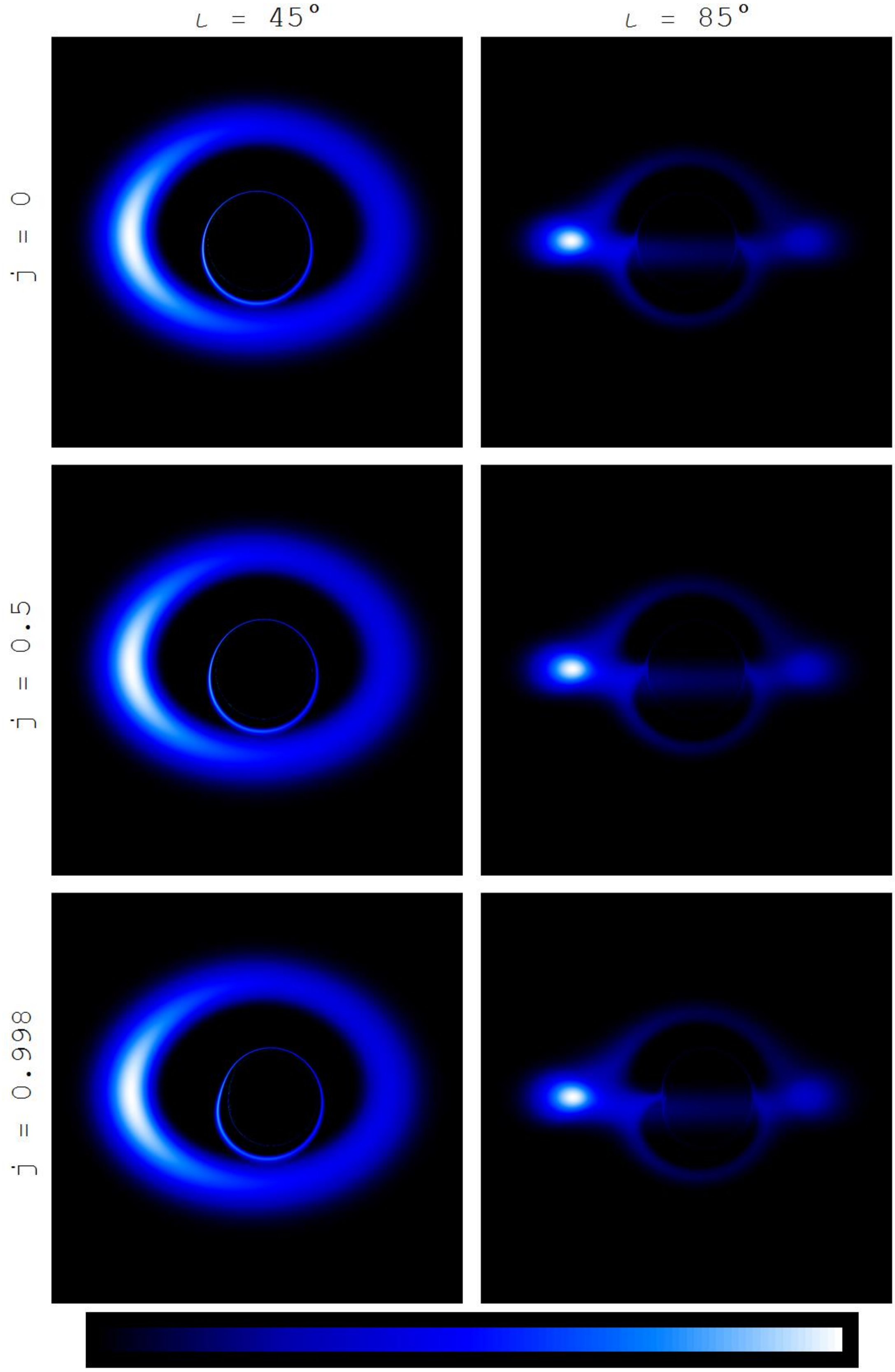

Figure 5.23: Frequency-integrated specific intensity for a translucent PD by `Elysium`. On the *left*, the disk is at a 45° and on *the right* at an 85° inclination. Each line has a different black hole spin parameter, from *top to bottom*: $j = 0$, $j = 0.5$, and $j = 0.998$. The color scheme legend is displayed at the bottom from minimum to maximum.

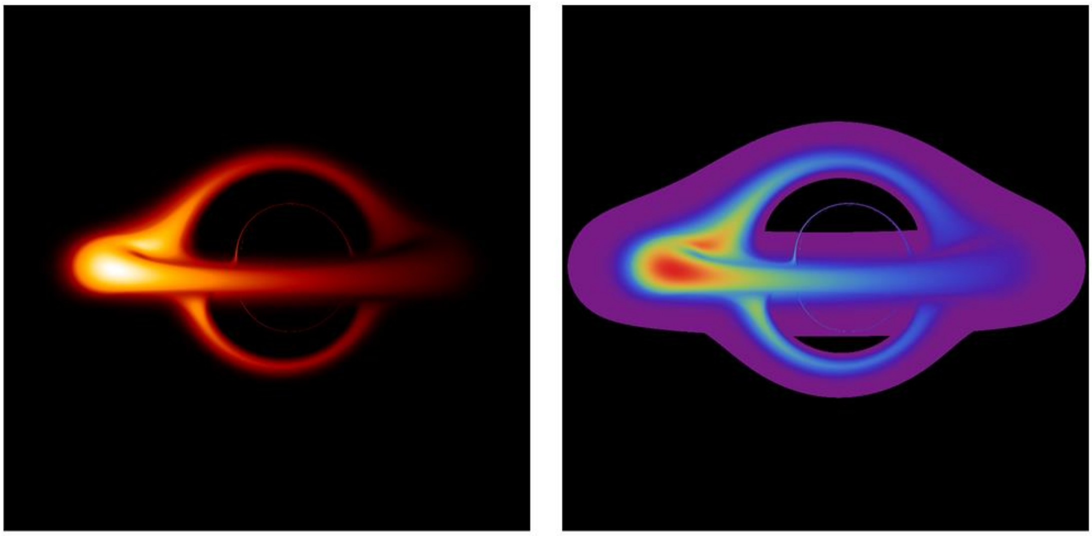

Figure 5.24: `Elysium` generated pictures of the same semi-opaque polish doughnut shown in natural colors (*left*) and in pseudocolor (*right*). In pseudocolor, material of low density is displayed in purple color instead of the natural black. This way, the actual volume of the accretion disk is revealed and clearly appears significantly larger than what is visible in more natural colors.

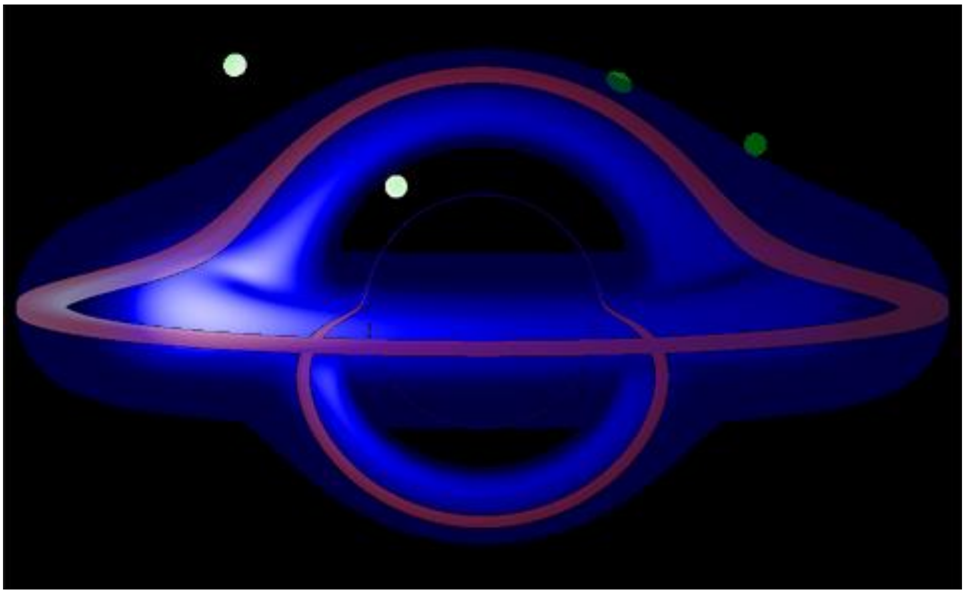

Figure 5.25: `Elysium` generated picture of an accretion disk in multiple wavelengths (see e.g., Urry & Padovani 1995). The disk's inner regions include large numbers of electrons emitting X-rays (*blue*). The outer regions include colder or obscured regions with gas, dust or atoms and molecules emitting strongly in infrared (*red*). In addition, blobs of material in the halo can be noted above the disk in medium temperatures emitting in optical wavelengths (*green*).

further capabilities than simple photographical depiction. These for instance include the picturing of systems in a multitude of wavelengths. An example of this procedure can be seen in Figure 5.25, where we observe an accretion disk emitting in various wavelengths depending on its material's temperature. That is to say, that its inner domain with higher temperatures ($T \approx 10^7 K, E \approx 1 keV$, Zhang et al. 1997, Kylafis et al. 2012) contains large concentrations of free electrons emitting in X-rays. At the same time, the outer regions of the setup contain partially obscured material in lower temperatures that can manage to sustain ions, gas, or even dust grains. These regions are expected to emit strongly in infrared and radio wavelengths. Additionally, we can observe the presence of intermediate-temperature, partially ionized material a certain height above the disk that receives light from the hot matter and reemits it in optical wavelengths. We can thus use this application in order to depict systems with multiple components visible in a variety of frequencies. Finally, we can again observe here the particular geometrical characteristics of the spacetime curvature. The intermediate-temperature material (green-white ovals) is assumed to be in the form of small spheres of the same size and situated closer or further away from the system center. Looking at the figure, nevertheless, we note the assorted objects appearing in varying sizes and shifting shapes, both a direct result of the differentiating form of the spacetime.

We continue on to investigate and describe possible extensions of `Elysium`. The first expansion is one combined with the possible expansion of the `Omega` code. Namely, the program can be enhanced in order to research and study gravitational lensing effects and paradigms (see e.g., Refsdal 1964, Blandford & Narayan 1992, Narayan & Bartelmann 1996, Bozza 2010, Gralla & Lupsasca 2020a, 2020b, Gralla 2020). For this purpose, we can add various astronomical objects, such as stars and galaxies behind the compact-object system and survey their observation under varying characteristics of the intervening curved spacetime or even modified gravity environments.

One more application that can be undertaken by `Elysium` is the attentive monitoring of the primary Einstein – Khvolson echo rings for varying black hole spins. For instance, we can look at Figures 5.20 – 5.23 and notice that the echo does not have a constant size in the "photographs" taken, but greatly depends on the accretion disk's inner edge radius. Namely, we note that for a disk situated closer to the event horizon (Fig. 5.20), the echo is far larger than for cases where the edge is further away (Figs. 5.21 – 5.23). We can also note that the phenomenon can extend so much, that there are extreme cases where the echo is larger in visual size than the accretion disk itself (see e.g., Fig. 5.20 bottom row). Therefore, it is perhaps worth examining the cases where the observation of the first echo can provide information about the object that its primary image cannot. This pertains, for example, to cases where the primary image of the object is too small or too close to the event horizon to clearly discern details, or when it is partially concealed by interceding matter. In cases such as those, the echo rings can be directly used to gather information about the system composition, its velocity profiles, and possibly the disk dimensions.

5.5. Code `Tranquillity`

(URL: https://gitlab.com/leelamichaels/Tranquillity)

5.5.1. The algorithm and capabilities

The `Tranquillity` code was written in early 2019, but was conceived and presented much earlier in 2014. It currently has about 25 versions. Its main purpose is to establish if it is possible to find a quick but reliable enough way to have an estimation of the black hole spin parameter (see also de Vries 2005, Wu et al. 2008b, Younsi et al. 2016). Its first step is to provide an estimation for the accretion disk plane inclination ι compared to the line of sight and then using that, give an estimation of the central black hole spin. This is achieved by gathering information from incoming photons reaching the observer after traveling closer to the event horizon and hence deeper in the gravitational well[11].

For the code execution, we assume an observer at infinity looking toward the black hole and the accretion disk spiraling around it. This observer documents the incoming radiation in high resolution, recording the relative position of the accretion disk and its first Einstein – Khvolson[8] echo[9] ring. This is the gravitationally lensed higher-order image produced by photons circumnavigating the black hole in close proximity and we prefer the term "echo" as this designation is more intuitive and easier to visualize and comprehend. We notice here that for a nonrotating central black hole, the spacetime would be Schwarzschild and static. This means that the main disk image and the echo ring are concentric. If, however, the black hole is rotating, the frame dragging results in a small displacement of the echo center, dependent on the black hole spin. This fact is in reality expected, since the photons composing the echo are forced to move much closer to the black hole and the greatly perturbed spacetime frame there. Therefore, we expect and do observe that the higher the black hole spin is, the greater this displacement is.

The initial stage of `Tranquillity` is to ascertain the inclination of the accretion disk plane compared to the line of sight. Subsequently, the algorithm estimates the first echo divergence compared to the accretion disk image. Finally, we utilize the inclination – divergence plots produced as scales in order to acquire an estimation of the central black hole spin.

Our results show that the estimation for the accretion disk inclination returns values very close to the real numbers. The average declination from the real inclination is below 0.8 degrees for the 240 events of diverse inclinations and spin parameters studied (Table 6). From these, only three study cases demonstrated inclination errors far above average, but even in those cases, the estimation error was at five degrees or less. These cases of inclination errors developed due to specific conditions of the configuration

---

[11] *The process quite easily brings to mind the Eddington experiment, Príncipe & Sobral, 29 May 1919, since it is in fact based on similar relativistic principles. In close proximity to large masses, rotating or not, the spacetime grid perturbations are more pronounced and easier to detect.*

ι \ j (°)	0 (°)	0.2 (°)	0.5 (°)	0.7 (°)	0.9 (°)
0	0.	0.	0.	0.	0.
10	0.64	0.4	0.22	0.19	0.07
20	1.38	0.25	0.96	0.68	0.55
30	1.85	1.28	1.08	0.81	0.68
40	1.85	1.47	1.11	0.89	0.69
50	1.85	1.2	1.06	0.92	0.67
60	1.73	1.25	0.95	0.78	0.56
70	1.34	0.99	0.77	3.87	2.00
80	0.55	0.53	0.44	0.35	0.37
90	0.	0.	0.	0.	0.

Table 6: `Tranquillity` disk inclination estimation errors in degrees.

Notes: The estimations are given for assorted black hole spin parameters j (*columns*) and accretion disk inclinations ι (*lines*). Some of the largest erroneous results for the inclination are included in the table. These are due to special cases of the echo ring placement in the observation images. In general, we note that the disk inclination assessment appears acceptable.

that had a black hole's first echo appearing in very peculiar and particular loci. The selected model for the accretion disk studied each time, does not so far seem to have an important role in the inclination assessment.

It is important to note here that the chosen disk model considered for each run seems to play an essential role in the divergence calculations. This is because different disk models can have very different profiles and cross section and can thus have their inner edge at very different radii (see Krolik & Hawley 2002, Abramowicz et al. 2010, Contopoulos & Papadopoulos 2012). We clearly state in this point that our algorithm does not utilize or rely at all on the inner edge of the disk, but only on the appearance of the entire disk as a whole. This means that the redeployment of the disk material for each disk model does not create an insurmountable obstacle for our method, but instead it only causes a recalibration to the divergence plots.

5.5.2. Results: Black hole spin estimation

In the execution of this program, the algorithm creates a recording screen and simulates precisely registering the accretion disk and the first echo's location at infinity. In the first segment of the execution, the program provides an assessment of the accretion disk inclination relative to the line of sight. Subsequently, it documents and stores the observational information combined with the actual black hole spin parameter. The compilation of all such data from the assorted executions is then processed in order to construct the inclination – divergence plots for the spin tem-

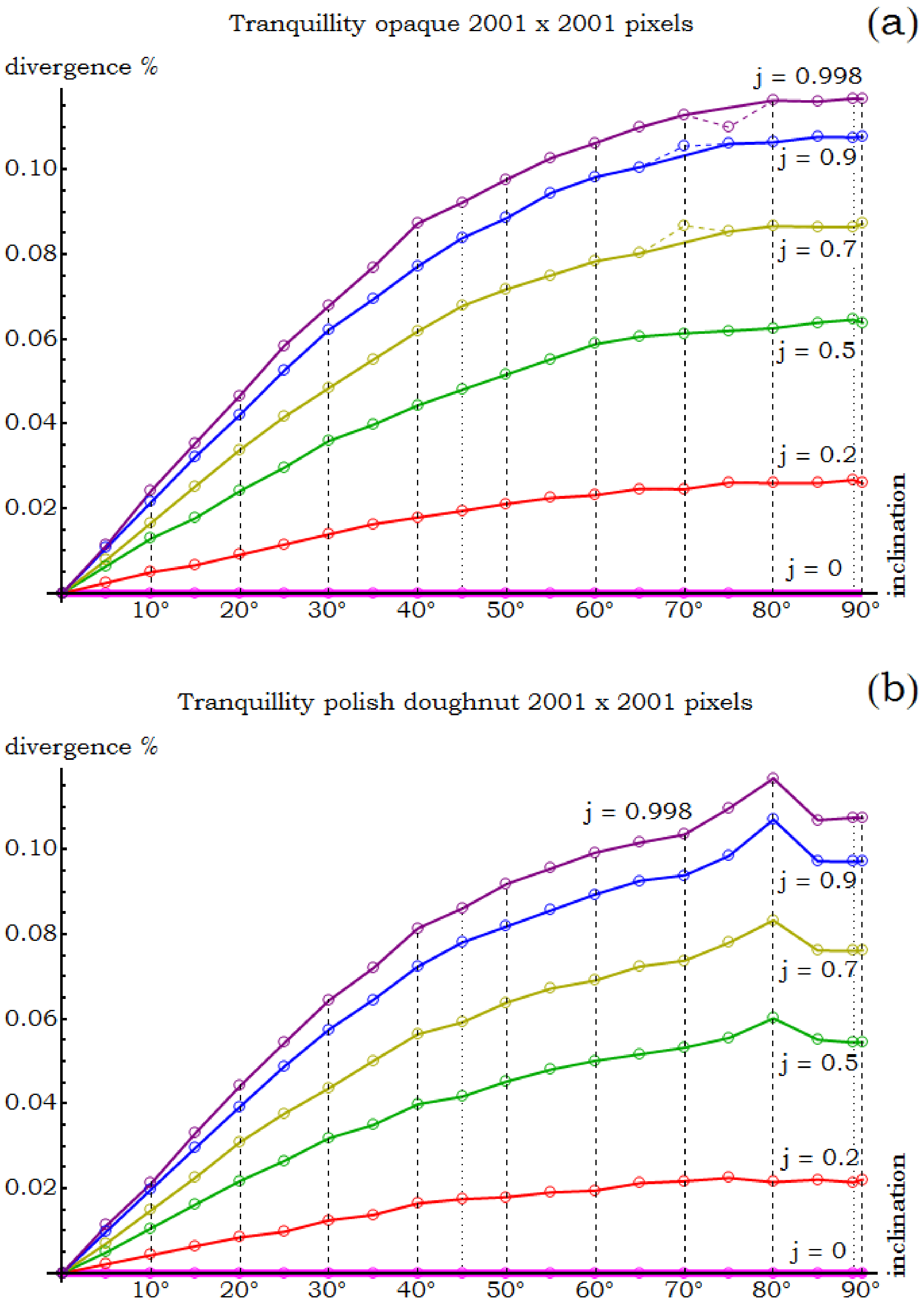

Figure 5.26: Inclination – divergence plots created using `Tranquillity` results, each circle representing one execution. On *the top plot* (*a*) we have results created using an ORST disk (Sect. 4.2f) that alters its structure substantially for increasing spins. The PD disk (Sect. 4.3b) used in *the bottom plot* (*b*), instead remains nearly unaffected. We notice an explicit trend for the divergence curve and evolution. The dashed color lines *on the top*, as well as the irregular maxima *on the bottom* are due to special placement of the first echo ring.

plates. These plots can then be used as scales in order to provide an estimation of the black hole spin in a system using observational data.

We continue on to investigate Figure 5.26. There, we can examine two different inclination – divergence plots created by studying the evolution of two different accretion disk setups for increasing values of the black hole spin. These results document the inclination to divergence correlation points in 240 high-resolution executions of `Tranquillity`. The accretion disk in these cases can have any inclination to the line of sight, from 0° (face-on) to 90° (edge-on). The executions are run for inclinations every 5°, plus an angle on 89°. The first disk model is an ORST disk (Sect. 4.2f) that considerably changes its size, shape, inner, and outer edge radii for increasing values of a. The other disk is a radiation pressure supported polish doughnut (Sect. 4.3b), which maintains an approximately constant shape and size for all black hole spins. From Figure 5.26 we discern an evident pattern for the divergence evolution for increasing spins. Namely, we detect that for nonrotating black holes, the echo and the disk image are concentric and thus the centers divergence is zero. Subsequently, as the spin increases, the echo divergence follows different increase rate curves for different inclinations, a fact we may use for the spin estimation.

We now carry on to appraise our program's results and their quality. We surveyed earlier the disk inclination estimations, shown in Table 6. These assessments appear to be adequate for the different circumstances we have tested. That is to say, that it appears possible to use the disk inclination estimations in order to obtain a predicted spin for the central black hole. We thus execute and review a list of randomized tests about all

Disk model	Inclin. (°)	Est. incl. (°)	Spin	Est. spin	Spin error (%)
disk	15	16.	0.13	0.13	2
disk	72	72.	0.49	0.49	0
slab	9	9.	0.06	0.07	8
slab	79	79.	0.25	0.24	3
wedge	11	11.	0.39	0.39	0
wedge	86	86.	0.4	0.39	3
torus	39	39.	0.12	0.14	13
torus	64	64.	0.32	0.32	0
ORST	80	84.8	0.41	0.41	1
ORST	82	86.3	0.86	0.81	7
PD	15	14.9	0.98	0.98	0
PD	48	47.5	0.75	0.76	1

Table 7: `Tranquillity` code results for spin estimation.

Notes: We have a representative list of various disk setups, along with the real accretion disk inclination and its algorithm estimation. Subsequently, we have the real spin of the black hole and the code estimation. Finally, we see a percentage of the error in spin estimation that also appears satisfactory.

the disk models considered and evaluate the results, shown in Table 7. There, we encounter juxtapositions between the system properties real values, namely the disk inclination and the black hole spin, along with their estimated values using the functions and results of `Tranquillity`. Comparisons between the real and the estimated property values appear to be sufficiently good and the errors turn out within acceptable limits.

Before concluding this Section, we explain the possible extensions that could be applied onto `Tranquillity`. As we explained earlier, the spin estimation greatly depends upon the disk setup considered, since a choice of this kind considerably affects fundamental qualities of the disk, such as its inner edge. We again note, however, that the algorithm does not rely on this perplexing and possibly precarious piece of information. Instead, the code investigates the black hole – accretion disk image as an integrated entity. This fact signifies that, first of all, the central massive object is not required to be exclusively a black hole, but any type of a massive object. Furthermore, we recognize that the quality of the observational information is pivotal to the quality of the estimations. Namely, we can see that a better quality of observational information gives a more accurate prediction of the central object spin.

From the above discussion, we see that a notable improvement of the algorithm would be the creation of a more complete, thorough, and dense sampling. Such a library will allow the algorithm to automatically recall large specimens of systems that display a multitude of characteristics and effects. Using these specimens, the code will then be able to automatically compare the observational data with the theoretical catalogs and hence establish the best-fit model for every circumstance. We do note here, nonetheless, that an endeavor of such magnitude will require considerable amounts of objectives, duties, and testing. In addition to the above, the algorithm would greatly benefit from extended functions that allow it to automatically recognize and deal with particular cases of spacetime or disk situations.

5.6. Code `Burning Arrow`

(URL: https://gitlab.com/leelamichaels/Burning_Arrow)

5.6.1. The algorithm and capabilities

`Burning Arrow` was initially written in late 2019, but was revisited and radically rewritten in 2020. At this moment, there are about 17 versions of the algorithm. Its main purpose is to calculate and plot massive particle trajectories close to a black hole and accretion disk system, while taking into consideration the different effects and reverberations of radiation. This thus leads to the ability to plot the initially circular and then degenerating particle orbit due to the disk's thermal radiation at various points.

Our first step in order to study particle motion is to get the general relativistic form of Newton's laws of motion. We start from the first law, that in the absence of general relativistic (nongravitational) forces, the particle under study follows a geodesic through spacetime. This geodesic thus follows the equation:

$$\frac{\mathrm{d}^2 x^\mu}{\mathrm{d}\tau^2} + \Gamma^\mu_{\alpha\beta}\, u^\alpha u^\beta = 0\,, \tag{5.6.1}$$

where τ is the proper time, $u^\alpha = \frac{dx^\alpha}{d\tau}$ is the four-velocity, and $\Gamma^\mu_{\alpha\beta}$ the Christoffel symbols, with $\Gamma^\mu_{\alpha\beta} = \frac{1}{2} g^{\mu\nu}\left(g_{\alpha\nu,\beta} + g_{\beta\nu,\alpha} - g_{\alpha\beta,\nu}\right)$ where commas denote partial derivatives. The zero term on the right hand side of the above formula signifies the absence of acceleration, same as in Newton's first law. When we solve this equation, we uncover the assorted geodesic solutions that specify, among other things, particular circular orbits such as the innermost stable circular orbit for massive particles, the photon sphere, and more. The above equation can also be rewritten as:

$$\frac{\mathrm{d}^2 x^\mu}{\mathrm{d}t^2} + \Gamma^\mu_{\alpha\beta} \frac{\mathrm{d}x^\alpha}{\mathrm{d}t}\frac{\mathrm{d}x^\beta}{\mathrm{d}t} - \Gamma^t_{\alpha\beta} \frac{\mathrm{d}x^\alpha}{\mathrm{d}t}\frac{\mathrm{d}x^\beta}{\mathrm{d}t}\frac{\mathrm{d}x^\mu}{\mathrm{d}t} = 0\,, \tag{5.6.2}$$

by applying the chain rule in order to obtain derivations by the coordinate time $x^0 = t$. This, however, has demonstrated to be more susceptible to error accumulation in this study and thus we select to follow the proper time equations instead.

The previous equation can be then accordingly used to get Newton's second law of motion and acquire a method to estimate the radiation acceleration. We have considered various cases of velocity behaviors and we display later on results for three different velocity profiles, the circular orbit velocity given by Bardeen et al. 1972, and the SANE and MAD velocity profiles given by Narayan et al. 2003 and 2012, and Penna et al. 2013a).

In the first stages of the implementation and depending on the investigation required, the code searches into the `Infinity` radiation force files and reads the suitable ones, appropriate for the specific case. It then utilizes the results to construct proper functions that supply the radiation

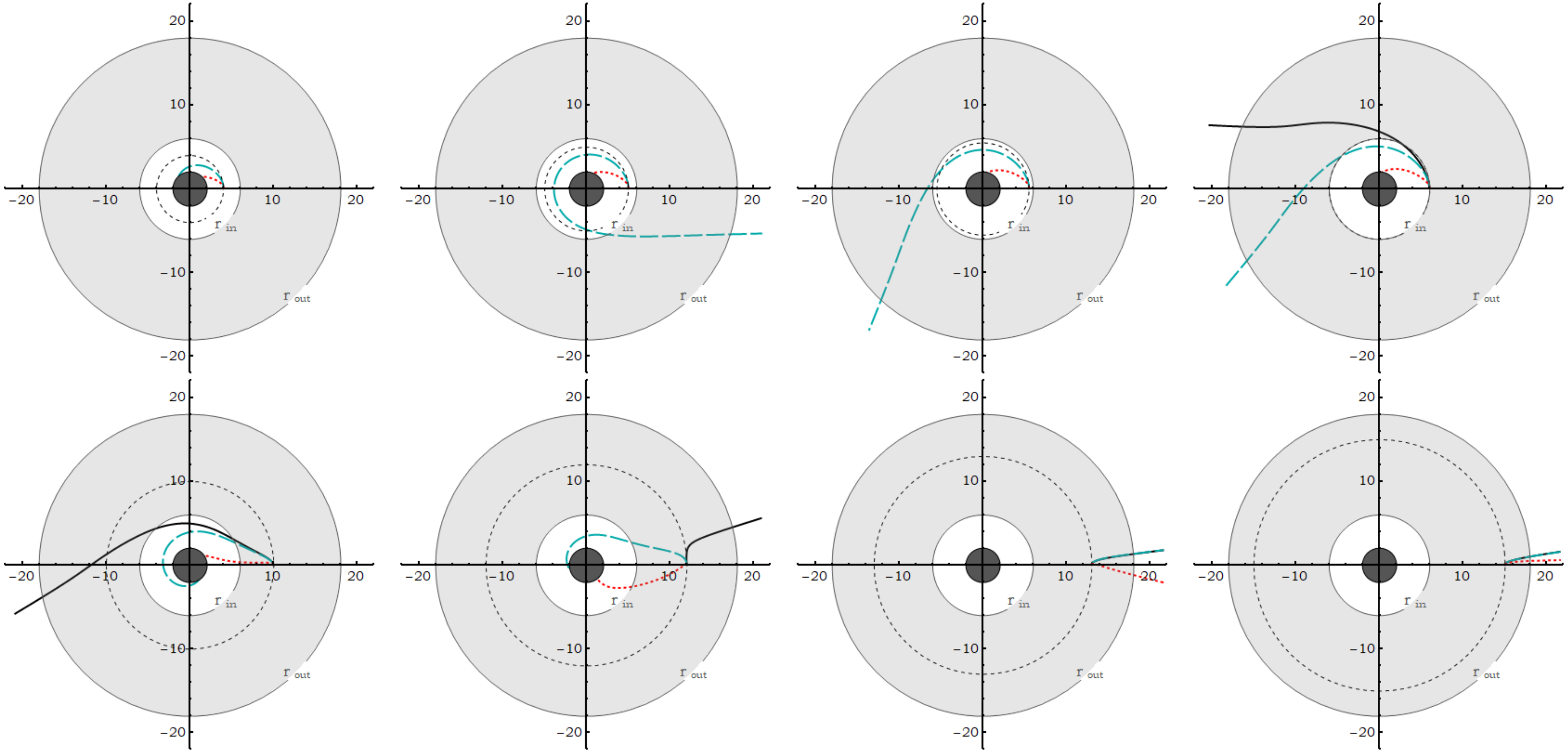

Figure 5.27: `Burning Arrow`: degrading equatorial particle orbits around a Schwarzschild black hole. The accretion disk is a quasi-opaque LFM disk (Sect. 4.3d). The *dashed circle* is the trajectory the target particle would follow without the presence or radiation. The *solid black* lines are particles moving with the velocity profile Ω (Eq. (2.2.13)) from Bardeen et al. 1972. With the *dashed cyan* line, we have the SANE profile and with the *dotted red* line the MAD profile (Narayan et al. 2003 & 2012, Penna et al. 2013a).

stress – energy tensor at each spacetime point considered for the subject under study. This then provides the four-acceleration due to radiation, a^{μ}_{rad}, for all points from the extension of the preceding equation as:

$$a^{\mu}_{rad} = \frac{\mathrm{d}^2 x^{\mu}}{\mathrm{d}\tau^2} + \Gamma^{\mu}_{\alpha\beta}\, u^{\alpha} u^{\beta}\,. \tag{5.6.3}$$

Since the radiation acceleration is known from the previously mentioned results in spacetime, we can solve the above eight differential equations and obtain the required four-velocity and four-positions for the particle trajectory.

We can here study Figure 5.27 and survey some examples of circular orbit degradation in a quasi-opaque LFM disk (Sect. 4.3d) in a Schwarzschild spacetime. Particle trajectories with no radiation influence would be circular, following the dashed orbit. If we examine, however, the situation where thermal radiation is emitted by the disk material, the degeneration of these circular orbits is easily noticed when ignoring the emerging secondary electromagnetic phenomena. The particle trajectories are promptly destabilized by the radiation incidence and the electrons either plummet into the black hole or are launched rapidly out of the system. In the aforementioned figure, we can see the degradation of particle trajectories followed by targets in three distinct velocity profiles: Bardeen et al. 1972 (*solid line*), SANE (*dashed cyan* line), and MAD (*dotted red* line) found in Narayan et al. 2003 and 2012, Penna et al. 2013a. Further on, we examine more environments and discuss noteworthy situations of orbit evolutions.

5.6.2. Results: Orbit degradation due to radiation

`Burning Arrow` was developed as a means to investigate the deterioration of massive particle trajectories in the accretion disk orbiting a black hole. As we explained earlier, if we ignore the incident radiation, the targets would move circularly due to the absence of general relativistic forces.

The `Burning Arrow` algorithm is executed in combination with the `Infinity` code and its results. That is to say, that first we need to execute `Infinity` and acquire a list of files describing the radiation acceleration or deceleration exerted on the receiving targets. Then, `Burning Arrow` allows us to select the desired list of output files we wish to employ in order to calculate the ensuing target trajectories. Subsequently, the program is executed and reads the output files, calculates the accelerations, and plots the consequent particle launch trajectories for the various velocity profiles. Before reviewing some of the results, we should remember one substantial piece of information. This is the fact that the exerted radiation forces are directly proportional to the receiving particle's velocity. This means that the same radiation field has different effects and distinct aftermath on material moving with diverse velocity profiles.

We can go further on and examine Figure 5.28, where we see the degradation of equatorial electron orbits. This is due to the thermal radi-

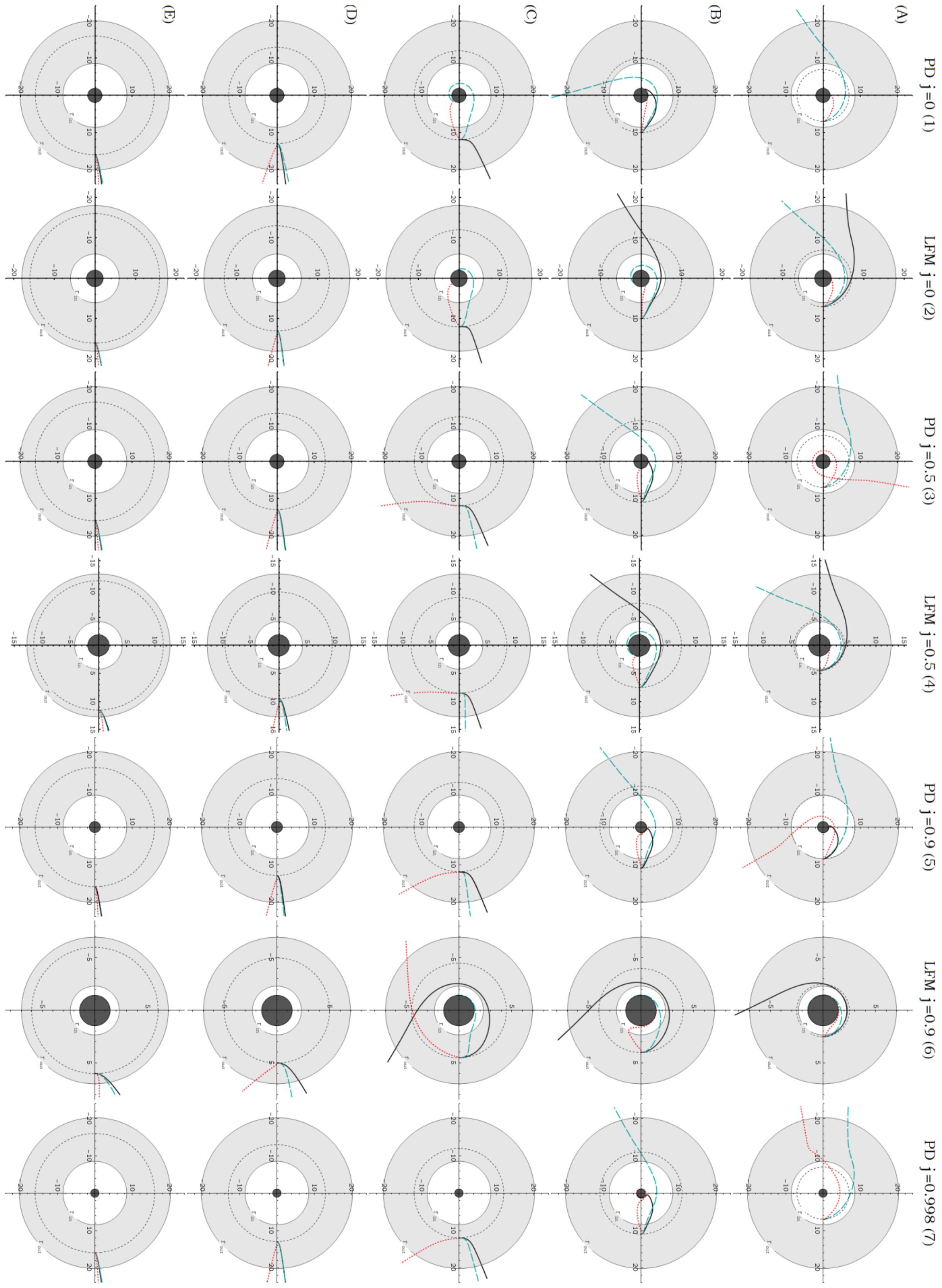

Figure 5.28: `Burning Arrow` collective results: circular equatorial electron trajectories degradation due to radiation. Here we inspect a multitude of black hole spins, spacetimes, and disk models. The *solid black* orbit follows Bardeen et al. 1972, and the *cyan* and *red* SANE and MAD respectively (Narayan et al. 2003 & 2012, Penna et al. 2013a).

ation of the quasi-opaque LFM disk (Sect. 4.3d) and the PD (Sect. 4.3b) around black holes of various spin parameters. The target electrons we examine start from various radii from the axes origin (*dashed circle*) and thus encounter different environments of material and radiation density each. Subsequently, they alter their velocity by braking or accelerating and destabilize, depending on the incident radiation. These changes cause the orbits modification and lead to the expulsion or the accretion of material onto the black hole.

It is worth noticing in the aforementioned Figure 5.28 the existence of some noteworthy and peculiar particle trajectories. First of all, we examine trajectories of particles initially situated at the center of the local radiation field (e.g., Fig. 5.28 *C1*, *C2*). For such circumstances, we should always remember that the radiation force is directly proportional to the flux of radiation. This means that regardless of the incoming radiation density or magnitude, if its distribution is isotropic, then the flux and consequently the radiation force is zero (see e.g., Rybicki & Lightman 1986). The repercussions of such procedures are particularly significant in the cases where the target is positioned in the "local center of radiation". Under these circumstances, the radiation field is perceived as close to isotropic as relativistic effects and Doppler boosting for the moving target allows it to be. This fact implies that any deviation of the target particle from its original trajectory drives it into more anisotropic domains of radiation. This results in the orbits steadily becoming more unstable and erratic. Therefore, the electron orbits promptly get out of equilibrium and the absorbing targets either accrete onto the compact object or get slingshot out of the system. This mainly depends on their velocity profile, as we can see faster orbits with Ω (Eq. (2.2.13)) escaping and slower orbits, following SANE or MAD, accreting. We thus conclude that the center of the local radiation field in a way resembles an unstable equilibrium point.

Further on, we notice circumstances where significant changes are recorded in the particle's environment, decidedly affecting its motion. One such situation is when the target begins in an area of certain radiation conditions and subsequently moves to areas of softer, stronger, or even counterbalanced radiation forces. Another noteworthy trajectory event is when the traveling target particle crosses through areas of notably varying spacetime curvature. Examples of such events can be observed in Figure 5.28 *A5*, *A7*, and *C6*. These phenomena then induce the emergence of instabilities that affect and conclusively influence the particle orbits.

Moreover, we encounter cases where the target converges to the static limit and possibly crosses into the ergosphere (e.g., Fig. 5.28 *B5*-*B7*). This transition is particularly interesting and notable as the black hole spin increases. That is so, because as the particle crosses the static limit, it is forced to modify its motion and rotation prompted by the compact object's rotation.

Before concluding this Section, we discuss some feasible extensions for the `Burning Arrow` program. Firstly, additional applications examining the trajectory modifications can be researched. As discussed earlier, the radiation forces act unilaterally and promote the charge separation process. This, however, does not occur within the disk due to various electric or magnetic processes taking place inside the material, which we could further explore. Moreover, we can additionally investigate upon the aforementioned matter of generated ring currents in the setup and survey the ensuing magnetic phenomena and their repercussions on the system components and dynamics.

The aforesaid processes that affect the electron, and therefore the ion, motional stability could have additional consequences of notable significance. Namely, slight deviations from the circular motion appear capable of resulting in local instabilities or miniscule movements and thus turbulence. This turbulence, nonetheless, is not expected to generally lead to the disruption or dissolution of the accretion disk and the particulate orbits. It is instead anticipated to modify the disk stability conditions and influence, or transpose the various equilibrium points. These procedures hence warrant further inspection in order to evaluate their potency and repercussions.

Extending more on the generated instabilities, we turn our attention toward the outer disk sectors. In these areas, we note stronger accelerations by the radiation exerted on the material. At the same time, the disk material in these areas is sparser and thus the electromagnetic binding of the matter to the disk becomes weaker in comparison. The outcomes encountered in such situations are increased probabilities of particle orbit instabilities and orbital displacement. Therefore, the further out we move in the disk, the stronger the imbalance gets and hence the more likely it is to register occurrences of cataclysmic material expulsion events, magnetic reconnection, and magnetorotational instabilities. In light of these electromagnetic effects that redefine the system dynamics, we ponder on the necessity to reexamine typical particle trajectories in the systems and their development in these environments (see e.g., Lovelace et al. 2009, Bini et al. 2011b, Contopoulos & Papadopoulos 2012). Finally, considering all the aforementioned convoluted phenomena and processes that influence the disk stability and evolution, we contemplate on their consequences on the assorted battery mechanisms we discussed earlier.

CHAPTER 6

THE POYNTING – ROBERTSON COSMIC BATTERY

6.1. Cosmic Battery

The Cosmic Battery model was first stated and described in 1998 by Ioannis Contopoulos and Demosthenes Kazanas (Contopoulos & Kazanas 1998). In the original paper, it was stated that this model was inspired by the Biermann battery[12] (Biermann 1950, Biermann & Schlüter 1951). The Biermann battery was thoroughly revisited and the new battery model was designed and stated in the appropriate way to apply to a partially different physical mechanism than the original model. The new mechanism uses the Poynting – Robertson drag and depending on the accretion disk composition and physical processes, it can generate strong azimuthal electric currents. These electric currents then in turn give rise to astrophysically significant magnetic fields. The mechanism was later criticized by Bisnovatyi-Kogan et al. 2002. The model was then revisited and certain misconceptions where cleared up in Contopoulos et al. 2006. Subsequently, in Christodoulou et al. 2008, simulations of the mechanism were examined in resistive accretion.

A pertinent astrophysical topic, strongly related to magnetic fields and compact objects that still remains open are jets. Jets are known to be magnetically driven (see e.g., Blandford & Payne 1982, Contopoulos 1995, Lynden-Bell 1996, Contopoulos et al. 2009, Gabuzda et al. 2012, Kylafis et al. 2012, Koutsantoniou & Contopoulos 2014, Contopoulos 2015, Christodoulou et al. 2016, Contopoulos et al. 2018) and display a wide variety of evidence hinting that they incorporate helical magnetic fields (also Contopoulos et al. 2015, Gabuzda 2015). Moreover, simulations of the area close to the possible origin of the jet disclose the mandatory existence of large-scale magnetic fields that are directly responsible for the formation and the acceleration of the jet (Kylafis et al. 2012, Koutsantoniou & Contopoulos 2014, Contopoulos 2015). Furthermore, assiduous examination of the problem reveals that without the presence of steady and

---

[12] *The Biermann battery is a procedure that allows the generation of large-scale electric currents and thus magnetic fields from a zero seed magnetic field. This is done via the operation of the thermoelectric effect (the direct conversion of differences in temperature into electric voltage), where the material electrons and ions acquire varying pressure and thermal directions.*

enduring large-scale dipolar magnetic fields in the area that extract energy from the central object and the accretion disk (see Lovelace 1976, Blandford 1976, Blandford & Znajek 1977, Christodoulou et al. 2008, Komissarov 2009, Kylafis et al. 2012, Lasota 2014, Koutsantoniou & Contopoulos 2014, Koutsantoniou 2022, 2023), the generation of a jet is unattainable. Therefore, the operation of the Cosmic Battery appears to be a valid solution, capable of paving the way for jet formation (see e.g., Contopoulos & Kazanas 1998, Christodoulou et al. 2008, Contopoulos et al. 2009, 2015, Gabuzda et al. 2012, Kylafis et al. 2012, Koutsantoniou & Contopoulos 2014, Gabuzda 2015, Contopoulos 2015, Christodoulou et al. 2016, Contopoulos et al. 2018). In the end, the aforementioned magnetic fields generated by the Cosmic Battery mechanism are expected to be dispensed by the jets into the interstellar or intergalactic space (e.g., Contopoulos et al. 2009, Gabuzda et al. 2012, Contopoulos et al. 2015).

Under this light, the magnetic field line structure and evolution in relativistic jets was examined and the results were closely looked upon. The theoretically expected results, along with relevant observational data (Faraday rotation measurement) were then discussed in Contopoulos et al. 2009. Further on, the possible effects of magnetic field generation in an accretion disk were investigated about their possible effects on the stability or destabilization of the disk’s inner edge. The results were presented in Contopoulos & Papadopoulos 2012. Subsequently, the usage of observational data was thoroughly considered and used in order to collect information about magnetically active systems, such as active galactic nuclei (AGN) jets and X-ray binaries. Results of this work were presented in Mahmud & Gabuzda 2007, 2009, Mahmud et al. 2009, Kylafis et al. 2012, Gabuzda et al. 2012, Reichstein & Gabuzda 2012, Kylafis & Belloni 2015a, 2015b, Gabuzda 2015, and Park et al. 2019.

Additional work on system radiation, dynamics, and early stages of the phenomenon manifestation were later studied and presented in Koutsantoniou & Contopoulos 2014, Koutsantoniou 2014, and 2015. We there explained our work up to that point and described the first steps in creating computational codes that study the phenomenon and give relevant results for the magnetic field generation. Later on, the refined magnetic field evolution depending on dissimilar accretion disk material characteristics was investigated in Contopoulos et al. 2015. In addition to the above, we should also mention the detailed assortment of related articles discussing the various facets and effects concerning astrophysical jets presented in The Formation and Disruption of Black Hole Jets (2015). Thereafter, more observational information were collected and discussed in Christodoulou et al. 2016, concerning the electric currents in extragalactic jets further away from their source. Furthermore, a different approach of the phenomenon, applying numerical simulations of a photon fluid in black hole system environments was explored in Contopoulos et al. 2018. In more recent times, we can find and examine Koutsantoniou 2022, 2023 and online material [4]. There, we additionally explain why it is necessary to develop a specially designed and relativistic ray tracing code. These codes also take into consideration the volume and the rotation of the accretion disk, which in our study are the sources of the entire physical process. In these works, we also explain the extra steps necessary to be taken in order to account for the purely relativistic effects present in such environments. We mention and account for the gravitational redshift caused by time dilation, the Doppler shift caused by the emitting surface motion, and the frame dragging shift encountered in spacetimes including a rotating massive object.

The main goal of Contopoulos and Kazanas in their work was to describe a mechanism in which simple, yet common and omnipresent physical procedures could give rise to astrophysical magnetic fields. These processes would then generate dipolar magnetic fields from zero and build them up to notable magnitudes, and in cases all the way up to equipartition values (Contopoulos & Kazanas 1998, Contopoulos et al. 2006, Christodoulou et al. 2008, Contopoulos & Papadopoulos 2012, Koutsantoniou & Contopoulos 2014, Contopoulos 2019). From this short description, one could see that the Cosmic Battery model is immediately applicable to astrophysical plasmas of all categories and statuses, and has noteworthy effects on their physics and evolution.

An argument of paramount importance that should be mentioned here explicitly is that a battery-type mechanism is positively necessary, since it proves to be the only possible solution for the existence of magnetic fields in the Universe. This is because the preexistence of large-scale magnetic fields in any environment is prohibited by the initial state of the Universe, which is considered to be isotropic and homogeneous to a very high degree (Contopoulos & Kazanas 1998). A battery mechanism, depending on its modus operandi, follows its procedure and exerts on the disk material the particular fields and forces of the process. These fields and forces, nevertheless, operate differently upon the matter positive and negative charges (ions and electrons), something that results in the appearance of varying component velocities. During the operation of the Cosmic Battery mechanism, for instance, the material electrons are the main recipients of the disk's thermal radiation and due to the aberration of light experience a drag. This results in the negative charges to somewhat decelerate and lag behind the positive charges motion. We hence note the appearance of a ring electric current in the disk, which generates a dipolar seed magnetic field. The protons later on experience the radiation drag through the electric field that develops between their population and the electrons (see Contopoulos & Kazanas 1998, Contopoulos et al. 2009, Koutsantoniou & Contopoulos 2014, Koutsantoniou 2022, 2023).

After the creation of seed magnetic fields, a variety of electromagnetic mechanisms can operate and amplify the initial field. One of these processes is the typical dynamo mechanism (see e.g., Schekochihin et al. 2002a, 2002b, 2004, 2005, 2007, Iskakov et al. 2007), which converts the material kinetic energy into magnetic field energy density. Subsequently, the field lines are extended and folded by the material motion. This field development then results in the dispersion of the field, but its entanglement and containment as well. This plasma "back reaction" is critical of the field evolution, since it eventually renders the mechanism quite ineffective (e.g., Contopoulos & Kazanas 1998, Contopoulos 2015). The Poynting – Robertson Cosmic Battery mechanism, nonetheless, proves to be adequately sufficient in order to provide the required magnetic field without the need for further amplification (Contopoulos & Kazanas 1998, Koutsantoniou & Contopoulos 2014, Contopoulos et al. 2015). This is in contrast to the majority of other processes, including the aforementioned Biermann battery. A very good environment for the operation of the Cosmic Battery, for example, is Advection-Dominated Accretion Flows (thick and Keplerian disk, Narayan & Yi 1994, 1995a, 1995b, Abramowicz et al. 1995, 1996), where the mechanism displays very high efficiency (Contopoulos & Kazanas 1998, Contopoulos et al. 2006, Kylafis et al. 2012, Contopoulos 2015).

The Cosmic Battery mechanism has a very significant advantage compared to the typical consideration of the magnetic fields necessary for the various systems and phenomena. The magnetic field is not preexistent or brought in from larger distances "outside" the system, a procedure that demands zero diffusivity and whose possibility is highly debated in the scientific community. Instead of these unreliable processes, the magnetic field is generated in situ by the Cosmic Battery and then used by the system components (see Contopoulos & Kazanas 1998, Contopoulos & Papadopoulos 2012, Koutsantoniou & Contopoulos 2014, Contopoulos 2015, Contopoulos 2019, Koutsantoniou 2022, 2023). This is in contrast with the vast majority of studies, where a seed magnetic field of unknown origin is considered present or preexistent in these environments. The seed field generated by other processes should then be amplified by dynamo mechanism procedures, which very often, however, prove to be notably insufficient (see Vainshtein & Cattaneo 1992, Zrake & MacFadyen 2012).

The Cosmic Battery mechanism, nevertheless, easily generates magnetic fields from zero in the vicinity of the accretion disk's inner edge (Contopoulos et al. 2006, Christodoulou et al. 2008, Contopoulos et al. 2009, Kylafis et al. 2012, Koutsantoniou & Contopoulos 2014, Contopoulos 2015, Koutsantoniou 2022, 2023; Fig. 6.1). These generated fields can subsequently evolve in different ways, depending on the disk material and its properties (see Contopoulos & Kazanas 1998, Contopoulos et al. 2006, Christodoulou et al. 2008, Contopoulos & Papadopoulos 2012, Kylafis et al. 2012, Koutsantoniou & Contopoulos 2014, Contopoulos et al. 2015, Contopoulos 2015, Contopoulos 2019). Namely, if the disk material records a high enough magnetic diffusivity, the generated field can diffuse outward and not get dragged inward along with the freefalling matter. In this case, the magnetic field footpoints anchored further inward in the disk and close to its inner edge are dragged along by the infalling matter. The lines thus move toward the central mass, accumulate, and thread the event horizon and the outflow region near the system rotation axis. On the contrary, the field footpoints initially situated further out can freely diffuse outward and spread in the disk outer regions and the interstellar or intergalactic environment. Under these circumstances, we anticipate the unremitted accumulation of magnetic field flux in the inner regions of the system and the continual escape of the return polarity to infinity through the disk's outer areas (Contopoulos et al. 2006, Christodoulou et al. 2008, Contopoulos & Papadopoulos 2012, Koutsantoniou & Contopoulos 2014). This process continues to operate and build up the magnetic field until it reaches high enough values that affect and modify the disk stability and evolution, videlicet the equipartition limit. This limit can be successfully reached by the Cosmic

Battery mechanism in a few hundred million dynamical times. This translates into few hours or days for a stellar mass black hole and a few million years for a supermassive black hole (Contopoulos & Kazanas 1998, Kylafis et al. 2012, Koutsantoniou & Contopoulos 2014, Contopoulos 2019).

At this point we should be aware of the fact that as soon as a magnetic flux starts to surface, the disk equilibrium begins to change and perhaps weaken somewhat (Contopoulos & Kazanas 1998, Contopoulos et al. 2006, Christodoulou et al. 2008, Contopoulos et al. 2009, Contopoulos & Papadopoulos 2012, Kylafis et al. 2012, Koutsantoniou & Contopoulos 2014, Contopoulos et al. 2018, Koutsantoniou 2022, 2023). This happens because with the gradual formation of a magnetic field, we also notice the appearance of magnetorotational instabilities. Namely, as the magnetic field increases near the inner edge of the accretion disk, even small displacements of the orbiting matter cause parts of the disk to destabilize in their orbits and consequently infall and accrete onto the central object. That is to say, that the creation of a magnetic field in combination with the material viscosity leads to the generation of magnetorotational instabilities that can trigger accretion events. We should clearly mark here that the Cosmic Battery mechanism is independent of any other magnetic fields and processes possibly present in the systems and does not prohibit the appearance of other

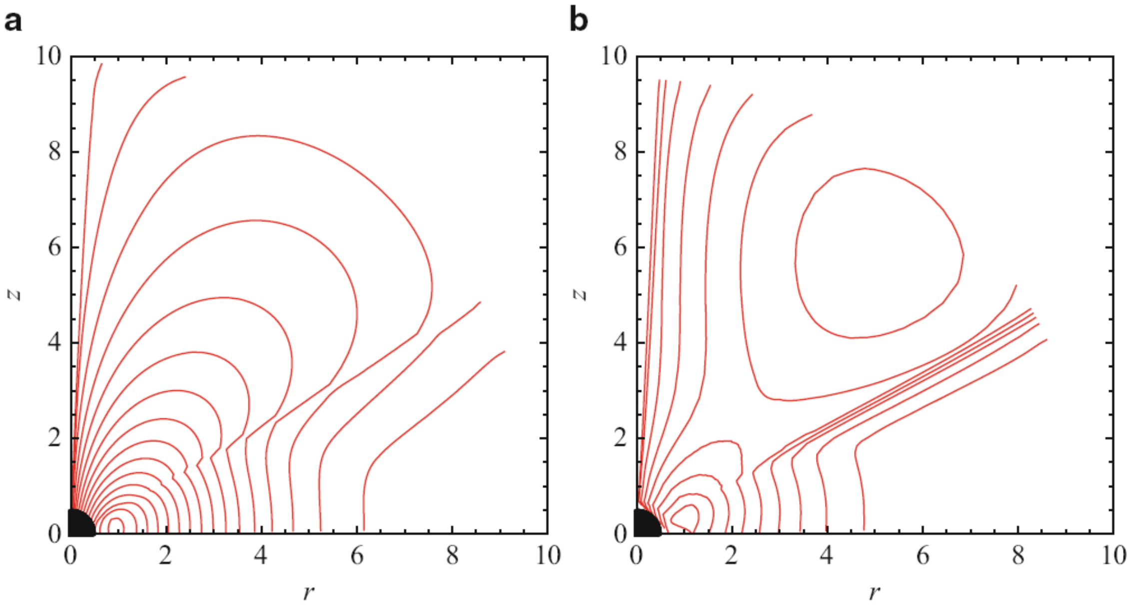

Figure 6.1: Magnetic field lines evolution inside and outside the disk material (*left to right*). The magnetic loops are generated by the Cosmic Battery mechanism in the area of the disk's inner edge (length unit of the axes). In this region, the braking forces are maximized for quasi-opaque accretion disks. The accretion disk's differential rotation then causes these loops to expand and subsequently open up. During the loop expansion, their inner parts are advected inward by the material infall, while the exterior parts are diffused outward. This leads to an increasing generation of magnetic field by the Cosmic Battery up to equipartition values. Figure 9.4, *The Formation and Disruption of Black Hole Jets*, Contopoulos, Gabuzda, Kylafis 2015.

phenomena, such as the aforesaid magnetorotational instability.

In the opposite case, we can have a disk with highly conductive plasma that efficiently hinders the magnetic accumulation after limited periods of time (e.g., Contopoulos et al. 2006, Christodoulou et al. 2008). This impediment is in certain cases somewhat restricted and in other cases more severe, quickly leading to saturation well below equipartition values (Contopoulos & Kazanas 1998, Contopoulos et al. 2006, Christodoulou et al. 2008, Koutsantoniou & Contopoulos 2014, Contopoulos et al. 2015). Compared to the Biermann battery, however, even in cases of high conductivity, the Cosmic Battery manages to generate notably higher magnetic field magnitudes (Contopoulos et al. 2006). If we consider a typical example of compact object and accretion disk systems, what we can observe is increased resistivity, and therefore magnetic diffusivity, in the turbulent, viscous disk, and suppressed resistivity further inside the disk's inner edge. This leads to a steady state where one polarity of the field is carried inward and deposited in the system core by the accretion, and the opposite polarity being carried away toward the system exterior by diffusion. This means that the mechanism does not saturate and the process continues with a steady, linear in time growth of the dipolar magnetic field in the system (Contopoulos & Kazanas 1998, Contopoulos et al. 2006, Christodoulou et al. 2008, Contopoulos et al. 2015, Contopoulos 2019).

Another fact about the Cosmic Battery, particularly noteworthy here, is that under any circumstances, even in cases of less curved spacetimes or increased material conductivity the mechanism is still effective. This means that even in cases of limited contribution, the procedure is capable of generating ample amounts of magnetic flux in the systems, since it is a secular process that operates steadily and incessantly (Contopoulos & Kazanas 1998, Contopoulos et al. 2006, Christodoulou et al. 2008, Kylafis et al. 2012, Contopoulos 2019). This way, the generation and accumulation of magnetic field continues functioning uninterrupted through the alternating periods of increased and diminished activity, with the field being continuously amplified. The only point at which the process stops functioning, or at least operating in the same manner, is when the generated magnetic field reaches dynamically significant values, namely the equipartition limit. At that point the generated magnetic field modifies the entire system and its dynamics, possibly redeploying the disk material and setup entirely, dictating new equilibrium conditions and conformities (see e.g., Bini et al. 2011b, Contopoulos & Papadopoulos 2012).

We should, nonetheless, also note here something rather important concerning the system properties and evolution. The system and field progression are not predetermined or of a single possible nature. Namely, the structures are not created exclusively as diffusive or conductive. Instead, on the contrary, we expect the assorted setups to periodically traverse intervals of both situations in alternation (see e.g., Christodoulou et al. 2008, Kylafis et al. 2012). This means that at various stages of their evolution, the systems interchange conditions. They may commence an era as diffusive, promoting the generation of magnetic flux and poloidal magnetic field loops. Subsequently, the field is spread inward by accretion and outward by diffusion. As the field expands, however, the reverse polarities can come into contact and magnetic reconnection takes place. At that point, the magnetic field locally "vanishes" along with the forces and flux threading the area, transforming the disk into an unmagnetized conductive structure that does not, or in this case cannot, diffuse any magnetic field. Later on, the Cosmic Battery mechanism operates again, generating magnetic flux and the cycle begins anew. From all of the above, we see that the material's magnetic diffusivity plays a more important and pivotal role in the accretion disk dynamics and evolution, far more significant than what was originally considered.

After the generation of magnetic field loops by the Cosmic Battery we thoroughly observe and record the magnetic field evolution and expansion. The initially purely poloidal field loops develop into an accretion disk that is not a typical solid body, but clearly displays differential rotation with increasing cylindrical distances from the central body. This fact is of paramount importance, since it has eminently critical consequences on the field evolution. The disk's differential rotation causes its inner regions to rotate faster than the outer ones, dragging the matter along with the magnetic field footpoints. This causes the originally poloidal field lines to get bent and twisted by the rotation, leading to the establishment of toroidal components in the magnetic field (see Christodoulou et al. 2008, Contopoulos et al. 2009). From the above, we understand that the material velocity and vorticity is of utmost importance, since it is directly responsible for the magnetic field evolution and warping. As the arrangement continues to develop, we note the parts of the field lines closer to the equatorial plane to warp further on. Moving vertically along the lines' length, nevertheless, we notice the diminishing twisting and thus the resulting opening up of the field lines (Fig. 6.1b; Contopoulos et al. 2006, Contopoulos et al. 2009, Contopoulos et al. 2015, Contopoulos 2015).

This coupling of the disk rotation and the ensuing toroidal magnetic field component is of such significant importance because it breaks the symmetry for these systems. That is to say, that with the typical magnetohydrodynamics laws and equations there should not be any correlation between the disk rotation and the toroidal magnetic field. Namely, according to magnetohydrodynamics, the magnetic field direction should not bear any dependence upon flow direction, unless any type of battery mechanism is involved in the process. Observational data concerning Faraday rotation measurements, nonetheless, strongly point toward an interconnection between the two (Contopoulos et al. 2009, Lynden-Bell 2015, Gabuzda 2015). All these data appear to support the theoretically expected results that Faraday rotation gradients should be mainly recorded in the clockwise direction relative to the origin of the jet close to the outflow and in the counterclockwise direction further out, independently of the disk's rotation (Contopoulos et al. 2009, Gabuzda et al. 2012, Gabuzda 2015, Contopoulos 2015, Christodoulou et al. 2016). In the first case, the observations record the innermost, near-axis jet component and main magnetic field, while in the latter case the data register the extended jet component and the return field. In addition, evidence also agrees with the Cosmic Battery supposition that reversing the direction of the accretion disk rotation flips the axial field but maintains the same toroidal field direction (Contopoulos et al. 2006, Contopoulos et al. 2015). Namely, the data is not biased by the observed target and the results are independent of the disk rotation.

Before continuing on, we present and discuss the assorted observational data supporting the validity of the Cosmic Battery mechanism. The primary source of information is none other than system outflows and in particular jets. The first piece of evidence retrieved is the aforementioned Faraday rotation measurement and gradients recorded in jets. When examining such objects in parsec scales (Very-long-baseline interferometry, VLBI data) we document the magnetic field evidence in the inner jet component that also displays the strongest field. What we record is a clear asymmetry, with the majority of rotation measurements displaying a clockwise gradient increase. This means that in the inner areas of the jets we note electric currents moving inward and toward its origin. On the contrary, kiloparsec-scale data (Very Long Baseline Array, VLBA data) positively record a counterclockwise gradient increase and electric currents flowing away from the jet origin (e.g., Kronberg et al. 2013). These trends are in agreement with what is proposed by the Cosmic Battery about the main, inner magnetic field and the outer, return field present in such situations.

Another very important piece of information is the encouraging agreement between the Cosmic Battery field evolution predictions and the observational data concerning X-ray binaries and the accompanying jets. The Cosmic Battery effortlessly explain the various stages of the systems' evolution as they periodically move along the hardness – intensity diagram (HID; hardness – luminosity HLD, or q-diagram, see Miyamoto et al. 1995, Kylafis et al. 2012, Kylafis & Belloni 2015a, 2015b). During this process, the arrangements regularly display the appearance of steady jets that later turn variable, intermittent, and episodic. Subsequently, these jets get far dimmer, less energetic and with far less observable magnetic energy. Afterward, the systems reenter quiescent states and the cycle is completed in order to restart once again.

Last but not least, there are some other environments where the Cosmic Battery mechanism could be applied and extract adequate result for the possible magnetic field generation. The first setting is the Solar interior, where the functioning Cosmic Battery can combine with the differential rotation of the assorted Solar layers. The association of the two processes can then contribute to the recorded Solar torsional oscillations influencing aspects of the Solar cycle (see e.g., Layzer et al. 1979, Goode & Dziembowski 1991, Contopoulos & Kazanas 1998). After that, we can examine the situations under which the currently observed Galactic magnetic field may have been formed with the assistance of the Cosmic Battery. We can see in Contopoulos & Kazanas 1998 that if we assume an AGN phase for the Milky Way, when the Galactic black hole grew to its current size and the magnetic field to equipartition, the galactic differential rotation has had sufficient time available to amplify and diffuse the field to its presently observed value.

The open question that we would now like to investigate is how effective and potent the Cosmic Battery mechanism is and how significant its reverberations are. We would therefore like to estimate its potential and if it could, at least in some cases, account for the generation of the large-scale magnetic fields recorded in astrophysical accretion disks as well as jets.

6.2. The Cosmic Battery model and smaller scales

An astrophysical battery mechanism in general consists of a bulk of matter, which is ionized and thus consisting of positive and negative matter electric units. The heart of any battery mechanism is the possibility to apply different forces to these aforementioned positively and negatively charged populations of particles. This results in the two groups developing different velocities orbiting the central object creating and sustaining hence an electric ring current.

The Cosmic Battery mechanism is present and functioning in all astrophysical environments that include an accretion disk and a radiation source, whatever that might be. The process in the assorted systems is of varying efficiencies, inversely proportional to their size. This is due to the radial distance of the innermost orbits from the central object, with black holes showing the fastest results and galaxies the more time consuming ones (see e.g., Contopoulos & Kazanas 1998, Table 1). We mark, nonetheless, that even in very low efficiency environments, the Cosmic Battery, for instance, can still account for the creation of the observed magnetic fields (see e.g., Lynden-Bell 2013, 2015). We want to clearly state, nevertheless, that the Poynting – Robertson Cosmic Battery is a secular process. The magnetic field generated by this procedure might in some cases be insignificant at small time intervals, but the process works continuously. This means that the buildup of magnetic field is unceasing and steadfast. This results in the consequent accumulation of dynamically significant field values, even in settings of lower efficiency.

In the environments we study, the systems consist of a central black hole and an accretion disk orbiting around it. This accretion disk can have a great variety of geometrical shapes, temperature profiles and mass distributions, azimuthal and radial velocity behaviors, etc. Theoretical works along with observational data suggest that objects like the ones studied here have an average temperature around 10^7 K. This means that the orbiting material in the disk possesses a temperature distribution high enough to radiate in the X-rays ($\mathrm{T} \gtrsim 10^7 K, E \gtrsim 1 keV$, Zhang et al. 1997, Kylafis et al. 2012). In addition, the data show that it is regularly expected from these systems to mostly consist purely of proton and electron populations.

We study the Poynting – Robertson drag and following the equations we deduce that a simple nonrelativistic approximation of the radiation force exerted on a plasma electron is equal to:

$$f_{PR}^{\phi} = -\frac{\mathcal{L}\,\sigma_T}{4\pi r^2 c}\frac{V_\phi}{c}, \qquad (6.2.1)$$

where V_ϕ is the target electron's azimuthal three-velocity and the Thomson cross section σ_T for an electron is:

$$\sigma_T = \frac{8\pi}{3}\left(\frac{\alpha\hbar c}{m_e c^2}\right)^2, \qquad (6.2.2)$$

with α the fine structure constant, $\hbar$ the reduced Planck constant, and m_e

the electron mass. The negative sign of the Poynting – Robertson force shows exactly that it acts against the disk's direction of motion, slowing thus down the material electrons. We additionally notice here that the corresponding force acting upon the disk ions f_i is at least about four and a half million times weaker than the force on electrons f_e, since from the Thomson cross section we have that:

$$\frac{f_e}{f_i} \propto \left(\frac{m_i}{m_e}\right)^2, \tag{6.2.3}$$

where m_i is the mass of the ions. From the above, we note that the smallest possible difference is achieved for plasma consisting of electrons and protons with $f_i = f_p$. The above means that in order for the calculations to be simplified, the radiation force acting upon the plasma ions can be very safely neglected. This one-sided radiation force results in the material electrons in the disk's inner edge having a smaller azimuthal velocity than the protons and thus lagging behind them. This mechanism is precisely the heart of the Cosmic Battery process and the source of the generated astrophysically significant poloidal magnetic fields (Fig. 6.2).

We now take a closer look at the system under examination. We wish to make the occurring process completely clear and understand how the radiation force is transferred throughout the disk volume and all its components. As explained above, the radiation acts predominantly on the

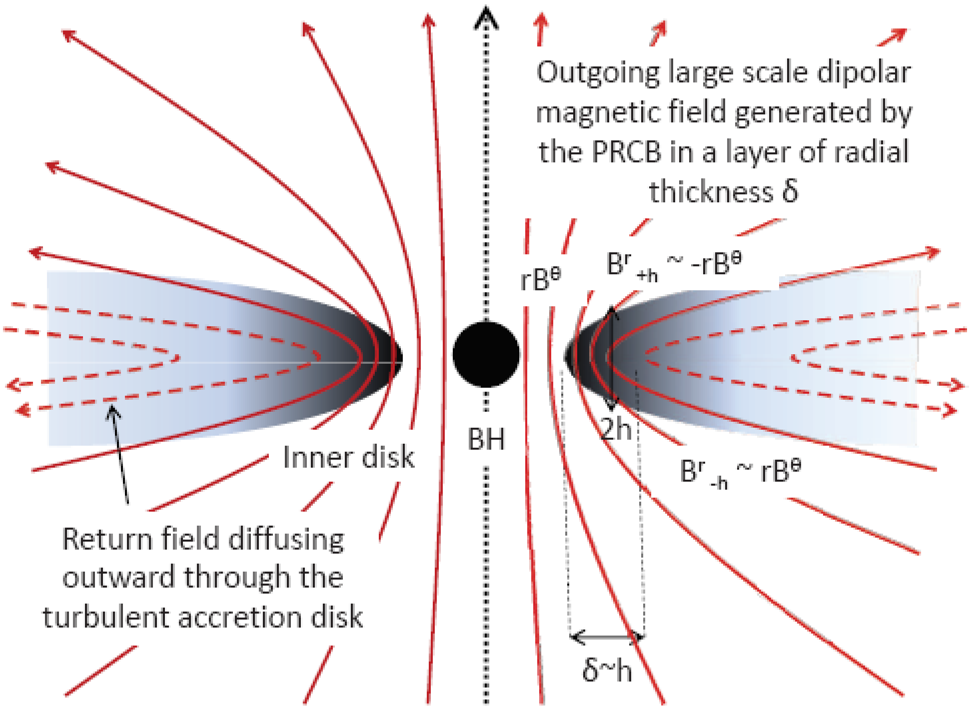

Figure 6.2: Innermost region of the accretion disk. The Cosmic Battery here is most effective in generating a dipolar magnetic field. Solid lines represent the outgoing straight field and dashed lines the return field. Figure 1 of Contopoulos and Papadopoulos 2012, MNRAS.

plasma electrons with the strongest force magnitude expected at the disk's inner edge, where the incoming radiation is maximally misaligned with the disk velocity ($\sim 90^\circ$). We yet detect the force being distributed to all the particles of the setup and the disk remaining, as a whole, in balance. If the radiation did not cause the electrons to brake, their orbits would remain circular, or at least elliptical. The presence of radiation, however, causes the less massive electrons to absorb photons anisotropically in their rest frame due to aberration of light and reemit them isotropically. This results in the electrons gradually losing angular momentum and inspiraling toward the central object as an inductive electric field develops. The effects of this radiation braking on electrons are then transferred to the material protons or ions through charge separation and the radial electric field that would develop between the two populations (e.g, Koutsantoniou & Contopoulos 2014).

We continue on to study the material situation by investigating its equations of motion. The equation of motion in General Relativity for a particle of mass m can be written as:

$$\frac{\mathrm{d}^2 x^\mu}{\mathrm{d}\tau^2} + \Gamma^\mu_{\alpha\beta}\, u^\alpha u^\beta = \frac{f^\mu}{m}\,, \tag{6.2.4}$$

where x^μ is the particle four-position, u^μ its four-velocity, τ the proper time, $\Gamma^\mu_{\alpha\beta}$ the Christoffel symbols (Choquet-Bruhat et al. 1977, Mueller & Grave 2009), and f^μ the present nongravitational four-forces. Applying the above equation to the radiation force on the plasma electrons and protons separately, we get for their four-positions x_e^μ, x_p^μ and four-velocities u_e^α, u_p^α respectively:

$$m_e \frac{\mathrm{d}^2 x_e^\mu}{\mathrm{d}\tau^2} + m_e \Gamma^\mu_{\alpha\beta}\, u_e^\alpha u_e^\beta = -e\mathcal{E}^\mu + f^\mu_{rad}\,, \tag{6.2.5}$$

$$m_p \frac{\mathrm{d}^2 x_p^\mu}{\mathrm{d}\tau^2} + m_p \Gamma^\mu_{\alpha\beta}\, u_p^\alpha u_p^\beta = e\mathcal{E}^\mu\,, \tag{6.2.6}$$

where $-e$ is the electron charge and $\mathcal{E}^\mu$ are the so-called "impressed electromotive field" components. Since for the masses of electron and proton we have that $m_e \ll m_p$, from the above equations we deduce that:

$$\mathcal{E}^\mu \approx \frac{f^\mu_{rad}}{e} \tag{6.2.7}$$

and hence, for the protons, we have the equation of motion:

$$\frac{\mathrm{d}^2 x_p^\mu}{\mathrm{d}\tau^2} + \Gamma^\mu_{\alpha\beta}\, u_p^\alpha u_p^\beta \approx \frac{f^\mu_{rad}}{m_p}\,. \tag{6.2.8}$$

We thus conclude that this is the way the radiation force acting practically only on the plasma electrons is transferred to the material protons or ions and hence the disk evolves as a whole while remaining in balance.

We continue on to carefully investigate the initial steps in the process that changes the considered environment and initiates the subsequent generation of magnetic fields. Keeping the above in mind, we expect the plasma, particularly near the disk's inner edge, to be turbulent. This plasma fluid, specifically due to its turbulence, induces the manifestation of finite conductivity in the matter flow, something that leads to the emergence of anomalous resistivity and anomalous magnetic diffusivity. In cases where this resistivity is of high enough values inside the disk and tenuous in the matter freefall regions, a steady state of magnetic field generation is reached. During this process, magnetic field loops are generated at the disk's inner edge with their inner footpoints accreting onto the compact object and their outer footpoints escaping to the system exterior at a steady rate. These procedures of viscosity and turbulence lead to the thermalization of the disk material and consequently to the dispersion of the rotation kinetic energy, and potential transformation of the disk into an ADAF equivalent (e.g., Contopoulos et al. 2006, Kylafis et al. 2012).

After the generation of magnetic fields with the processes and in the situations described above, we expect the subsequent evolution and expansion of the magnetic field loops and flux. In order to explore this procedure, we make use of the induction equation in one of its forms. For example, if we wish to study the evolution of the vertical component of the magnetic field B_z (G) in a system, we can utilize the following:

$$\frac{\partial B_z}{\partial t}=\frac{1}{r}\frac{\partial}{\partial r}\left\{\frac{\mathcal{L}\sigma_T V_\phi}{4\pi rce}-rV_rB_z+\eta r\frac{\partial B_z}{\partial r}\right\}, \tag{6.2.9}$$

where V_r the radial flow velocity, V_ϕ the rotational velocity, and η the magnetic diffusivity (see Contopoulos & Kazanas 1998, Contopoulos et al. 2006, and also Reyes-Ruiz & Stepinski 1996). This equation includes the Poynting – Robertson drag (first term), the material advection (second term), and the magnetic diffusion (third term).

The above equation is somewhat simplistic and utilizes the approximate, nonrelativistic form of the Poynting – Robertson force, as given from Equation (6.2.1). The main objective of this research, nevertheless, is the detail calculation of this Poynting – Robertson force and its aftermath on the various particles motion and trajectory, including all the relativistic effects. We hence consider some of the accretion disk models chosen for this study and select noteworthy regions for each one. We thus look into the models and select the inner and outer edge of these disks, their cross section central regions, and the maximum radiation magnitude areas. The cylindrical coordinates for these notable circular orbits can be found in Table 8a for the simplistic disk models (Sect. 4.2c, d, e) and in Table 8b for the complex disk models (Sect. 4.2f, 4.3b, d). For these special orbits, we show in Table 9a and Table 9b the recorded azimuthal radiation drag forces for the simplistic and the complex disk models respectively.

We continue further on to consider the above and we see that the consequent evolution of the magnetic field relies greatly on the material properties. Namely, if the material has large magnetic diffusivity further out and no diffusivity in the inner or central regions, we expect to encounter a steady magnetic field growth near the disk's inner edge. We should remember, nonetheless, that this field increase does not continue beyond

Disk	Slab				Wedge				Torus			
Spin	inner edge	center	outer edge	maximum	inner edge	center	outer edge	maximum	inner edge	center	outer edge	maximum
0	(6,0)	(12,0.5)	(18,0)	(6,0)	(6,0)	(12,0.5)	(18,0)	(6,0)	(6,0)	(12,0)	(18,0)	(6,0)
0.5	(4.233,0)	(7.699,0.5)	(12.709,0)	(4.233,0)	(4.233,0)	(7.699,0.5)	(12.709,0)	(4.233,0)	(4.233,0)	(7.699,0.5)	(12.709,0)	(4.233,0)
0.9	(2.321,0)	(4.5,0.5)	(6.983,0)	(2.312,0)	(2.321,0)	(4.5,0.5)	(6.983,0)	(2.312,0)	(2.321,0)	(4.5,0.5)	(6.983,0)	(2.312,0)

Table 8a: Cylindrical coordinates $\left(\varpi, z\right)$ of the radius of notable orbits in simplistic disk models.

Notes: We look into the inner and outer edge of each disk, the cross section central region, and the maximum radiation force magnitude area. The "Slab" disk can be found in Sect. 4.2c, "Wedge" in Sect. 4.2d, and "Torus" in Sect. 4.2e.

Disk	ORST				LFM				PD			
Spin	inner edge	center	outer edge	maximum	inner edge	center	outer edge	maximum	inner edge	center	outer edge	maximum
0	(10.488,0)	(12.420,1.136)	(13.952,0)	(6,0)	(6,0)	(12,0)	(18,0)	(6,0)	(8.608,0)	(14,0)	(20.103,0)	(8.608,0)
0.5	(9.464,0)	(12.822,2.287)	(16.180,0)	(4.330,2.5)	(4.233,0)	(7.699,0.5)	(12.709,0)	(4.233,0)	(8.567,0)	(14,0)	(20.174,0)	(8.567,0)
0.9	(8.665,0)	(14.547,3.756)	(19.105,0)	(2.598,1.5)	(2.321,0)	(4.5,0.5)	(6.983,0)	(2.312,0)	(8.536,0)	(14,0)	(20.229,0)	(8.536,0)
0.998	(8.478,0)	(15.019,4.222)	(20.071,0)	(2.598,1.5)	(2.25,0)	(2.5,0)	(3.711,0)	(2.25,0)	(8.529,0)	(14,0)	(20.242,0)	(8.529,0)

Table 8b: Cylindrical coordinates $\left(\varpi, z\right)$ of the radius of notable orbits in complex disk models.

Notes: We look into the inner and outer edge of each disk, the cross section central region, and the maximum radiation force magnitude area. The "ORST" disk can be found in Sect. 4.2f, "LFM" in Sect. 4.3d, and "PD" in Sect. 4.3b.

Disk	Slab				Wedge				Torus			
Spin	inner edge ($\times 10^{-14}$)	center ($\times 10^{-15}$)	outer edge ($\times 10^{-16}$)	maximum ($\times 10^{-13}$)	inner edge ($\times 10^{-14}$)	center ($\times 10^{-15}$)	outer edge ($\times 10^{-16}$)	maximum ($\times 10^{-13}$)	inner edge ($\times 10^{-14}$)	center ($\times 10^{-15}$)	outer edge ($\times 10^{-16}$)	maximum ($\times 10^{-13}$)
0	29.506	1.737	-2.565	2.951	28.933	8.017	-3.084	2.893	58.185	0.153	-1.830	5.818
0.5	198.919	26.641	-15.545	19.892	199.291	51.335	-19.375	19.929	340.212	12.177	-10.650	34.021
0.9	6005.161	466.971	-372.572	600.516	6275.739	1361.650	-500.786	627.574	7895.969	531.134	-231.979	789.597

Table 9a: Notable orbits azimuthal radiation drag (ergs) for simplistic disk models.

Notes: A positive sign reveals braking and a negative sign acceleration. We look into the inner and outer edge of each disk, the cross section central region, and the maximum radiation force magnitude area. The “Slab” disk can be found in Sect. 4.2c, “Wedge” in Sect. 4.2d, and “Torus” in Sect. 4.2e.

Disk	ORST				LFM				PD			
Spin	inner edge ($\times 10^{-14}$)	center ($\times 10^{-15}$)	outer edge ($\times 10^{-16}$)	maximum ($\times 10^{-13}$)	inner edge ($\times 10^{-14}$)	center ($\times 10^{-15}$)	outer edge ($\times 10^{-16}$)	maximum ($\times 10^{-13}$)	inner edge ($\times 10^{-14}$)	center ($\times 10^{-15}$)	outer edge ($\times 10^{-16}$)	maximum ($\times 10^{-13}$)
0	1.243	1.082	-4.143	-1.731	-11.283	-0.307	4.610	-1.128	-2.934	2.540	3.215	-0.293
0.5	2.979	3.992	-2.330	-10.170	-20.621	0.614	7.616	-2.062	-2.899	2.452	3.058	-0.290
0.9	5.438	1.019	-1.055	-2585.490	-140.917	-7.332	20.665	-14.092	-2.873	2.407	2.724	-0.287
0.998	6.206	0.802	-0.843	-877.246	14.179	-1.672	31.820	-5986.970	-2.902	2.400	2.690	-0.290

Table 9b: Notable orbits azimuthal radiation drag (ergs) for complex disk models.

Notes: A positive sign reveals braking and a negative sign acceleration. We look into the inner and outer edge of each disk, the cross section central region, and the maximum radiation force magnitude area. The “ORST” disk can be found in Sect. 4.2f, “LFM” in Sect. 4.3d, and “PD” in Sect. 4.3b.

the equipartition limit in the disk's inner edge, since at that point the disk gets critically perturbed and destabilizes. We note here that the generation of magnetic fields in the disk, even of small scales, is an event of paramount importance. This is because of the fact that these fields are responsible for regulating or triggering accretion procedures (see e.g., Lovelace et al. 2009). Namely, with the first appearance of a small-scale field and particle orbit alterations we detect the development of magnetorotational instabilities. These processes are persistent and mainly locally runaway, something that results in noteworthy field turbulence that increases viscosity and promotes accretion (see, however, Bisnovatyi-Kogan & Lovelace 2007, Christodoulou et al. 2008, Rothstein & Lovelace 2008). Similar processes also occur in the presence of a large-scale magnetic field. In such cases, nevertheless, instead of the appearance of MRI, we detect magnetized disk winds, material outflows, or jets, which also increase matter viscosity and bolster accretion. We therefore infer that a brand new analysis and magnetohydrodynamic approximation should be utilized in order to correctly study the material laws and evolution under these circumstances. In particular, such a reevaluation appears to be somewhat necessary when the field magnitude surpasses an amount of approximately 30% the equipartition value and the magnetic stresses, proportional to B^2 (see, Koutsantoniou & Contopoulos 2014), become significant. We return to this essential mechanism and the ensuing phenomena in the subsequent Section.

Our earlier approaches on the Cosmic Battery model were discussed in Koutsantoniou & Contopoulos 2014, Koutsantoniou 2014, and 2015. We explain our work up to that point and describe the first steps in creating computational codes that study the phenomenon and give relevant results for the magnetic field generation. We then examine Koutsantoniou 2022, 2023 and online material. There, we additionally explain why it is necessary to develop a specially designed and relativistic ray tracing code. These codes also take into consideration the volume and the rotation of the accretion disk, which in our study are the sources of the entire physical process. In these works, we also explain the extra steps necessary to be taken in order to account for the purely relativistic effects present in such environments. We take into consideration the time dilation caused by the black hole mass and the ensuing gravitational redshift, the Doppler shift due to the relative motion of the source, and the frequency shifts due to the frame dragging.

We should clearly state here that, as mentioned earlier, this emergence of magnetic flux ensues to the occurrence of magnetorotational instabilities. These instabilities are, nevertheless, rather mild and, apart from certain accretion events, do not greatly destabilize or damage the accretion disk. They do, however, contribute to the outward transfer of angular momentum (see Christodoulou et al. 2008, Koutsantoniou 2022, 2023). During these accretion incidents, we record quantities of matter experiencing orbit destabilization and infalling toward the central object. As they move inward, they drag the generated magnetic field along with them and form a nuclear, magnetized disk. This disk also rotates differentially, same as the outer, main accretion disk further out. This differential rotation further warps and amplifies the field up to the point where it can no longer be contained vertically. When the field magnitude reaches equipartition values, we expect the uncontainable field to violently erupt vertically and discharge blobs of magnetized material. These lumps rapidly move outward carrying away magnetic field loops along with them and are recorded as an episodic jet or outflow event (more details in Christodoulou et al. 2008).

As this unfolds, the field evolution in the main disk continues obeying the matter properties. That is to say, that depending on the magnetic diffusivity, one field footpoint may escape outward while the other moves inward and accretes onto the central object. This process leads to unsaturated and linear increase of the field magnitude. If, nonetheless, the disk possesses restricted magnetic diffusivity, the field cannot escape outward and gets dragged inward by the accreting material (see e.g., Contopoulos et al. 2006, Christodoulou et al. 2008, Koutsantoniou & Contopoulos 2014, Contopoulos 2019). This is anticipated to bring the reverse polarity near the straight polarity initiating magnetic reconnection and resulting in episodic asymmetric outflows (e.g., Christodoulou et al. 2008) and irreversible magnetic saturation. The governing magnitude determining the outcome is the magnetic Prandtl number $\mathcal{P}r_m$ (scalar), the ratio of kinematic viscosity to magnetic diffusion. Theoretical calculations (e.g., Lovelace et al. 2009, Contopoulos et al. 2015) revealed the existence of a critical magnetic Prandtl number $\mathcal{P}r_m^{crit}$ with a value $1 < \mathcal{P}r_m^{crit} < 10$, above which the field generation is restrained.

Moreover, computational simulations of relevant situations reveal that for certain values of magnetic diffusivity, and therefore resistive frequencies, the magnetic field diffusion itself leads to the constraint of MRI and further enhances disk stability (e.g., Fleming et al. 2000, Christodoulou et al. 2008). Such situations including anomalous resistivity are also often related to jet launch events. Furthermore, MRI simulations additionally show that as the systems develop, turbulent magnetic diffusivities appear in the accretion disks. These diffusivities are, nevertheless, not negligible but instead comparable to the turbulent viscosity. This means that as a large-scale magnetic field is generated in the configuration, the material freely allows it to diffuse outward and escape (Lubow et al. 1994, Kylafis et al. 2012).

We should mention, however, that there are cases where the presence of magnetic fields in the system is strong enough to modify their stability and restructure their matter distribution. Such a circumstance is expected to occur when the magnetic field is strong enough to influence the equilibrium of the innermost disk regions or the theoretically predicted radius of the innermost stable circular orbit as seen in an unmagnetized disk (Bardeen et al. 1972). Such situations were examined for example in Contopoulos & Papadopoulos 2012, where the impact of strong magnetic fields in the inner regions of accretion disks were explored. The study demonstrated that the radius of the innermost orbit varies noticeably, depending on the magnetic field encountered in the system. In particular, it was shown that the field present tends to destabilize the disk's inner edge and in certain spin – field conditions, even abolish the ISCO or an equivalent instance altogether. Calculations in general relativistic magnetohydrodynamics revealed that for smaller spin values $a < 0.8M$ with magnetic fields near equipartition, the ISCO, if it can be created, moves further out than expected. For faster spinning black holes with $a \gtrsim 0.8M$, on the contrary, the inner edge of the disk is expected to move further in than anticipated. It is additionally worth mentioning that such circumstances have noteworthy reverberations on any attempts of estimating the black hole spin utilizing emission lines or thermal continuum data.

Another noteworthy circumstance, where the present magnetic fields provide a notable contribution to accretion disk equilibrium and evolution are the aforementioned magnetically arrested disks (Narayan et al. 2003 and 2012, Penna et al. 2013a). In such environments, gas from a disk freefalls and accretes onto a central object while dragging along a substantial poloidal magnetic field. As these field components get pulled inward and accumulate, they concentrate and thus amplify furthermore until a point is reached, when they can markedly disrupt the accretion. The primary aftermath of this situation is that the matter accretion ceases to be axisymmetric and taking place from the disk's inner edge. On the contrary, the material is expected to elude the disk from larger radii than anticipated and in more episodic processes. Namely, instead of the typical smooth infall of matter, we expect more frequently accretion of discrete lumps of material, plunging with velocities notably below freefall. This has important consequences on the system evolution since it undoubtedly changes the energy conversion and transfer procedures.

6.3. The Cosmic Battery and the magnetic field evolution

In this Section, we look into the observational evidence pointing toward the operation and functionality of the Cosmic Battery. We examine how magnetic field information is broadcast outward via the magnetized material's motion and provides details about stellar or supermassive black hole systems. We investigate the disk material's physical characteristics and consider how these can affect the field evolution or suppression by looking into the plasma conductivity, the momentum diffusivity, and hence the induction equation. Finally, we execute some dimensional analysis calculations to estimate the necessary time needed for the Cosmic Battery mechanism to generate a magnetic field of equipartition values magnitude.

We start our magnetic field evolution investigation by mentioning that several studies of observational data reveal evidence pointing toward the presence and the effectiveness of the Cosmic Battery mechanism. This evidence is, for example, the apparent system preference to exhibit a specific Faraday rotation in their different areas (Fig. 6.3, Mahmud & Gabuzda 2007, 2009, Mahmud et al. 2009, Contopoulos et al. 2009, Gabuzda et al. 2012, Reichstein & Gabuzda 2012, Gabuzda 2015, and Park et al. 2019). The magnetized systems tend to display in their inner regions a helical magnetic field that increases the Faraday rotation in the clockwise direction on the sky relative to the jet origin. In contrast, in their outer regions the Faraday rotation increases in the counterclockwise direction. This means that the systems must be following a model where their inner and outer

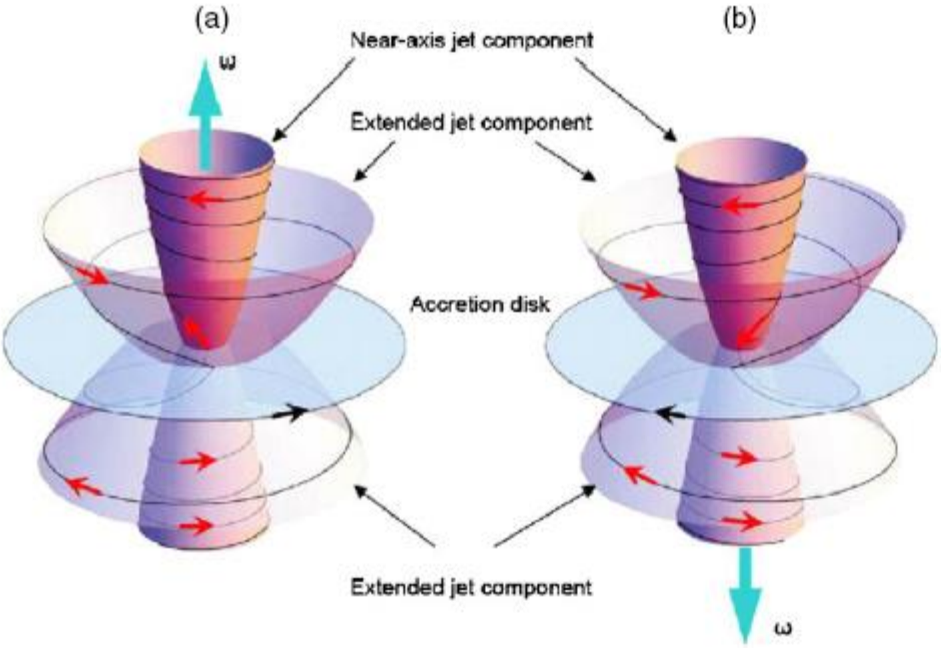

Figure 6.3: Magnetic field generation in a jet by the Cosmic Battery. The disk rotates as shown by the black arrows and with the angular velocity shown by the cyan arrows. The observer is located in the northern hemisphere at the *left* and in the southern hemisphere at the *right* figure. Figure 1 of Contopoulos et al. 2009, Astrophysical Journal.

magnetic fields are wound up and develop a specific form of amplification. In addition to the above, there are also studies examining magnetic evidence concerning jets and galaxies indicating the structure and evolution of magnetic fields (e.g., Lynden-Bell 1996, 2013, 2015). These studies collect and explain various evidence that furthermore provide confirmation of the operation of a battery-type mechanism. The provided evidence correlates, for instance, the galactic rotation with the line-of-sight magnetic field in the central regions of spiral galaxies, a fact that is in agreement with the expected Cosmic Battery magnetic asymmetry $B \| \omega$.

The aforementioned observations are not only in agreement with the Cosmic Battery model, but are one of its predictions. The inner regions of the system are governed by the outgoing straight magnetic field and the outer regions by the return field. We notice that, since magnetohydrodynamics does not have any “misbalanced” equations (only quadratic terms), it cannot display any preference toward any of the two directions of Faraday rotation. Namely, in case of random initial poloidal field, there should appear to be equal amounts of clockwise and counterclockwise gradients, since there is no relation between the disk rotation and the magnetic field polarity. The observational data, however, appear to be highly asymmetric and this asymmetry cannot be explained by any of the magnetohydrodynamic models. On the contrary, with the Cosmic Battery mechanism, the poloidal magnetic field direction is dictated by the disk’s rotation (see e.g., Contopoulos et al. 2009, Koutsantoniou & Contopoulos 2014, Gabuzda 2015). This means that, if the magnetic fields are indeed generated by this battery mechanism, these systems should have a near-axis poloidal magnetic field parallel to the angular velocity of the disk and an outer poloidal magnetic field antiparallel. Judging by the amount of observational data collected thus far, it is estimated that the probability of this asymmetry being recorded by chance is minimal, less than 1% (see Contopoulos et al. 2015).

From the description of the Cosmic Battery mechanism, we expect to note its greater impact in areas of larger velocities, areas with greater radiation disproportionality, or areas with larger velocity separation between the ions and the electrons. Considering the setups, we anticipate the consequent magnetic field generation and evolution to be highly dependent on the physical properties of the disk material. A significant factor for the field development is the plasma conductivity σ_{pl} (s^{-1}), and hence the magnetic diffusivity $\eta = c^2 / (4\pi\sigma_{pl})$, that primarily determines the field creation and buildup.

The best method to estimate the field development is by using the ratio of viscosity to magnetic diffusivity, or the inverse Prandtl number:

$$\left(\mathcal{P}r_m\right)^{-1} = \frac{\eta}{\nu}, \tag{6.3.1}$$

where ν the momentum diffusivity or viscosity ($g \cdot cm^{-1} \cdot s^{-1}$) and η the magnetic diffusivity ($cm^2 \cdot s^{-1}$). Examining the environments using the inverse Prandtl number, we note the presence of a critical magnetic Prandtl number

$\mathcal{P}r_m^{crit}$ with a value of $1<\mathcal{P}r_m^{crit}<10$. For $\mathcal{P}r_m \lesssim \mathcal{P}r_m^{crit}$ the material resistivity is high and the magnetic diffusion dominates the system (Contopoulos & Kazanas 1998). The generated magnetic loops have two sections with their footpoints moving in opposite directions. The exterior footpoint drifts and diffuses outward assisted by viscosity and turbulence, escaping the system along rapidly rotating outflows, while the inner footpoint infalls toward the central object. This process leads to consistent field amplification and the increase of the magnetic flux of the area linearly in time and without limit, possibly sustained even up to equipartition values. This environment of robust magnetic fields can often additionally result in episodic expulsion events and structures (e.g., Christodoulou et al. 2008, Contopoulos 2015).

If, on the contrary, it is $\mathcal{P}r_m > \mathcal{P}r_m^{crit}$ we detect low resistivity and thus the magnetic field not diffusing outward. Instead, the field gathers up toward the central object as much as the inner edge of the disk allows (see Matsumoto 1996, Lovelace et al. 2009, Contopoulos & Papadopoulos 2012). The Poynting – Robertson mechanism thus gets balanced by the dominant inward advection of the return field. We then expect to note only a restricted or moderate amplification of the magnetic field that reaches saturation within a few accretion times (Fig. 6.4). In such situations, we also expect to see the field growth hindered by magnetic reconnection and material outflows.

In more detail, let us examine anew the disk condition along with the induction equation for the plasma. The rate of change of the magnetic field B concerning material of velocity u and magnetic diffusivity η, including radiation forces f_{rad} is given by:

$$\frac{\partial B}{\partial t}=-\nabla\times\left(-u\times B+\eta\nabla\times B+\frac{f_{rad}}{e}c\right). \qquad (6.3.2)$$

Respectively, the equation providing the development rate of the poloidal magnetic flux Ψ ($1Mx=1G\cdot cm^2$) inside radius r is:

$$\frac{\partial\Psi}{\partial t}\approx 2\pi rc\left[(u\times B)^{\phi}+\eta(\nabla\times B)^{\phi}-\frac{f_{rad}}{e}\right]. \qquad (6.3.3)$$

(Macdonald & Thorne 1982 and also Bisnovatyi-Kogan et al. 2002 for a generalized expression). Each of the above equations includes three components of the phenomenon and the involved processes. The first term $u\times B$ of the sums measures the advection effects on the field generation as parts of the material are drawn inward by accretion. The second term $\eta\nabla\times B$ measures the effects brought on by the field diffusion and is, as expected, directly proportional to the magnetic diffusivity η. We anticipate the magnetic diffusivity dominating in the outer regions of the accretion disk, where it is rather significant (see van Ballegooijen 1989, Lubow et al. 1994, Lovelace et al. 1994). Consequently, we expect there the return field diffusing and spreading outward in the disk, a fact directly responsible for the sustained magnetic field generation and the avoidance of saturation. The third term f_{rad}/e is what calculates and determines the impact of the Poynting – Robertson drag force exerted onto the plasma particles (for this

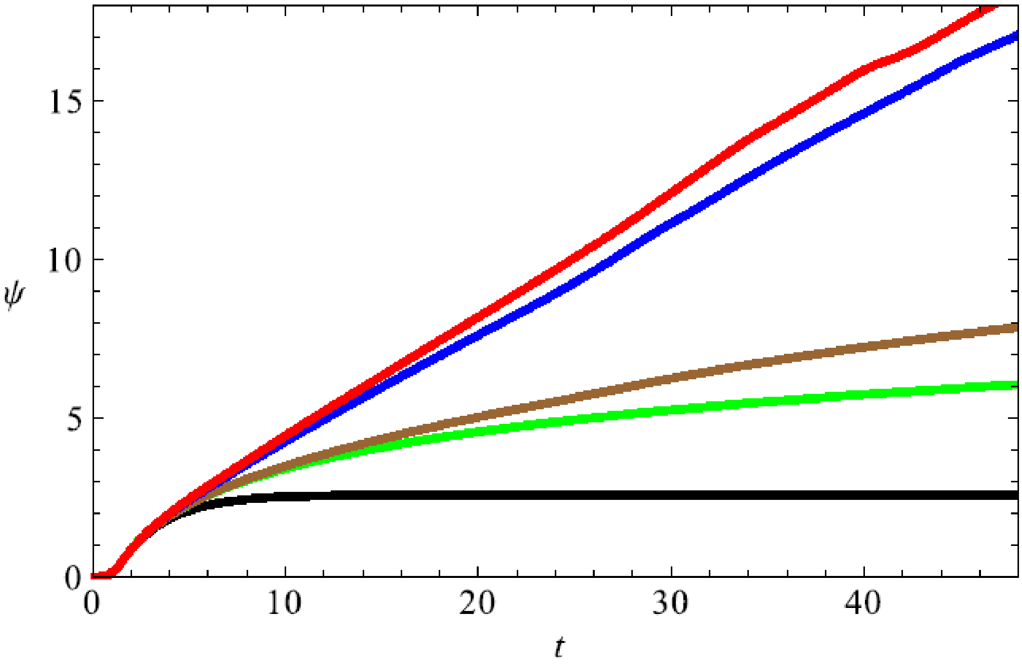

Figure 6.4: Cosmic Battery at work: evolution of the magnetic flux Ψ over time for various values of the inverse magnetic Prandtl number. Curves from *top to bottom*: $\left(\mathcal{P}r_m\right)^{-1} = \frac{\eta}{\mathrm{v}} = 0.2,\ 0.4,\ 1,\ 10,\ 100$ with finite optical depth. Figure 3 of Contopoulos et al. 2015, Astrophysical Journal.

work, the electrons). This hence provides the Cosmic Battery contribution to the generation of axial magnetic field lines near the disk's inner edge that subsequently close further out. There are studies, nonetheless, that, contrary to the above, suggest that amplified viscosity and magnetic diffusivity in the disk counteract the magnetic field generation and eventually avert the creation of large-scale fields (e.g., Lovelace et al. 2009).

Let us now assume that the ratio $\left(\mathcal{P}r_m\right)^{-1} = \eta/\mathrm{v}$ is close to the critical value $\mathcal{P}r_m^{crit}$ discussed above. Near the disk's inner edge the material motion and the Poynting – Robertson braking cause the vigorous creation of new magnetic field loops that are locked onto the matter and move along with it. Subsequently, we record the disk's differential rotation causing these loops to twist and creating electric currents accompanied by toroidal magnetic torques at their central parts. Moving upward, away from the equatorial plane and the main disk quantity, we note the lines' twisting to lessen and further away the loops extending and opening up (see Newman et al. 1992 and Goodson et al. 1997). This opening and restructuring of the loops then creates two parts, an inner and an outer segment, which as expected have the opposite polarity. The main disk field polarity remains as mentioned earlier: the inner footpoints possess a field parallel to the disk's angular velocity and the outer footpoints, antiparallel.

Disk Spin	Slab (h)	Wedge (h)	Torus (h)	ORST (d)	LFM (d)	PD (d)
0	670.6	683.9	340.1	1159.7	73.1	403.2
0.5	70.2	70.1	41.0	436.5	28.2	406.1
0.9	1.27	1.22	0.97	219.0	2.26	408.3
0.998	-	-	-	187.7	-	403.8

Table 10: Time required for equipartition magnetic fields generation around a $M = 5M_{Solar}$ black hole by the Cosmic Battery.

Notes: The first three columns measure time in hours and the rest in days. Models Slab, Wedge, Torus, and LFM have their inner edge at the ISCO radius. When approaching maximal black hole spin ($a \to 1$) these disks' inner edge converges toward the static limit, a fact that precludes the disk's stability and thus lifetime expectancy. Models ORST and PD require significantly more time since the disk's inner edge is notably further out. LFM disk is geometrically identical to Torus, but is instead quasi-opaque. Comparison of the two setups reveals the importance of the material opacity and its consequences on the exerted radiation forces.

Accreting material later on brings one polarity of the field toward the compact object, with high conductivity holding there. At the same time, diffusion carries the opposite polarity outward to larger distances. The result is that the magnetic field does not get trapped in the system; it keeps expanding and covering steadily larger areas, and thus growing without limit. If, in contrast to the aforementioned processes, the magnetic field lines do not open up, the magnetic field gets trapped in the system and cannot grow. This results in quick saturation of the Cosmic Battery mechanism, with its final values remaining well below equipartition. The opening up of the magnetic field lines is thus of crucial importance for the mechanism and after being a theorized process, its significance was also shown numerically with computational simulations (e.g., Contopoulos et al. 2015).

Another additionally important topic concerning the generation of the magnetic field, albeit perhaps surprising, is the structure of the material velocity vector field. This is because the material vorticity is, mostly for topological reasons, closely related to the development of magnetic fields (see Kulsrud et al. 1997).

Finally, something that should also be stated explicitly here, is that the Cosmic Battery mechanism can perhaps at some point no longer be considered as potent due to its own effects. In the case where the generated magnetic field becomes so strong as to approach equipartition and affect the stability, dynamics, and evolution of the accretion disk (e.g., a MAD state disk) and hence the heart of the entire procedure (see Contopoulos et al. 2018), the process of fields generation should be revisited and redrawn.

Before concluding, we calculate the approximate time required for the Cosmic Battery to create an equipartition-level magnetic field $B_{eq} = 10^7 G$ at the inner edge r_{inner} of various accretion disks. The central black hole is assumed to be of mass $M = 5M_{Solar}$ and the assorted disks are those discussed in Chapter 4. In order to acquire this information we perform dimensional analysis of the aforementioned induction equation and obtain:

$$\tau_{CB} \sim \frac{e\, B_{eq}\, r_{inner}}{c\, f_{rad}^{\phi}}\,. \qquad (6.3.4)$$

The results of our calculations are drawn using the `Infinity` code results and can be seen in Table 10.

We move on to examine Table 10 and discuss the results presented along with their significance. Let us remember that disks Slab, Wedge, Torus, and ORST are opaque (Sect. 4.2) and disks LFM and PD are semi-opaque (Sect. 4.3). Additionally we remember that disks Slab, Wedge, Torus, and LFM have their inner radii situated closer to the central object, while disks ORST and PD are of quite broader diameters. Keeping in mind the above information, the provided numerical results for the time necessary to generate equipartition-level magnetic fields via the Cosmic Battery are intelligible and comply with their expected behavior.

First, we mark models Slab, Wedge, and Torus rapidly generating strong magnetic fields in all situations. This is due to the facts that they are very condensed and also opaque radiation sources. This thus allows for increased quantities of light reaching the disk material and consequently modifying the electron kinematics promptly. Among these three models, we detect Slab being the weakest one, something that is expected since it is also the model with the smallest emitting surface. Wedge follows closely after Slab since it is a similar setup, but with a somewhat increased surface and more effective geometrical characteristics. Torus again proves to be the most potent arrangement as it is very voluminous with a fairly extended emitting surface (surpasses all), is opaque (surpasses LFM and PD), and has a more compact structure (surpasses ORST and PD). Further on, we find LFM which in general is weaker than PD, but quite more concentrated and thus positively more effective. Afterward, we encounter PD that is a model with increased material density but with larger radius and hence more spread out, something that rather decreases its efficiency. Finally, we apply a special evaluation for the ORST disk, whose time capabilities vary significantly with the spin. This is, however, also anticipated since the disk's volume considerably changes with the spin and thus so do the required time intervals. Namely, for small spins the emitting surface is rather limited and therefore inadequate. As the spin increases, nonetheless, the disk volume increases and soon its capabilities surpass PD.

We thus conclude that depending on the disk characteristics (opacity, inner edge radius, etc.) and the central object's spin, we detect varying but fairly promising results about the effectiveness of the Cosmic Battery in generating equipartition-level magnetic fields. The required time interval for this ranges from less than an hour up to several days or months for wider, colder, or more translucent disks. Additional information about the Poynting – Robertson Cosmic Battery timescales to equipartition-order magnetic fields can be found in Kylafis et al. 2012.

6.4. The Cosmic Battery mechanism further out

In this Section, we examine additional applications and effects the Cosmic Battery mechanism can have further away from the accretion disk and its usually perturbed inner edge. We consider thus the connection between the Cosmic Battery and the magnetorotational instability, the jet region and formation, and finally look into the ramifications of this mechanism on X-ray binary outflows and cycles.

As we have explained earlier, all of the aforementioned phenomena are connected or can be triggered and regulated by the Cosmic Battery mechanism through its processes, which extract energy from the black hole and the accretion disk rotation. This is because, as we mentioned previously, the radiation absorption cross section is inversely proportional to the square of the target particle's mass. This results in the disk's thermal radiation to be unilaterally absorbed and mostly utilized by the plasma electrons and not the ions. This fact then leads to the deceleration of the negative charges and the development of a relative motion and an ensuing electric ring current inside the disk. This current is recorded in the azimuthal plane and thus causes the generation of magnetic field loops in the poloidal plane. This procedure that modifies the electron velocity and consequently generates a magnetic field in the disk is what we record as the Cosmic Battery mechanism. Depending then on the disk material characteristics, these fields can sometimes be negligible and at some other times they can reach equipartition values, possibly even leading to disk or accretion disruptions (e.g., magnetically arrested disks).

6.4.1. Magnetorotational instability

We start by reexamining the magnetorotational instability, which is one of the primary aftermaths of magnetic field presence in the disk plasma. The field developed by the Poynting – Robertson Cosmic Battery is expected to trigger somewhat mild events of MRI that perturb, yet do not destroy the disk. Events of the sort, however, are anticipated to lead to the outward expulsion of notable amounts of angular momentum from the disk (e.g., Christodoulou et al. 2008). This results in increased material viscosity that can initiate accretion, but does not intensify the instabilities brought on by the field. On the contrary, we expect the poloidal magnetic field generated by the Cosmic Battery, along with its subsequent diffusion, to eventually suppress any turbulence or instability brought on (see Contopoulos et al. 2006, Christodoulou et al. 2008).

Specifically, this instability attenuation is anticipated to be amplified by increasing values of the resistive frequency. This is principally determined by the plasma resistivity and in particular the anomalous resistivity. The anomalous plasma resistivity has been repeatedly looked into as a possible source of magnetorotational instability suppression and a factor that facilitates the formation of jets. The models looked upon involved moderate to high resistivity and demonstrated a steady and robust magnetic field amplification that results in episodic bipolar outflows. In general, we should remember it has been shown in many studies that field diffusion works against the magnetorotational instability and hence contributes to the accretion disk stability (see e.g., Christodoulou et al. 2008, but also Lovelace et al. 2009).

We should also note here, that the generated magnetic turbulence could additionally reorganize the accretion disk structure in notable ways. One such example is the event where the generated magnetic field can transpose the innermost stable circular orbit of the disk away from the typical ISCO radius and into a different equilibrium radius (see e.g., (Contopoulos & Papadopoulos 2012).

6.4.2. Blandford – Znajek process

Another relevant phenomenon that is active in this environment and should be mentioned here is the Blandford – Znajek process. When magnetic fields of nonnegligible magnitude are present in arrangements of compact objects surrounded by an accretion disk, they give rise to phenomena that affect the structure of the disk and determine its evolution (see Blandford & Znajek 1977, Livio et al. 1999, Lee et al. 2000, Komissarov 2001, McKinney 2005, Komissarov et al. 2007, Penna et al. 2013a, Parfrey et al. 2019, Mahlmann et al. 2020, Konoplya et al. 2021).

In principle, the Blandford – Znajek process and the Penrose process (Penrose & Floyd 1971) are the two most promising procedures capable of initializing and affecting the launch of astrophysical jets. The generation and expansion of noticeable poloidal magnetic fields in the system allows for the escape of angular momentum from the rotating magnetosphere of the black hole inside the ergosphere. This consequently leads to the extraction of spin energy and angular momentum from the rotating compact object.

We therefore deduce that the operation of the Cosmic Battery generates magnetic fields whose presence introduces new physical components and circumstances (e.g., Bini et al. 2011b, Contopoulos & Papadopoulos 2012). This is because the presence of electric or magnetic fields within the disk material transposes the theoretically anticipated radii of equilibrium and the stable orbits (Bardeen et al. 1972, Misner et al. 1973). Furthermore, under many circumstances the field interactions can force the particles to follow trajectories that do not track the typically expected geometries (circular, elliptic, or accreting). These altered physical conditions and equilibria are anticipated to result in different geometrical forms and shapes for the accretion disk, as well as new radii for the disk's inner edge, its maximum height, the material density profiles, etc. (see e.g., geometrically thicker magnetically arrested accretion flows).

We consequently understand that under such convoluted circumstances, we may record structural forms and equilibrium conditions in the entire configuration that are very different from the expected ones. These particular situations should thus be considered and examined anew, since increased accuracy and more exact predictions including the extra fields for the system evolution are necessary.

6.4.3. Jets and outflows

We continue further on to examine the next fairly common phenomenon related to accretion disks around compact objects, the collimated and accelerated system outflows, the structures we call jets. The Blandford – Znajek process we examined above is for example capable of adequately describing the formation, ejection, and development of outflow streams from supermassive black holes. Furthermore, this process is considered to play a very important part in the generation and evolution of gamma-ray burst phenomena (e.g., Popham et al. 1999, Lee et al. 2000, Wheeler 2004).

Substantial and extended work considering astrophysical jets originating in compact object systems can be found in Blandford & Payne 1982, Contopoulos & Lovelace 1994, Contopoulos 1995, Komissarov 1999, Blandford 2001, Blandford et al. 2002, Vlahakis & Königl 2004, Nakamura et al. 2018, Park et al. 2019, Yuan et al. 2019, Chatterjee et al. 2019, Spruit 2020, Mahlmann et al. 2020, and Komissarov & Porth 2021. Theoretical and observational studies of collimated outflows have thus far strongly indicated that astrophysical jets are magnetically driven and encompass helical magnetic fields. In addition to theoretical researches, abundant observational studies provide valuable information on the subject. For example, we can see Gabuzda et al. (2004, 2008, 2012, 2014a, 2014b, 2015a, 2015b), Gabuzda (2006, 2015), Mahmud & Gabuzda (2007, 2008, 2009), Mahmud et al. (2009), Contopoulos et al. (2009), O'Sullivan & Gabuzda (2009), Reichstein & Gabuzda (2012), Murphy et al. (2013), Mahmud et al. (2013), Murphy & Gabuzda (2013), and Christodoulou et al. (2016).

One of the most significant questions still remaining unanswered is the nature and the sequence of procedures leading to the ejection of these magnetized and collimated outflows. The Cosmic Battery mechanism discussed here is a simple and straightforward mechanism applicable in numerous environments that can effortlessly provide explanations for these situations. These suggestions include the formation and the disappearance of strongly or mildly relativistic jets, as well as their variability in various configurations such as X-ray binaries (see e.g., Kylafis et al. 2012, Kylafis & Belloni 2015a, 2015b). This is because the mechanism is anticipated to commonly generate poloidal magnetic fields at the origin of jets that can progressively reach equipartition-level values. These fields are subsequently transformed into large-scale helical magnetic fields due to the disk's differential rotation and the matter outflow.

The field loops examined are generated centered near the disk's inner edge. As discussed earlier, when the material resistivity is moderate or high, the magnetorotational instability developing allows angular momentum to steadily leak outward. This results in matter components falling into lower orbits dragging along magnetic field segments, creating a new and magnetized nuclear disk (Christodoulou et al. 2008). Since this disk is also rotating differentially, the field is subsequently further intensified until it is uncontainable and unwinds vertically in episodic, usually bipolar but asymmetric jet events and field bubbles (e.g., Shibata et al. 1990, Contopoulos 1995, Matsumoto et al. 1996). Since the helical magnetic field remains strong, the outflows remain collimated and escape the system concentrated along the rotation axis. This point is rather important, as we should remember that the generation of astrophysical jets is unattainable without the presence of steady large-scale dipolar magnetic fields threading the driving engine near the source. We should also remember that even in cases where the Cosmic Battery is not at maximum efficiency, as a secular mechanism it works continuously. Therefore, under all circumstances the Cosmic Battery has ample time to generate and accumulate the required magnetic flux magnitude in order to allow the launch of a jet.

Studies of relativistic compact object jets strongly indicate that these outflows are comprised of two separate main segments, an inner and an outer component. The very narrow inner component is expected to record strongly relativistic speeds and to possess a more tightly wound up magnetic field. The outer component is anticipated to be of a significantly more extended volume and of notably lower velocity, almost certainly nonrelativistic (see e.g., Pelletier et al. 1988, Ferreira et al. 2006). The inner, electron – positron component is what we consider as the jet spine and is governed by the Blandford – Znajek effect, while the outer part, the sheath, is created and seeded by the electron – proton disk wind (see e.g., Contopoulos 2019). The ejected material is subsequently accelerated and pushed outward along the inner outflow region, dragging the generated magnetic field along with it and seeding it into the interstellar or intergalactic space. Following the Cosmic Battery method and the field warping, we also deduce that these inner jets should carry a poloidal magnetic field parallel to the disk angular velocity and the extended outer jets, the disk winds, antiparallel.

Apart from the ejection of jets, the radiation field created by the hot disk also has further consequences on the subsequent evolution of the accretion flow and hence the development of the outflows themselves. For example, it is suggested in certain researches that large-scale magnetic fields trigger matter outflows or jets that additionally facilitate accreting events (see e.g., Lovelace et al. 2009). The magnetic loops at the bottom of the structure, as explained earlier, due to the disk's differential rotation gradually inflate, twist, and open up. The axial magnetic field, nonetheless, along with the outflowing and expanding plasma interlocked with it, remains very well collimated and close to the system axis and jet line. This has a significant repercussion, especially when applied to objects such as quasars that have not yet had enough time to build up large enough magnetic fields. What one would expect to happen in such a case is that these systems keep generating magnetic flux until they cross a certain threshold. After they do so and the magnetic fields start playing a more important and perhaps decisive part in the system evolution, these fields could be responsible for the generation and launching of radio jets. In such a case, the arrangement transforms from radio quiet to radio loud (see e.g., Tchekhovskoy et al. 2010).

We continue on to review the collected observational data that provide information about the Cosmic Battery mechanism and its connection to jets. Observations about compact object jets are provided by numerous instruments and experiments such as the Very-long-baseline interferometry (VLBI, e.g., Zavala & Taylor 2003, Pushkarev et al. 2005. Vitrishchak & Gabuzda 2007, Croke & Gabuzda 2008, Kharb et al. 2009, Croke et al. 2010, Taylor & Zavala 2010), the Very Long Baseline Array (VLBA, Walker et al. 2000, Zavala & Taylor 2002, 2003, 2004, 2005, Taylor & Zavala 2010), Monitoring Of Jets in Active galactic nuclei with VLBA Experiments (MOJAVE, e.g., Homan & Lister 2006, Coughlan 2010, Hovatta et al. 2012, 2014), *Hubble* Space Telescope (HST, e.g., Tsvetanov et al. 1999), Very Large Array (VLA, e.g., Zavala & Taylor 2002, 2004, Herrnstein et al. 2005, Carilli & Taylor 2002, Krause & Löhr 2004, Govoni et al. 2010), *Chandra* (e.g., Kronberg et al. 2001 and references therein), International Gamma-Ray Astrophysics Laboratory (INTEGRAL) and *Swift* (e.g., Bonafede et al. 2010 and references therein), Röntgensatellit (ROSAT, e.g., Widrow 2002), *XMM-Newton* (e.g., Widrow 2002 and references therein), Skinakas Observatory (SKO, e.g., Reig & Fabregat 2015, Reig et al. 2016), Event Horizon Telescope (EHT, e.g., M87: Event Horizon Telescope Collaboration 2019a, 2019b, 2019c, 2021a, 2021b, Sgr A*: Event Horizon Telescope Collaboration 2022a, 2022b, 2022c, 2022d).

Careful examination of all the aforementioned studies reveals valuable information about the accreting systems, the jets, and the indispensable magnetic field. As we see, one of the best methods available to use in such researches is the examination of the Faraday rotation[13]. Namely, we investigate the noted Faraday rotation gradient around the central object, which is also the assumed source of the jet. The observational data exhibit a highly preferable configuration for these systems to display clockwise rotation measurement gradients in parsec to decaparsec scales and a counterclockwise one in kiloparsec scales (e.g., Contopoulos et al. 2009, Gabuzda et al. 2012, 2015, Christodoulou et al. 2016). This inner clockwise and outer counterclockwise Faraday rotation gradient predominance robustly suggests a direct coupling between the disk rotation and the poloidal magnetic field detected. This is because the disk's differential rotation leads to the twisting and expansion of the generated magnetic loops, an event that breaks the symmetry in the toroidal field direction. This datum consequently conduces to the observed prevalence of the clockwise Faraday rotation gradients on the sky for smaller scales and counterclockwise for larger scales, independently of the disk rotation direction.

The above facts also translate to a stronger electric current moving toward the compact object and the origin of the jet or smaller regions and a weaker electric current flowing outward in the jet's outer sheath and external system regions (see e.g., Kronberg et al. 2011 & 2013). We should additionally note that this fact also agrees with the Cosmic Battery model operation and the interweaving between an explicit axial electric current and

---

[13] *Faraday rotation or Faraday effect is a magneto-optical phenomenon that induces the incoming radiation's polarization rotation proportionally to the projection of the magnetic field along the incoming light's direction. In such situations, the left and right light polarizations propagate in slightly dissimilar speeds, resulting in a relative phase shift and thus the rotation of linear polarization.*

a steady Faraday rotation gradient. The observational evidence provided by a multitude of extragalactic radio jets observations indicate a distinct majority of jets displaying monotonic Faraday rotation gradients, a fact that strongly indicates the presence of a (nested) helical magnetic field in the jets.

We should also mention here that the aforementioned researches were designed in the best way possible and taking every precaution to avoid biases in every step of the observational selection and the theoretical analysis. Therefore, it is rather safe to assume the validity of the provided results and the consequent conclusions, since the probability of such outcomes being caused by observational selection biases or chance, is estimated to be below 1%.

6.4.4. X-ray binaries and hardness – intensity diagrams

In this final Section, we examine the smaller-scale evolutionary processes of X-ray binaries and look into the possible influences of the Cosmic Battery. X-ray binaries are systems of binary stars that include one typical "donor" star (main sequence star, red giant, or white dwarf) and one "accretor" compact star (neutron star or black hole). These X-ray binary systems are illuminated due to matter transference from the more gas-rich companion to the compact component. During this process, matter is stripped off the companion star's external layers and creates a short-lived accretion disk around the compact object (e.g., Lasota 2016). This reconfiguration compels the infalling matter to release its gravitational potential energy and emit it as luminous energy in the band of X-rays. Abundant theoretical and observational information concerning these intriguing arrangements can be found for instance in Podsiadlowski et al. (2002), Tauris & van den Heuvel (2006), Tetarenko et al. (2016). Considering the X-ray binaries' evolutionary sequence, periodicity, and variability timescales we can find detailed information for the various different situations in van der Klis & Bonnet-Bidaud (1989), van der Klis (1995, 2004), Uttley et al. (2005), Koljonen et al. (2010), Kazanas (2015), Reig & Fabregat (2015), Reig et al. (2016), Lasota (2016). Valuable information about these systems, their evolution, cycles, and jets can be found, for example, in Belloni 2010a, 2010b, & 2010c. Additional information also including the assorted effects of the Cosmic Battery mechanism, the disk variability, and the recurring hardness – intensity diagram loops (HID, also known as q-diagram, see Miyamoto et al. 1995) can be found in Kylafis et al. 2012, Kylafis & Belloni 2015a, 2015b.

What is known from observations (see e.g., in Sect. 6.4.3) is that XRBs including a black hole, typically display the presence of outflows periodically. Namely, we detect a steady and compact radio jet in their hard state, a discontinuous and eruptive jet as they move toward a softer state, and a weaker, not always easily observable yet still present jet in their soft state. There is huge phenomenology concerning the XRBs and their changes as they follow the hardness – intensity diagram over and over again with multiple different ways from system to system. There appears, however, to be no concrete answer up to this point, as to what triggers all these changes and what is responsible for the variability of these environments.

From the previous Sections and arguments, we can see that the Cosmic Battery is a phenomenon capable of providing some explanations and predictions for these objects, especially concerning the launching and disappearance of jets, which is closely coupled to the accretion disk's form and state. We therefore contemplate the possibility of a connection between the XRBs and the Cosmic Battery, since they appear to be closely related. This is because the Cosmic Battery can effortlessly provide the formation and evolution of magnetic fields and therefore jets in XRBs. As we can see below, the Poynting – Robertson Cosmic Battery provides the appropriate conditions for jet formation and destruction as the accretion disk changes forms following the typical XRB cycles (Fig. 6.5).

A fact also worth mentioning here is that X-ray binaries evolution timelines in the vast majority of cases can be approximated with the Cosmic Battery magnetic field generation and total diffusion very sufficiently. Whatever the precise mechanism responsible for the jet formation might be, the necessary condition for the launching to take place is the existence of a large-scale magnetic field. Without the existence of such a field, the formation of a jet is unfeasible. The magnetic field generation capability of the Cosmic Battery model can therefore provide a crucial part of the XRBs cycle and a solution to this puzzling process. Even though in some cases the

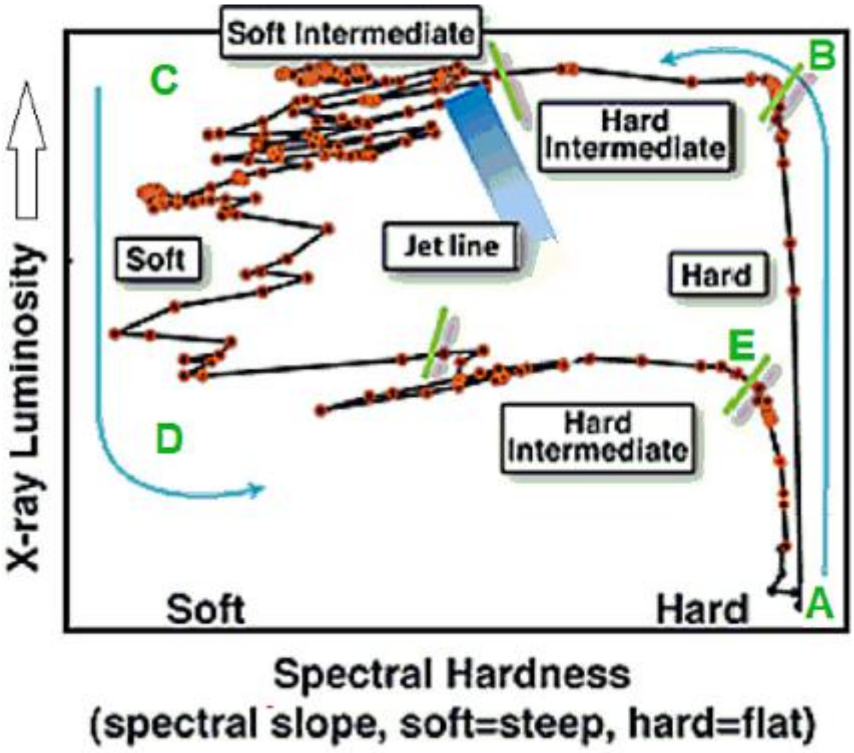

Figure 6.5: Hardness – Intensity Diagram (HID), also known as q-diagram. It depicts the cycle X-ray binaries follow changing their spectral hardness and intensity. We can see their rise into high state, the multiple crosses of the jet line and their return to the quiescent state (see Belloni 2010a, 2010b & 2010c, Kylafis et al. 2012).

Cosmic Battery is not efficient enough to quickly produce the necessary magnetic fields, we should keep in mind that these binaries reside in situations like this for extended periods of time. This implies that the sources, even in cases of small field generation rate, have abundant and enough time to build up the field they need in order to continue onto the jet formation.

We go on to investigate attentively the outflows development in these configurations and their interconnection with the magnetic fields present, as well as the accretion disk status. First of all, we should state clearly that the formation and accelerations of jets in such circumstances are expected to be initiated and supported by two classes of mechanisms, centrifugal driving (Blandford & Payne 1982) or the plasma gun (magnetic towers, Contopoulos 1995). These mechanisms are an essential part of the process, since the presence of large-scale magnetic fields at the origin of jets is a necessary condition for their ejection. Therefore, we need to investigate the situations where the Cosmic Battery operates efficiently and generate such large-scale fields near the central object. When, nonetheless, the occurring procedure is of reduced efficiency, we expect the magnetic fields generated to be notably weaker, directly affecting thus the outflows emission and power.

We start by assuming an X-ray binary system in a quiescent state (region “A”, Fig. 6.5). A steady jet formation exists in these quiet circumstances and emits in hard X-rays (high frequency, and hence the name “hard state”), even though it is of markedly lower luminosity and usually rather difficult to detect. In the vast majority of cases, these objects spend a lot of time in situations like these, where the Cosmic Battery is active and in high efficiency. Therefore, we can reasonably expect that the Cosmic Battery has ample time in order to generate the magnetic fields necessary for the consequent jet ejection.

We subsequently follow the diagram vertically upward (moving toward region “B”) and we note the rapid luminosity increase as the structure enters into the outburst phase. At this stage, we can detect a steady and compact, partially self-absorbed jet (see Stirling et al. 2001) with increasing radio and X-ray luminosity. This jet is recorded as mildly relativistic with Lorentz factor $\gamma < 2$ (see Fender et al. 2004). The configuration’s disk is expected to be highly advective and of low radiation efficiency (ADAF, Advection Dominated Accretion Flow, Narayan & Yi 1994, 1995a, 1995b). Both the system outflow and the accretion disk are anticipated to radiate in hard X-rays (see e.g., Giannios 2005). This registered luminosity increase in the setup has the direct consequence of a surge in the electric current generated and consequently the magnetic field produced by the Cosmic Battery mechanism. Additionally, since the X-ray luminosity is intertwined with the radio luminosity, we also detect a luminosity rise in the radio frequencies, as well.

Continuing on, the configuration keeps increasing its luminosity and eventually reaches its peak at region point “B”. The accretion disk is expected to be geometrically thick and advection dominated in a considerable fraction of the inner region areas. In contrast, only the outer, colder, and darker regions of the disk are anticipated to form a disk portion that is geometrically thin and opaque (e.g., Cabanac et al. 2009). In this environment, the setup's outflow is expected to be a robust and steady jet operating at full strength and the Cosmic Battery mechanism active in its highest efficiency.

Further on, the arrangement maintains its high X-ray luminosity but decreases its spectral hardness, moving in the HID leftward from region "B" toward region "C" and approaching the "jet line". This line, which stretches diagonally from the top left of the diagram to the bottom right, separates the cycle regions where the jet is compact or intermittent. As the setup reaches the jet line, radio emissions peak and the outflow properties are notably altered (see Fender et al. 2009). Namely, rather than being steady, the jet becomes discontinuous and eruptive and is also noted to emit discrete material blobs with $\gamma > 2$. During this period, we usually also detect extended radio and X-ray flares. This episodic nature of events also influences the disk, making it more turbulent and affecting its format, as well as its processes. The geometrically thin disk component of smaller height extends inward and the geometrically thick component shrinks and progressively recedes. By the time the arrangement reaches and crosses the jet line, the geometrically thick and optically thin disk component has dissolved completely and the geometrically thin and optically thick component extends until the disk's inner edge.

From the disk specifics and format described above, we understand that the magnetic field lines are not expected to be retainable by the thin disk structure and eventually escape outward. Kylafis et al. 2012 suggest that this causes the disk to develop 'non-axisymmetric magnetic "Rayleigh-Taylor-type" instability modes' (sic). These instabilities consequently alter the disk equilibrium and allow the field to gradually escape the configuration as magnetic filaments. They additionally reason that such an evolution can sufficiently describe the jet flaring events near the hard-to-soft jet line transition.

After crossing the jet line, the system continues decreasing its hardness and attempts to reach region "C", settling in a soft state (soft X-rays emission). The jet keeps being notably disrupted and not as optically thick, losing its ability to robustly emit light and transmit noteworthy radiative energy to the surroundings. The radio emissions thus decrease drastically and in most cases become undetectable. The accretion disk remains in a geometrically thin and optically thick condition and is expected to be adequately described by the Shakura & Sunyaev (1973) model. The Cosmic Battery is, as anticipated, still functioning under these circumstances, but rather inefficiently due to the volume of the disk. This consequently means that in these conditions the mechanism requires significantly extended periods of time in order to generate equipartition-level magnetic fields.

The arrangement then continues its evolution attempting to move from region "C" to region "D", while lowering and raising its emission frequencies, and slowly decreasing its luminosity. Looking at the q-diagram, we comprehend that this translates in the object's strives to cross and clear the jet line. Some setups are successful in this passage in a single try, while others require multiple ventures. As these systems repeatedly transverse the jet line, we expect them to periodically display the presence of a jet as they move from softer to harder states. This jet becomes notably flaring when crossing the line in the opposite direction, moving from hard to soft states and the accretion disk becomes thin and unstable.

After reaching region “D” in the HID with low energy emissions and intermediate luminosity, the configurations move toward region “E”. We record the objects gradually increasing their hardness ratio and crossing the jet line anew at its lower segment in considerably diminished intensity. The accretion disk is also expected to change its format, progressively transforming from geometrically thin, optically thick into a geometrically thick, optically thin structure. Namely, the disk starts transforming from a Shakura – Sunyaev disk into an ADAF, where the Cosmic Battery mechanism is anticipated to operate at high efficiency, promoting again the formation of a jet. Finally, after reaching region “E”, the system again displays a steady jet that endures and remains present as the arrangement reaches the lowest luminosity and maximum frequency emission, the quiescent state in region “A”.

From the above we see that the Cosmic Battery appears to be a mechanism of high potential and of many applications. It can provide valuable information, while shedding light and possibly explaining several unanswered questions about all types of X-ray binaries, their cycles, jets, and evolution. It is therefore a process that merits further consideration and requires research in its effects on a multitude of environments, systems, and phenomena.

6.5. The Cosmic Battery and the retrograde photon sphere

In mid-2020 there were discussions concerning cases where the spin of the black hole and the assumed disk model are such that could cause the retrograde photon sphere (Claudel et al. 2001, Teo 2003, Cederbaum & Jahns 2019) to interact strongly with the disk material. We thus investigate the possibility of the occurrence of resonance situations, where the recorded radiation forces in regions near the photon sphere would peak and provoke instabilities and material reconfigurations.

In more detail, we wished to investigate cases where the black hole spin is high enough to bring the retrograde photon sphere close or inside the accretion disk (Fig. 6.6). The equatorial radius of the retrograde photon sphere r_{ph}^{retro} is given by:

$$r_{ph}^{retro} = 2M\left\{1+\cos\left[\frac{2}{3}\cos^{-1}\left(\frac{a}{M}\right)\right]\right\}. \qquad (6.5.1)$$

Therefore, for different black hole spins the outer, retrograde photon sphere can approach and surpass the disk's inner edge, moving outward.

Some additional important information about the photon sphere can be found in the aforementioned studies. First of all, we notice that what is called a "photon sphere" is not always or necessarily a sphere. In reality, it is a mathematically three-dimensional volume of space and not a two-dimensional sphere. Its shape and volume evolves with the increase of the black hole spin. Also, its cross sections can in cases be concave for a high enough spin parameter. Furthermore, we should note that the photon sphere is not an area of space where photons accumulate. On the contrary, the photon sphere is an unstable equilibrium point in photon trajectories. This means that photons do not pool in the area and even if they enter the sphere surface, even with an optimal trajectory, interactions with other photons swiftly cause them to escape the sphere and be flung outward.

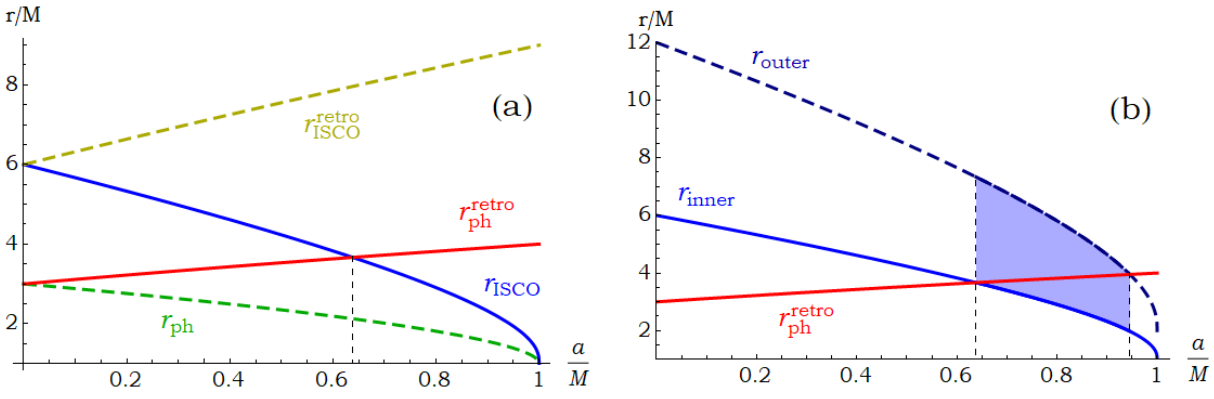

Figure 6.6: Equatorial radii of notable surfaces for increasing values of black hole spin (*left*). For the disk models considered, the equatorial retrograde photon orbit radius (red) crosses the disk's inner edge (ISCO, blue) for spin $a \approx 0.64M$ and remains inside the disk area (*right*) until $a \approx 0.95M$ or more, depending on the disk's outer edge (darker blue).

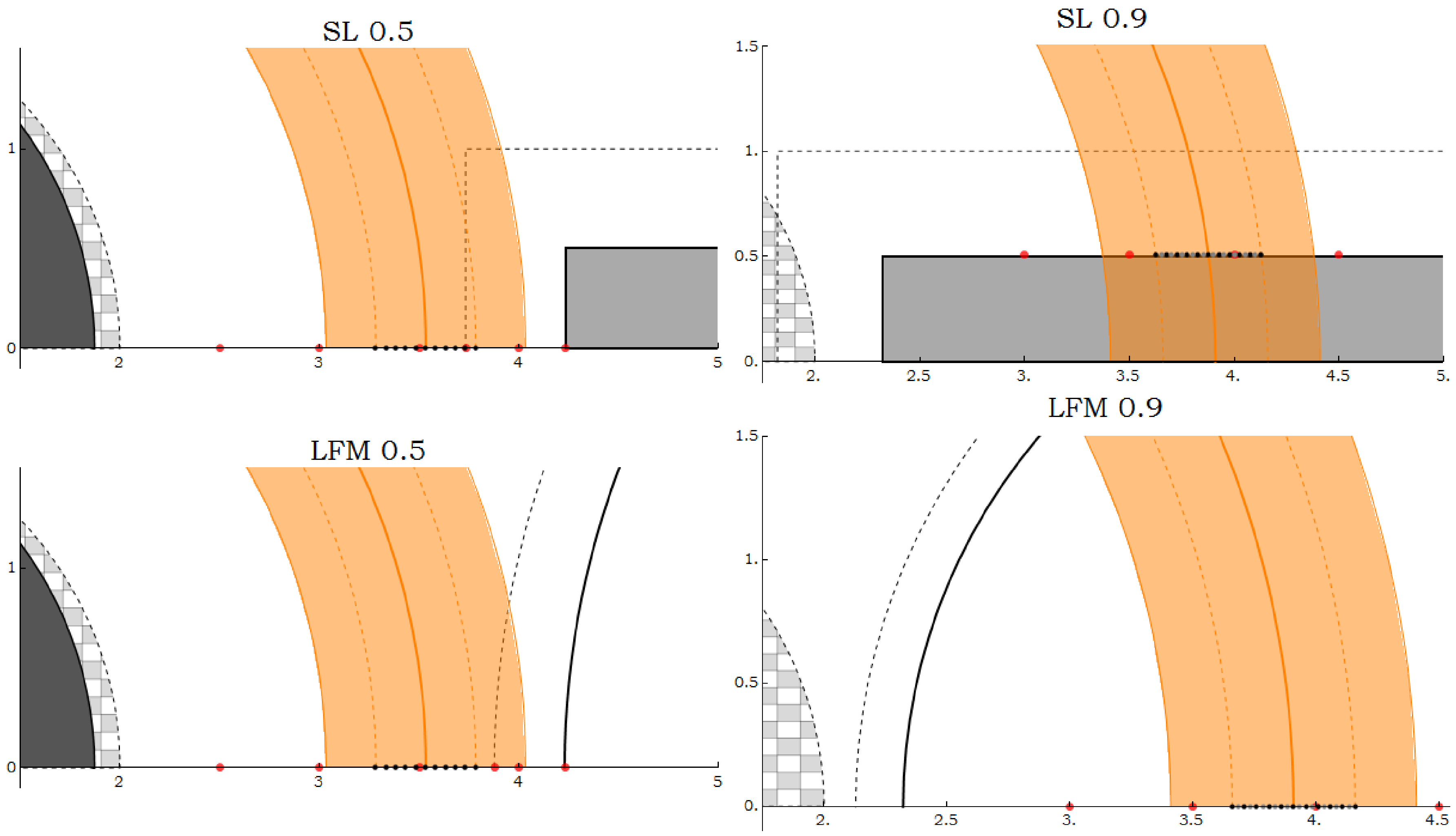

Figure 6.7: Opaque slab (*top*) and semi-opaque LFM (*bottom*) disk models considered for spins $a = 0.5M$ (*left*) and $a = 0.9M$ (*right*). In large red dots are the original grid runs which are sparser. In small black and gray dots are the runs of the new, denser grid, centered in the photon sphere's radius (thick solid arc). The thicker grid extends for a radius of $0.25M$ around the photon sphere radius and includes 11 (*left*) and 21 (*right*) new observer points.

In order to perform an examination of the assorted procedures, we construct the relevant accretion disk models and investigate for possible interactions between the retrograde photon sphere and the accretion disk. We hence inquire if these interactions could cause the material to receive notable radiation forces and possibly react, restructure, and even possibly destabilize. For this purpose, we investigated two distinct black hole spins, $a = 0.5M$ and $a = 0.9M$, as well as two different accretion disk models. One of the disks is a geometrically thin and optically thick Shakura – Sunyaev slab disk and the other one a geometrically thick and optically thin LFM disk. For $a = 0.5M$, the retrograde photon sphere is slightly further inside than the disk's inner edge and for $a = 0.9M$, the retrograde photon sphere crosses the accretion disk close to its geometrical center (Fig. 6.7).

For the code executions, we set up a thick grid of observer points onto the equatorial plane, or close to it, if that is not possible. The center of these grids is located in the radius of the retrograde photon sphere and the grids themselves extend a small distance inside and outside the reverse photon sphere radius. In each point of this grid, we establish an observer there and record the incoming radiation from a large number of possible photon directions. From this incoming radiation, we calculate the exerted radiation four-force components looking for spikes of unusually high radiation forces near the area of the retrograde photon sphere. The plots for the accumulated results for the four-force components are shown in the following Figures 6.8 – 6.9 and the online material[7].

Looking closely at the above force plots, we can see that there appears to be no indication of special conditions or interactions between the disk material and the radiation of the retrograde photon sphere. This applies for all the radiation force components and all the considered target velocity profiles. This means that even when the retrograde photon sphere passes straight through the disk, it does not appear to cause instances of imbalance or strong interactions with the disk material. In fact, the passage of the theoretically expected photon sphere is not even noticed by the disk matter. We must note here, nonetheless, that the retrograde photon sphere is not necessarily an insignificant structure, as it may contain certain photon samples, even though very sparse and rather transient. This aforesaid considerably low density of photons moving there is, however, too small to create interactions or secondary effects.

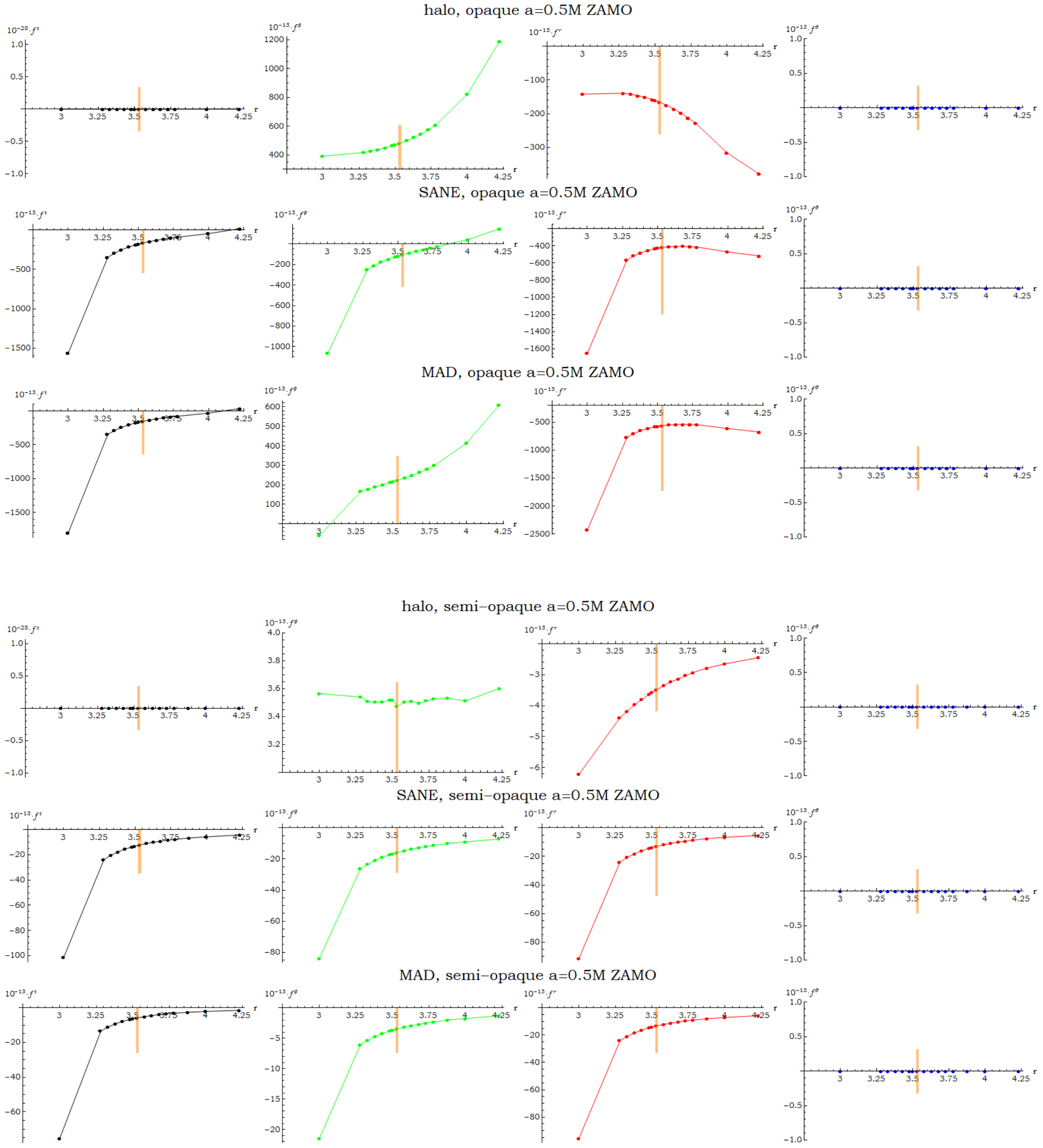

Figure 6.8: Radiation forces on an opaque (*top*) and a quasi-opaque (*bottom*) disk in the vicinity of the photon sphere. The central black hole is of spin $a = 0.5M$. The columns are for the $t, \phi, r, \theta -$components respectively. The lines are explained in Sect. 5.3 and Fig. 5.14.

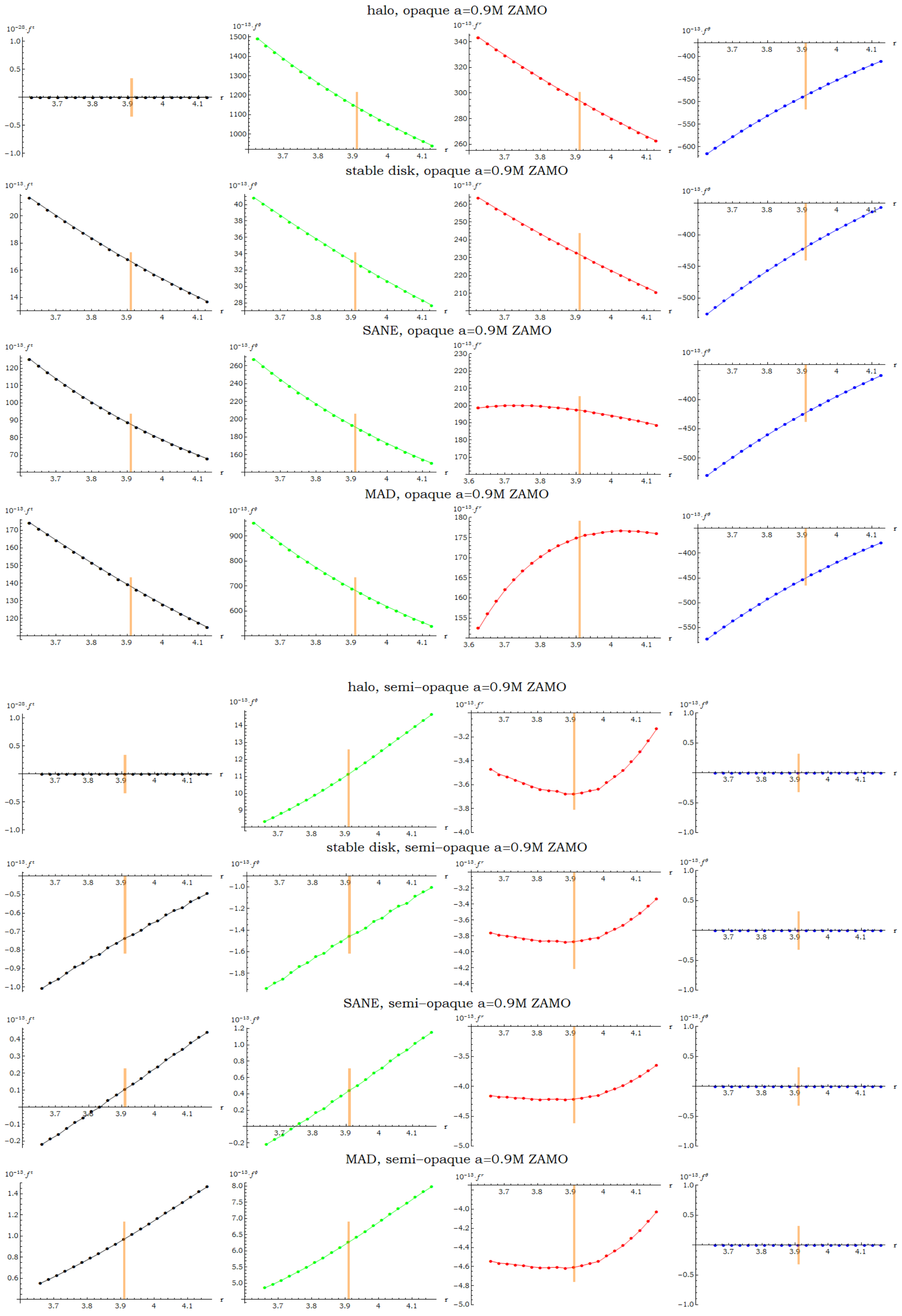

halo, opaque a=0.9M ZAMO

stable disk, opaque a=0.9M ZAMO

SANE, opaque a=0.9M ZAMO

MAD, opaque a=0.9M ZAMO

halo, semi–opaque a=0.9M ZAMO

stable disk, semi–opaque a=0.9M ZAMO

SANE, semi–opaque a=0.9M ZAMO

MAD, semi–opaque a=0.9M ZAMO

Figure 6.9: Radiation forces on an opaque (*top*) and a quasi-opaque (*bottom*) disk in the vicinity of the photon sphere. The central black hole is of spin $a = 0.9M$. Columns and lines as for Fig. 6.8.

CHAPTER 7

CONCLUSIONS AND FUTURE PROSPECTS

In this chapter, we summarize our research, discuss our conclusions, and share our thoughts on possible future prospects that can use our study or extend it. In this work, we examined the physics and the setup required in order to investigate the radiation field produced by the hot accretion disk orbiting a black hole. This field is very complex for many reasons, some of which are the general relativistic effects present and also the fact that the radiation source is no longer central. Instead, these sources of light extend in a large azimuthal and poloidal volume of space encompassing the absorbing target material.

We began by presenting the mathematical tools required to study objects of this kind and introduced the zero angular momentum observers. We subsequently established the appropriate Hamiltonian formulation that is better suited in order to solve the particle equations of motion and trajectories. Then, we went on to study radiation along with its equations in Classical Physics and discussed the necessary steps for a general relativistic approach.

Following that, we examined a broad assortment of accretion disk models (Figs. 4.3 - 4.7, 5.1, 5.12, Table 1). These disks were geometrically thick and thin, as well as optically thick and thin with diverse degrees of density gradients. In addition, we chose to apply certain radial and azimuthal velocity profiles that follow and agree with the majority of researches in environments such as the ones we study here. Moreover, we examined different disk temperature profiles, such as disks heated up by the accretion process ($\mathrm{T} \propto r^{-3/4}$) and isothermal disks. For the geometrical profiles of the disks, we examined an assortment of different shapes and sizes. We thus investigated situations of different disk characteristics, such as the maximum material height and the inner edge radius. Various alterations and reassessments can be made, however, in order to better suit other situations, other disk models, prograde or retrograde material motion, spacetime environments, etc.

The aforementioned research course was deemed necessary since we are interested in a variety of environments and their evolution, with one such case being the intricate X-ray binaries. These systems, for example, regularly change their configuration due to the gravitational and radiation interactions of the two stars and their material. This leads to repeated cycles, where the accretion disk gathers up material, heats up, and radiates intensely. This then causes the structure to inflate, become sparser and permeable, and thus occupy a different form in a much larger volume of space. Later on, the disk cools down, deflates, and returns to a geometrically thin and optically thick format. In order to better investigate the physical properties of various systems, we looked into twelve different disk models that can adequately approximate the various stages of the X-ray binaries periodic evolution or many other situations.

In total for this work, we developed more than 12 hundred editions of programs, we ran more than 23 thousand code executions, and we studied more than 12 billion particle trajectories. First, we discussed the codes `Omega`, written in order to solve single particle or bundle deployment geodesic equations near massive objects that modify the spacetime and its structure. We studied various particle source and spacetime setups, and noted the trajectories' behavior under the assorted circumstances. We marked the diverse equilibrium trajectories for massless or massive test particles (Fig. 5.3) and inspected their orbits evolving while tracking the spacetime static grid (Figs. 5.4, 5.5). Subsequently, we investigated how the particle motion is additionally reshaped when examining the stationary area around a rotating central mass, where extended time curvature consequences are included (Fig. 5.8). Finally, we demonstrated how the trajectories are modified when studying the entirety of the four-dimensional spacetime grid around the rotating compact object (Figs. 5.6, 5.7). What we registered was the particle motion conforming to the spacetime warping in the various situations, altering its incurvation, and obeying the grid bending in spatial or temporal particular areas, such as the ergosphere and the frame-dragged periphery. Possible extensions of the program include various new spacetime formats, gravitational lensing and multiple object images, multiple-source systems, and investigations of modified gravity theories.

We then discussed the `Infinity` codes that document the incoming radiation from various source setups, recording their image, and calculating the resulting radiation field and forces on the disk particles. We first looked at central emitting stars, verifying the validity of our programs (Tables 2, 3, 4) and presented our resolution enhancement algorithms (Fig. 5.9). We then surveyed extended thermally emitting accretion disks for the radiation intensity appearance (Figs. 4.1, 4.2, 5.11, 5.13) and the ensuing field generated (Figs. 5.14, 5.15). In addition, we presented comparative bar plots about the radiation force magnitude for the assorted locations and target velocity profiles (Fig. 5.17).

The numerical results showed that optically thick accretion tori are more efficient in producing radiation forces for the material, as expected. Semi-opaque tori, nevertheless, can approach this limit under certain conditions. The results reveal that the primary factor affecting the radiation forces recorded appears to be the density gradient. Namely, considering disks with comparable structures, we see that the faster the material density increases, the larger the radiation forces exerted are. We clarify here that the quasi-opaque disks we used for this research are not tenuous. Their number density promptly rises to optical depth $\tau \geq 1$ and thus we anticipate limited radiation losses due to a possibly smaller effective source extent. Furthermore, we observed opaque disk models of small volume recording higher radiation forces than significantly more voluminous quasi-opaque disks with optical depths $\tau \sim 1-5$. We thus consider the primary factor influencing the recorded radiation forces to be the material density increase rate and not the volume occupied by the disk material.

The radiation density plots (Figs. 5.14, 5.15) revealed the forces' sign, magnitude, and spatial distribution. They also disclosed the differences between the disk models concerning the radiation field structure and its possible effects on the disk dynamics. We noted the energy loss rate getting stronger the closer we get to the compact object. Additionally, we observed the energy gain rate getting stronger, yet quite milder than the loss rate, somewhat further out the disk's inner edge, where the field is more isotropic and further beamed. The azimuthal radiation field follows the same pattern, being robustly braking in the system interior sectors and mildly accelerating further out the disk's inner edge. In the radial direction, we mark the radiation pushing matter radially inward in the inner disk regions and propelling particles outward in the cross section central or outer areas. The poloidal field components display a noticeable tendency to push the matter toward the rotation axis and further outward. This fact is especially noteworthy, since it provides indications about the propensity of an early material outflow collimation.

The radiation force comparative bar plots (Fig. 5.17) provide a new perspective on the force results that reveal additional information about the field. We hence obtain information about the significance of the material density gradient over the emitting material's volume, the disk maximum height significance, and the role of the disks' inner edge or average radius. Firstly, we have the force magnitude ranking for the models. The strongest field is generated by the voluminous and opaque disk model Torus. Then follows the inclined-surface Wedge along with the flat-surface Slab, both opaque disks. These two models are similar and record interweaving force magnitudes, depending on the target's location and the velocity profile. Examination of this pair and the selected disk surface inclination reveals the consequences of this inclination and the increase of maximum disk height. We first notice that even though Wedge has twice the material height of Slab, there do not appear to be significant radiation force magnitude differences recorded. The force minimum and maximum ranges intertwine for the assorted regions, motion profiles, and force components, although the Wedge field appears to be somewhat stronger in general. Then follows the opaque ORST, with a greatly varying volume for increasing spins. This model also displays stronger forces registered in the disk outflow regions.

Afterward, we encounter the semi-opaque disks field. The PD model, also displays quite strong radiation forces in the outflow regions. Finally, we have the LFM, which is the semi-opaque version of Torus. Comparisons between the two models can provide conclusions about the reverberations of the disk opacity gradients and the material stratification. Namely, we see that the disk volume is not the property of prime significance for the strength magnitude, as the forces exerted by the LFM are far weaker than those of its opaque counterpart, Torus. Extending on the above, we also note the exceedance of the quite smaller yet opaque ORST over LFM in the exerted radiation forces. Furthermore, we can additionally compare LFM with PD, whose density gradient is steeper that LFM and proves to exert far stronger radiation forces. The aforementioned arguments thus suggest that the material density gradient is a property of great importance and possibly, in certain cases, even greater than the volume of the emitting disk itself. Finally, we generally note the models Slab, Wedge, and Torus recording stronger radiation field forces. This fact is a direct aftermath of the more condensed nature of these systems, which have a notably smaller radial extent. This then has immediate repercussions on the recorded radiation forces, since for the radiation force f_{rad} , it is $f_{rad} \propto r^{-2}$.

The exerted radiation forces discussed above have significant consequences on the occurring processes, the disk dynamics, and the system’s further evolution. This is because the radiation accelerations are primarily exerted on the material electrons; they decelerate them, causing them to spiral inwards or accelerate them, causing them to be flung outward. Although a procedure of this kind would instigate charge separation processes, such an event does not occur due to the electromagnetic processes taking place in the microphysics scale. These processes, instead, drive the material ions to lower or higher orbits following the electrons and thus maintaining the material neutrality. There are, however, instances of somewhat episodic but contained material expulsion events in either direction.

This electron trajectory modification has a further upcoming result, the launch and the operation of the Cosmic Battery mechanism. This variant electron orbit with a different azimuthal velocity than the ions causes the generation of a ring electric current in the disk, which is quite stronger near the disk’s inner edge. This azimuthal current hence leads to the consequent generation of poloidal magnetic field loops in the system. Depending then on the ratio of the magnetic diffusivity to the momentum diffusivity, the setup material can bring one magnetic polarity inward due to accretion and allow the return polarity to diffuse outward. This subsequently leads to the linear and uninterrupted growth of the magnetic field. If we then also take into account the disk’s differential rotation, we can observe an additional phenomenon, the magnetic loops further extension, twist, and entanglement. As this process is maintained, we record the extended magnetic loops opening up at various points and releasing expanded loops into the entire system area and its surrounding space. We hence note the initial electron orbit deceleration leading to the accumulation of magnetic field lines and their eventual escape to the interstellar or intergalactic environment.

In addition to the above, we should also mention the ensuing related electromagnetic phenomena in the systems evolving in the way we described here. Firstly, the presence of magnetic fields inside the highly ionized black hole accretion disks significantly alters the equilibrium conditions. This means that the notions of the standard expected notable orbits collapse and new equilibrium trajectories arise in different areas or at different radii. Furthermore, the gradual expansion of the generated magnetic loops permits the opposite polarities approaching each other and, depending on the material particular characteristics, this allows for magnetic reconnection in certain areas, possibly accompanied by episodic events. Moreover, a more attentive look should be taken when examining the registered radiation forces on outflowing material. This is due to the particular accelerations to targets in such regions and velocity profiles. The incident thermal radiation further accelerates the outward material motion, it decelerates the azimuthal spiraling, and also exerts force components that promote the escaping bundles' collimation.

There are numerous possible extensions for a program of such extent and capabilities. Firstly, we can broaden our source environments and study more complex systems, such as X-ray binaries or systems with multiple light sources. We can additionally examine arrangements that included atypical stellar objects, such as dwarves, giants, or neutron stars. Moreover, we should also mention that all the aforesaid researches do not have to be performed within the limits of the General Theory of Relativity. Instead, the same problem setups can be solved using some of the proposed modified gravity theories.

Further on, we looked into the `Elysium` codes. They were used to generate photograph pictures of the assorted black hole and accretion disk arrangements at various inclinations from far away, with no particular details on the microphysics, but with the entire system as a whole. We hence studied the results examining the depictions and the radiation intension results on various arrangements for relative conclusions. These programs can give us information about the mass and the angular momentum distribution and diffusion, as well as the equilibrium locations and conditions. They can additionally give us quite valuable details about the central object's spin.

Our executions provided numerous high-resolution observation-like images for various disk setups with different shapes, sizes, temperature profiles, and spins (Figs. 5.19, 5.20, 5.21 5.22, 5.23). The generated radiation specific intensity matrices revealed satisfactory results that included some observationally expected phenomena, such as limb darkening (Figs. 5.19, 5.22) and partial transparency (Figs. 5.19, 5.23). We have also seen here some additional capabilities of the program. One such ability is the potential to take into account up to very-low-density disk portions for the emitted radiation that are not visible or discernible (Fig. 5.24). Furthermore, this program has the option of recording incoming light of various wavelengths. This radiation is in general expected to be emitted by matter segments situated in different disk areas that are also possibly disconnected from the main bulk of matter (Fig. 5.25).

An additional intriguing prospect of the program that can be further exploited is a more extended investigation of the Einstein – Khvolson echo ring. We showed that its size closely relates to the disk's inner edge radius and that in certain cases it can also provide information about the accretion disk that the primary image cannot. Moreover, we observe that more detailed examination of the images produced by the code can also divulge useful information about the spacetime grid curvature and its particular characteristics at certain points. Such cases include, for example, instances of weak lensing or gravitationally induced frequency adjustments. These situations also provide us with useful information about the spacetime properties, its curvature, and its symmetries. We can therefore also use this program in order to draw conclusions about the validity of the widely used metrics, lensing phenomena, and some of the suggested modified gravity theories.

Afterward, we looked into the depiction results and attempted to locate the type of information we could draw for the configuration from each of the figures. Namely, we examined the possibility of estimating a black hole's spin by using observational data and images. This led to the development of the `Tranquillity` codes. The algorithms collect observable arrangement information and create inclination – divergence plots. These plots are later on used as a scale, providing a quick appraisal of the spin of random environments of black holes encircled by accretion disks. This is done by comparing the relative observed positions of the disk and its first Einstein – Khvolson echo ring.

The first step of the program is estimating the accretion disk's plane inclination relative to the line of sight. The results of our code for the disk inclination assessment were proven to be rather good, as we see in Table 6. Considering later the inclination as the independent variable, we create the inclination – divergence plots (Fig. 5.26) that display the pattern for the divergence evolution for increasing spins. We then subjected our program to a series of randomized tests and attempted to estimate the spin of random black holes by observing the accretion disk spiraling around them. The results turned out to be good approximations for the spin of these systems, with spin errors lying below 5% (Table 7). Further possible expansions of the program include a larger disk model database, additional disk setups, and models with fewer symmetries. The algorithm can be also additionally improved in order to automatically recognize the best-fit models for each observed structure or to manage and process particular situations for the disk or the spacetime.

Finally, we investigated the repercussions of the disk's thermal radiation onto the material itself. For this purpose, we created and used the `Burning Arrow` codes. We thus calculated the degenerating massive particle trajectories that take into account the disk's thermal radiation and drew the destabilized orbits followed by the disk electrons absorbing the high energy light. We examined the phenomenon taking place in a Schwarzschild (Figure 5.27) and a Kerr spacetime around a black hole of various spins (Figure 5.28). We surveyed the launch orbits of material following three different initial velocity profiles and noted the rapid trajectory modifications when ignoring secondary electromagnetic phenomena. We also traced interesting changes for targets at the center of the local radiation field, particles entering different radiation environments, and targets moving through particular spacetime areas. Extensions of the program include a closer examination of the electromagnetic aftereffects, the ensuing magnetic field, its dynamics, or reconnection, as well as possible instabilities and turbulence.

We mark here that the codes discussed are highly adaptable and modifiable (publicly available and kept updated, see here). This means that adjustments and expansions can be made in order to accommodate any related research required for configurations in such spacetime conditions or in relevant arrangement setups. Additionally, we note that any further results can be made available upon request.

Various parts of our work thus revealed that the effects of thermal radiation onto the disk material itself are significant and should not be overlooked or deemed inconsequential. This radiation proves to be larger and stronger than anticipated, and creates noticeable accelerations far from negligible. Even though as mentioned earlier these radiation forces act upon the material electrons, they undoubtedly exert forces onto the disk protons as well, even indirectly. Radiation thus results in material orbit destabilizations that affect the accretion process. These destabilizations could be in the form of restricted magnetorotational instability occurrences, turbulence, or any other sort of instability. Depending on the destabilization area characteristics and properties, these processes can then lead to episodic, but limited, events of matter accretion or expulsion. Hence, the presence of radiation appears to be a factor that decidedly influences the accretion processes, rate, and aftermath. This phenomenon therefore merits more investigation and comparison with other relevant ones. In a particularly interesting situation, the electron motion change leads to the formulation of electromagnetic effects, such as an electric ring current and an ensuing battery mechanism. Depending then on the material's viscosity and magnetic diffusivity, this battery mechanism can be of varying efficiencies. The cases where the generated magnetic field becomes strong enough to induce notable alterations in the system structure and evolution, or bring in further instabilities should thus be looked into attentively.

In order to examine these situations, in the last Section we discussed the Cosmic Battery mechanism along with its capability to create magnetic fields from zero in situ inside the arrangements. We first examined the operation of the Cosmic Battery in larger and smaller scales. We then analyzed the occurring procedures and attempted to predict the configuration’s evolution, as well as its effects outside the narrow system boundaries. Namely, other than the magnetic field generation, we are also interested in its subsequent diffusion and its flow out of the arrangement. We thus selected four noteworthy disk regions for each model (Table 8) and examined the radiation’s recorded specific intensity there, in order to better investigate the disk dynamics for the assorted spins (Table 9). Further on, we applied a dimensional analysis calculation and estimated the time necessary for the Cosmic Battery operation to generate an equipartition-level magnetic field in the disk (Table 10). The numerical results extracted proved very promising for the mechanism since they reveal that, depending on the disk model and the black hole spin, this procedure can require just few days or even some hours. We noted, nevertheless, that there can also be circumstances that the mechanism is not quite effective and needs some months to generate the field. This field is, however, created at full strength without the need for further amplification via a dynamo mechanism. Keeping thus in mind that we examine phenomena that may last for astronomical timescales, even these extended periods of time do not appear inhibitory for certain cases of larger structures.

Moreover, we investigated the possible interactions between the Cosmic Battery and X-ray binaries. We looked in their periodic behavior along with their hardness – intensity diagrams (Fig. 6.5) and contended that the Cosmic Battery is capable of explaining the configurations' observed attitude. These situations are accompanied by a multitude of observational data and the interactions of the two phenomena interconnect them, allowing them to explain each other naturally and effortlessly. Finally, we investigated the possibility of interactions between the disk material and the retrograde photon sphere strongly triggering the Cosmic Battery mechanism when the black hole spin is high enough to bring the latter close to or inside the accretion disk (Fig. 6.6). Although, however, we looked into multiple environments of disk models, spins, and velocity profiles we did not detect any evidence of strong interactions or reinforcement of the Cosmic Battery mechanism (Figs. 6.8, 6.9).

This work is novel in the sense that it is one of the very first times the radiation field created by the accretion disk orbiting a black hole is extensively studied, measured, and depicted. This field is computationally calculated in a large volume of space for many configurations inward, outward and if possible, inside the accretion disk itself. Additionally, the radiation created is examined in the vicinity of notable system areas, such as the disk's edges, the material outflow and inflow regions, the ergosphere, the event horizon, and more. A broad quantity of numerical results, images, and plots has been produced and can be surveyed for many purposes. After the compilation of the material, we can contemplate on the conclusions we can draw about the physics and the phenomena of these systems, their dynamical condition, their equilibrium, and perhaps their evolution.

A matter worth looking further into could be the effects of these significant radiation forces on the dynamics, the stability, and the evolution of the disk itself. The modifications brought upon these systems could be noteworthy, since long considered concepts, such as the innermost stable circular orbit, must take radiation effects corrections into account.

Another matter worth examining in the future is the radiation effects and possible repercussions on outflowing material close to the object's rotation axis. For instance, we could investigate the ramifications of radiation onto the very early stages of material outward movement, which from our current results seem appreciable. Additionally, the radiation density plots we showed here, demonstrate the accretion disk radiation promoting an early collimation tendency to the jet material. Finally, something that could be considered in the future is how the calculated radiation affects more complex situations, such as the disk evolution in X-ray binaries and the observed hardness – intensity diagrams.

Bibliography

Abbott, B. P., “GW190425: Observation of a Compact Binary Coalescence with Total Mass ~ 3.4 $M_{\odot}$”, *The Astrophysical Journal*, vol. 892, no. 1, 2020. doi:10.3847/2041-8213/ab75f5.

Abramowicz, M., Jaroszynski, M., and Sikora, M., “Relativistic, accreting disks.”, *Astronomy and Astrophysics*, vol. 63. pp. 221–224, 1978.

Abramowicz, M. A., Czerny, B., Lasota, J. P., and Szuszkiewicz, E., “Slim Accretion Disks”, *The Astrophysical Journal*, vol. 332. p. 646, 1988. doi: 10.1086/166683.

Abramowicz, M. A., Ellis, G. F. R., and Lanza, A., “Relativistic Effects in Superluminal Jets and Neutron Star Winds”, *The Astrophysical Journal*, vol. 361. p. 470, 1990. doi: 10.1086/169211.

Abramowicz, M. A., Chen, X., Kato, S., Lasota, J.-P., and Regev, O., “Thermal Equilibria of Accretion Disks”, *The Astrophysical Journal*, vol. 438, p. L37, 1995. doi:10.1086/187709.

Abramowicz, M. A., Chen, X.-M., Granath, M., and Lasota, J.-P., “Advection-dominated Accretion Flows around Kerr Black Holes”, *The Astrophysical Journal*, vol. 471, p. 762, 1996. doi:10.1086/178004.

Abramowicz, M. A., Almergren, G. J. E., Kluzniak, W., and Thampan, A. V., “The Hartle-Thorne circular geodesics”, *arXiv e-prints*, 2003. doi:10.48550/arXiv.gr-qc/0312070.

Abramowicz, M. A., “Super-Eddington black hole accretion: Polish doughnuts and slim disks”, in *Growing Black Holes: Accretion in a Cosmological Context*, 2005, pp. 257–273. doi: 10.1007/11403913_49.

Abramowicz, M. A., Jaroszyński, M., Kato, S., Lasota, J.-P., Różańska, A., and Sądowski, A., “Leaving the innermost stable circular orbit: the inner edge of a black-hole accretion disk at various luminosities”, *Astronomy and Astrophysics*, vol. 521. 2010. doi: 10.1051/0004-6361/201014467.

Abramowicz, M. A. and Fragile, P. C., “Foundations of Black Hole Accretion Disk Theory”, *Living Reviews in Relativity*, vol. 16, no. 1, 2013. doi:10.12942/lrr-2013-1.

Adamo, T., Newman, E. T., “The Kerr-Newman metric: A Review”, *Scholarpedia* 9(10): 31791, *arXiv e-prints*, 2016.

Artemova, I. V., Bisnovatyi-Kogan, G. S., Bjoernsson, G., and Novikov, I. D., “Structure of Accretion Disks with Optically Thick--Optically Thin Transitions”, *The Astrophysical Journal*, vol. 456, p. 119, 1996. doi:10.1086/176632.

Asada, K. and Nakamura, M., “The Structure of the M87 Jet: A Transition from Parabolic to Conical Streamlines”, *The Astrophysical Journal*, vol. 745, no. 2, 2012. doi:10.1088/2041-8205/745/2/L28.

Asada, K., Nakamura, M., and Pu, H.-Y., “Indication of the Black Hole Powered Jet in M87 by VSOP Observations”, *The Astrophysical Journal*, vol. 833, no. 1, 2016. doi:10.3847/1538-4357/833/1/56.

Balbus, S. A. and Hawley, J. F., “A Powerful Local Shear Instability in Weakly Magnetized Disks. I. Linear Analysis”, *The Astrophysical Journal*, vol. 376. p. 214, 1991. doi: 10.1086/170270.

Balbus, S. A. and Hawley, J. F., “A Powerful Local Shear Instability in Weakly Magnetized Disks. IV. Nonaxisymmetric Perturbations”, *The Astrophysical Journal*, vol. 400, pp. 610–621, 1992. doi:10.1086/172022.

Balbus, S. A. and Hawley, J. F., “Instability, turbulence, and enhanced transport in accretion disks”, *Reviews of Modern Physics*, vol. 70, no. 1, pp. 1–53, 1998. doi:10.1103/RevModPhys.70.1.

Balbus, S. A., “On the behaviour of the magnetorotational instability when the Rayleigh criterion is violated”, *Monthly Notices of the Royal Astronomical Society*, vol. 423, no. 1. pp. L50–L54, 2012. doi: 10.1111/j.1745-3933.2012.01255.x.

Bardeen, J. M., “Kerr Metric Black Holes”, *Nature*, vol. 226, no. 5240. pp. 64–65, 1970. doi: 10.1038/226064a0.

Bardeen, J. M., “Stability of Circular Orbits in Stationary, Axisymmetric Space-Times”, *The Astrophysical Journal*, vol. 161. p. 103, 1970. doi: 10.1086/150515.

Bardeen, J. M., “A Variational Principle for Rotating Stars in General Relativity”, *The Astrophysical Journal*, vol. 162. p. 71, 1970. doi: 10.1086/150635.

Bardeen, J. M. and Wagoner, R. V., “Relativistic Disks. I. Uniform Rotation”, *The Astrophysical Journal*, vol. 167. p. 359, 1971. doi: 10.1086/151039.

Bardeen, J. M., Press, W. H., and Teukolsky, S. A., “Rotating Black Holes: Locally Nonrotating Frames, Energy Extraction, and Scalar Synchrotron Radiation”, *The Astrophysical Journal*, vol. 178. pp. 347–370, 1972. doi: 10.1086/151796.

Belloni, T., *The Jet Paradigm: From Microquasars to Quasars, Lecture Notes in Physics,* vol. 794. 2010. doi: 10.1007/978-3-540-76937-8.

Belloni, T. M., “States and Transitions in Black Hole Binaries”, in *Lecture Notes in Physics, Berlin Springer Verlag*, vol. 794, 2010, p. 53. doi: 10.1007/978-3-540-76937-8_3.

Belloni, T. M., “Fast variability from X-ray binaries”, from ‘*High Time Resolution Astrophysics IV - The Era of Extremely Large Telescopes - HTRA-IV*’, *arXiv e-prints*, 2010.

Beloborodov, A. M., “Super-Eddington accretion discs around Kerr black holes”, *Monthly Notices of the Royal Astronomical Society*, vol. 297, no. 3, pp. 739–746, 1998. doi:10.1046/j.1365-8711.1998.01530.x.

Beloborodov, A. M., “Accretion Disk Models”, in *High Energy Processes in Accreting Black Holes*, 1999, vol. 161, p. 295.

Beloborodov, A. M., “Accretion disk models of luminous black holes”, *Advances in Space Research*, vol. 28, no. 2–3, pp. 411–423, 2001. doi:10.1016/S0273-1177(01)00402-1.

Biermann, L., “Über den Ursprung der Magnetfelder auf Sternen und im interstellaren Raum (miteinem Anhang von A. Schlüter)”, *Zeitschrift Naturforschung Teil A*, vol. 5. p. 65, 1950.

Biermann, L. and Schlüter, A., “Cosmic Radiation and Cosmic Magnetic Fields. II. Origin of Cosmic Magnetic Fields”, *Physical Review*, vol. 82, no. 6. pp. 863–868, 1951. doi: 10.1103/PhysRev.82.863.

Bildsten, L. and Rutledge, R. E., by Kouveliotou, C., Ventura, J., and van den Heuvel, E., “The neutron star - black hole connection”, in *The Neutron Star - Black Hole Connection*, 2001, vol. 567.

Bini, D., Jantzen, R. T., and Stella, L., “The general relativistic Poynting Robertson effect”, *Classical and Quantum Gravity*, vol. 26, no. 5. 2009. doi: 10.1088/0264-9381/26/5/055009.

Bini, D. and Geralico, A., “Spinning bodies and the Poynting-Robertson effect in the Schwarzschild spacetime”, *Classical and Quantum Gravity*, vol. 27, no. 18. 2010. doi: 10.1088/0264-9381/27/18/185014.

Bini, D., Geralico, A., Jantzen, R. T., Semerák, O., and Stella, L., “The general relativistic Poynting-Robertson effect: II. A photon flux with nonzero angular momentum”, *Classical and Quantum Gravity*, vol. 28, no. 3. 2011. doi: 10.1088/0264-9381/28/3/035008.

Bini, D., de Felice, F., and Geralico, A., “Accelerated orbits in black hole fields: the static case”, *Classical and Quantum Gravity*, vol. 28, no. 22. 2011. doi: 10.1088/0264-9381/28/22/225012.

Bini, D. and Geralico, A., “Spin-geodesic deviations in the Kerr spacetime”, *Physical Review D*, vol. 84, no. 10. 2011. doi: 10.1103/PhysRevD.84.104012.

Bini, D. and Geralico, A., “Equilibrium Orbits of Particles Undergoing Poynting-Robertson Effect in Schwarzschild Spacetime”, in *International Journal of Modern Physics Conference Series*, 2012, vol. 12, pp. 247–255. doi: 10.1142/S2010194512006447.

Bini, D., Boshkayev, K., Ruffini, R., and Siutsou, I., “Equatorial circular geodesics in the Hartle-Thorne spacetime”, *Nuovo Cimento C Geophysics Space Physics C*, vol. 36, pp. 31–36, 2013. doi:10.1393/ncc/i2013-11483-8.

Bini, D., Geralico, A., and Passamonti, A., “Radiation drag in the field of a non-spherical source”, *Monthly Notices of the Royal Astronomical Society*, vol. 446, no. 1. pp. 65–74, 2015. doi: 10.1093/mnras/stu2082.

Bini, D., Geralico, A., Jantzen, R. T., and Semerák, O., “Particles under radiation thrust in Schwarzschild space-time from a flux perpendicular to the equatorial plane”, *Monthly Notices of the Royal Astronomical Society*, vol. 446, no. 3. pp. 2317–2329, 2015. doi: 10.1093/mnras/stu2242.

Bini, D., Bittencourt, E., Geralico, A., and Jantzen, R. T., “Slicing black hole spacetimes”, *International Journal of Geometric Methods in Modern Physics*, vol. 12, no. 7. 2015. doi: 10.1142/S021988781550070X.

Bini, D. and Geralico, A., “Scattering by a Schwarzschild black hole of particles undergoing drag force effects”, *General Relativity and Gravitation*, vol. 48, no. 7. 2016. doi: 10.1007/s10714-016-2094-6.

Bisnovatyi-Kogan, G. S. and Blinnikov, S. I., “Disk accretion onto a black hole at subcritical luminosity.”, *Astronomy and Astrophysics*, vol. 59. pp. 111–125, 1977.

Bisnovatyi-Kogan, G. S., “Dynamic processes during accretion into a black hole”, *Discrete Dynamics in Nature and Society”*, vol. 6. pp. 247-261, 2001.

Bisnovatyi-Kogan, G. S., Lovelace, R. V. E., and Belinski, V. A., “A Cosmic Battery Reconsidered”, *The Astrophysical Journal*, vol. 580, no. 1. pp. 380–388, 2002. doi: 10.1086/342876.

Bisnovatyi-Kogan, G. S. and Lovelace, R. V. E., “Large-Scale B-Field in Stationary Accretion Disks”, *The Astrophysical Journal*, vol. 667, no. 2, pp. L167–L169, 2007. doi:10.1086/522206.

Blaes, O. M., “Course 3: Physics Fundamentals of Luminous Accretion Disks around Black Holes”, in *Accretion Discs, Jets and High Energy Phenomena in Astrophysics*, 2004, vol. 78, pp. 137–185.

Blandford, R. D., “Accretion disc electrodynamics - a model for double radio sources.”, *Monthly Notices of the Royal Astronomical Society*, vol. 176, pp. 465–481, 1976. doi:10.1093/mnras/176.3.465.

Blandford, R. D. and Znajek, R. L., “Electromagnetic extraction of energy from Kerr black holes.”, *Monthly Notices of the Royal Astronomical Society*, vol. 179, pp. 433–456, 1977. doi:10.1093/mnras/179.3.433.

Blandford, R. D. and Payne, D. G., “Hydromagnetic flows from accretion disks and the production of radio jets.”, *Monthly Notices of the Royal Astronomical Society*, vol. 199, pp. 883–903, 1982. doi:10.1093/mnras/199.4.883.

Blandford, R. D. and Narayan, R., “Cosmological applications of gravitational lensing.”, *Annual Review of Astronomy and Astrophysics*, vol. 30, pp. 311–358, 1992. doi:10.1146/annurev.astro.30.1.311.

Blandford, R. D., “Black Holes and Relativistic Jets”, *Progress of Theoretical Physics Supplement*, vol. 143, pp. 182–201, 2001. doi:10.1143/PTPS.143.182.

Blandford, R., Agol, E., Broderick, A., Heyl, J., Koopmans, L., and Lee, H.-W., “Compact objects and accretion disks”, in *Astrophysical Spectropolarimetry*, 2002, pp. 177–223.

Bombaci, I., “The maximum mass of a neutron star.”, *Astronomy and Astrophysics*, vol. 305, p. 871, 1996.

Bonafede, A., “The Coma cluster magnetic field from Faraday rotation measures”, *Astronomy and Astrophysics*, vol. 513, 2010. doi:10.1051/0004-6361/200913696.

Bondi, H., “On spherically symmetrical accretion”, *Monthly Notices of the Royal Astronomical Society*, vol. 112, p. 195, 1952. doi:10.1093/mnras/112.2.195.

Boyer, R. H. and Lindquist, R. W., “Maximal Analytic Extension of the Kerr Metric”, *Journal of Mathematical Physics*, vol. 8, no. 2. pp. 265–281, 1967. doi: 10.1063/1.1705193.

Bozza, V., “Gravitational lensing by black holes”, *General Relativity and Gravitation*, vol. 42, no. 9, pp. 2269–2300, 2010. doi:10.1007/s10714-010-0988-2.

Broderick, A. E. and Loeb, A., “Imaging bright-spots in the accretion flow near the black hole horizon of Sgr A*”, *Monthly Notices of the Royal Astronomical Society*, vol. 363, no. 2, pp. 353–362, 2005. doi:10.1111/j.1365-2966.2005.09458.x.

Broderick, A. E. and Loeb, A., “Imaging optically-thin hotspots near the black hole horizon of Sgr A* at radio and near-infrared wavelengths”, *Monthly Notices of the Royal Astronomical Society*, vol. 367, no. 3, pp. 905–916, 2006. doi:10.1111/j.1365-2966.2006.10152.x.

Broderick, A. E. and Loeb, A., “Testing General Relativity with High-Resolution Imaging of Sgr A*”, in *Journal of Physics Conference Series*, 2006, vol. 54, pp. 448–455. doi:10.1088/1742-6596/54/1/070.

Broderick, A. E. and Loeb, A., “Imaging the Black Hole Silhouette of M87: Implications for Jet Formation and Black Hole Spin”, *The Astrophysical Journal*, vol. 697, no. 2, pp. 1164–1179, 2009. doi:10.1088/0004-637X/697/2/1164.

Broderick, A. E., Loeb, A., and Narayan, R., “The Event Horizon of Sagittarius A*”, *The Astrophysical Journal*, vol. 701, no. 2, pp. 1357–1366, 2009. doi:10.1088/0004-637X/701/2/1357.

Cabanac, C., Fender, R. P., Dunn, R. J. H., and Körding, E. G., “On the variation of black hole accretion disc radii as a function of state and accretion rate”, *Monthly Notices of the Royal Astronomical Society*, vol. 396, no. 3, pp. 1415–1440, 2009. doi:10.1111/j.1365-2966.2009.14867.x.

Carilli, C. L. and Taylor, G. B., “Cluster Magnetic Fields”, *Annual Review of Astronomy and Astrophysics*, vol. 40, pp. 319–348, 2002. doi:10.1146/annurev.astro.40.060401.093852.

Carter, B., “Global Structure of the Kerr Family of Gravitational Fields”, *Physical Review*, vol. 174, no. 5. pp. 1559–1571, 1968. doi: 10.1103/PhysRev.174.1559.

Cederbaum, C. and Jahns, S., “Geometry and topology of the Kerr photon region in the phase space”, *General Relativity and Gravitation*, vol. 51, no. 6, 2019. doi:10.1007/s10714-019-2561-y.

Chandrasekhar, S., *The mathematical theory of black holes*. 1983.

Chatterjee, K., Liska, M., Tchekhovskoy, A., and Markoff, S. B., “Accelerating AGN jets to parsec scales using general relativistic MHD simulations”, *Monthly Notices of the Royal Astronomical Society*, vol. 490, no. 2, pp. 2200–2218, 2019. doi:10.1093/mnras/stz2626.

Chen, X., Abramowicz, M. A., Lasota, J.-P., Narayan, R., and Yi, I., “Unified Description of Accretion Flows around Black Holes”, *The Astrophysical Journal*, vol. 443, p. L61, 1995. doi:10.1086/187836.

Chen, W.-C. and Podsiadlowski, P., “Evolution of Intermediate-mass X-Ray Binaries Driven by the Magnetic Braking of AP/BP Stars. I. Ultracompact X-Ray Binaries”, *The Astrophysical Journal*, vol. 830, no. 2, 2016. doi:10.3847/0004-637X/830/2/131.

Choquet-Bruhat, Y., DeWitt-Morette, C., and Dillard-Bleik, M., *Analysis, manifolds and physics*. 1977.

Christodoulou, D. M., Contopoulos, I., and Kazanas, D., “Simulations of the Poynting-Robertson Cosmic Battery in Resistive Accretion Disks”, *The Astrophysical Journal*, vol. 674, no. 1. pp. 388–407, 2008. doi: 10.1086/524699.

Christodoulou, D. M., Gabuzda, D. C., Knuettel, S., Contopoulos, I., Kazanas, D., and Coughlan, C. P., “Dominance of outflowing electric currents on decaparsec to kiloparsec scales in extragalactic jets”, Astronomy and Astrophysics, vol. 591, 2016. doi:10.1051/0004-6361/201527448.

Claudel, C.-M., Virbhadra, K. S., and Ellis, G. F. R., “The geometry of photon surfaces”, *Journal of Mathematical Physics*, vol. 42, no. 2, pp. 818–838, 2001. doi:10.1063/1.1308507.

Contopoulos, J. and Lovelace, R. V. E., “Magnetically Driven Jets and Winds: Exact Solutions”, *The Astrophysical Journal*, vol. 429, p. 139, 1994. doi:10.1086/174307.

Contopoulos, J., “A Simple Type of Magnetically Driven Jets: an Astrophysical Plasma Gun”, *The Astrophysical Journal*, vol. 450. p. 616, 1995. doi: 10.1086/176170.

Contopoulos, I. and Kazanas, D., “A Cosmic Battery”, *The Astrophysical Journal*, vol. 508, no. 2. pp. 859–863, 1998. doi: 10.1086/306426.

Contopoulos, I., Kazanas, D., and Christodoulou, D. M., “The Cosmic Battery Revisited”, *The Astrophysical Journal*, vol. 652, no. 2. pp. 1451–1456, 2006. doi: 10.1086/507600.

Contopoulos, I., Christodoulou, D. M., Kazanas, D., and Gabuzda, D. C., “The Invariant Twist of Magnetic Fields in the Relativistic Jets of Active Galactic Nuclei”, *The Astrophysical Journal*, vol. 702, no. 2, pp. L148–L152, 2009. doi:10.1088/0004-637X/702/2/L148.

Contopoulos, I. and Papadopoulos, D. B., “The Cosmic Battery and the inner edge of the accretion disc”, *Monthly Notices of the Royal Astronomical Society*, vol. 425, no. 1. pp. 147–152, 2012. doi: 10.1111/j.1365-2966.2012.21408.x.

Contopoulos, I., Gabuzda, D., and Kylafis, N., *The Formation and Disruption of Black Hole Jets*, vol. 414. 2015. doi: 10.1007/978-3-319-10356-3.

Contopoulos, I., “A Cosmic Battery around Black Holes”, in *The Formation and Disruption of Black Hole Jets*, 2015, vol. 414, p. 227. doi:10.1007/978-3-319-10356-3_9.

Contopoulos, I., Nathanail, A., and Katsanikas, M., “The Cosmic Battery in Astrophysical Accretion Disks”, *The Astrophysical Journal*, vol. 805, no. 2, 2015. doi:10.1088/0004-637X/805/2/105.

Contopoulos, I., Nathanail, A., Sądowski, A., Kazanas, D., and Narayan, R., “Numerical simulations of the Cosmic Battery in accretion flows around astrophysical black holes”, *Monthly Notices of the Royal Astronomical Society*, vol. 473, no. 1, pp. 721–727, 2018. doi:10.1093/mnras/stx2249.

Contopoulos, I., “A Cosmic Battery in accretion flows around astrophysical black holes”, from ‘*International Conference on Black Holes as Cosmic Batteries: UHECRs and Multimessenger Astronomy*’, *arXiv e-prints*, 2019.

Coughlan, C., Murphy, R., McEnery, K., Patrick, H., Hallahan, R., and Gabuzda, D., “First results from 18-22cm VLBA polarisation observations of the MOJAVE-I AGNs”, in *10th European VLBI Network Symposium and EVN Users Meeting: VLBI and the New Generation of Radio Arrays*, 2010, vol. 10. doi:10.22323/1.125.0046.

Croke, S. M. and Gabuzda, D. C., “Aligning VLBI images of active galactic nuclei at different frequencies”, *Monthly Notices of the Royal Astronomical Society*, vol. 386, no. 2, pp. 619–626, 2008. doi:10.1111/j.1365-2966.2008.13087.x.

Croke, S. M., O'Sullivan, S. P., and Gabuzda, D. C., “The parsec-scale distributions of intensity, linear polarization and Faraday rotation in the core and jet of Mrk501 at 8.4-1.6 GHz”, *Monthly Notices of the Royal Astronomical Society*, vol. 402, no. 1, pp. 259–270, 2010. doi:10.1111/j.1365-2966.2009.15923.x.

Cunningham, C. T., “The effects of redshifts and focusing on the spectrum of an accretion disk around a Kerr black hole.”, *The Astrophysical Journal*, vol. 202, pp. 788–802, 1975. doi:10.1086/154033.

Cunningham, C., “Returning radiation in accretion disks around black holes.”, *The Astrophysical Journal*, vol. 208, pp. 534–549, 1976. doi:10.1086/154636.

Curd, B. and Narayan, R., “GRRMHD simulations of MAD accretion discs declining from super-Eddington to sub-Eddington accretion rates”, *Monthly Notices of the Royal Astronomical Society*, vol. 518, no. 3, pp. 3441–3461, 2023. doi:10.1093/mnras/stac3330.

Davelaar, J., Bronzwaer, T., Kok, D., Younsi, Z., Mościbrodzka, M., and Falcke, H., “Observing supermassive black holes in virtual reality”, *Computational Astrophysics and Cosmology*, vol. 5, no. 1, 2018. doi:10.1186/s40668-018-0023-7.

De Falco, V., Bakala, P., Battista, E., Lančová, D., Falanga, M., and Stella, L., “Three-dimensional general relativistic Poynting-Robertson effect: Radial radiation field”, *Physical Review D*, vol. 99, no. 2. 2019. doi: 10.1103/PhysRevD.99.023014.

De Falco, V., “Coupling Poynting-Robertson Effect in Mass Accretion Flow Physics”, from *Universität Basel*, *arXiv e-prints*, 2019.

De Falco, V., “New approaches to the general relativistic Poynting-Robertson effect”, *arXiv e-prints*, 2020.

de Vries, A., “Shadows of rotating black holes approximated by Duerer-Pascal limaçons”, *http://haegar.fh-swf.de/publikationen/pascal.pdf*, *South Westphalia University of Applied Sciences*, 2005.

Dewitt, C. and Dewitt, B. S., “Black holes (Les astres occlus)”, in *Black Holes (Les Astres Occlus)*, 1973.

Done, C., Gierliński, M., and Kubota, A., “Modelling the behaviour of accretion flows in X-ray binaries. Everything you always wanted to know about accretion but were afraid to ask”, *Astronomy and Astrophysics Review*, vol. 15, no. 1. pp. 1–66, 2007. doi: 10.1007/s00159-007-0006-1.

Dubus, G., “Thin discs, thick discs and transition zones”, in *EAS Publications Series*, 2003, vol. 7, p. 283. doi:10.1051/eas:2003044.

Einstein, A., “Zur Elektrodynamik bewegter Körper”, *Annalen der Physik*, vol. 322, no. 10, pp. 891–921, 1905. doi:10.1002/andp.19053221004.

El-Badry, K., “Unicorns and giraffes in the binary zoo: stripped giants with subgiant companions”, *Monthly Notices of the Royal Astronomical Society*, vol. 512, no. 4, pp. 5620–5641, 2022. doi:10.1093/mnras/stac815.

Esin, A. A., McClintock, J. E., and Narayan, R., “Advection-Dominated Accretion and the Spectral States of Black Hole X-Ray Binaries: Application to Nova Muscae 1991”, *The Astrophysical Journal*, vol. 489, no. 2, pp. 865–889, 1997. doi:10.1086/304829.

Event Horizon Telescope Collaboration, “First M87 Event Horizon Telescope Results. I. The Shadow of the Supermassive Black Hole”, *The Astrophysical Journal*, vol. 875, no. 1, 2019. doi:10.3847/2041-8213/ab0ec7.

Event Horizon Telescope Collaboration, “First M87 Event Horizon Telescope Results. IV. Imaging the Central Supermassive Black Hole”, *The Astrophysical Journal*, vol. 875, no. 1, 2019. doi:10.3847/2041-8213/ab0e85.

Event Horizon Telescope Collaboration, “First M87 Event Horizon Telescope Results. VI. The Shadow and Mass of the Central Black Hole”, *The Astrophysical Journal*, vol. 875, no. 1, 2019. doi:10.3847/2041-8213/ab1141.

Event Horizon Telescope Collaboration, “First M87 Event Horizon Telescope Results. VII. Polarization of the Ring”, *The Astrophysical Journal*, vol. 910, no. 1, 2021. doi:10.3847/2041-8213/abe71d.

Event Horizon Telescope Collaboration, “First M87 Event Horizon Telescope Results. VIII. Magnetic Field Structure near The Event Horizon”, *The Astrophysical Journal*, vol. 910, no. 1, 2021. doi:10.3847/2041-8213/abe4de.

Event Horizon Telescope Collaboration, “First Sagittarius A* Event Horizon Telescope Results. I. The Shadow of the Supermassive Black Hole in the Center of the Milky Way”, *The Astrophysical Journal*, vol. 930, no. 2, 2022. doi:10.3847/2041-8213/ac6674.

Event Horizon Telescope Collaboration, “First Sagittarius A* Event Horizon Telescope Results. II. EHT and Multiwavelength Observations, Data Processing, and Calibration”, *The Astrophysical Journal*, vol. 930, no. 2, 2022. doi:10.3847/2041-8213/ac6675.

Event Horizon Telescope Collaboration, “First Sagittarius A* Event Horizon Telescope Results. III. Imaging of the Galactic Center Supermassive Black Hole”, *The Astrophysical Journal*, vol. 930, no. 2, 2022. doi:10.3847/2041-8213/ac6429.

Event Horizon Telescope Collaboration, “First Sagittarius A* Event Horizon Telescope Results. IV. Variability, Morphology, and Black Hole Mass”, *The Astrophysical Journal*, vol. 930, no. 2, 2022. doi:10.3847/2041-8213/ac6736.

Fender, R., “Relativistic Outflows from X-ray Binaries ('Microquasars')”, in *Relativistic Flows in Astrophysics*, vol. 589, 2002, p. 101.

Fender, R. P., Belloni, T. M., and Gallo, E., “Towards a unified model for black hole X-ray binary jets”, *Monthly Notices of the Royal Astronomical Society*, vol. 355, no. 4, pp. 1105–1118, 2004. doi:10.1111/j.1365-2966.2004.08384.x.

Fender, R. P., Homan, J., and Belloni, T. M., “Jets from black hole X-ray binaries: testing, refining and extending empirical models for the coupling to X-rays”, *Monthly Notices of the Royal Astronomical Society*, vol. 396, no. 3, pp. 1370–1382, 2009. doi:10.1111/j.1365-2966.2009.14841.x.

Ferreira, J., Petrucci, P.-O., Henri, G., Saugé, L., and Pelletier, G., “A unified accretion-ejection paradigm for black hole X-ray binaries. I. The dynamical constituents”, *Astronomy and Astrophysics*, vol. 447, no. 3, pp. 813–825, 2006. doi:10.1051/0004-6361:20052689.

Fleming, T. P., Stone, J. M., and Hawley, J. F., “The Effect of Resistivity on the Nonlinear Stage of the Magnetorotational Instability in Accretion Disks”, *The Astrophysical Journal*, vol. 530, no. 1, pp. 464–477, 2000. doi:10.1086/308338.

Frank, J., King, A., and Raine, D. J., *Accretion Power in Astrophysics: Third Edition*. 2002, p. 398.

Frolov, V. P. and Novikov, I. D., *Black hole physics: basic concepts and new developments*. 1998.

Fuerst, S. V. and Wu, K., “Radiation transfer of emission lines in curved space-time”, *Astronomy and Astrophysics*, vol. 424. pp. 733–746, 2004. doi: 10.1051/0004-6361:20035814.

Fuerst, S. V., “General Relativistic Radiative Transfer”, *University of London*, PhDT, 2006.

Fuerst, S. V. and Wu, K., “Line emission from optically thick relativistic accretion tori”, *Astronomy and Astrophysics*, vol. 474, no. 1. pp. 55–66, 2007. doi: 10.1051/0004-6361:20066008.

Gabuzda, D. C., Murray, É., and Cronin, P., “Helical magnetic fields associated with the relativistic jets of four BL Lac objects”, *Monthly Notices of the Royal Astronomical Society*, vol. 351, no. 9, pp. L89–L93, 2004. doi:10.1111/j.1365-2966.2004.08037.x.

Gabuzda, D., “The compact polarised emission of AGN”, in *Proceedings of the 8th European VLBI Network Symposium*, 2006. doi:10.22323/1.036.0011.

Gabuzda, D. C., Vitrishchak, V. M., Mahmud, M., and O'Sullivan, S. P., “Radio circular polarization produced in helical magnetic fields in eight active galactic nuclei”, *Monthly Notices of the Royal Astronomical Society*, vol. 384, no. 3, pp. 1003–1014, 2008. doi:10.1111/j.1365-2966.2007.12773.x.

Gabuzda, D. C., Christodoulou, D. M., Contopoulos, I., and Kazanas, D., “Evidence for Helical Magnetic fields in Kiloparsec-Scale AGN Jets and the Action of a Cosmic Battery”, in *Journal of Physics Conference Series*, 2012, vol. 355, no. 1. doi:10.1088/1742-6596/355/1/012019.

Gabuzda, D. C., Cantwell, T. M., and Cawthorne, T. V., “Magnetic field structure of the extended 3C 380 jet”, *Monthly Notices of the Royal Astronomical Society*, vol. 438, no. 1, pp. L1–L5, 2014. doi:10.1093/mnrasl/slt129.

Gabuzda, D. C., Reichstein, A. R., and O'Neill, E. L., “Are spine-sheath polarization structures in the jets of active galactic nuclei associated with helical magnetic fields?”, *Monthly Notices of the Royal Astronomical Society*, vol. 444, no. 1, pp. 172–184, 2014. doi:10.1093/mnras/stu1381.

Gabuzda, D. C., “Parsec-Scale Jets in Active Galactic Nuclei”, in *The Formation and Disruption of Black Hole Jets*, 2015, vol. 414, p. 117. doi:10.1007/978-3-319-10356-3_5.

Gabuzda, D. C., Knuettel, S., and Reardon, B., “Transverse Faraday-rotation gradients across the jets of 15 active galactic nuclei”, *Monthly Notices of the Royal Astronomical Society*, vol. 450, no. 3, pp. 2441–2450, 2015. doi:10.1093/mnras/stv555.

Gabuzda, D. C., Knuettel, S., and Bonafede, A., “Evidence for a toroidal magnetic-field component in 5C 4.114 on kiloparsec scales”, *Astronomy and Astrophysics*, vol. 583, 2015. doi:10.1051/0004-6361/201527185.

Gammie, C. F. and Popham, R., “Advection-dominated Accretion Flows in the Kerr Metric. I. Basic Equations”, *The Astrophysical Journal*, vol. 498, no. 1, pp. 313–326, 1998. doi:10.1086/305521.

Giannios, D., “Spectra of black-hole binaries in the low/hard state: From radio to X-rays”, *Astronomy and Astrophysics*, vol. 437, no. 3, pp. 1007–1015, 2005. doi:10.1051/0004-6361:20041491.

Goode, P. R. and Dziembowski, W. A., “Solar-cycle dependence of the Sun's deep internal rotation shown by helioseismology”, *Nature*, vol. 349, no. 6306, pp. 223–225, 1991. doi:10.1038/349223a0.

Goodson, A. P., Winglee, R. M., and Böhm, K.-H., “Time-dependent Accretion by Magnetic Young Stellar Objects as a Launching Mechanism for Stellar Jets”, *The Astrophysical Journal*, vol. 489, no. 1, pp. 199–209, 1997. doi:10.1086/304774.

Govoni, F., “Rotation measures of radio sources in hot galaxy clusters”, *Astronomy and Astrophysics*, vol. 522, 2010. doi:10.1051/0004-6361/200913665.

Gralla, S. E., Porfyriadis, A. P., and Warburton, N., “Particle on the innermost stable circular orbit of a rapidly spinning black hole”, *Physical Review D*, vol. 92, no. 6, 2015. doi:10.1103/PhysRevD.92.064029.

Gralla, S. E., Holz, D. E., and Wald, R. M., “Black hole shadows, photon rings, and lensing rings”, *Physical Review D*, vol. 100, no. 2, 2019. doi:10.1103/PhysRevD.100.024018.

Gralla, S. E. and Lupsasca, A., “Lensing by Kerr black holes”, *Physical Review D*, vol. 101, no. 4, 2020. doi:10.1103/PhysRevD.101.044031.

Gralla, S. E. and Lupsasca, A., “Null geodesics of the Kerr exterior”, *Physical Review D*, vol. 101, no. 4, 2020. doi:10.1103/PhysRevD.101.044032.

Gralla, S. E., “Measuring the shape of a black hole photon ring”, *Physical Review D*, vol. 102, no. 4, 2020. doi:10.1103/PhysRevD.102.044017.

Gralla, S. E. and Lupsasca, A., “Observable shape of black hole photon rings”, *Physical Review D*, vol. 102, no. 12, 2020. doi:10.1103/PhysRevD.102.124003.

Gralla, S. E., Lupsasca, A., and Marrone, D. P., “The shape of the black hole photon ring: A precise test of strong-field general relativity”, *Physical Review D*, vol. 102, no. 12, 2020. doi:10.1103/PhysRevD.102.124004.

Grossman, R. and Levin, J., “Dynamics of black hole pairs. II. Spherical orbits and the homoclinic limit of zoom-whirliness”, *Physical Review D*, vol. 79, no. 4. 2009. doi: 10.1103/PhysRevD.79.043017.

Gualtieri, L. and Ferrari, V., “Black holes in General Relativity”, *Dipartimento di Fisica, Universita` degli studi di Roma “Sapienza”*, 2011

Guess, A. W., “Poynting-Robertson effect for a spherical source of radiation”, *The Astrophysical Journal*, vol. 135. pp. 855–866, 1962. doi: 10.1086/147329.

Haggard, D., “Hubble Space Telescope Advanced Camera for Surveys Imaging of ω Centauri: Optical Counterpart for the Quiescent Low-Mass X-Ray Binary”, *The Astrophysical Journal*, vol. 613, no. 1, pp. 512–516, 2004. doi:10.1086/421549.

Hartle, J. B. and Thorne, K. S., “Slowly Rotating Relativistic Stars. II. Models for Neutron Stars and Supermassive Stars”, *The Astrophysical Journal*, vol. 153, p. 807, 1968. doi:10.1086/149707.

Hawley, J. F. and Balbus, S. A., “A Powerful Local Shear Instability in Weakly Magnetized Disks. II. Nonlinear Evolution”, *The Astrophysical Journal*, vol. 376. p. 223, 1991. doi: 10.1086/170271.

Hawley, J. F. and Balbus, S. A., “A Powerful Local Shear Instability in Weakly Magnetized Disks. III. Long-Term Evolution in a Shearing Sheet”, *The Astrophysical Journal*, vol. 400, p. 595, 1992. doi:10.1086/172021.

Hawley, J. F., Gammie, C. F., and Balbus, S. A., “Local Three-dimensional Magnetohydrodynamic Simulations of Accretion Disks”, *The Astrophysical Journal*, vol. 440, p. 742, 1995. doi:10.1086/175311.

Heinke, C. O., “Galactic Ultracompact X-Ray Binaries: Disk Stability and Evolution”, *The Astrophysical Journal*, vol. 768, no. 2, 2013. doi:10.1088/0004-637X/768/2/184.

Herrnstein, J. R., Moran, J. M., Greenhill, L. J., and Trotter, A. S., “The Geometry of and Mass Accretion Rate through the Maser Accretion Disk in NGC 4258”, *The Astrophysical Journal*, vol. 629, no. 2, pp. 719–738, 2005. doi:10.1086/431421.

Homan, D. C. and Lister, M. L., “MOJAVE: Monitoring of Jets in Active Galactic Nuclei with VLBA Experiments. II. First-Epoch 15 GHz Circular Polarization Results”, *The Astronomical Journal*, vol. 131, no. 3, pp. 1262–1279, 2006. doi:10.1086/500256.

Hovatta, T., “MOJAVE: Monitoring of Jets in Active Galactic Nuclei with VLBA Experiments. VIII. Faraday Rotation in Parsec-scale AGN Jets”, *The Astronomical Journal*, vol. 144, no. 4, 2012. doi:10.1088/0004-6256/144/4/105.

Hovatta, T., “MOJAVE: Monitoring of Jets in Active Galactic Nuclei with VLBA Experiments. XI. Spectral Distributions”, *The Astronomical Journal*, vol. 147, no. 6, 2014. doi:10.1088/0004-6256/147/6/143.

Hughes, S. A., “Trust but verify: The case for astrophysical black holes”, *2005 SLAC Summer Institute*, *arXiv e-prints*, 2005.

Ichimaru, S., “Bimodal behavior of accretion disks: theory and application to Cygnus X-1 transitions.”, The Astrophysical Journal, vol. 214, pp. 840–855, 1977. doi:10.1086/155314.

Igumenshchev, I. V., Narayan, R., and Abramowicz, M. A., “Three-dimensional Magnetohydrodynamic Simulations of Radiatively Inefficient Accretion Flows”, *The Astrophysical Journal*, vol. 592, no. 2. pp. 1042–1059, 2003. doi: 10.1086/375769.

Inoue, H. and Hoshi, R., "X-Ray Irradiated Accretion Disks and Bimodal States", *The Astrophysical Journal*, vol. 322, p. 320, 1987. doi:10.1086/165728.

Iskakov, A. B., Schekochihin, A. A., Cowley, S. C., McWilliams, J. C., and Proctor, M. R. E., "Numerical Demonstration of Fluctuation Dynamo at Low Magnetic Prandtl Numbers", *Physical Review Letters*, vol. 98, no. 20, 2007. doi:10.1103/PhysRevLett.98.208501.

Jayasinghe, T., "A unicorn in monoceros: the 3 $M_\odot$ dark companion to the bright, nearby red giant V723 Mon is a non-interacting, mass-gap black hole candidate", *Monthly Notices of the Royal Astronomical Society*, vol. 504, no. 2, pp. 2577–2602, 2021. doi:10.1093/mnras/stab907.

Jeffery, G. B., "The Field of an Electron on Einstein's Theory of Gravitation", *Proceedings of the Royal Society of London Series A*, vol. 99, no. 697, pp. 123–134, 1921. doi:10.1098/rspa.1921.0028.

Kalogera, V. and Baym, G., "The Maximum Mass of a Neutron Star", *The Astrophysical Journal*, vol. 470, p. L61, 1996. doi:10.1086/310296.

Kazanas, D., "X-Ray Binary Phenomenology and Their Accretion Disk Structure", in *The Formation and Disruption of Black Hole Jets*, 2015, vol. 414, p. 207. doi:10.1007/978-3-319-10356-3_8.

Kerr, R. P., "Gravitational Field of a Spinning Mass as an Example of Algebraically Special Metrics", *Physical Review Letters*, vol. 11, no. 5. pp. 237–238, 1963. doi: 10.1103/PhysRevLett.11.237.

Kharb, P., Gabuzda, D. C., O'Dea, C. P., Shastri, P., and Baum, S. A., "Rotation Measures Across Parsec-Scale Jets of Fanaroff-Riley Type I Radio Galaxies", *The Astrophysical Journal*, vol. 694, no. 2, pp. 1485–1497, 2009. doi:10.1088/0004-637X/694/2/1485.

Koliopanos, P., Menis, I., Pantiskos, N., «Σημειώσεις & Προβλήματα στην Ειδική Σχετικότητα» ("Notes & Problems in Special Relativity"), *Copy Factory*, 2010

Koljonen, K. I. I., Hannikainen, D. C., McCollough, M. L., Pooley, G. G., and Trushkin, S. A., "The hardness-intensity diagram of Cygnus X-3: revisiting the radio/X-ray states", *Monthly Notices of the Royal Astronomical Society*, vol. 406, no. 1, pp. 307–319, 2010. doi:10.1111/j.1365-2966.2010.16722.x.

Komissarov, S. S., "Numerical simulations of relativistic magnetized jets", *Monthly Notices of the Royal Astronomical Society*, vol. 308, no. 4, pp. 1069–1076, 1999. doi:10.1046/j.1365-8711.1999.02783.x.

Komissarov, S. S., "Direct numerical simulations of the Blandford-Znajek effect", *Monthly Notices of the Royal Astronomical Society*, vol. 326, no. 3, pp. L41–L44, 2001. doi:10.1046/j.1365-8711.2001.04863.x.

Komissarov, S. S., Barkov, M. V., Vlahakis, N., and Königl, A., "Magnetic acceleration of relativistic active galactic nucleus jets", *Monthly Notices of the Royal Astronomical Society*, vol. 380, no. 1, pp. 51–70, 2007. doi:10.1111/j.1365-2966.2007.12050.x.

Komissarov, S. S., "Blandford-Znajek Mechanism versus Penrose Process", *Journal of Korean Physical Society*, vol. 54, no. 61, p. 2503, 2009. doi:10.3938/jkps.54.2503.

Komissarov, S. and Porth, O., "Numerical simulations of jets", *New Astronomy Reviews*, vol. 92, 2021. doi:10.1016/j.newar.2021.101610.

Konoplya, R. A., Kunz, J., and Zhidenko, A., "Blandford-Znajek mechanism in the general stationary axially-symmetric black-hole spacetime", *Journal of Cosmology and Astroparticle Physics*, vol. 2021, no. 12, 2021. doi:10.1088/1475-7516/2021/12/002.

Koutsantoniou, L. E. 2014, «Το φαινόμενο Poynting – Robertson στο πλαίσιο της Γενικής Θεωρίας της Σχετικότητας και η εφαρμογή του σε δίσκους προσαύξησης και το μοντέλο της Κοσμικής Μπαταρίας» ("The Poynting – Robertson effect in General Relativity and its applications on accretion disks and the Cosmic Battery"), Master's thesis, *Department of Astrophysics, Astronomy and Mechanics, Faculty of Physics, University of Athens*, Panepistimiopolis Zografos, Athens 15784, Greece

Koutsantoniou, L. E. and Contopoulos, I., "Accretion Disk Radiation Dynamics and the Cosmic Battery", *The Astrophysical Journal*, vol. 794, no. 1. 2014. doi: 10.1088/0004-637X/794/1/27.

Koutsantoniou E., "*Black holes, radiation and the accretion disk*", Hel.A.S. conference 2015

Koutsantoniou, L. E., "Algorithms and radiation dynamics for the vicinity of black holes. I. Methods and codes", *Astronomy and Astrophysics*, vol. 657, 2022. doi:10.1051/0004-6361/202140682.

Koutsantoniou, L. E., “Algorithms and radiation dynamics for the vicinity of black holes. II. Results”, *Astronomy and Astrophysics*, vol. 671, 2023. doi:10.1051/0004-6361/202244319.

Koutsantoniou, L. E., “Algorithms and radiation dynamics for the vicinity of black holes. II. Results. Online material”, *Astronomy and Astrophysics*, vol. 671, 2023. doi:10.1051/0004-6361/202244319.

Kozlowski, M., Jaroszynski, M., and Abramowicz, M. A., “The analytic theory of fluid disks orbiting the Kerr black hole.”, *Astronomy and Astrophysics*, vol. 63, no. 1–2. pp. 209–220, 1978.

Krause, M. and Löhr, A., “The magnetic field along the jets of NGC 4258. as deduced from high frequency radio observations”, *Astronomy and Astrophysics*, vol. 420, pp. 115–123, 2004. doi:10.1051/0004-6361:20034165.

Krolik, J. H., “Instabilities is α-Disks”, in *High Energy Processes in Accreting Black Holes*, 1999, vol. 161, p. 315.

Krolik, J. H., *Active galactic nuclei : from the central black hole to the galactic environment.* 1999.

Krolik, J. H. and Hawley, J. F., “Where Is the Inner Edge of an Accretion Disk around a Black Hole?”, *The Astrophysical Journal*, vol. 573, no. 2. pp. 754–763, 2002. doi: 10.1086/340760.

Kronberg, P. P., Dufton, Q. W., Li, H., and Colgate, S. A., “Magnetic Energy of the Intergalactic Medium from Galactic Black Holes”, *The Astrophysical Journal*, vol. 560, no. 1, pp. 178–186, 2001. doi:10.1086/322767.

Kronberg, P. P., Lovelace, R. V. E., Lapenta, G., and Colgate, S. A., “Measurement of the Electric Current in a kpc-scale Jet”, *The Astrophysical Journal*, vol. 741, no. 1, 2011. doi:10.1088/2041-8205/741/1/L15.

Kronberg, P. P., Lovelace, R. V. E., Coplgate, S. A., and Lapenta, G., “Measurement and Simulation of the Electric Current in a kpc-Scale Jet”, *APS Division of Plasma Physics Meeting Abstracts*, vol. 2013, 2013.

Kulsrud, R. M., Cen, R., Ostriker, J. P., and Ryu, D., “The Protogalactic Origin for Cosmic Magnetic Fields”, *The Astrophysical Journal*, vol. 480, no. 2, pp. 481–491, 1997. doi:10.1086/303987.

Kylafis, N. D., Contopoulos, I., Kazanas, D., and Christodoulou, D. M., “Formation and destruction of jets in X-ray binaries”, *Astronomy and Astrophysics*, vol. 538. 2012. doi: 10.1051/0004-6361/201117052.

Kylafis, N. D. and Belloni, T. M., “Accretion and Ejection in Black-Hole X-Ray Transients”, in *The Formation and Disruption of Black Hole Jets*, 2015, vol. 414, p. 245. doi:10.1007/978-3-319-10356-3_10.

Kylafis, N. D. and Belloni, T. M., “Accretion and ejection in black-hole X-ray transients”, *Astronomy and Astrophysics*, vol. 574, 2015. doi:10.1051/0004-6361/201425106.

Lamb, F. K. and Miller, M. C., “Critical Radiation Fluxes and Luminosities of Black Holes and Relativistic Stars”, *The Astrophysical Journal*, vol. 439. p. 828, 1995. doi: 10.1086/175221.

Landau, L. D. and Lifshitz, E. M., *The classical theory of fields.* 1975.

Larmor, J., “Radiation-Pressure, Astrophysical Retardation, and Relativity”, *Nature*, vol. 99, no. 2490. p. 404, 1917. doi: 10.1038/099404c0.

Lasota, J.-P., “ADAFs-models, observations and problems.”, *Physics Reports*, vol. 311, pp. 247–258, 1999. doi:10.1016/S0370-1573(98)00103-3.

Lasota, J.-P., Gourgoulhon, E., Abramowicz, M., Tchekhovskoy, A., and Narayan, R., “Extracting black-hole rotational energy: The generalized Penrose process”, *Physical Review D*, vol. 89, no. 2, 2014. doi:10.1103/PhysRevD.89.024041.

Lasota, J.-P., “Black Hole Accretion Discs”, in *Astrophysics of Black Holes: From Fundamental Aspects to Latest Developments*, 2016, vol. 440, p. 1. doi:10.1007/978-3-662-52859-4_1.

Layzer, D., Rosner, R., and Doyle, H. T., “On the origin of solar magnetic fields.”, *The Astrophysical Journal*, vol. 229, pp. 1126–1137, 1979. doi:10.1086/157047.

Lee, H. K., Wijers, R. A. M. J., and Brown, G. E., “The Blandford-Znajek process as a central engine for a gamma-ray burst”, *Physics Reports*, vol. 325, no. 3, pp. 83–114, 2000. doi:10.1016/S0370-1573(99)00084-8.

Levin, J. and Perez-Giz, G., “A periodic table for black hole orbits”, *Physical Review D*, vol. 77, no. 10. 2008. doi: 10.1103/PhysRevD.77.103005.

Levin, J. and Grossman, R., “Dynamics of black hole pairs. I. Periodic tables”, *Physical Review D*, vol. 79, no. 4. 2009. doi: 10.1103/PhysRevD.79.043016.

Livio, M., Ogilvie, G. I., and Pringle, J. E., “Extracting Energy from Black Holes: The Relative Importance of the Blandford-Znajek Mechanism”, *The Astrophysical Journal*, vol. 512, no. 1, pp. 100–104, 1999. doi:10.1086/306777.

Longair, M. S., *High Energy Astrophysics*. 2011.

Lovelace, R. V. E., “Dynamo model of double radio sources”, *Nature*, vol. 262, no. 5570. pp. 649–652, 1976. doi: 10.1038/262649a0.

Lovelace, R. V. E., Romanova, M. M., and Newman, W. I., “Implosive Accretion and Outbursts of Active Galactic Nuclei”, *The Astrophysical Journal*, vol. 437. p. 136, 1994. doi: 10.1086/174981.

Lovelace, R. V. E., Rothstein, D. M., and Bisnovatyi-Kogan, G. S., “Advection/Diffusion of Large-Scale B Field in Accretion Disks”, *The Astrophysical Journal*, vol. 701, no. 2. pp. 885–890, 2009. doi: 10.1088/0004-637X/701/2/885.

Lubow, S. H., Papaloizou, J. C. B., and Pringle, J. E., “Magnetic field dragging in accretion discs”, *Monthly Notices of the Royal Astronomical Society*, vol. 267, no. 2. pp. 235–240, 1994. doi: 10.1093/mnras/267.2.235.

Lynden-Bell, D., “Magnetic collimation by accretion discs of quasars and stars”, *Monthly Notices of the Royal Astronomical Society*, vol. 279, no. 2, pp. 389–401, 1996. doi:10.1093/mnras/279.2.389.

Lynden-Bell, D., “Magnetism Along Spin”, *The Observatory*, vol. 133. pp. 266–269, 2013.

Lynden-Bell, D., “Jets at Birth and Death”, in *The Formation and Disruption of Black Hole Jets*, 2015, vol. 414, p. 1. doi:10.1007/978-3-319-10356-3_1.

MacDonald, D. and Thorne, K. S., “Black-hole electrodynamics - an absolute-space/universal-time formulation”, *Monthly Notices of the Royal Astronomical Society*, vol. 198. pp. 345–382, 1982. doi: 10.1093/mnras/198.2.345.

Mahlmann, J. F., Levinson, A., and Aloy, M. A., “Striped Blandford/Znajek jets from advection of small-scale magnetic field”, *Monthly Notices of the Royal Astronomical Society*, vol. 494, no. 3, pp. 4203–4225, 2020. doi:10.1093/mnras/staa943.

Mahmud, M. and Gabuzda, D., “Evidence for the generation of helical magnetic fields in active galactic nuclei”, in *From Planets to Dark Energy: the Modern Radio Universe*, 2007.

Mahmud, M. and Gabuzda, D. C., “Using Faraday Rotation Gradients to probe Magnetic Tower Models”, from the proceedings for *'The 9th European VLBI Network Symposium on The role of VLBI in the Golden Age for Radio Astronomy and EVN Users Meeting' 2008*, arXiv e-prints, 2009.

Mahmud, M. and Gabuzda, D. C., “Searching For Helical Magnetic Fields in Active Galactic Nuclei”, in *Extragalactic Jets: Theory and Observation from Radio to Gamma Ray*, 2008, vol. 386, p. 494.

Mahmud, M., Gabuzda, D. C., and Bezrukovs, V., “Surprising evolution of the parsec-scale Faraday Rotation gradients in the jet of the BL Lac object B1803+784”, *Monthly Notices of the Royal Astronomical Society*, vol. 400, no. 1. pp. 2–12, 2009. doi: 10.1111/j.1365-2966.2009.15013.x.

Mahmud, M., Coughlan, C. P., Murphy, E., Gabuzda, D. C., and Hallahan, D. R., “Connecting magnetic towers with Faraday rotation gradients in active galactic nuclei jets”, *Monthly Notices of the Royal Astronomical Society*, vol. 431, no. 1, pp. 695–709, 2013. doi:10.1093/mnras/stt201.

Mastichiadis, A., “Radiative Processes in Relativistic Outflows”, in *Relativistic Flows in Astrophysics*, vol. 589, 2002, p. 1.

Matsumoto, R., Uchida, Y., Hirose, S., Shibata, K., Hayashi, M. R., Ferrari, A., Bodo, G., and Norman, C., “Radio Jets and the Formation of Active Galaxies: Accretion Avalanches on the Torus by the Effect of a Large-Scale Magnetic Field”, *The Astrophysical Journal*, vol. 461. p. 115, 1996. doi: 10.1086/177041.

McKinney, J. C., “Total and Jet Blandford-Znajek Power in the Presence of an Accretion Disk”, *The Astrophysical Journal*, vol. 630, no. 1, pp. L5–L8, 2005. doi:10.1086/468184.

McKinney, J. C., Tchekhovskoy, A., and Blandford, R. D., “General relativistic magnetohydrodynamic simulations of magnetically choked accretion flows around black holes”, *Monthly Notices of the Royal Astronomical Society*, vol. 423, no. 4, pp. 3083–3117, 2012. doi:10.1111/j.1365-2966.2012.21074.x.

Meyer-Hofmeister, E., Liu, B. F., and Meyer, F., “The hard to soft spectral transition in LMXBs-affected by recondensation of gas into an inner disk”, *Astronomy and Astrophysics*, vol. 508, no. 1, pp. 329–337, 2009. doi:10.1051/0004-6361/200913044.

Miller, M. C. and Lamb, F. K., “Effect of Radiation Forces on Disk Accretion by Weakly Magnetic Neutron Stars”, *The Astrophysical Journal*, vol. 413. p. L43, 1993. doi: 10.1086/186955.

Miller, M. C. and Lamb, F. K., “Motion of Accreting Matter near Luminous Slowly Rotating Relativistic Stars”, *The Astrophysical Journal*, vol. 470. p. 1033, 1996. doi: 10.1086/177929.

Minkowski, H., “Space and Time”, *Jahresbericht der Deutschen Mathematiker-Vereinigung, vol. 18, p. 75-88*, 1909, translation in English by M. N. Saha, *Calcutta University Press*, 1920.

Minkowski, H., “Spazio e tempo”, *Il Nuovo Cimento*, vol. 18, no. 1, pp. 333–352, 1909. doi:10.1007/BF02832892.

Minkowski, H., “The Fundamental Equations for Electromagnetic Processes in Moving Bodies”, *Nachrichten von der Gesellschaft der Wissenschaften zu Göttingen*, Mathematisch-Physikalische Klasse, pp. 53–111, 1908, translation in English by M. N. Saha, *Calcutta University Press*, 1920.

Misner, C. W., Thorne, K. S., and Wheeler, J. A., *Gravitation*. 1973.

Miyamoto, S., Kitamoto, S., Hayashida, K., and Egoshi, W., “Large Hysteretic Behavior of Stellar Black Hole Candidate X-Ray Binaries”, *The Astrophysical Journal*, vol. 442, p. L13, 1995. doi:10.1086/187804.

Moeen, M., Ghanbari, J., and Ghodsi, A., “Shear Tensor and Dynamics of Relativistic Accretion Disks around Rotating Black Holes”, *Publications of the Astronomical Society of Japan*, vol. 64. 2012. doi: 10.1093/pasj/64.6.137.

Mościbrodzka, M., Gammie, C. F., Dolence, J. C., Shiokawa, H., and Leung, P. K., “Radiative Models of SGR A* from GRMHD Simulations”, *The Astrophysical Journal*, vol. 706, no. 1, pp. 497–507, 2009. doi:10.1088/0004-637X/706/1/497.

Mościbrodzka, M., Falcke, H., Shiokawa, H., and Gammie, C. F., “Observational appearance of inefficient accretion flows and jets in 3D GRMHD simulations: Application to Sagittarius A*”, *Astronomy and Astrophysics*, vol. 570, 2014. doi:10.1051/0004-6361/201424358.

Mościbrodzka, M., Falcke, H., and Noble, S., “Light from the supermassive black hole in the Galactic center”, in *Fourteenth Marcel Grossmann Meeting - MG14*, 2018, pp. 3519–3524. doi:10.1142/9789813226609_0455.

Mueller, T. and Grave, F., “Catalogue of Spacetimes”, *arXiv e-prints*, 2009.

Müller, A. 2004, Ph.D. Thesis: Black hole astrophysics: Magnetohydrodynamics on the Kerr geometry, Landessternwarte Heidelberg, Germany

Murphy, E., Cawthorne, T. V., and Gabuzda, D. C., “Analysing the transverse structure of the relativistic jets of active galactic nuclei”, Monthly Notices of the Royal Astronomical Society, vol. 430, no. 3, pp. 1504–1515, 2013. doi:10.1093/mnras/sts561.

Murphy, E. and Gabuzda, D., “Monte Carlo Studies of Transverse Faraday Rotation Profiles”, in European Physical Journal Web of Conferences, 2013, vol. 61. doi:10.1051/epjconf/20136107005.

Nakamura, M. and Asada, K., “The Parabolic Jet Structure in M87 as a Magnetohydrodynamic Nozzle”, *The Astrophysical Journal*, vol. 775, no. 2, 2013. doi:10.1088/0004-637X/775/2/118.

Nakamura, M. et al., “Parabolic Jets from the Spinning Black Hole in M87”, *The Astrophysical Journal*, vol. 868, no. 2, 2018. doi:10.3847/1538-4357/aaeb2d.

Narayan, R. and Yi, I., “Advection-dominated Accretion: A Self-similar Solution”, *The Astrophysical Journal*, vol. 428. p. L13, 1994. doi: 10.1086/187381.

Narayan, R. and Yi, I., “Advection-dominated Accretion: Self-Similarity and Bipolar Outflows”, *The Astrophysical Journal*, vol. 444. p. 231, 1995. doi: 10.1086/175599.

Narayan, R. and Yi, I., “Advection-dominated Accretion: Underfed Black Holes and Neutron Stars”, *The Astrophysical Journal*, vol. 452. p. 710, 1995. doi: 10.1086/176343.

Narayan, R. and Bartelmann, M., “Lectures on Gravitational Lensing”, *arXiv e-prints*, 1996.

Narayan, R., Kato, S., and Honma, F., “Global Structure and Dynamics of Advection-dominated Accretion Flows around Black Holes”, The Astrophysical Journal, vol. 476, no. 1, pp. 49–60, 1997. doi:10.1086/303591.

Narayan, R., Igumenshchev, I. V., and Abramowicz, M. A., “Magnetically Arrested Disk: an Energetically Efficient Accretion Flow”, *Publications of the Astronomical Society of Japan*, vol. 55. pp. L69–L72, 2003. doi: 10.1093/pasj/55.6.L69.

Narayan, R. and McClintock, J. E., “Advection-dominated accretion and the black hole event horizon”, *New Astronomy Reviews*, vol. 51, no. 10–12. pp. 733–751, 2008. doi: 10.1016/j.newar.2008.03.002.

Narayan, R., Sądowski, A., Penna, R. F., and Kulkarni, A. K., “GRMHD simulations of magnetized advection-dominated accretion on a non-spinning black hole: role of outflows”, *Monthly Notices of the Royal Astronomical Society*, vol. 426, no. 4. pp. 3241–3259, 2012. doi: 10.1111/j.1365-2966.2012.22002.x.

Newman, E. T., Couch, E., Chinnapared, K., Exton, A., Prakash, A., and Torrence, R., “Metric of a Rotating, Charged Mass”, *Journal of Mathematical Physics*, vol. 6, no. 6, pp. 918–919, 1965. doi:10.1063/1.1704351.

Newman, W. I., Newman, A. L., and Lovelace, R. V. E., “Initiation of Bipolar Flows by Magnetic Field Twisting in Protostellar Nebulae”, *The Astrophysical Journal*, vol. 392, p. 622, 1992. doi:10.1086/171462.

Noble, S. C., Leung, P. K., Gammie, C. F., and Book, L. G., “Simulating the emission and outflows from accretion discs”, *Classical and Quantum Gravity*, vol. 24, no. 12, pp. S259–S274, 2007. doi:10.1088/0264-9381/24/12/S17.

Noble, S. C., Krolik, J. H., Schnittman, J. D., and Hawley, J. F., “Radiative Efficiency and Thermal Spectrum of Accretion onto Schwarzschild Black Holes”, *The Astrophysical Journal*, vol. 743, no. 2, 2011. doi:10.1088/0004-637X/743/2/115.

Nordström, G., “On the Energy of the Gravitation field in Einstein's Theory”, *Koninklijke Nederlandse Akademie van Wetenschappen Proceedings Series B Physical Sciences*, vol. 20, pp. 1238–1245, 1918.

Novikov, I. D. and Thorne, K. S., “Astrophysics of black holes.”, in *Black Holes (Les Astres Occlus)*, 1973, pp. 343–450.

Oh, J. S., Kim, H., and Lee, H. M., “Trajectory of a test particle around a slowly rotating relativistic star emitting isotropic radiation”, *Physical Review D*, vol. 81, no. 8. 2010. doi: 10.1103/PhysRevD.81.084005.

O'Sullivan, S. P. and Gabuzda, D. C., “Three-dimensional magnetic field structure of six parsec-scale active galactic nuclei jets”, *Monthly Notices of the Royal Astronomical Society*, vol. 393, no. 2, pp. 429–456, 2009. doi:10.1111/j.1365-2966.2008.14213.x.

Paczynski, B., “Advection Dominated Accretion Flows. A Toy Disk Model”, Acta Astronomica, vol. 48, pp. 667–676, 1998.

Page, L., “Is a Moving Star Retarded by the Reaction of Its Own Radiation?”, *Proceedings of the National Academy of Science*, vol. 4, no. 2, pp. 47–49, 1918. doi:10.1073/pnas.4.2.47.

Page, L., “Is a Moving Mass Retarded by the Reaction of its own Radiation?”, *Physical Review*, vol. 11, no. 5, pp. 376–400, 1918. doi:10.1103/PhysRev.11.376.

Page, L., “The Motion of an Electrical Doublet”, *Physical Review*, vol. 12, no. 5, pp. 371–380, 1918. doi:10.1103/PhysRev.12.371.

Parfrey, K., Philippov, A., and Cerutti, B., “First-Principles Plasma Simulations of Black-Hole Jet Launching”, *Physical Review Letters*, vol. 122, no. 3, 2019. doi:10.1103/PhysRevLett.122.035101.

Park, J., Hada, K., Kino, M., Nakamura, M., Ro, H., and Trippe, S., “Faraday Rotation in the Jet of M87 inside the Bondi Radius: Indication of Winds from Hot Accretion Flows Confining the Relativistic Jet”, *The Astrophysical Journal*, vol. 871, no. 2, 2019. doi:10.3847/1538-4357/aaf9a9.

Pelletier, G., Sol, H., and Asseo, E., “Magnetized Langmuir wave packets excited by a strong beam-plasma interaction”, *Physical Review A*, vol. 38, pp. 2552–2563, 1988. doi:10.1103/PhysRevA.38.2552.

Penna, R. F., McKinney, J. C., Narayan, R., Tchekhovskoy, A., Shafee, R., and McClintock, J. E., “Simulations of magnetized discs around black holes: effects of black hole spin, disc thickness and magnetic field geometry”, *Monthly Notices of the Royal Astronomical Society*, vol. 408, no. 2. pp. 752–782, 2010. doi: 10.1111/j.1365-2966.2010.17170.x.

Penna, R. F., Sądowski, A., Kulkarni, A. K., and Narayan, R., “The Shakura-Sunyaev viscosity prescription with variable α (r)”, *Monthly Notices of the Royal Astronomical Society*, vol. 428, no. 3. pp. 2255–2274, 2013. doi: 10.1093/mnras/sts185.

Penna, R. F., “*Black hole accretion disks and jets: Connecting simulations and theory*”, PhDT, 2013.

Penna, R. F., Kulkarni, A., and Narayan, R., “A new equilibrium torus solution and GRMHD initial conditions”, *Astronomy and Astrophysics*, vol. 559. 2013. doi: 10.1051/0004-6361/201219666.

Penna, R. F., Narayan, R., and Sądowski, A., “General relativistic magnetohydrodynamic simulations of Blandford-Znajek jets and the membrane paradigm”, *Monthly Notices of the Royal Astronomical Society*, vol. 436, no. 4. pp. 3741–3758, 2013. doi: 10.1093/mnras/stt1860.

Penrose, R. and Floyd, R. M., “Extraction of Rotational Energy from a Black Hole”, *Nature Physical Science*, vol. 229, no. 6, pp. 177–179, 1971. doi:10.1038/physci229177a0.

Pessah, M. E., Chan, C.-. kwan ., and Psaltis, D., “Angular Momentum Transport in Accretion Disks: Scaling Laws in MRI-driven Turbulence”, *The Astrophysical Journal*, vol. 668, no. 1, pp. L51–L54, 2007. doi:10.1086/522585.

Planck, M., “Zur Theorie der Wärmestrahlung”, *Annalen der Physik*, vol. 336, no. 4, pp. 758–768, 1910. doi:10.1002/andp.19103360406, “The Theory of Heat Radiation”, translation in English by M. Masius, *P. Blakiston's Son & Co*, 1914.

Podsiadlowski, P., Rappaport, S., and Pfahl, E. D., “Evolutionary Sequences for Low- and Intermediate-Mass X-Ray Binaries”, *The Astrophysical Journal*, vol. 565, no. 2, pp. 1107–1133, 2002. doi:10.1086/324686.

Popham, R. and Gammie, C. F., “Advection-dominated Accretion Flows in the Kerr Metric. II. Steady State Global Solutions”, The Astrophysical Journal, vol. 504, no. 1, pp. 419–430, 1998. doi:10.1086/306054.

Popham, R., Woosley, S. E., and Fryer, C., “Hyperaccreting Black Holes and Gamma-Ray Bursts”, *The Astrophysical Journal*, vol. 518, no. 1, pp. 356–374, 1999. doi:10.1086/307259.

Poynting, J. H., “Radiation in the solar system : its effect on temperature and its pressure on small bodies”, *Monthly Notices of the Royal Astronomical Society*, vol. 64. p. 1, 1903.

Pushkarev, A. B., Gabuzda, D. C., Vetukhnovskaya, Y. N., and Yakimov, V. E., “Spine-sheath polarization structures in four active galactic nuclei jets”, *Monthly Notices of the Royal Astronomical Society*, vol. 356, no. 3, pp. 859–871, 2005. doi:10.1111/j.1365-2966.2004.08535.x.

Qian, L., Abramowicz, M. A., Fragile, P. C., Horák, J., Machida, M., and Straub, O., “The Polish doughnuts revisited. I. The angular momentum distribution and equipressure surfaces”, *Astronomy and Astrophysics*, vol. 498, no. 2. pp. 471–477, 2009. doi: 10.1051/0004-6361/200811518.

Quataert, E., “Low Radiative-Efficiency Accretion Flows”, in *Probing the Physics of Active Galactic Nuclei*, 2001, vol. 224, p. 71.

Rees, M. J., Begelman, M. C., Blandford, R. D., and Phinney, E. S., “Ion-supported tori and the origin of radio jets”, Nature, vol. 295, no. 5844, pp. 17–21, 1982. doi:10.1038/295017a0.

Refsdal, S., “The gravitational lens effect”, *Monthly Notices of the Royal Astronomical Society*, vol. 128, p. 295, 1964. doi:10.1093/mnras/128.4.295.

Reichstein, A. and Gabuzda, D., “The Use of Faraday Rotation Sign Maps as a Diagnostic for Helical Jet Magnetic Fields”, in *Journal of Physics Conference Series*, 2012, vol. 355, no. 1. doi:10.1088/1742-6596/355/1/012021.

Reig, P. and Fabregat, J., “Long-term variability of high-mass X-ray binaries. I. Photometry”, *Astronomy and Astrophysics*, vol. 574, 2015. doi:10.1051/0004-6361/201425008.

Reig, P., Nersesian, A., Zezas, A., Gkouvelis, L., and Coe, M. J., “Long-term optical variability of high-mass X-ray binaries. II. Spectroscopy”, *Astronomy and Astrophysics*, vol. 590, 2016. doi:10.1051/0004-6361/201628271.

Reissner, H., “Über die Eigengravitation des elektrischen Feldes nach der Einsteinschen Theorie”, *Annalen der Physik*, vol. 355, no. 9, pp. 106–120, 1916. doi:10.1002/andp.19163550905.

Reyes-Ruiz, M. and Stepinski, T. F., “Axisymmetric Two-dimensional Computation of Magnetic Field Dragging in Accretion Disks”, *The Astrophysical Journal*, vol. 459, p. 653, 1996. doi:10.1086/176930.

Rezzolla, L., “Three Little Pieces for Computer and Relativity”, in *General Relativity, Cosmology and Astrophysics*, vol. 177, 2014, p. 391. doi: 10.1007/978-3-319-06349-2_19.

Robertson, H. P., “Dynamical effects of radiation in the solar system”, *Monthly Notices of the Royal Astronomical Society*, vol. 97. p. 423, 1937. doi: 10.1093/mnras/97.6.423.

Rothstein, D. M. and Lovelace, R. V. E., “Advection of Magnetic Fields in Accretion Disks: Not So Difficult After All”, *The Astrophysical Journal*, vol. 677, no. 2, pp. 1221–1232, 2008. doi:10.1086/529128.

Russell, H. N., “On Meteoric Matter Near the Stars”, *The Astrophysical Journal*, vol. 69, p. 49, 1929. doi:10.1086/143158.

Rybicki, G. B. and Lightman, A. P., *Radiative Processes in Astrophysics*. 1986

Sądowski, A., “Slim Disks Around Kerr Black Holes Revisited”, *The Astrophysical Journal Supplement Series*, vol. 183, no. 2. pp. 171–178, 2009. doi: 10.1088/0067-0049/183/2/171.

Sadowski, A., “Slim accretion disks around black holes”, from *Nicolaus Copernicus Astronomical Center, arXiv e-prints*, 2011.

Sądowski, A., Narayan, R., Tchekhovskoy, A., and Zhu, Y., “Semi-implicit scheme for treating radiation under M1 closure in general relativistic conservative fluid dynamics codes”, *Monthly Notices of the Royal Astronomical Society*, vol. 429, no. 4. pp. 3533–3550, 2013. doi: 10.1093/mnras/sts632.

Sądowski, A., Narayan, R., Penna, R., and Zhu, Y., “Energy, momentum and mass outflows and feedback from thick accretion discs around rotating black holes”, *Monthly Notices of the Royal Astronomical Society*, vol. 436, no. 4. pp. 3856–3874, 2013. doi: 10.1093/mnras/stt1881.

Sądowski, A., Narayan, R., McKinney, J. C., and Tchekhovskoy, A., “Numerical simulations of super-critical black hole accretion flows in general relativity”, *Monthly Notices of the Royal Astronomical Society*, vol. 439, no. 1. pp. 503–520, 2014. doi: 10.1093/mnras/stt2479.

Sądowski, A., Narayan, R., Tchekhovskoy, A., Abarca, D., Zhu, Y., and McKinney, J. C., “Global simulations of axisymmetric radiative black hole accretion discs in general relativity with a mean-field magnetic dynamo”, *Monthly Notices of the Royal Astronomical Society*, vol. 447, no. 1. pp. 49–71, 2015. doi: 10.1093/mnras/stu2387.

Sądowski, A., Lasota, J.-P., Abramowicz, M. A., and Narayan, R., “Energy flows in thick accretion discs and their consequences for black hole feedback”, *Monthly Notices of the Royal Astronomical Society*, vol. 456, no. 4. pp. 3915–3928, 2016. doi: 10.1093/mnras/stv2854.

Sądowski, A., “Thin accretion discs are stabilized by a strong magnetic field”, *Monthly Notices of the Royal Astronomical Society*, vol. 459, no. 4. pp. 4397–4407, 2016. doi: 10.1093/mnras/stw913.

Sądowski, A., “Magnetic flux stabilizing thin accretion discs”, *Monthly Notices of the Royal Astronomical Society*, vol. 462, no. 1. pp. 960–965, 2016. doi: 10.1093/mnras/stw1852.

Sauer, T., “Nova Geminorum 1912 and the origin of the idea of gravitational lensing”, *Archive for History of Exact Sciences*, vol. 62, no. 1, pp. 1–22, 2008.

Schekochihin, A. A., Boldyrev, S. A., and Kulsrud, R. M., “Spectra and Growth Rates of Fluctuating Magnetic Fields in the Kinematic Dynamo Theory with Large Magnetic Prandtl Numbers”, *The Astrophysical Journal*, vol. 567, no. 2, pp. 828–852, 2002. doi:10.1086/338697.

Schekochihin, A. A., Maron, J. L., Cowley, S. C., and McWilliams, J. C., “The Small-Scale Structure of Magnetohydrodynamic Turbulence with Large Magnetic Prandtl Numbers”, *The Astrophysical Journal*, vol. 576, no. 2, pp. 806–813, 2002. doi:10.1086/341814.

Schekochihin, A. A., Cowley, S. C., Maron, J. L., and McWilliams, J. C., "Critical Magnetic Prandtl Number for Small-Scale Dynamo", *Physical Review Letters*, vol. 92, no. 5, 2004. doi:10.1103/PhysRevLett.92.054502.

Schekochihin, A. A., Haugen, N. E. L., Brandenburg, A., Cowley, S. C., Maron, J. L., and McWilliams, J. C., "The Onset of a Small-Scale Turbulent Dynamo at Low Magnetic Prandtl Numbers", *The Astrophysical Journal*, vol. 625, no. 2, pp. L115–L118, 2005. doi:10.1086/431214.

Schekochihin, A. A., Iskakov, A. B., Cowley, S. C., McWilliams, J. C., Proctor, M. R. E., and Yousef, T. A., "Fluctuation dynamo and turbulent induction at low magnetic Prandtl numbers", *New Journal of Physics*, vol. 9, no. 8, p. 300, 2007. doi:10.1088/1367-2630/9/8/300.

Schutz, B. F., *A First Course in General Relativity*. 1985.

Schutz, B., *A First Course in General Relativity*. 2009.

Schwarzschild, K., "On the Gravitational Field of a Mass Point According to Einstein's Theory", *Abh. Konigl. Preuss. Akad. Wissenschaften Jahre 1906,92, Berlin,1907*, vol. 1916, pp. 189–196, 1916, translation and foreword in English by S. Antoci & A. Loinger, 1999.

Shakura, N. I. and Sunyaev, R. A., "Reprint of 1973A&A....24..337S. Black holes in binary systems. Observational appearance.", *Astronomy and Astrophysics*, vol. 500. pp. 33–51, 1973.

Shapiro, S. L., Lightman, A. P., and Eardley, D. M., "A two-temperature accretion disk model for Cygnus X-1: structure and spectrum.", *The Astrophysical Journal*, vol. 204. pp. 187–199, 1976. doi: 10.1086/154162.

Shapiro, S. L. and Teukolsky, S. A., *Black holes, white dwarfs, and neutron stars : the physics of compact objects*. 1983.

Shibata, K., Tajima, T., and Matsumoto, R., "Magnetic Accretion Disks Fall into Two Types", *The Astrophysical Journal*, vol. 350, p. 295, 1990. doi:10.1086/168382.

Spruit, H. C., "Theory of Magnetically Powered Jets", in *Lecture Notes in Physics, Berlin Springer Verlag*, vol. 794, 2010, p. 233. doi:10.1007/978-3-540-76937-8_9.

Stirling, A. M., Spencer, R. E., de la Force, C. J., Garrett, M. A., Fender, R. P., and Ogley, R. N., "A relativistic jet from Cygnus X-1 in the low/hard X-ray state", *Monthly Notices of the Royal Astronomical Society*, vol. 327, no. 4, pp. 1273–1278, 2001. doi:10.1046/j.1365-8711.2001.04821.x.

Synge, J. L., *Relativity: The special theory*, North-Holland Publishing Company, Amsterdam, 1956.

Synge, J. L., *Relativity: The general theory*, North-Holland Publishing Company, Amsterdam, 1960.

Takahashi, A., Fukue, J., Sanbuichi, K., and Umemura, M., "Dynamical Stability of Cosmological Accretion Disks Embedded in External Radiation Fields: Optically-Thick Case", *Publications of the Astronomical Society of Japan*, vol. 47, pp. 425–428, 1995.

Takahashi, R., "Equations of general relativistic radiation hydrodynamics in Kerr space-time", *Monthly Notices of the Royal Astronomical Society*, vol. 382, no. 3. pp. 1041–1049, 2007. doi: 10.1111/j.1365-2966.2007.12030.x.

Tauris, T. M., van den Heuvel, E. P. J., and Savonije, G. J., "Formation of Millisecond Pulsars with Heavy White Dwarf Companions:Extreme Mass Transfer on Subthermal Timescales", *The Astrophysical Journal*, vol. 530, no. 2, pp. L93–L96, 2000. doi:10.1086/312496.

Tauris, T. M. and van den Heuvel, E. P. J., "Formation and evolution of compact stellar X-ray sources", in *Compact stellar X-ray sources*, vol. 39, 2006, pp. 623–665.

Taylor, G. B. and Zavala, R., "Are There Rotation Measure Gradients Across Active Galactic Nuclei Jets?", *The Astrophysical Journal*, vol. 722, no. 2, pp. L183–L187, 2010. doi:10.1088/2041-8205/722/2/L183.

Tchekhovskoy, A., Narayan, R., and McKinney, J. C., "Black Hole Spin and The Radio Loud/Quiet Dichotomy of Active Galactic Nuclei", *The Astrophysical Journal*, vol. 711, no. 1, pp. 50–63, 2010. doi:10.1088/0004-637X/711/1/50.

Tchekhovskoy, A., Narayan, R., and McKinney, J. C., “Efficient generation of jets from magnetically arrested accretion on a rapidly spinning black hole”, *Monthly Notices of the Royal Astronomical Society*, vol. 418, no. 1, pp. L79–L83, 2011. doi:10.1111/j.1745-3933.2011.01147.x.

Teo, E., “Spherical Photon Orbits Around a Kerr Black Hole”, *General Relativity and Gravitation*, vol. 35, no. 11, pp. 1909–1926, 2003. doi:10.1023/A:1026286607562.

Tetarenko, B. E., Sivakoff, G. R., Heinke, C. O., and Gladstone, J. C., “WATCHDOG: A Comprehensive All-sky Database of Galactic Black Hole X-ray Binaries”, *The Astrophysical Journal Supplement Series*, vol. 222, no. 2, 2016. doi:10.3847/0067-0049/222/2/15.

Thompson, T. A., “A noninteracting low-mass black hole-giant star binary system”, *Science*, vol. 366, no. 6465

Thorne, K. S. and Price, R. H., “Cygnus X-1: an interpretation of the spectrum and its variability.”, *The Astrophysical Journal*, vol. 195, pp. L101–L105, 1975. doi:10.1086/181720.

Thorne, K. S. and MacDonald, D., “Electrodynamics in Curved Spacetime - 3+1 Formulation”, *Monthly Notices of the Royal Astronomical Society*, vol. 198. p. 339, 1982. doi: 10.1093/mnras/198.2.339.

Tsvetanov, Z. I., Allen, M. G., Ford, H. C., and Harms, R. J., “Morphology of the Nuclear Disk in M 87”, in *The Radio Galaxy Messier 87*, vol. 530, 1999, p. 301. doi:10.1007/BFb0106441.

Turner, N. J., Stone, J. M., Krolik, J. H., and Sano, T., “Local Three-dimensional Simulations of Magnetorotational Instability in Radiation-dominated Accretion Disks”, *The Astrophysical Journal*, vol. 593, no. 2, pp. 992–1006, 2003. doi:10.1086/376615.

Urry, C. M. and Padovani, P., “Unified Schemes for Radio-Loud Active Galactic Nuclei”, *Publications of the Astronomical Society of the Pacific*, vol. 107, p. 803, 1995. doi:10.1086/133630.

Uttley, P., McHardy, I. M., and Vaughan, S., “Non-linear X-ray variability in X-ray binaries and active galaxies”, *Monthly Notices of the Royal Astronomical Society*, vol. 359, no. 1, pp. 345–362, 2005. doi:10.1111/j.1365-2966.2005.08886.x.

Vainshtein, S. I. and Cattaneo, F., “Nonlinear Restrictions on Dynamo Action”, *The Astrophysical Journal*, vol. 393. p. 165, 1992. doi: 10.1086/171494.

van Ballegooijen, A. A., “Magnetic Fields in the Accretion Disks of Cataclysmic Variables”, in *Accretion Disks and Magnetic Fields in Astrophysics*, vol. 156, 1989, p. 99. doi: 10.1007/978-94-009-2401-7_10.

van der Klis, M. and Bonnet-Bidaud, J. M., “The X-ray ephemeris of Cygnus X-3.”, *Astronomy and Astrophysics*, vol. 214, pp. 203–208, 1989.

van der Klis, M., “Rapid Variability in X-ray Binaries - Toward a Unified Description”, in *The Lives of the Neutron Stars*, 1995, vol. 450, p. 301.

van der Klis, M., “A review of rapid X-ray variability in X-ray binaries”, *arXiv e-prints*, 2004.

van Haaften, L. M., Nelemans, G., Voss, R., Wood, M. A., and Kuijpers, J., “The evolution of ultracompact X-ray binaries”, *Astronomy and Astrophysics*, vol. 537, 2012. doi:10.1051/0004-6361/201117880.

Verbunt, F., “Observations of Accretion Discs in X-ray Binaries”, in *Astrophysical Discs - an EC Summer School*, 1999, vol. 160, p. 21.

Visser, M., “The Kerr spacetime: A brief introduction”, *arXiv e-prints*, 2007.

Vitrishchak, V. M. and Gabuzda, D. C., “New measurements of the circular polarization of the radio emission of Active Galactic Nuclei on parsec scales”, *Astronomy Reports*, vol. 51, no. 9, pp. 695–708, 2007. doi:10.1134/S1063772907090016.

Vlahakis, N. and Königl, A., “Magnetic Driving of Relativistic Outflows in Active Galactic Nuclei. I. Interpretation of Parsec-Scale Accelerations”, *The Astrophysical Journal*, vol. 605, no. 2, pp. 656–661, 2004. doi:10.1086/382670.

Wald, R. M., *General relativity*. 1984.

Walker, R. C., Dhawan, V., Romney, J. D., Kellermann, K. I., and Vermeulen, R. C., “VLBA Absorption Imaging of Ionized Gas Associated with the Accretion Disk in NGC 1275”, *The Astrophysical Journal*, vol. 530, no. 1, pp. 233–244, 2000. doi:10.1086/308372.

Weinberg, S., *Gravitation and Cosmology: Principles and Applications of the General Theory of Relativity*. 1972.

Weyl, H., “Zur Gravitationstheorie”, *Annalen der Physik*, vol. 359, no. 18, pp. 117–145, 1917. doi:10.1002/andp.19173591804.

Wheeler, Craig J., “Summary of the workshop on gamma-ray burst afterglows at the 34th COSPAR meeting”, *Advances in Space Research*, vol. 34, no. 12, pp. 2744–2749, 2004. doi:10.1016/j.asr.2003.01.042.

Widrow, L. M., “Origin of galactic and extragalactic magnetic fields”, *Reviews of Modern Physics*, vol. 74, no. 3, pp. 775–823, 2002. doi:10.1103/RevModPhys.74.775.

Wilkins, D. C., “Bound Geodesics in the Kerr Metric”, *Physical Review D*, vol. 5, no. 4. pp. 814–822, 1972. doi: 10.1103/PhysRevD.5.814.

Wu, K. and Fuerst, S. V., “General Relativistic Radiative Transfer”, in *Astrophysics of Compact Objects*, 2008, vol. 968, pp. 411–413. doi: 10.1063/1.2840444.

Wu, K., Fuerst, S. V., Mizuno, Y., Nishikawa, K.-I., Branduardi-Raymont, G., and Lee, K.-G., “General Relativistic Radiative Transfer: Applications to Black-Hole Systems”, *Chinese Journal of Astronomy and Astrophysics Supplement*, vol. 8. pp. 226–236, 2008.

Wu, K., Ball, W., and Fuerst, S. V., “Radiative transfer in black hole systems”, from *Vulcano08 Workshop* on *"Frontier Objects in Astrophysics and Particle Physics"*, *arXiv e-prints*, 2008.

Younsi, Z., Wu, K., and Fuerst, S. V., “General relativistic radiative transfer: formulation and emission from structured tori around black holes”, *Astronomy and Astrophysics*, vol. 545. 2012. doi: 10.1051/0004-6361/201219599.

Younsi, Z., “General relativistic radiative transfer in black hole systems”, PhDT, 2014.

Younsi, Z., Zhidenko, A., Rezzolla, L., Konoplya, R., and Mizuno, Y., “New method for shadow calculations: Application to parametrized axisymmetric black holes”, *Physical Review D*, vol. 94, no. 8. 2016. doi: 10.1103/PhysRevD.94.084025.

Younsi, Z., Psaltis, D., and Özel, F., “Black Hole Images as Tests of General Relativity: Effects of Spacetime Geometry”, *The Astrophysical Journal*, vol. 942, no. 1, 2023. doi:10.3847/1538-4357/aca58a.

Yuan, F. and Narayan, R., “Hot Accretion Flows Around Black Holes”, *Annual Review of Astronomy and Astrophysics*, vol. 52, pp. 529–588, 2014. doi:10.1146/annurev-astro-082812-141003.

Yuan, Y., Blandford, R. D., and Wilkins, D. R., “Black hole magnetosphere with small-scale flux tubes”, *Monthly Notices of the Royal Astronomical Society*, vol. 484, no. 4, pp. 4920–4932, 2019. doi:10.1093/mnras/stz332.

Zavala, R. T. and Taylor, G. B., “Faraday Rotation Measures in the Parsec-Scale Jets of the Radio Galaxies M87, 3C 111, and 3C 120”, *The Astrophysical Journal*, vol. 566, no. 1, pp. L9–L12, 2002. doi:10.1086/339441.

Zavala, R. T. and Taylor, G. B., “A View through Faraday's Fog: Parsec-Scale Rotation Measures in Active Galactic Nuclei”, *The Astrophysical Journal*, vol. 589, no. 1, pp. 126–146, 2003. doi:10.1086/374619.

Zavala, R. T. and Taylor, G. B., “A View through Faraday's Fog. II. Parsec-Scale Rotation Measures in 40 Active Galactic Nuclei”, *The Astrophysical Journal*, vol. 612, no. 2, pp. 749–779, 2004. doi:10.1086/422741.

Zavala, R. T. and Taylor, G. B., “Faraday Rotation Measure Gradients from a Helical Magnetic Field in 3C 273”, *The Astrophysical Journal*, vol. 626, no. 2, pp. L73–L76, 2005. doi:10.1086/431901.

Zhang, S. N., Cui, W., and Chen, W., “Black Hole Spin in X-Ray Binaries: Observational Consequences”, *The Astrophysical Journal*, vol. 482, no. 2, pp. L155–L158, 1997. doi:10.1086/310705.

Zrake, J. and MacFadyen, A. I., “Numerical Simulations of Driven Relativistic Magnetohydrodynamic Turbulence”, *The Astrophysical Journal*, vol. 744, no. 1. 2012. doi: 10.1088/0004-637X/744/1/32.